TU Clausthal

UNIVERSITÉ DE LORRAINE

Numerical and Analytical Modeling of Gas Mixing and Bio-Reactive Transport during Underground Hydrogen Storage

Doctoral Thesis
(Dissertation)

to be awarded under international thesis co-mentorship the degree

Doctor of Engineering (Dr.-Ing.)
approved by the Faculty of Energy and Economic Sciences,
Clausthal University of Technology

Docteur de l'Université de Lorraine
(Mention Mécanique et Energétique)

submitted by
Birger Hagemann

Date of oral examination
July 3, 2017

Bibliografische Information der Deutschen Nationalbibliothek
Die Deutsche Nationalbibliothek verzeichnet diese Publikation in der Deutschen Nationalbibliografie; detaillierte bibliografische Daten sind im Internet über http://dnb.d-nb.de abrufbar.
1. Aufl. - Göttingen: Cuvillier, 2018

Dissertation Technische Universität Clausthal

D 104

Dean of the Faculty of Energy and Economic Sciences
Prof. Dr. rer. nat. Bernd Lehmann

Director of the Doctoral School EMMA
Prof. Dominique Daloz

Chairperson of the Board of Examiners:
Prof. Dr. rer. nat. Bernd Lehmann

Supervising Tutors:
Prof. Dr. mont. Leonhard Ganzer
Prof. Mikhail Panfilov

External Reviewers:
Prof. Dr. rer. nat. Reinhard Gaupp
Prof. Dr. rer. nat. Dr. rer. pol. Rudolf Hilfer

Nonnenstieg 8, 37075 Göttingen
Telefon: 0551-54724-0
Telefax: 0551-54724-21
www.cuvillier.de

1. Auflage, 2018
Gedruckt auf umweltfreundlichem, säurefreiem Papier aus nachhaltiger Forstwirtschaft.

ISBN 978-3-7369-9714-1
eISBN 978-3-7369-8714-2

Abstract

In the context of energy revolution large quantities of storage capacity are required for the integration of strongly fluctuating energy production from wind and solar power plants. The conversion of electrical energy into chemical energy in the form of hydrogen is one of the technical possibilities. The technology of underground hydrogen storage (UHS), where hydrogen is stored in subsurface formations similar to the storage of natural gas, is currently in the exploratory focus of several European countries.

Hydrogen has a very low density and viscosity. Consequently, a high tendency for an instable displacement in the subsurface including gravity overriding and viscous fingering during the injection period is expected. Despite that, bio-chemical reactions could have an important role in UHS. The fact that hydrogen is a favored substrate for several anaerobic microorganisms induces their growth and results in a degradation of hydrogen. In particular the activity of methanogenic archaea can lead to drastic variations in the gas composition of the produced gas which were observed in some former town gas storages. To investigate the hydrodynamic and bio-chemical behavior in UHS, different analytical and numerical approaches were applied.

The gravity-driven displacement, when hydrogen is injected at the bottom of a water saturated stratified reservoir, was modeled analytically. The analytical solution was obtained by combining the method of characteristics with a graphical construction. The exact rising velocity was determined for different stratified reservoirs and for fluid phases out of two and three components. Comparisons to the numerical solution are also shown. In addition, a mathematical model for the bio-reactive transport in UHS was developed. The model is based on continuum scale and couples compositional two-phase flow with microbial growth and bio-chemical reactions within the porous medium. The stability of the mathematical model was investigated by reducing it to a pair of differential equations. Based on the results, numerical simulations were performed under limit cycle and Turing

conditions which show different oscillatory regimes. Finally, the mathematical model was implemented numerically on the basis of DuMu$^{\mathrm{X}}$ which is an open-source C++ code for the simulation of multi-phase multi-component flow and transport in porous media. Storage scenarios were simulated which include the development of the storage and the subsequent cyclic injection and production over several years. It was proven that the low density and viscosity of hydrogen make the displacement of water more instable than in the case of methane injection. Additionally, it was shown that mechanical dispersion and bio-chemical reactions have an important influence in predictive studies. Significant energy losses could occur due to bio-chemical gas transformations.

Kurzfassung

Im Zusammenhang mit der Energiewende sind große Mengen an Speicherkapazität erforderlich, um die stark fluktuierende Energieerzeugung durch Wind- und Solarkraftwerke zu integrieren. Die Umwandlung von elektrischer Energie in chemische Energie in der Form von Wasserstoff ist eine der technischen Möglichkeiten. Die Technologie der Untergrundwasserstoffspeicherung, wobei Wasserstoff in unterirdischen Gesteinsformationen, ähnlich wie bei der Speicherung von Erdgas, gespeichert wird, ist derzeit ein Forschungsschwerpunkt mehrerer europäischer Länder.

Wasserstoff hat eine sehr geringe Dichte und Viskosität. Folglich wird eine hohe Tendenz für eine instabile Verdrängung erwartet, einschließlich einer gravitationsbedingten Segregation und der Bildung von viskosen Fingern. Zusätzlich können biochemische Reaktionen eine wichtige Rolle in Untergrundwasserstoffspeichern spielen. Die Tatsache, dass Wasserstoff ein geeignetes Substrat für viele anaerobe mikrobielle Spezies ist, regt ihr Wachstum an und führt zu einer Umsetzung des Wasserstoffs. Insbesondere kann die Aktivität von methanogenen Archaeen zu drastischen Veränderungen in der Zusammensetzung des Gases führen, wie es bei einigen ehemaligen Stadtgasspeichern beobachtet wurde. Um das hydrodynamische und biochemische Verhalten in Untergrundwasserstoffspeichern zu untersuchen, wurden unterschiedliche analytische und numerische Methoden angewandt.

Die schwerkraftgetriebene Verdrängung, wenn Wasserstoff am Boden einer wassergesättigten Lagerstätte injiziert wird, wurde analytisch modelliert. Die analytische Lösung ist durch Kombination der Methode der Charakteristiken und einer grafischen Konstruktion hergeleitet worden. Die exakte Aufstiegsgeschwindigkeit wurde für verschiedene geschichtete Lagerstätten und für Fluidphasen aus zwei und drei Komponenten bestimmt. Vergleiche mit der numerischen Lösung werden ebenfalls gezeigt. Darüber hinaus wurde ein mathematisches Modell für den bioreaktiven Transport in Untergrundwasserstoffspeichern entwickelt. Das Modell ist auf der Kontinuumsskala

formuliert und koppelt die Mehrkomponenten-Zweiphasenströmung mit mikrobiellem Wachstum und biochemischen Reaktionen innerhalb des porösen Mediums. Die Stabilität des mathematischen Modells ist untersucht worden, indem es auf ein Paar von Differentialgleichungen reduziert wurde. Basierend auf den Ergebnissen wurden numerische Simulationen unter Grenzzyklus- und Turing-Bedingungen durchgeführt, die unterschiedliche oszillierende Regime zeigen. Das mathematische Modell ist numerisch auf der Basis von DuMu$^{\mathrm{X}}$, einem Open-Source-Code für die Simulation der Mehrkomponenten-Mehrphasenströmung und Transports in porösen Medien, implementiert worden. Verschiedene Speicherszenarien wurden simuliert, die die Errichtung des Speichers und die anschließende zyklische Injektion und Produktion über mehrere Jahre umfassen. Es ist bewiesen worden, dass die geringe Dichte und Viskosität von Wasserstoff die Verdrängung von Wasser instabiler macht als bei der Methaninjektion. Darüber hinaus zeigte sich, dass mechanische Dispersion und biochemische Reaktionen einen wichtigen Einfluss in Vorhersagestudien haben. Signifikante Energieverluste können durch biochemische Umwandlungen des gespeicherten Gases auftreten.

Résumé

En rapport avec la transition énergétique, d'importantes capacités de stockage énergétique sont nécessaires pour intégrer la forte variation de la production énergétique au travers des centrales éoliennes et photovoltaïques. La transformation de l'énergie électrique en énergie chimique sous forme d'hydrogène est l'une des possibles techniques. La technologie de stockage de l'hydrogène souterrain, selon laquelle l'hydrogène est stocké dans les formations souterraines semblables au stockage du gaz naturel est actuellement un axe de recherche de plusieurs états européens.

L'hydrogène a une très faible densité et une très faible viscosité. Par conséquent une forte tendance à un déplacement instable est à attendre, en particulier la séparation gravitationnelle et la formation de doigts visqueux. En outre, les réactions biochimiques peuvent jouer un rôle majeur dans le stockage de l'hydrogène souterrain. Le fait que l'hydrogène soit un substrat approprié pour de nombreuses espèces microbiennes anaérobiques, stimule son accroissement et conduit à sa transformation. En particulier, l'activité des archéens méthanogènes peut conduire à un changement drastique dans la composition du gaz, comme observé dans certains anciens stockages de gaz de ville. Pour analyser le comportement hydrodynamique et biochimique dans les stockages de l'hydrogène souterrains, diverses méthodes analytiques et numériques ont été appliquées.

Le déplacement par gravité lorsque l'hydrogène est injecté au fond d'un lieu de stockage saturé en eau a été analytiquement modélisé. La solution analytique a été déduite à travers la méthode des caractéristiques et une construction graphique. La vitesse exacte de montée a été déterminée pour différentes couches de stockage et pour des phases de fluides à deux et trois composants. Les comparaisons avec le résultat numérique seront également montrées. En outre, un modèle mathématique pour le transport bioréactif dans le stockage de l'hydrogène souterrain a été développé. Le modèle est formulé à l'échelle du continuum et couple le flux multiconstituants à deux phases avec la croissance microbienne et les réactions biochi-

miques dans le milieu poreux. La stabilité du modèle mathématique a été analysée, ceci en le réduisant à une paire d'équations différentielles. En se basant sur les résultats, les simulations numériques qui montrent différents régimes oscillatoires, ont été réalisées sous les conditions de cycle limite et de Turing. Le modèle mathématique a été implémenté numériquement sur la base de DuMu$^{\mathrm{X}}$, un code open source pour la simulation de flux et transport multiphasique-multiconstituant dans un milieu poreux. Différents scénarios de stockage ont été simulés, ces derniers incluant la formation de stockage et les injections et productions cycliques sur plusieurs années. Il a été prouvé que la faible densité et viscosité de l'hydrogène sont à l'origine du déplacement plus instable de l'eau comparé à l'injection du méthane. De plus, il a été constaté que la dispersion mécanique et les réactions biochimiques ont une influence importante dans les études de prédiction. Les pertes notables d'énergie peuvent apparaître au travers des transformations biochimiques des gaz stockés.

Preface

This dissertation was written under French-German thesis co-mentorship. The idea resulted from joint research activities between the Clausthal University of Technology and the University of Lorraine in the research project H2STORE. During the work on this thesis I have lived for 14 months in Nancy where I worked at the LEMTA (University of Lorraine) in the research group "Multiphase flow in porous media and geo-energy" headed by Prof. Mikhail Panfilov. The remaining time I was working at the Institute of Petroleum Engineering (Clausthal University of Technology) in the reservoir engineering department headed by Prof. Dr. Leonhard Ganzer. I would like to thank all colleagues, students and friends who have accompanied me during this time, especially I would like to thank:

- Prof. Leonhard Ganzer for providing me a stable fundament to perform my research and his always helpful advices
- Prof. Mikhail Panfilov for guiding me in the right scientific way but still leaving me the freedom to work independently and to develop my own ideas
- Prof. Reinhard Gaupp and Prof. Rudolf Hilfer for preparing the external reviews of my thesis
- Mojdeh Rasoulzadeh for all the advices during my work with DuMu$^{\mathrm{X}}$ and her always kind help concerning the administrative barriers during my time in France
- Bernd Flemisch for his kind and fast help when I faced any troubles with DuMu$^{\mathrm{X}}$
- Felix Feldmann for his contribution in the 3D simulation study
- Gion Strobel for his help with the numerical studies
- Rayner Susanto for his help in the literature search for microbial kinetic parameters

Contents

Abstract III

Kurzfassung V

Résumé VII

Preface IX

Contents XV

List of Figures XVII

List of Tables XXIII

1 Introduction 1
- 1.1 Motivation . . . 2
- 1.2 Underground hydrogen storage . . . 3
- 1.3 State of the art (applications) . . . 5
- 1.4 Recent related research projects . . . 6
  - 1.4.1 H2STORE . . . 6
  - 1.4.2 HyUnder . . . 6
  - 1.4.3 Hychico . . . 7
  - 1.4.4 ANGUS+ . . . 7
  - 1.4.5 Underground Sun Storage . . . 8
  - 1.4.6 HyINTEGER . . . 8
- 1.5 Outline of the thesis . . . 8

2 Literature review 11
- 2.1 Hydrodynamics in UHS . . . 11
  - 2.1.1 Gas-water flow . . . 12
  - 2.1.2 Mixing in gas-gas displacement . . . 17
- 2.2 Microbiology in UHS . . . 20

2.2.1 Cell structure of archaea and bacteria 20
2.2.2 Cell duplication and metabolism 21
2.2.3 Microbial populations and growth 23
2.2.4 Relevant microbial species in UHS 25
2.2.5 Microbial transport and structures in porous media . . 26
2.3 Modeling of bio-reactive transport in porous media 29
2.3.1 Single-phase models for groundwater applications . . . 29
2.3.2 Two-phase models for gas storage applications 32
2.3.3 Review of tools for (bio-)reactive transport modeling . 34

3 Analytical modeling of gravity-driven displacement 39
3.1 Case study description 41
3.2 Balance equations for compositional two-phase flow 42
3.3 Reduction to a canonical model 45
3.4 Initial and boundary conditions 47
3.5 Hugoniot conditions, stability conditions and continuity of fractional flow 48
3.6 Two-component flow 49
3.6.1 Structure of the generalized fractional flow function . 50
3.6.2 Graphical construction of the solution 51
3.6.3 Solution before reaching the barrier 54
3.6.4 Solution after reaching the barrier 54
3.6.5 Characteristic points of the solution 56
3.6.6 Solution after reaching the second barrier 58
3.6.7 Gas rising velocity and growth velocity of gas accumulations 59
3.6.8 Comparison with immiscible two-phase flow 60
3.7 Three-component flow 62
3.7.1 Thermodynamics of three-component mixtures 62
3.7.2 Canonical model for three-component flow 64
3.7.3 Structure of the solution 65
3.7.4 Solution of the problem before reaching the barrier . . 66
3.7.5 Moment of reaching the barrier 67
3.7.6 Evolution of the reverse wave under the barrier 68
3.8 Comparison to two-dimensional problem 69
3.8.1 Formulation of 2D problem 69
3.8.2 Numerical implementation 70

3.8.3 Equivalence between 2D flow around impermeable barriers and 1D flow through low-permeable barriers . . . 73
3.9 Summary and conclusions . . . 74

4 Mathematical model for bio-reactive two-phase transport 77
4.1 Physico-chemical processes . . . 77
4.2 Bio-chemical processes . . . 80
4.3 Review of models for microbial growth and decay . . . 82
4.4 Coupling of processes . . . 84
4.5 Transformation to dimensionless form . . . 87
4.6 Parameters for microbial population dynamics . . . 89
4.7 Summary and conclusions . . . 92

5 Stability of the dynamic system 95
5.1 Reduction to a system of two ordinary differential equations . 96
5.2 Linear stability analysis . . . 99
5.3 Turing conditions . . . 104
5.4 Numerical simulations . . . 110
5.4.1 Limit cycle behavior . . . 111
5.4.2 Turing instability . . . 111
5.5 Summary and conclusions . . . 112

6 Numerical modeling of storage cycles 115
6.1 Numerical implementation . . . 115
6.1.1 Spatial and temporal discretization . . . 116
6.1.2 Iterative procedure . . . 118
6.1.3 Adaptation of the governing equation system . . . 119
6.1.4 Phase equilibrium and hydrodynamic parameters . . . 120
6.1.5 Grid generation and rock parameters . . . 122
6.1.6 Adjustments for heterogeneous corner-point grids . . . 125
6.1.7 Storage initialization . . . 129
6.1.8 Modeling of storage wells . . . 131
6.1.8.1 Rate-controlled storage wells . . . 131
6.1.8.2 Pressure-controlled storage wells . . . 132
6.1.9 Operation schedule and time stepping . . . 133
6.1.10 Material balance error . . . 134
6.1.11 Post-processing and visualization . . . 136
6.2 Case studies . . . 136

6.2.1 Gas-water displacement in a 2D synthetic reservoir . . 136
6.2.2 Storage scenario in a 2D synthetic reservoir 140
6.2.3 Storage scenario in a 3D realistic reservoir 146
6.3 Summary and conclusions 153

7 Conclusions **157**

Bibliography **161**

Appendices **175**

A Excerpts from the source code **177**
A.1 Evaluation of source/sink terms 177
A.2 Reservoir initialization 178
A.3 Rate-controlled injection well 180
A.4 Rate-controlled production well 181
A.5 Pressure-controlled injection well 182
A.6 Pressure-controlled production well 182

B Spatial plots from the 2D storage scenario **185**

C Spatial plots from the 3D storage scenario **193**
C.1 100 $mol\%$ H_2 injection 194
C.2 95 $mol\%$ H_2 and 5 $mol\%$ CO_2 injection 197

D Ausführliche Zusammenfassung **201**
Einleitung 201
Literaturrecherche 202
Analytische Modellierung des schwerkraftgetriebenen Zweiphasenflusses 205
Mathematisches Modell für den bioreaktiven Zweiphasenfluss . . . 207
Stabilität des dynamischen Systems 208
Numerische Modellierung von Speicherzyklen 209
Schlussfolgerungen 210

E Résumé détaillé **213**
Introduction 213
Revue de la littérature 215
Modélisation analytique de flux à deux phases par gravité 217

Modèle mathématique pour le transport bioréactif à deux phases . 219
Stabilité du système dynamique 220
Modélisation numérique des cycles de stockage 221
Conclusions 222

List of Figures

2.1 Sketch of fluid distribution on pore scale: For a gas-water system the wetting phase is water and the non-wetting phase is gas [59] . . . 13
2.2 From pore scale to continuum scale [59] . . . 13
2.3 Saturation versus distance in two-phase displacement process: The example shows the displacement of oil by water what is qualitatively equal to the displacement of water by gas [31] . . . 14
2.4 Viscous fingers around an injection point in a Hele-Shaw cell [101] . . . 16
2.5 Segregated downdip displacement process: a) instable, b) stable [31] . . . 17
2.6 The injection of gas into an anticline trap [102] . . . 18
2.7 Outflow concentration of the injected tracer versus produced pore volume [67] . . . 19
2.8 Sketch of the cell structure [30] . . . 21
2.9 Duplication of a microbial cell [30] . . . 22
2.10 Typical growth curve of a microbial population [122] . . . 23
2.11 Image of a biofilm from a scanning electron microscope, B: microorganism, F: EPS, P: particulate matter, S: substrate [14] 28

3.1 Sketch of "selective technology" . . . 40
3.2 1D geometry . . . 41
3.3 Diagram of fractional flow F^1 versus total concentration C^1 of the light component and the solution pathway for the two-component mixture of (a) H_2 and H_2O and (b) CO_2 and H_2O; curves I and II correspond to media I and II. Red lines are the upward shocks, green lines are the reverse downward shocks under the barriers, blue lines are the immobile shocks at the contact between two media. . . . 52
3.4 Propagation of the total concentration C^1 before reaching the first barrier . . . 55

3.5 Propagation of the total concentration C^1 after passing the first barrier . . . 56
3.6 Diagram of fractional flow F^1 versus total concentration C^1 for H_2 and H_2O, for highly permeable medium I and two low-permeable barriers II and III: Red lines are the upward shocks, green lines are the reverse downward shocks under the barriers, blue lines are the immobile shocks at the contact between two media. . . . 59
3.7 Propagation of the total concentration C^1 after passing the second barrier for the system H_2 and H_2O (after 3 days) . . . 60
3.8 Dimensionless rate of hydrogen rising along x . . . 61
3.9 Dimensionless growth velocity of the gas accumulation below the barriers . . . 61
3.10 Comparison of the two-phase miscible flow and immiscible flow 62
3.11 Ternary phase diagram for the mixture H_2, CO_2, H_2O at 400 bar and 125 $°C$ . . . 63
3.12 Fractional flow of the lightest component, F^1, for α^0 (black curves) and α^{inj} (blues curves) for media I and media II; the straight lines correspond to upward shocks (red), reserve downward shocks (green) and immobile discontinuities (blue) 66
3.13 Total concentration of the light component (hydrogen) . . . 67
3.14 Graphical construction of the reverse wave: Decomposition of the unstable shock EB into two shocks EM and MB . . . 69
3.15 Evolution of reserve wave for the light component (hydrogen) 70
3.16 H_2 concentration in the 2D domain . . . 73
3.17 Average total concentration of hydrogen along the vertical axis for the 2D model with impermeable barriers (red curve) and the 1D analytical solution with low permeable barriers (black curve) . . . 74

4.1 Comparison of different models for microbial population dynamics . . . 84

5.1 Gas composition at well 44 of the Lobodice town gas storage, +: H_2 vol %, □: CH_4 vol %, ◇: CH_4/N_2 ratio [21] . . . 96
5.2 Determinant-trace diagram [2] . . . 101

5.3 Bifurcation diagram for n vs. q based on an example parameter set (α = 1, β = 1, δ^{H_2} = 1, δ^{CO_2} = 0.25 and $C^{H2,0}$ = 1, $C^{CO2,0}$ = 1) . . . 104
5.4 Bifurcation diagram for C vs. q based on an example parameter set (α = 1, β = 1, δ^{H_2} = 1, δ^{CO_2} = 0.25 and $C^{H2,0}$ = 1, $C^{CO2,0}$ = 1) . . . 105
5.5 Limit cycle in the three-dimensional space according to equation system 5.7 to 5.9 for α = 1, β = 1, δ^{H_2} = 1, δ^{CO_2} = 0.25, $C^{H2,0}$ = 1, $C^{CO2,0}$ = 1, q^{H_2} = 0.8 and q^{CO_2} = 0.2 . . . 105
5.6 Turing space for the rate q versus the ratio of diffusion coefficients d for a fixed set of parameters (α = 1, β = 1, δ^{H_2} = 1, δ^{CO_2} = 0.25, $C^{H2,0}$ = 1 and $C^{CO2,0}$ = 1) . . . 110
5.7 Temporal evolution of the microbial density and gas phase concentrations in the reservoir . . . 111
5.8 Temporal evolution of number of microorganisms . . . 112
5.9 Temporal evolution of H_2 concentration in the gas phase . . . 113
5.10 Temporal evolution of CH_4 concentration in the gas phase . . . 114

6.1 Schematic 2D grid for a cell-centered finite volume method . 116
6.2 Structure of the fully implicit scheme in DuMu$^{\text{X}}$ [43] . . . 118
6.3 2D grid model representing a vertical slice through an anticline structure . . . 123
6.4 2D grid model representing the top view of an storage reservoir 123
6.5 3D grid model . . . 124
6.6 Porosity shown on a slice through the 3D grid model (vertically stretched by a factor of 5) . . . 125
6.7 Horizontal permeability shown on a slice through the 3D grid model (vertically strechted by a factor of 5) . . . 125
6.8 Sketch of two cells in an unstructured grid with heterogeneous permeability . . . 127
6.9 Sketch of a "degenerate cell": It can be seen that L and $L^\star$ significantly deviate for the different cell centers . . . 129
6.10 Initial pressure on the vertical axis . . . 130
6.11 Initial water saturation on the vertical axis . . . 131
6.12 Material balance error versus time (3D study with 100 $mol\%$ H_2 injection and methanogenesis) . . . 135
6.13 Gas injection into the top center of a synthetic two-dimensional anticline structure . . . 138

6.12 Gas injection into the top center of a synthetic two-dimensional anticline structure (continued) . . . 139
6.13 Initial gas saturation (2D study) . . . 140
6.14 H_2 mole fraction for the base case after the first injection and the first idle period . . . 142
6.15 H_2 mole fraction for the case with mechanical dispersion after the first injection and the first idle period . . . 142
6.16 H_2 mole fraction for the case with bio-reactive effects after the first injection and the first idle period . . . 143
6.17 Microbial densities after $\tau = 0.3$ . . . 143
6.18 Microbial densities after the first injection period . . . 143
6.19 Mole fraction of the reaction products after the first injection period . . . 144
6.20 H_2S concentration in the produced gas stream (2D study) . . . 144
6.21 H_2 concentration in the produced gas stream (2D study) . . . 145
6.22 Hysteresis plot: Gas inventory versus average gas phase pressure (2D study) . . . 145
6.23 Initial gas phase pressure in $[Pa]$ (3D study) . . . 146
6.24 Initial gas saturation (3D study) . . . 146
6.25 Rate versus time: A positive rate refers to injection and a negative rate refers to withdrawal (3D study with 100 mol% H_2 injection) . . . 148
6.26 Average gas phase pressure versus time (3D study with 100 $mol\%$ H_2 injection) . . . 148
6.27 Hysteresis plot: Gas inventory in $[mol]$ versus average gas phase pressure (3D study) . . . 149
6.28 H_2 concentration in the withdrawn gas stream (3D study with 100 $mol\%$ H_2 injection) . . . 149
6.29 Total bio-chemical reaction rate versus time (3D study with 100 $mol\%$ H_2 injection) . . . 150
6.30 Rate versus time: A positive rate refers to injection and a negative rate refers to withdrawal (3D study with 95 $mol\%$ H_2 and 5 $mol\%$ CO_2 injection) . . . 152
6.31 Average gas phase pressure versus time (3D study with 95 $mol\%$ H_2 and 5 $mol\%$ CO_2 injection) . . . 152
6.32 Hysteresis plot: Gas inventory in $[mol]$ versus average gas phase pressure (3D study with 95 $mol\%$ H_2 and 5 $mol\%$ CO_2 injection) . . . 153

6.33 H_2 concentration in the withdrawn gas stream (3D study with 95 $mol\%$ H_2 and 5 $mol\%$ CO_2 injection) 153
6.34 Total bio-chemical reaction rate versus time (3D study with 95 $mol\%$ H_2 and 5 $mol\%$ CO_2 injection) 154

B.1 Spatial plots for the 2D case study after at dimensionless time of 2 (after the first injection period) 186
B.2 Spatial plots for the 2D case study after at dimensionless time of 2 (after the first injection period) 187
B.3 Spatial plots for the 2D case study after at dimensionless time of 4 (after the first idle period) 188
B.4 Spatial plots for the 2D case study after at dimensionless time of 4 (after the first idle period) 189
B.5 Spatial plots for the 2D case study after at dimensionless time of 6 (after the first production period) 190
B.6 Spatial plots for the 2D case study after at dimensionless time of 6 (after the first production period) 191

C.1 Spatial plots for the case study with 100 $mol\%$ H_2 injection after two months 194
C.2 Spatial plots for the case study with 100 $mol\%$ H_2 injection after 14 months 195
C.3 Spatial plots for the case study with 100 $mol\%$ H_2 injection after 36 months 196
C.4 Spatial plots for the case study with 95 $mol\%$ H_2 and 5 $mol\%$ CO_2 injection after two months 197
C.5 Spatial plots for the case study with 95 $mol\%$ H_2 and 5 $mol\%$ CO_2 injection after 14 months 198
C.6 Spatial plots for the case study with 95 $mol\%$ H_2 and 5 $mol\%$ CO_2 injection after 36 months 199

List of Tables

2.1 Comparison of tools for modeling (reactive) transport in underground reservoirs (some information is taken from Steefel et al. [120]) . . . 37

3.1 Fluid properties at 400 *bar* and 125 $^{\circ}C$ . . . 42
3.2 Two-phase equilibrium composition at 400 *bar* and 125 $^{\circ}C$ . . . 42

4.1 Kinetic parameters for methanogenic archaea . . . 91
4.2 Kinetic parameters for sulfate-reducing bacteria . . . 92
4.3 Kinetic parameters for homoacetogenic archaea . . . 92
4.4 Density of methanogenic archaea . . . 93
4.5 Density of sulfate-reducing bacteria . . . 93
4.6 Density of homoacetogenic archaea . . . 93
4.7 Density of iron(III)-reducing bacteria . . . 93

5.1 Stability of ODE systems [66] . . . 100
5.2 Stability behaviors for different rates q based on an example parameter set ($\alpha = 1, \beta = 1, \delta^{H_2} = 1, \delta^{CO_2} = 0.25, C^{H_2,0} = 1, C^{CO_2,0} = 1$): The bifurcation occurs at $q_{c2} = 0.219$, the limit cycle disappears when q is reduced below $q_{c1} = 0.195$ . . . 103

6.1 List of rock parameters (2D models) . . . 124
6.2 List of rock parameters (3D model) . . . 125
6.3 List of characteristic parameters . . . 137
6.4 List of dimensionless microbial kinetic parameters . . . 141
6.5 List of microbial kinetic parameters . . . 147

Chapter 1

Introduction

The idea of taking hydrogen as the energy carrier for a renewable energy supply system can be traced back to the early 20th century. In February 1923 the Briton J.B.S. Haldone hold a speech at the Cambridge University where he suggested a power supply system based on hydrogen producing windmills [61]. This idea was continued by J.O. Bockris who published the first article about a so-called "hydrogen economy", where energy is stored and distributed in the form of hydrogen gas, in 1972 [17]. A new impulse is given by the change from nuclear to renewable energy in many European countries which demands an increasing amount of storage capacities for electrical energy [44]. The renewable energy supply which is generated primary by wind and solar power plants is strongly fluctuating. The reasons are changing weather conditions which take place in different time scales [29]. It is possible that long times of recession in the energy production have to be bridged. Additionally, the demand of electricity also varies on a daily and seasonal time scale [70]. The balance implies the temporal storage of electricity wherefore several storage options are currently under discussion. Battery storages have a high energy density but they are cost-intensive [83]. Compressed air energy storages and pumped hydro storages, where the energy is stored as potential or compression energy, have a relatively low energy density of 0.7 to 3 kWh/m^3 [70]. These options are preferred for the short term storage, the so-called minute and hour reserve [70]. Underground hydrogen storages (UHS), where the energy is stored as chemical energy, have an energy density which is higher by two orders of magnitude [70]. Consequently, they provide the possibility to store electrical energy in the long term or even seasonal period [29]. The technology comprises an electrolyzer which uses excessive electrical energy to split water into oxygen and hydrogen [70]. Different concepts for the subsequent storage and usage of hydrogen are available [91, 45, 29]:

- ”POWER-to-GAS”: The produced hydrogen will be fed into the existing natural gas grid. Investigations have shown that concentrations in the single-digit percentage area are supposable [36]. This means that also the existing underground gas storages will be charged with natural gas containing low percentages of hydrogen.
- ”POWER-to-GAS-to-POWER”: The hydrogen is stored purely in subsurface formations such as depleted gas or oil reservoirs, aquifers and solution mined caverns [111]. At times of energy demand the hydrogen is withdrawn and can be used as energy fuel for stationary fuel cells or engine-generators connected to the electrical grid or for fuel cell vehicles.

1.1 Motivation

In September 2010 the German Federal Government announced a new energy concept [44]. The objectives are essential changes in the energy supply until the year 2050 [44]:

- A reduction of greenhouse gas emission by 80-95%
- An expansion of renewable energy supply by 60%
- A reduction of the primary energy consumption by 50%

A critical interface for these targets is the storage of electrical energy [44]. The increasing share of renewable energy results in strong fluctuations in the electricity generation [44]. Consequently, large buffers are required to balance the base load and additional reserves need to be provided for peak shaving. However, the realization is detained by technical aspects [44]. For the promotion of applicable technologies the ”funding initiative energy storages” was started in 2011 by the Federal Ministry for Economy and Technology, the Federal Ministry for Environment, Nature Conservation and Nuclear Safety and the Federal Ministry for Education and Research. The initiative has a budget of €200 Mio. and supports research and development projects in the area of electrical, substance-based and thermal storages [44]. The projects span from fundamental research to economic efficiency improvements [44]. A substantial part of this intention is on UHS which is currently regarded as a promising solution for the large scale storage of

electrical energy. However, UHS is an unexperienced new technology and the suitable technical and geological conditions need to be determined before an UHS can be placed into operation. The supported research projects should make progress in this area which brings the implementation one step closer. This includes the project H2STORE which was carried out from 2011 to 2015 and HyINTERGER which is subsequently carried out until 2018, both partly at the Institute of Petroleum Engineering (Clausthal University of Technology) and the University of Lorraine, France. Also involved in these projects are the University of Jena and the GFZ Potsdam, both in Germany.

1.2 Underground hydrogen storage

The term "underground hydrogen storage" refers to the cyclic storage of hydrogen gas in subsurface formations as similarly done with natural gas. The cycle starts with the production of hydrogen from excessive electrical energy. Pressure electrolyzers are used which split water into hydrogen and oxygen [70]. Subsequently, gas installations with compressors are required to further compress and transport the hydrogen to the wells. The hydrogen continues to flow from surface into a geological formation through these wells. Within the storage formation, it remains until it is withdrawn during times of energy demand. At surface the pressure is released and in some cases a gas processing is required before the hydrogen is again available as energy fuel [70].

In this process the geological formation has to meet some basic requirements:

- An adequate volume need to be provided to store large amounts of hydrogen
- The structure need to be enclosed to prevent losses in the adjacent rocks
- Its properties have to allow the injection and withdrawal at efficient rates

Two different options come into consideration: solution-mined salt caverns or porous rock formations such as aquifers and depleted gas/oil reservoirs.

Salt caverns are large void spaces which can be created in bedded or domed salt formations by a solution mining process [121]. The advantage is that salt rock features a very high gas tightness and therefore losses can be practically neglected [29]. Additionally, the injection and withdrawal rates are only limited by the wells and legal regulations [29]. Consequently, they are well suited for several storage cycles per year. The operation is typically done by compressing and decompressing the gas within a defined pressure range [29]. Thereby a portion of the gas remains in the cavern, the so-called cushion gas. The usable amount of gas volume is defined as working gas. For an ordinary salt cavern with a geometrical volume of $500,000\ m^3$ and a maximum pressure of 200 *bar* the working gas volume is around $6 \cdot 10^7\ Sm^3$. The large hydrogen volume, which is required as cushion gas, represents a significant upfront investment.

Capable porous rock formations consist of a high porous and high permeable geological structure which is covered by an almost impermeable cap rock [111]. Additionally, a trap structure is required which prevents the migration of gas. The difference between aquifers and depleted reservoirs is mainly given by the initial pore filling. Aquifers are saturated only by water whereas depleted reservoirs can be saturated by up to three phases including gas and oil. However, an imperfect structure or possible reactions of hydrogen with minerals and microorganisms can result in some gas losses [70]. The injection and withdrawal rates are limited by the permeability and therefore the number of storage cycle per year is restricted [111]. In this case again, a certain amount of gas always remains in the storage as cushion gas. The advantage is the high volume of these structures which allows a storage of more than $10^9\ Sm^3$ [111]. Additionally, the availability of these structures is not limited to minor regions in Germany. The storage in depleted gas reservoirs will not require large hydrogen volumes as cushion gas, but the produced gas will not contain pure hydrogen.

1.3 State of the art (applications)

The concept of storing gases in the underground is established since almost 100 years [111]. Although the experience is limited to natural gas and gas mixtures, the storage of hydrogen can be treated similarly in many issues [111].

The VDE association [80] reports an unproblematic storage of pure hydrogen in salt caverns. Such facilities are under operation since decades in Teesside, United Kingdom and Texas, USA to store hydrogen for the chemical and petrochemical industry [80]. The gas leakage is below 0.02% per cycle [80].

Operational experiences for porous media storages are only gained for hydrogen mixed gases such as town gas. The DVGW [90] reported some problems during the storage of town gas in depleted reservoirs and aquifers. An enormous reduction in the gas volume was observed whereby leakages through the cap rock and wells could be excluded [90]. The cause has not been clarified definitively. The detection of sulfate-reducing bacteria allows the assumption that microbiological induced reactions are accountable for the gas reduction [90]. However, not all town gas storages were affected and the experiences can not be transferred directly to UHS [90].

An unexpected behavior was also reported for the town gas storage in an anticline aquifer structure near Lobodice, Czech Republic. During a storage cycle of seven months a drastic increase in the CH_4 concentration and a decrease in the CO, CO_2 and H_2 concentrations as well as changes in the gas volume were reported [118, 21]. Smigan et al. [118] analyzed the existence of methanogenic microorganisms in the stratal water and concluded that microbiological induced reactions could be responsible for the methane enrichment.

The Argentinian company Hychico S.A. started a pilot test in 2013 [114]. They added hydrogen as tracer to the natural gas stream and stored the gas mixture in a depleted gas and oil field. Results of this test are unpublished so far.

RAG Austria (Rohöl-Aufsuchungs Aktiengesellschaft) started a pilot test in 2015 [12]. They were injecting a gas mixture of natural gas with 10% hydrogen into a small depleted gas reservoir in Austria. The back production

will started in summer of 2016. Results of the field test will be available in spring 2017.

1.4 Recent related research projects

The topic of hydrogen as energy storage or transfer medium increasingly attracts the worldwide interest. Many research projects were launched during the last 5 years to investigate and advance the different sections in the chain of hydrogen production, storage, transport and usage. Thereby the large scale storage of hydrogen is an important connection which is currently focused by several research projects.

1.4.1 H2STORE

The H2STORE project started in the mid of 2012 and ran until the end of 2015. It was a joint research project with project members from University of Jena, Clausthal University of Technology, GFZ Potsdam and University of Lorraine. The initiator was the Federal Ministry for Education and Research in the context of the funding initiative for energy storages. H2STORE aimed to investigate the feasibility of large scale hydrogen storage in porous geological formations [46]. Thereby the focus was on depleted gas reservoirs in Germany [46]. The project was divided into six sub projects which are based on laboratory experiments, numerical simulations and analytical work [46]. The field of activity covered the investigation of mineralogical, geochemical, physio-chemical, sedimentological, microbiological and gas mixing processes in reservoir and cap rocks [46].

1.4.2 HyUnder

The HyUnder project also started in the mid of 2012 and ran for a total time of two years. The list of project partners comprises 12 organizations from 7 countries: Germany, France, United Kingdom, Spain, Netherlands, Romania and Belgium [20]. The participators are small to large industrial companies and research institutes [20]. HyUnder purposed to assess an

implementation plan for UHS in the European Union [20]. The different working packages include a benchmarking against other large scale storage options, investigating the different geological formation options, mapping potential storage sites in Europe, simulating and comparing different case studies [20]. The results show the technical, economic and prospects of UHS [64].

1.4.3 Hychico

Hychico S.A. started one of the first field trials on the way to an UHS deployment. The Argentinian company was founded in 2006 by partners from the field of energy resources. Since 2009 they are running a hydrogen pilot plant in Diadema, Argentina [114]. The plant consists of two electrolyzers which are using the power from an attached wind park to split water into hydrogen and oxygen [114]. Subsequently, the high purity hydrogen is mixed with natural gas and combusted in an engine-generator whereby electrical power is regained [114]. The oxygen is stored at surface and sold to the industrial gas market [114]. Until now, Hychico was able to successfully test their energy conversion cycle [114]. Starting in 2013, the feasibility of storing hydrogen in a nearby depleted oil and gas reservoir was tested [114]. Thereby, hydrogen was injected as a tracer admixed to natural gas [114]. The storage of pure hydrogen is also planned [114].

1.4.4 ANGUS+

The ANGUS+ project started in the mid of 2013 and was completed in 2015. It was conducted by the University of Kiel and partners were UFZ Leipzig, GFZ Potsdam and Ruhr University Bochum [11]. Like the H2STORE project it was financed by the German Ministry of Education and Research in the context of the initiative for energy storages [11]. The project focused on the spatial interferences between different subsurface usages [11]. Thereby, the concentration was set on the storage of natural gas, synthetic methane, hydrogen and compressed air in caverns and porous media as well as the storage of heat [11]. The objective was the development of geological fundamentals for these storage types and also economical, political and legal conditions were considered [11].

1.4.5 Underground Sun Storage

The research project "Underground Sun Storage", which was initiated by the Austrian company RAG, started in 2012 [12]. Project partners are the Montan University Leoben, University of Natural Resources and Life Sciences Vienna, Johannes Kepler University Linz, VERBUND AG and Axiom Angewandte Prozesstechnik GmbH [12]. The project aims to investigate the feasibility of storing natural gas or synthesized methane with added hydrogen in porous underground storages. Within the 10 working packages it is planned to analyze the reservoir engineering, economical, legal and material characteristic aspects of UHS. Particularly interesting is the in-situ field test which involves the operation of one storage cycle with added 10% hydrogen [12].

1.4.6 HyINTEGER

HyINTEGER is the follow-up project of H2STORE which started in January 2016 with a duration of 3 years. The project consortium is the same as in H2STORE, additionally the University of Mainz has joined. The five sub projects aim to further investigate the chemical-mineralogical, microbiological and petrophysical-geohydraulic-geomechnical processes in reservoir and cap rocks whereby especially the interactions between technical and natural components of an UHS are considered. An additional aspect is the material behavior under the strongly corrosive conditions. Again the work is based on laboratory experiments, numerical simulations and analytical methods. The modeling part concerns the near-wellbore region, however, also an upscaling to field scale is planned.

1.5 Outline of the thesis

The thesis is structured as followed:

Chapter 2 is a literature review about the hydrodynamic and microbiological effects which can appear in UHS. Additionally, it contains a review about mathematical models which were developed to describe these effects in UHS or similar applications. The chapter summarizes decisive physical,

chemical and biological processes in UHS and provides the background for the development of the mathematical model.

In chapter 3 the gravity-driven displacement is modeled analytically when hydrogen is injected to the bottom of a water saturated reservoir. The analytical solution was obtained by combining the method of characteristics with a graphical construction. Comparisons are also shown to the numerical solution.

In chapter 4 the development of a mathematical model for the bio-reactive transport in UHS is described. The model is based on continuum scale and couples compositional two-phase flow with bio-chemical reactions and microbial growth and decay within the porous medium.

In chapter 5 the stability of the mathematical model is investigated. Therefore, the equation system is reduced to a set of ordinary differential equations or a set of reaction-diffusion equations by appropriate assumptions. Based on the results, numerical simulations were performed which show different oscillatory regimes.

Chapter 6 covers the numerical implementation of the mathematical model which was done on the basis of DuMu$^{\mathrm{X}}$ (an open-source C++ code for the simulation of multi-phase multi-component flow and transport in porous media). The chapter includes numerical studies in two-dimensional conceptional and three-dimensional realistic geological models. The simulated scenarios include the development of the storage and the subsequent cyclic injection and withdrawal over several years.

In chapter 7 the results from all chapters are concluded.

Chapter 2

Literature review

The storage of hydrogen in the subsurface implies different physical, chemical and biological processes which can be separated into two parts: The hydrodynamic effects are reviewed in section 2.1 and the microbiological effects are reviewed in section 2.2. In addition, section 2.3 provides a review about mathematical models and numerical tools for the prediction of the coupled dynamic system.

2.1 Hydrodynamics in UHS

As mentioned before both aquifers and depleted gas reservoirs can be used to develop an UHS. However, the governing processes during the development period will be different for aquifers which are initially saturated only by water or brine and depleted gas reservoirs which can have a residual gas saturation.

In aquifers a gas bubble has to be created during the development period, hence, the aquifer water has to be displaced. Dependent on the external factors a continuous or step-wise expansion of the gas bubble is conceivable. The efficiency of the displacement between two almost immiscible fluids depends on several factors which are focused in section 2.1.1.

In depleted gas reservoirs some residual gas remained in the reservoir. If the influx of aquifer water into the reservoir was weak, the residual gas saturation could almost corresponds to the initial gas saturation and only the pressure was depleted. In this case the residual gas has to be displaced by hydrogen and the pressure has to be re-increased. Different schemes are suggested in the literature for the transformation of gas storages from one gas to another, which can be also applied for the development of an UHS

[123]. A simple transformation could be performed by cyclic injection and production using the same wells. In other transformation schemes hydrogen is injected on one edge of the reservoir. Thereby, the residual gas is pushed to the other side of the reservoir or could be simultaneously produced on the opposite side. This displacement process between two completely miscible fluids is reviewed in section 2.1.2.

The operation of UHS will be done in a cyclic way with alternating periods of injection, withdrawal and idle. Depending on the energy production and demands the periods can be longer or shorter. At least a seasonal operation, where the storage is charged during the summer months and discharged during the winter months, is supposable. More frequent changes in the operation schedule are possible when the storage intends to balance electrical energy production. The storages have to provide high production rates, usually one or two orders of magnitude higher than during the depletion of a reservoir. Hence, the main driving force during the operation will be compression and expansion of the gas bubble. A certain amount of gas remains always in the reservoir as cushion gas. During this period mixing processes between different gases can still be important, e.g. when the residual gas was not completely displaced or when an alternative gas is used as cushion gas (e.g. N_2 or CO_2 as suggested in [123, 107, 97]). The displacement of gas by water from an aquifer potentially only plays a minor role as drive mechanism during withdrawal.

2.1.1 Gas-water flow

Gas and water are almost immiscible fluids which form a two-phase system within the porous rock. On pore scale the phases are separated by abrupt interfaces as illustrated in Fig. 2.1. The interaction between the phases is related to forces at the fluid-solid and fluid-fluid interfaces. For a gas-water system reservoir rocks are typically water-wet. This means that water tends more to adhere to the solid surfaces than gas [6]. As a consequence of the wettability water is rather present in smaller pores while the gas phase will inhibit larger pores or channels [6]. In addition to the adhesive forces, the behavior is influenced by the interfacial tension between gas and water [6]. The combination of these forces leads to a pressure difference across the

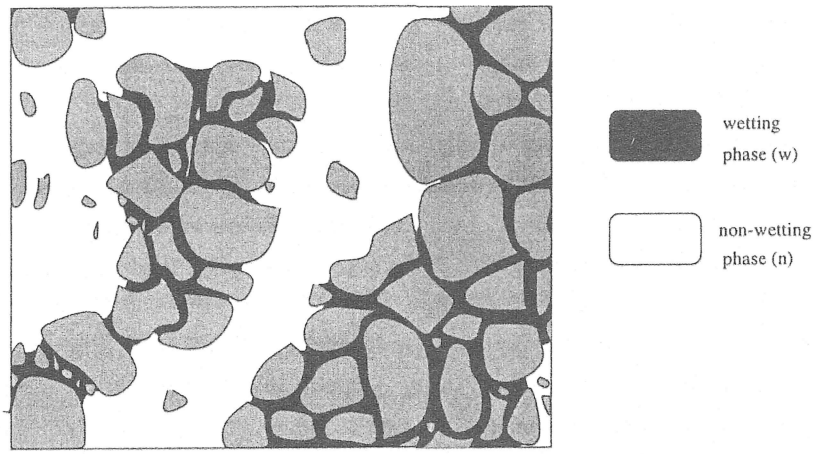

Figure 2.1: Sketch of fluid distribution on pore scale: For a gas-water system the wetting phase is water and the non-wetting phase is gas [59]

gas-water interface which is referred to as capillary pressure [6]. For a gas-water system the capillary pressure results that the gas pressure is higher than the water pressure. The mentioned pore scale effects influence also the flow of the fluid phases. Not the entire pore space is available for each phase and consequently the flow of the phases interferes with each other [6]. To be able to flow each phase needs to have a continuous pathway through the porous medium [6].

On macroscopic scale the two-phase system can be averaged over an representative elementary volume (REV) (cf. Fig. 2.2). The pore space occupied

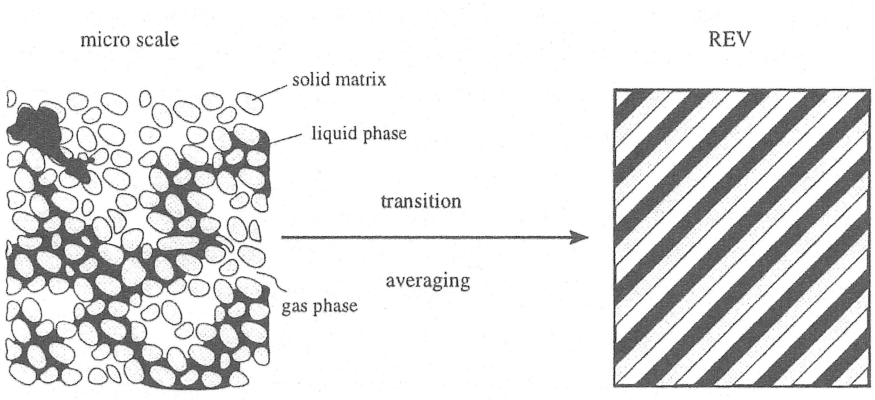

Figure 2.2: From pore scale to continuum scale [59]

by each phase divided through the total pore space is referred to as saturation [6]. The ability for each phase to flow through the porous medium

is described by the concept of relative permeability which was derived from laboratory experiments [6]. The relative permeability is the ratio between the effective permeability for one fluid phase and the absolute permeability as a function of saturation [6]. As a consequence of the necessity for a continuous flowpath for a phase, the relative permeability will become zero at some critical value for the saturation which is still larger than zero. This saturation is referred to as residual saturation [59]. The displacement processes when the wetting phase (water) displaces the non-wetting phase (gas) and vise versa have different characteristics [6]. During imbibition the wetting phase penetrates into the larger pores or channels while during drainage the non-wetting phase displaces the wetting phase in the smaller pores [59]. As a result the relative permeability curves as a function of saturation have different shapes for the wetting and for the non-wetting phase. In both cases some amount of the displaced fluid phase will be left behind.

The displacement problem between two immiscible fluids on macroscopic scale was solved by Buckley and Leverett in a simplified form [19]. They derived an analytical solution for the saturation in a one-dimensional domain when the displacing fluid is injected from one side. The solution consists of a displacement front followed by a rarefaction wave (cf. Fig. 2.3). The value

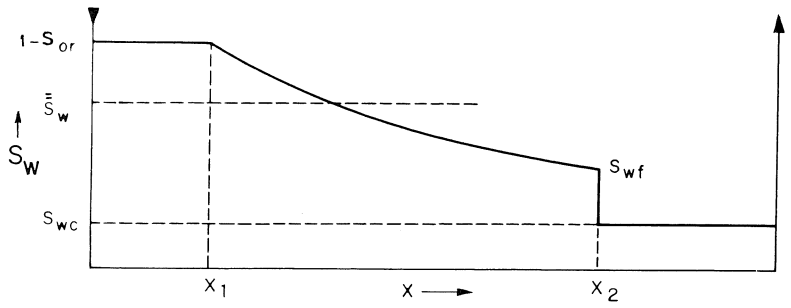

Figure 2.3: Saturation versus distance in two-phase displacement process: The example shows the displacement of oil by water what is qualitatively equal to the displacement of water by gas [31]

of saturation behind the displacement front depends on the mobility ratio between the phases. The characteristics of this behavior were also confirmed by laboratory flooding experiments [19].

However, the one-dimensional problem provides only an averaged solution for the effects on pore scale which are, as mentioned before, influenced by

the adhesive forces and interfacial tensions between the fluids and the solid. In a three-dimensional system the stability of the displacement front needs be considered additionally. Factors, which are important in this context, are the density difference between the phases, the mobility ratio, the permeability distribution and the positioning of storage wells. The low density and viscosity of hydrogen could make the displacement instable what results in a low volumetric displacement efficiency. Two physical effects which could arise and lower the efficiency are viscous fingering and gravity segregation:

- *Viscous fingering* arises due to a contrast in the mobilities of the displacing and displaced fluid. An assessment can be done by using the mobility ratio [124]:

$$M = \frac{k_{r1}\mu_2}{k_{r2}\mu_1} \tag{2.1}$$

  where k_{r1} is relative permeability of the displacing fluid at the average saturation behind the displacement front, k_{r2} is relative permeability of the displaced fluid at the average saturation ahead the displacement front and μ_1 and μ_2 are the viscosities respectively of the displacing and displaced fluid. In general it is accepted that mobility ratios smaller than one result in a stable displacement [62]. In contrast for mobility ratios higher than one the front becomes instable and fingers occur in the displacement front. A rough estimation for hydrogen storages results in mobility ratios in the order of 2 - 5 for the displacement of water. Consequently, an instable displacement is expected.

  The cause for viscous fingering are small perturbations which result from microscopic heterogeneities although the porous medium can be homogenous at macroscopic scale [77]. As destabilization forces are stronger than stabilization forces the small perturbations continue to propagate as large fingers. In laboratory experiments this effect can be visualized in a Hele-Shaw cell which consists of two glass plates with a small gap. In Fig. 2.4 the formation of fingers is shown around an injection point. The further spreading of fingers is conducted by several phenomena. The fingers spread perpendicular to the main flow direction what can either result in joining of two fingers or a splitting at the tip [62]. Additionally, a shielding can occur which means that only a smaller number of fingers continues to propagate and the remaining fingers become slower or stop [62]. The result is a tree-

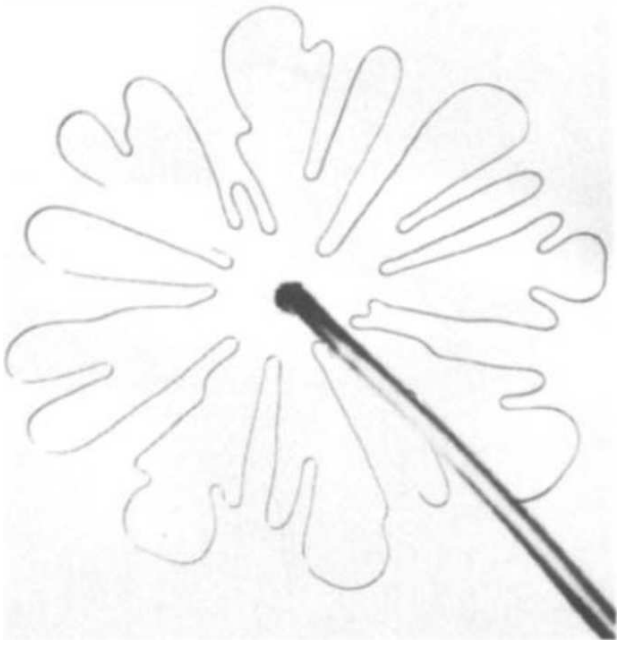

Figure 2.4: Viscous fingers around an injection point in a Hele-Shaw cell [101]

like structure [102]. The factors influencing this process are viscosity differences, density differences and surface tension forces [77]. However, underground structures also have permeability heterogeneities at macroscopic scale which result in different flow potentials. Thereby viscous fingers tend to propagate in the direction of high flow potential [77].

- *Gravity segregation* arises due to different densities and mobilities of the displacing and displaced fluid [123]. When a less dense displacing fluid prefers to flow at the top of the structure the behavior is referred to as density override. In contrast, when a more dense displacing fluid prefers to flow at the bottom of the structure it is referred to as density underride. This effect was investigated mathematically by Dietz [33]. Based on some assumptions he derived a balance for the viscous and gravitational forces which separate an instable from a stable displacement. His findings allow the following conclusions for UHS where the less dense and more mobile gas phase is usually above the more dense and less mobile water phase. The downdip displacement of water by gas during injection becomes instable at a critical velocity [123]. Above this velocity gravity override occurs. However,

the updip displacement of gas by water during withdrawal is stable at any velocity [123]. The behavior of top to bottom displacement is illustrated in Fig. 2.5.

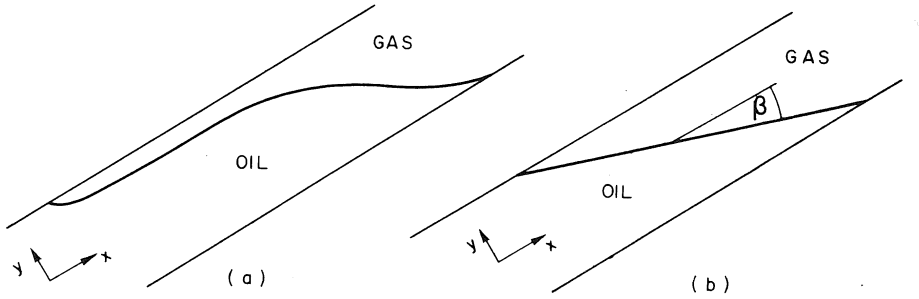

Figure 2.5: Segregated downdip displacement process: a) instable, b) stable [31]

In hydrogen storages especially in aquifers the instable displacement could be associated with several problems. At first fingers could spread laterally much further than expected and some of them could pass the spill point of the structure [102]. If this occurs the gas is carried away by buoyancy forces and consequently lost [102]. The injection rate provides a possible control of the extension of fingers. In Fig. 2.6 the spreading of gas is illustrated for three different injection rates where a spillage occurs only for the highest rate. Secondly, a low volumetric sweep efficiency is obtained which results in a small storage volume. Thirdly, the fingers provide a large contact area between hydrogen and the water phase where a dissolution could take place [102]. The dissolved amount of hydrogen becomes also unrecoverable. Finally, mobile fluids could be left behind which will be produced in the subsequent withdrawal process.

2.1.2 Mixing in gas-gas displacement

The mixing between gases with different composition plays a major role when a depleted gas reservoir is transformed to an UHS or when an alternative cushion gas is used. The principle difference compared to the mechanism of gas-water flow is the fact that there is no abrupt transition between the different gases at pore scale. In a one-dimensional displacement

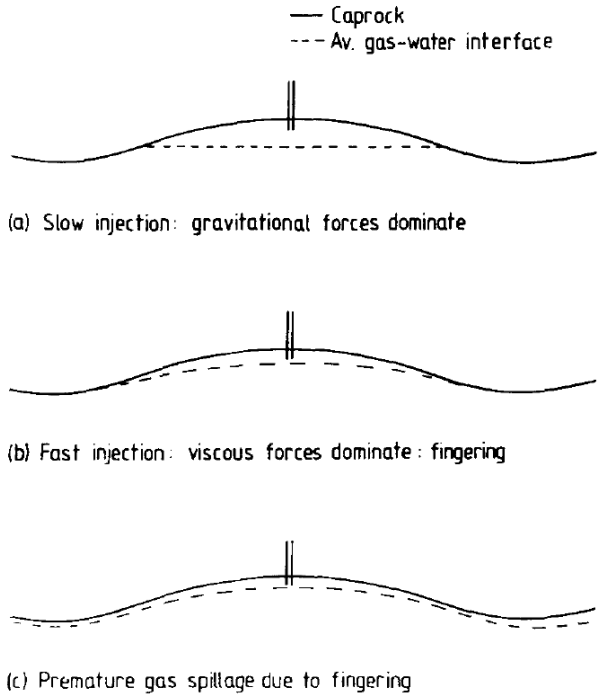

Figure 2.6: The injection of gas into an anticline trap [102]

this leads on one hand to a complete or piston-like displacement where no initial gas is left behind the front [15]. On the other hand the miscibility leads to a smearing out of the front due to diffusive or dispersive flux at the front [123]. In Fig. 2.7 the behavior of a miscible displacement is shown for different Peclet numbers. A high Peclet number means that the diffusive flux has a low influence and the displacement front is piston-like. In contrast, a small Peclet number means that the diffusive flux has an significant influence which results in a strong smearing out of the front. In a more-dimensional system the overall process is influenced by heterogeneities and anisotropies of the porous medium and mobility ratios, density differences, molecular diffusion and mechanical dispersion between the different gases [123].

Mobility differences in a gas-gas displacement arise mainly due to different dynamic viscosities. Hydrogen has a very low viscosity which results in a mobility ratio around 1.5 for the system H_2-CH_4 and 4 for the system H_2-CO_2. This could result again in an instable displacement when hydrogen is injected to displace another gas. However, this effect is much less than is the system of gas-water displacement because the miscibility leads to a high

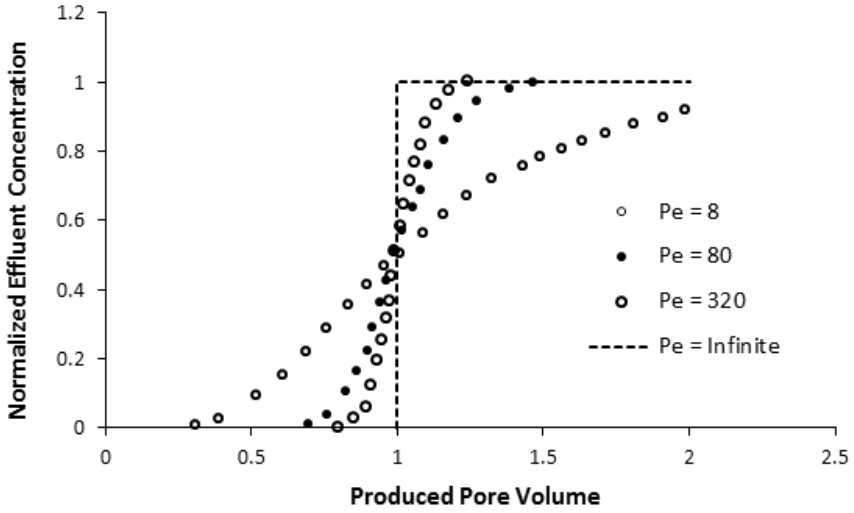

Figure 2.7: Outflow concentration of the injected tracer versus produced pore volume [67]

dispersion of the front which acts as stabilizing force [62].

Density differences are in the range of ~80% for the system H_2-CH_4 and ~95% for the system H_2-CO_2. The effect can have a negative influence when the injection aims to displace another gas but instead gravity override occurs. However, the effect can be also used to keep different gases segregated, e.g. when CO_2 is used as cushion gas [123].

Molecular diffusion is generally considered as a slow process when compared to advective/convective transport [123]. The molecular diffusion coefficient $\tilde{D}_{\text{diff}}$ for hydrogen in gaseous state is relatively high, in the order of $1{\cdot}10^{-6}\text{m}^2/\text{s}$. The effective molecular diffusion coefficient depends on porosity, saturation state and tortuosity of the porous medium and will be less. As molecular diffusion is proportional to the concentration gradient, it will be fast at the beginning but when the concentration gradients decrease its influence will also decrease. It is independent of advective/convective transport, thus, it could become the governing process during idle periods.

Mechanical dispersion, in contrast, is a mixing process which takes place due to the movement of fluids in the porous medium [123]. It arises from variations in the velocity which can occur on different scales, ranging from microscopic to reservoir scale [123]. The mechanical dispersion coefficient $\tilde{D}_{\text{disp}}$ depends on the velocity and direction of flow and can be formulated

as follows [115]:

$$\tilde{D}_{\text{disp,L}} = a_L \cdot \|v\| \qquad \tilde{D}_{\text{disp,T}} = a_T \cdot \|v\| \tag{2.2}$$

where a is the dispersivity in $[m]$, $\|v\|$ is the Darcy velocity in the principle direction, the subscript L refers the longitudinal direction and the subscript T refers the transverse direction. The dispersivity of the porous medium depends on its tortuosity and heterogeneity. Measurements of the dispersivity gave results which deviate by several orders of magnitude. As the process is strongly influenced on the considered scale, laboratory measurements can not be transferred directly to reservoir scale [123]. Tracer tests, which have been performed on reservoir scale, have shown that the longitudinal dispersivity is between 1 m to 100 m [123, 23, 78]. The transverse dispersivity is usually one or two orders of magnitude less. Assuming flow velocities of several meters per day, which are common in gas storages, the longitudinal mechanical dispersion coefficient will be around $5 \cdot 10^{-4}$ m^2/s. Hence, the mixing by mechanical dispersion is expected to be much more pronounced than only by molecular diffusion.

2.2 Microbiology in UHS

Living organisms are classified into three categories: Eukarya, archaea and bacteria [84]. Related to Pepper et al. [84], the term microorganism is defined as free-living organism which is too small to be seen by the naked eye. Based on the cell size only, organisms of all three categories fall under this definition. For most of them the conditions (pressure, temperature, oxygen absence, pH-value,...) in UHS are not preferable or make it even impossible to survive. Nevertheless, it is known that some archaea and bacteria are quite well adapted to these conditions. These two forms of living are introduced in the following sections.

2.2.1 Cell structure of archaea and bacteria

Microorganisms are simple constructed single cell organisms without cell nucleus [30]. The main types of microorganisms are archaea and bacteria which are similar in many aspects but have some differences. Subsequently

the term microorganism is used whenever a distinction between archaea and bacteria is not necessary. The usual size of a microbial cell is 0.5 to 1 μm in diameter and 1 to 2 μm in length [84]. The cell contains a full organism with all functionalities like orientation, mobility, nutrient intake, digestion and reproduction [30]. In Fig. 2.8 the structure of a microbial cell is sketched. The cell is constructed out of a cyst which encloses the cytoplasm. The cyst

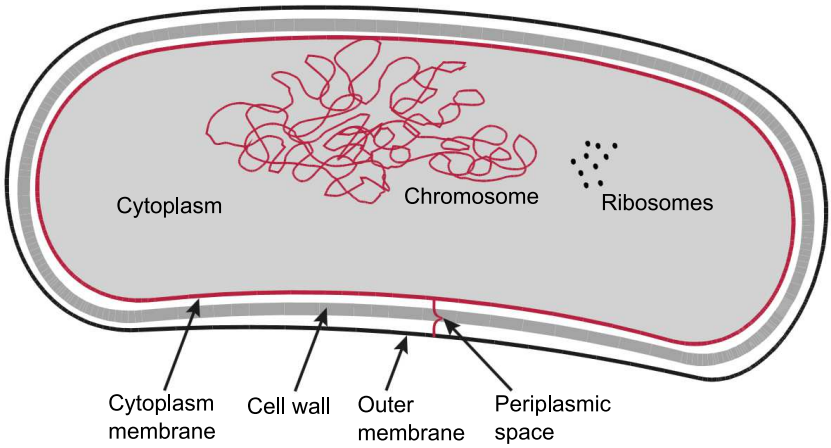

Figure 2.8: Sketch of the cell structure [30]

consists of a cell wall and membranes. The cell wall is relevant for the shape and compression resistance of the cell [30]. The cytoplasm membrane is impermeable for most chemical components but let some components which are required for the bio-chemical processes pass. The cytoplasm encloses the chromosome, ribosomes and additional substances which are used for different bio-chemical processes [30]. The chromosome which is in contrast to eukarya not enclosed by a nucleus is referred to as nucleoid and contains the genetic information [30]. The difference between archaea and bacteria is the material out of which the cell walls and membranes consist. Some microorganisms have a flagellum on one side which makes a target-oriented movement possible [84]. Other cell appendixes, i.e. pili, can be used for attachment processes (cf. section 2.2.5) [47].

2.2.2 Cell duplication and metabolism

Microbial cells reproduce themselves by cell division as illustrated in Fig. 2.9 [30]. The process consists of several steps. At first the chromosome is duplicated [30]. Then, the cell is growing to the double size [30]. Finally, a

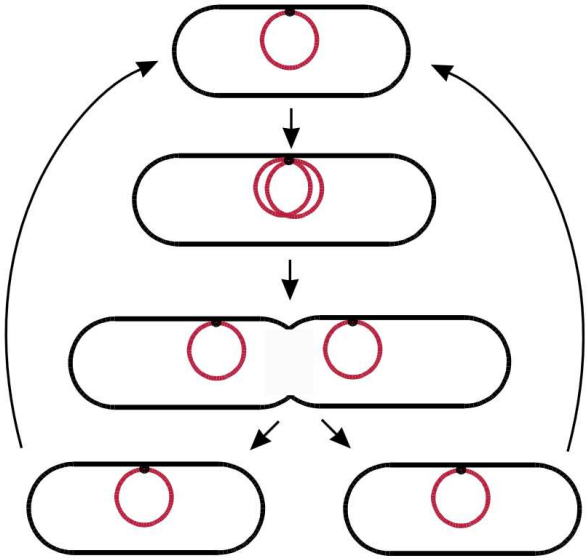

Figure 2.9: Duplication of a microbial cell [30]

ring-shaped contraction of the cell wall starts in the center and the cell is separated into two individual cells [30].

The process of cell duplication requires a series of chemical reactions within the microbial cell which is referred to as microbial metabolism [84]. The aim of metabolism is the increase of cell mass and finally the cell duplication. However, it has to be differentiated between growth metabolism and non-growth metabolism [84]. During non-growth metabolism the microbial cell does not increase its mass or duplicate but substrates and nutrients are still consumed for the maintenance of the cell structure.

For both types of metabolism the microorganism needs a source of energy and a source of carbon [84]. Under atmospheric conditions microorganisms tend to use a redox reaction (chemotrophic) by using oxygen or light (phototrophic) as the source of energy [84]. Under anaerobic conditions, e.g. in subsurface formations, they need to use a less energy efficient redox reaction. Different organic or inorganic substances can be used in this process as electron donor [84]. In UHS it appears reasonable that the microorganisms use hydrogen as the electron donor. In the literature these types of metabolism are referred to as hydrogenotrophic. The most important types are summarized in section 2.2.4. The source of carbon can be also differentiated as organic source (heterotrophic) or as inorganic source (autotrophic) [84]. An inorganic source of carbon would be CO_2.

2.2.3 Microbial populations and growth

So far microorganisms have been regarded as individual cells, however, they are very small and consequently the influence of a single microbial cell in an environmental system is almost zero. Microorganisms occur usually as populations with a very large number of microbial cells. These populations usually consist out of different species. Therefore, in the context of environmental processes the biomass or microbial counts are used. Biomass is the sum of the mass of the individual microorganisms in $[kg]$. From a chemical point of view, biomass consists approximately out of 80% H_2O [30]. The remaining mass is organic material. The chemical composition is often simplified by $< CH_2O >$ which roughly describes the compositional proportions of biomass [30]. Microbial counts relate the number of microbial cells to a volume or a total mass. The units used in the literature are $[cells/ml]$ or $[cells/g]$.

The growth behavior of microbial populations can be investigated in the laboratory. The microorganisms are inserted into a bottle containing a nutrient solution [30]. A fixed amount of substrate is added and samples are taken frequently to analyze them with respect to the cell number or biomass [30]. The number of cells or biomass is subsequently shown in a semi-logarithmic plot versus time. Such experiments are referred to as batch culture experiments. An example of the outcome is shown in Fig. 2.10. Usually four different growth phases can be observed [30]:

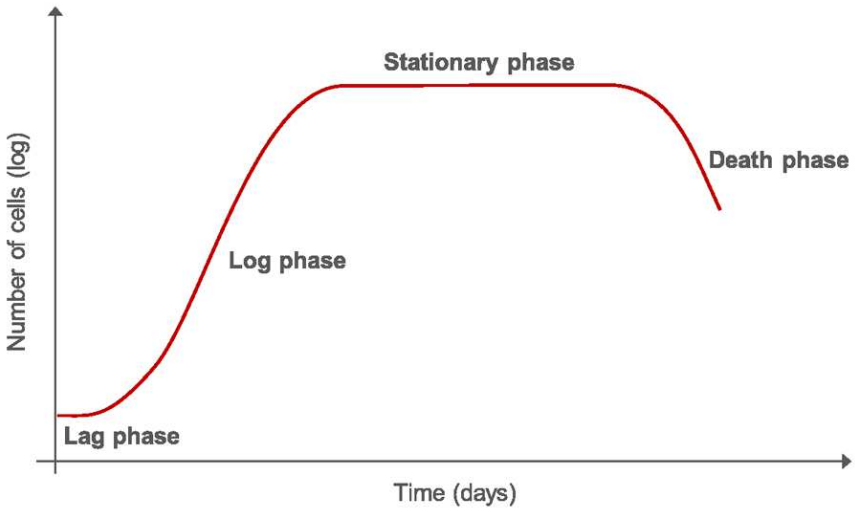

Figure 2.10: Typical growth curve of a microbial population [122]

- *Lag phase*: During the initial lag phase no growth of the microbial population occurs. The microorganisms need a certain time to physiologically adjust themselves to the new external conditions [84]. In the laboratory the lag phase usually lasts some minutes up to some hours. However, under environmental conditions it can last months or even years [84].

- *Exponential growth (log) phase*: After the lag phase the growth behavior shifts into the exponential growth phase. In this phase the number of cells is doubled during each generation. This means that the number of cells increases exponentially with a maximum rate [30]. This rate is specific for each substrate and the external conditions [30]. Under ideal condition this can be every 10 minutes, however, it can also last up to 100 years [84]. Mathematically, the growth during this phase can be described by the following differential equation [30]:

$$\frac{dn}{dt} = \mu n \tag{2.3}$$

  where n is the number of microbial cells and μ is the maximum growth rate in $[1/s]$.

  The exponential growth can be easily observed in the laboratory, however, under environmental conditions it usually does not occur for long periods [84]. The maximum rate of growth is also smaller under environmental conditions than measured in the laboratory [84].

- *Stationary phase*: When the carbon or energy source becomes limiting the growth behavior shifts into the stationary phase [84]. During this phase no net growth occurs. However, this does not mean that individual cells do not duplicate. It only means that growth and death are balanced [84]. When microbial cells are using dead microbial cells as carbon source the process is referred to as endogenous metabolism [84]. Mathematically the growth during the stationary phase can be formulated as follows [84]:

$$\frac{dn}{dt} = 0 \tag{2.4}$$

- *Decay/death phase*: Finally, the growth behavior shifts into the de-

cay phase during which the number of active cells shows a negative exponential decline [84]. However, individual cells can still duplicate. Mathematically the decay phase can be described as [84]:

$$\frac{dn}{dt} = -bn \tag{2.5}$$

where b is the decay rate in $[1/s]$.

Monod [87] introduced two additional phases in the life cycle of a microbial batch culture: The acceleration phase which is the transition between the lag and the exponential growth phase and the deceleration phase which is the transition between the exponential growth phase and the stationary phase.

2.2.4 Relevant microbial species in UHS

The injection of hydrogen into subsurface structures could stimulate the growth of all present microbial species which are able to use hydrogen for their metabolism. As introduced before such microbial species are referred to as hydrogenotrophs. Evidence for this behavior is given by observations in some of the former town gas storages where the activity of methanogenic archaea was concluded. The activity of sulfate-reducing bacteria was also observed in town gas and natural gas storages. Indications are often the production of H_2S and the resulting corrosion problems [72]. Other sources give hints that also homoacetogenic archaea and iron-reducing bacteria could be stimulated and contribute in the metabolism of hydrogen [27, 81].

According to the available literature it is expected that four hydrogenotrophic species could be important for UHS. Their metabolic reactions differ by the used electron acceptor.

- Methanogenic archaea obtain energy from the following metabolic reaction:

  $$CO_2 + 4H_2 \longrightarrow CH_4 + 2H_2O \tag{2.6}$$

  Most methanogenic archaea are autotrophs what means that they are using CO_2 as carbon source [125].

- Homoacetogenic archaea are also using H_2 and CO_2 for their metabolism:

$$2CO_2 + 4H_2 \longrightarrow CH_3COOH + 2H_2O \tag{2.7}$$

  They can use CO_2 (autotrophic) but also an organic source of carbon [113].

- Sulfate-reducing bacteria imply the following metabolic reaction:

$$SO_4^{2-} + 5H_2 \longrightarrow H_2S + 4H_2O \tag{2.8}$$

  Sulfate-reducing bacteria are mainly using inorganic compounds as carbon source (heterotrophic) but autotrophic species also exist [13].

- Iron(III)-reducing bacteria use the following metabolic reaction:

$$3Fe_2^{III}O_3 + H_2 \longrightarrow 2Fe_3^{II}O_4 + H_2O \tag{2.9}$$

  Iron-reducers can be heterotrophic or autotrophic [110].

Other variations of the reaction equations are possible, however, the stated equations represent the microbial processes in an adequate way. The coexistence of several species can thereby result in a concurrence between the different hydrogenotrophic processes which was investigated by Cord-Ruwisch et al. [27] and Lovley et al. [81]. They have shown that a simultaneous survival and also an out-competition is possible. The microorganisms have revealed to have different minimum threshold concentrations for the consumption of hydrogen. Iron-reducing bacteria have the lowest threshold concentration and consequently the best potential to out-compete other species. However, when hydrogen is available in excessive amount, several species can reproduce simultaneously depending on the presence of the corresponding electron acceptor.

2.2.5 Microbial transport and structures in porous media

The structure in which microorganisms live and the transport of microorganisms in porous media are strongly related. Microorganisms or biomass in porous media can appear in two different structures: Planktonic/suspended in the water phase or as biofilm associated with a surface [47].

- In the *planktonic/suspended* structure the microorganisms are freely living in the water phase. Consequently, they are transported with the flow of water. This process is governed by the pressure gradient and the hydrodynamic properties of the porous medium (porosity and permeability) [47]. In addition, hydrodynamic dispersion and random motion (similar to diffusion) plays a role in this process [47]. However, the advective transport of suspended microorganisms has some differences to the transport of dissolved chemical species [84]. The fact that living organisms are transported makes it much more complex [47]. The transport is influenced by straining and filtration. Filtration is the removal of microorganisms from suspension by collision and attachment to solid surfaces [47]. Straining means that microorganisms become trapped in too small pore throats [47]. This process can be relevant for rocks which have a recognizable portion of silt or clay particles [84]. Additionally, microorganisms are usually transported faster than a dissolved chemical species would be. Microorganisms tend to flow in the centerlines of the pores or pore throats where the flow velocity is higher than the average velocity [47]. This process is referred to as size exclusion. In addition to the passive transport by advection, microorganisms can also move actively. This process is referred to as chemotaxis and describes the movement of microorganisms in direction towards substrates/nutrient or away from toxic substances using their flagella [84]. The process is called positive chemotaxis when the microorganisms are moving towards a higher concentration or negative chemotaxis when they are moving towards a lower concentration [14].

- *Biofilms*, which are frequently denoted as slimy substance, are usually the dominant structure in porous media [108, 14]. A biofilm is an assembly of microorganisms which attaches to each other and to a surface by a structure of self-produced extracellular polymeric substances (EPS) [108, 14]. Biofilms can contain multiple microbial species [14]. An image of a biofilm from a scanning electron microscope is shown in Fig. 2.11. The creation of a biofilm can be explained by the four stages of a biofilm life cycle [130]: (1) Microorganisms attach to a solid surface or an interface between two fluid phases. Their first attachment due to physicochemical (van der Waals or electrostatic) forces is reversible [14, 47, 84]. Also microbial cell appendixes like pili can have an influence in the attachment process [47]. (2) Under favor-

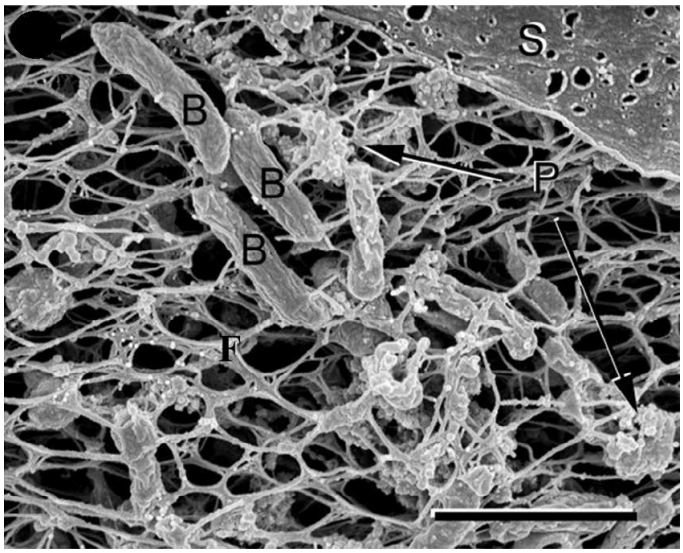

Figure 2.11: Image of a biofilm from a scanning electron microscope, B: microorganism, F: EPS, P: particulate matter, S: substrate [14]

able conditions the microorganisms attach irreversibly by creating a structure of EPS which holds the microorganisms together and where appropriate attaches them to the solid surface [84, 14, 47, 108]. (3) During the stage of growth a complex three-dimensional community is formed [130]. The biofilm can be a patchy or a continuous cover over the surface [14]. (4) In the final stage single cells or biofilm fragments can be detached by shear stresses [14, 130]. The detached cells are transported away and can attach elsewhere to create a new biofilm [130]. Compared to the planktonic structure the biofilm has some advantages for the survival of microorganisms [14]. The EPS structure provides a cohesive strength, protects from predator cells and serves as nutrient reservoir [14, 108]. Microorganisms which live in a biofilm are practically immobile [130]. Additionally, it has to be mentioned that biofilms influence the hydrodynamic parameters of the porous medium, i.e. a reduction of the effective porosity and effective permeability can occur [108].

2.3 Modeling of bio-reactive transport in porous media

The linkage between transport and growth of microorganisms, substrate availability and biodegradation results in a strongly coupled dynamic system [92]. Involved physicochemical processes are advection, diffusion, dispersion, size exclusion, straining and filtration and the biological processes are growth, decay, metabolism, chemotaxis, physiological adaptation, attachment and detachment [92]. The difficulty in the development of a general model is the inclusion of processes which appear on different length scales. While biological processes such as growth, chemotaxis or attachment occur on cell or pore scale, the hydrodynamic processes occur on Darcy scale or even above [92]. The present literature review concentrates on upscaled effective representations of the processes on Darcy scale. Additionally, the time scale of the processes needs to be considered. Processes which occur on a similar time scale as the time scale of transport can be treated kinetically [92]. In contrast, processes which are much faster can be treated instantaneously by using equilibrium laws. A model can contain both types of processes which means that the model becomes a coupled system of partial differential and algebraic equations [92]. In the following sections available models from groundwater and gas storage applications are reviewed.

2.3.1 Single-phase models for groundwater applications

The literature comprises a wide range of modeling approaches for bio-reactive transport in the subsurface. As most of them are developed for groundwater applications, they are limited to single-phase flow. The models differ by the considered processes and scales. A characteristic difference between the modeling approaches is the consideration of biomass structures. Structured models are taking into account the difference and interactions of attached biomass (biofilms) and suspended biomass [92]. Unstructured models do not take into account the different structures and treat biomass as a fully penetrable volumeless component [92]. The following list summarizes the major processes of structured bio-reactive transport models on Darcy scale:

1. The *flow* is described by Darcy's law and depends on the pressure gradient and the permeability:

$$u_w = -\frac{K}{\mu_w} \cdot (\nabla P - \rho_w g) \tag{2.10}$$

where u_w is the Darcy velocity of water in $[m/s]$, K is the absolute permeability in $[m^2]$, μ_w is the viscosity of water in $[Pa \cdot s]$ P is the pressure in $[Pa]$, ρ_w is the density of water in $[kg/m^3]$ and g is the gravity acceleration in $[m/s^2]$.

2. The *transport* of suspended microorganisms and other solutes, e.g. nutrients or substrates, is governed by advection and dispersion. The dispersion can be further separated into mechanical mixing and molecular diffusion [92]. The result is an advection-dispersion transport equation for microorganisms or other solutes [92]:

$$\frac{\partial C^i}{\partial t} + \nabla \cdot \left(C^i u_w\right) = \nabla \cdot \left(D^i \nabla C^i\right) \tag{2.11}$$

where C^i is the concentration of biomass or the concentration of a dissolved component in $[kg/m^3]$ and D^i is the effective dispersion coefficient in $[m^2/s]$.

3. The process of *attachment* represents the removal of microorganisms from the water phase by straining and filtration [92]. The simplest model is a linear rate of attachment. Furthermore, the attachment rate could be modeled as function of the flow velocity [92]. The exchange of microorganisms between the different structures can be modeled by the following terms for attachment and detachment:

$$\frac{dC^{im}}{dt} = K_f C^{mm} - K_r C^{im} \tag{2.12a}$$

$$\frac{dC^{mm}}{dt} = -K_f C^{mm} + K_r C^{im} \tag{2.12b}$$

where C^{im} is the concentration of attached (immobile) microorganisms, C^{mm} is the concentration of suspended (mobile) microorganisms, K_f is the rate of attachment in $[1/s]$ and K_r is the rate of detachment in $[1/s]$.

4. Microbial *growth* is usually modeled the by Monod model [87] which takes into account the limitation of the substrate or by the double Monod model which takes into account the limitation of the substrate and the electron acceptor [92]. For the *decay* usually a constant rate is accepted. It has to be differentiated between the growth in the biofilm structure and in the suspended structure:

$$\frac{dC^{im}}{dt} = \mu_m^{im} C^{im} \left(\frac{C^S}{K^{S,im} + C^S} \right) - b \cdot C^{im} \tag{2.13a}$$

$$\frac{dC^{mm}}{dt} = \mu_m^{mm} C^{mm} \left(\frac{C^S}{K^{S,mm} + C^S} \right) - b \cdot C^{mm} \tag{2.13b}$$

where μ_m is the maximum specific growth rate in $[1/s]$, C^S is the substrate concentration, K^S is the half-velocity constant and b is the decay rate in $[1/s]$.

5. The *biodegradation* of substrates and electron acceptors is modeled kinetically by treating it proportional to the microbial growth [92]. Consequently, it can be also modeled by Monod model including a yield coefficient:

$$\frac{dC^S}{dt} = -\frac{\mu_m^{mm}}{Y} C^{mm} \left(\frac{C^S}{K^{S,mm} + C^S} \right) - \frac{\mu_m^{im}}{Y} C^{im} \left(\frac{C^S}{K^{S,im} + C^S} \right) \tag{2.14}$$

where Y is the yield coefficient. The rate of growth and consequently the rate of biodegradation depends on the microbial structure. Usually, biomass in a biofilm structure degrades substrates slower than suspended biomass [92].

Many other processes could be included in the model: A lag phase in the growth, competition between different species for the same substrate, memorization effects in the attachment and detachment processes or chemotactic movement of microorganisms [92].

2.3.2 Two-phase models for gas storage applications

Bio-reactive transport models which consider the flow of two phases are very rare in the literature. Two different models are available which were developed for the application to UHS: Ebigbo et al. [38] developed a model at pore scale while Panfilov [100] and Toleukhanov et al. [126] developed a model at macroscopic scale. The model of Toleukhanov et al. [126] was the starting basis for this thesis and is therefore briefly reviewed in this section.

The model uses a structured approach for the biomass, however, not in the same way as introduced in the previous section. The model distinguishes between the following two biomass structures:

- Microorganisms in the water phase which include suspended biomass and attached biomass to the solid surface (biofilm)
- Microorganisms in a neuston biofilm which means that they are living in a coherent structure in the direct vicinity to the gas-water interface

One microbial species, i.e. methanogenic archaea, is considered which metabolizes by the following reaction equation:

$$CO_2 + 4H_2 \longrightarrow CH_4 + 2H_2O \tag{2.15}$$

The growth of microorganisms in the neuston and in the water structure are modeled qualitatively different. In the neuston structure the microorganisms consume the substrates directly from the gas phase. Hence, the growth depends on the concentrations in the gas phase. CO_2 is assumed to be limiting in a similar formulation as in the Monod model:

$$\frac{\partial n_{ns}}{\partial t} = \frac{1}{t_{e,ns}} \left(\frac{c_g^{CO_2}}{1 + a_{ns} c_g^{CO_2}} \right) n_{ns} \tag{2.16}$$

where n is the number of microorganisms in $[1/m^3]$, t_e is the characteristic time of eating in $[s]$, c is the molar concentration, a is an empirical coefficient and the subscript ns denotes the neuston structure. In contrast, the growth in the water structure depends on the concentrations of H_2 and CO_2 in the water phase. The formulation is similar to the double Monod model

but uses a variable maximum growth rate depending on the population size which was suggested by Panfilov [100]:

$$\frac{\partial n_w}{\partial t} = \frac{1}{t_{e,w}} \frac{n_w}{1 + \frac{n_w^2}{n_{w,\max}^2}} \left(\frac{c_w^{H_2}}{1 + a_{ns} c_w^{H_2}} \right) \left(\frac{c_w^{CO_2}}{1 + a_{ns} c_w^{CO_2}} \right) n_w \tag{2.17}$$

where $n_{w,\max}$ is the population number at which the rate of growth reaches its maximum and the subscript w denotes the water structure.

In addition to the growth in both structures the model for the population dynamics includes decay, advective transport, microbial diffusion and chemotaxis. Exchange processes (attachment and detachment) between the microbial structures are simplified by the assumption that the relative number of microroganisms in the neuston structure is equal to the gas saturation. This assumption makes it possible to model the dynamics of the microbial population by one equation:

$$\begin{aligned} \frac{\partial n}{\partial t} = & \underbrace{\frac{\eta_{\text{ns}} c_g^{CO_2} (1 - S) n}{t_{e,ns}}}_{\text{Growth in neuston}} + \underbrace{\frac{\eta_w c_w^{H_2} c_w^{CO_2} S n^2}{t_{e,w}}}_{\text{Growth in water}} - \underbrace{\frac{n}{t_d}}_{\text{Decay}} \\ & \underbrace{- \nabla \cdot (u_w n)}_{\text{Advection}} + \underbrace{\nabla \cdot (D_b \nabla n)}_{\text{Diffusion}} \underbrace{- \nabla \cdot (D_{ch} S n \nabla C^{H_2})}_{\text{Chemotaxis}} \end{aligned} \tag{2.18}$$

where η is the rendering coefficient which relates the growth of biomass to the consumption of substrates in $[1/mol]$, S is the water saturation, t_d is the characteristic time of death in $[s]$, u is the Darcy velocity in $[m/s]$, D_{ch} is the chemotaxis rate in $[m^2/s]$, the subscripts g and w denote gas and water. In this equation the growth models are simplified. C^{H_2} is the total mole fraction of hydrogen:

$$C^{H_2} = \frac{\rho_w c_w^{H_2} S + \rho_g c_g^{H_2} (1 - S)}{c_w^{H_2} S + c_g^{H_2} (1 - S)} \tag{2.19}$$

For the transport of the substrates the flow in both phases (gas and water) is considered. The consumption of substrates is included as sink terms which are proportional to the growth terms in the water and in the neuston

structure. Additionally, diffusive transport is included for both phases:

$$\phi\frac{\partial}{\partial t}\left(\rho_w c_w^k S + \rho_g c_g^k (1-S)\right) + \underbrace{\nabla\cdot\left(\rho_w c_w^k u_w + \rho_g c_g^k u_g\right)}_{\text{Advection}} = \underbrace{-\frac{\phi\gamma^k (1-S) c_g^{CO_2} n}{t_{e,ns}}}_{\text{Bio-reaction in neuston}}$$
$$\underbrace{-\frac{\phi\gamma^k S c_g^{H_2} c_g^{CO_2} n^2}{t_{e,w}}}_{\text{Bio-reaction in water}} + \underbrace{\nabla\cdot\left(\rho_w D_w^k \phi S \nabla c_w^k + \rho_g D_g^k \phi (1-S)\nabla c_g^k\right)}_{\text{Diffusion}} \tag{2.20}$$

where ϕ is the porosity, ρ is the molar density in $[mol/m^3]$, γ is the stoichiometric coefficient in reaction equation 2.15, i.e. 4 for H_2 and 1 for CO_2, in $[mol]$ and D is the effective diffusion coefficient in $[m^2/s]$.

The exchange of mass between the phases is assumed to take place instantaneously. Hence, the concentrations of components in the water phase is described by using an equilibrium law, i.e. Henry's law:

$$c_w^k = H^k P_w c_g^k, \quad k = H_2, CO_2 \tag{2.21}$$

where H is the Henry coefficient in $[1/Pa]$.

2.3.3 Review of tools for (bio-)reactive transport modeling

A wide choice of numerical tools, which could be used for the modeling of transport processes in UHS, is available. The selection ranges from commercial software packages from the petroleum industry, over combined commercial and scientific software packages to open-source codes, which are commonly only used for scientific applications.

Commercial software packages from the petroleum industry, e.g. Schlumberger Eclipse [116] or CMG's IMEX, GEM and STARS [82], usually provide two main mathematical models: A black-oil model and a compositional model. While the black-oil model is more adequate for modeling flow in oil and/or gas reservoirs with up to three phases, the compositional model could be adjusted and used for modeling the flow and transport processes in UHS. However, physical and biological processes like mechanical dispersion, micro-

bial growth and the coupled bio-chemical reactions are potentially difficult to implement because the software packages are inflexible in this regard.

COMSOL Multiphysics [1] is a commercial tool which allows the simulation of physical and chemical processes from many disciplines. COMSOL shows a higher flexibility compared to commercial reservoir simulators what makes it interesting also for scientific applications. It is possible to couple any kind of physical or chemical process with the flow equations. Additionally, the mathematical interfaces allow to enter user-defined equation systems. Thereby, the discretization and solving is still carried out by COMSOL and no extended programming is required. However, the finite element method which is used for the spatial discretization shows some disadvantages for the modeling of flow and transport processes. Oscillations tend to occur around discontinuities in saturations or concentrations. A stabilization of the solution is possible but potentially COMSOL is only adequate for simple conceptional simulations in one- or two-dimensional domains and not for three-dimensional field scale simulations.

TOUGHREACT [134] is a numerical simulation program which is available under commercial or academic license agreement. It was developed for reactive non-isothermal multi-component and multi-phase processes in porous and fractures media. It was successfully applied for nuclear waste disposal, CO_2 storage, groundwater and other hydrodynamic processes in subsurface systems. The source code of this tool is available so that potentially any physical or biological process could be included.

Different open-source codes, e.g. DuMu$^{\mathrm{X}}$ [43], OpenGeoSys [73] and OPM (Open Porous Media) [4], are available which were developed for the simulation of flow and transport processes in porous media with scientific purposes. While OPM is more related to petroleum reservoirs, OpenGeoSys and DuMu$^{\mathrm{X}}$ were developed for groundwater and other hydrological applications. Potentially all of them could be adjusted for the bio-reactive modeling in UHS. The tools differ by their discretization methods, available mathematical models and handling.

In Table 2.1 a comparison of the different tools with regard to available physical models, numerical aspects and handling is shown. None of these tools is capable to model all relevant processes in their original version. Consequently, it is reasonable to use a tool for which the source code is available and adjustments in the mathematical model are possible. The

selection for this thesis was DuMu^{X} which appeared to be most suitable for the implementation of a bio-reactive transport model for UHS.

	CMG	COMSOL	DuMu^{X}	Eclipse	OpenGeoSys	OPM	TOUGHREACT
Physical models							
Compositional multi-phase flow	×	×	×	×		×	×
multi-phase flow							
Molecular diffusion	×	×	×	×	×	×	×
Mechanical dispersion	×		×		×		
Chemical reactions	×	×		×	×		×
Biomass growth and decay					×		×
Non-isothermal flow	×	×	×	×	×	×	×
Solid mechanics	×	×	×		×		
Numerical scheme							
Spatial discretization	FDM	FEM	FVM	FDM	FEM	FVM	FVM
Time discretization	implicit*	implicit	BE*	implicit*	BE	BE	BE/CD
Handling							
Commercial	×	×		×			×
Graphical user interface	×	×		×	×		
Open-source			×		×	×	
Programming language			C++		C++	C++	Fortran

Table 2.1: Comparison of tools for modeling (reactive) transport in underground reservoirs (some information is taken from Steefel et al. [120])

⋆ IMPES (implicit pressure and explicit saturation) models are additionally available
FVM = finite volume method
FDM = finite difference method
FEM = finite element method
BE = backwards Euler
CD = central difference

Chapter 3

Analytical modeling of gravity-driven displacement

As introduced in the literature review, the operation of hydrogen storages is similar to natural gas storages, however, the hydrodynamic behavior of hydrogen could be different. In the papers of Paterson [102] and Carden and Paterson [22] some aspects of underground hydrogen storage are investigated. They stated that there is a high risk of arising viscous fingers during the displacement of formation water because of the high mobility ratio between the displacing and displaced fluid. This instance is combined with several negative impacts: (1) Hydrogen could disappear beyond the spill point of the structure when viscous fingers spread laterally very far, (2) the viscous fingers affect an increased interface between gaseous hydrogen and formation water where a dissolution takes place, (3) macroscopic gas volumes could be trapped during the withdrawal period and become unrecoverable.

An improvement can be obtained by injecting the hydrogen at the bottom of the structure. By doing so, the gas rises due to buoyant forces before it arrives below the cap rock. However, when the gas arrives at the top, the lateral spreading starts in the same way and the problem is only delayed by a few days. A possible solution is the operation in a storage formation with horizontal barriers where the rising of gas is drastically slowed down. Experiences for rising fluids in stratified geological formations were already gained for the injection of CO_2 into an aquifer by Boait et al. [16]. However, the once-only injection of CO_2 cannot be transferred directly to hydrogen storages which would be operated by cyclic gas injection and withdrawal. It is demanded that a preferable high percentage of the injected hydrogen can be recovered in the subsequent withdrawal period. The cyclic operation

can be achieved by the so-called ”selective technology” which is illustrated in Fig. 3.1.

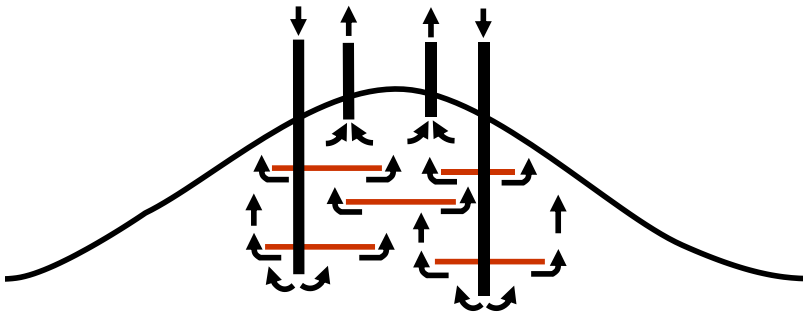

Figure 3.1: Sketch of ”selective technology”

This concept consists of two systems of wells in a stratified reservoir. The reservoir potentially consists of high porous and high permeable sandstones which are interrupted by thin shale or mud stone layers. The thin layers thereby play the role of horizontal low permeable or even impermeable barriers. One system of wells is used to inject the hydrogen at the bottom of the structure. The hydrogen starts to rise because of the buoyant forces. At the barriers the vertical migration is retarded until the hydrogen penetrates or flows around. Finally, when the hydrogen arrives at the top of the structure it will be withdrawn by the second system of wells. Alternatively, double completions could be deployed to the reduce the number of required wells. These completions should allow the injection at the bottom and the production at the top through the same well. It is important to produce the hydrogen before it has the chance to spread laterally. However, this method is not common and the application is complex. A detailed planning is required to coordinate the injection rate, withdrawal rate and time of gas rising. The cyclic operation leads to a continuous gas flow from the bottom to the top. Consequently, a potential residual gas in the reservoir would be produced first. The use of an alternative cushion gas is not possible because the stored gas is repeatedly exchanged. A key element is the selection of a suitable storage site. Once the storage is constructed it allows only low flexibilities in the storage cycle.

The present chapter was published in a similar form in the Journal of Natural Gas Science and Engineering [53].

3.1 Case study description

The derivation of an analytical solution for the problem is only possible for a one-dimensional domain. Consequently, the vertical dimension is used because gravity is the driving force in this investigation. However, the removal of the two horizontal dimensions avoids the possibility for gas spreading laterally and flowing around the barriers. Moreover, an impermeable barrier in a one-dimensional domain would block the flow completely. Consequently, the analytical solution requires an assumption. In the two- or three-dimensional case the barriers could be impermeable but limited in areal extend. For the representation in the one-dimensional case low permeable barriers with a defined thickness are used. Thereby, it is considered that the time of gas flowing through the low permeable barriers is equal to the time of gas flowing around the impermeable barriers in the two- or three-dimensional case. All solutions in this paper are obtained by using the same base case. A periodic geometry acts as the basis for the analytic model (Fig. 3.2). The barriers (medium II) have a permeability of $K_{\mathrm{II}} = 250$ mD whereby the reservoir rock (medium I) is defined with $K_{\mathrm{I}} = 500$ mD.

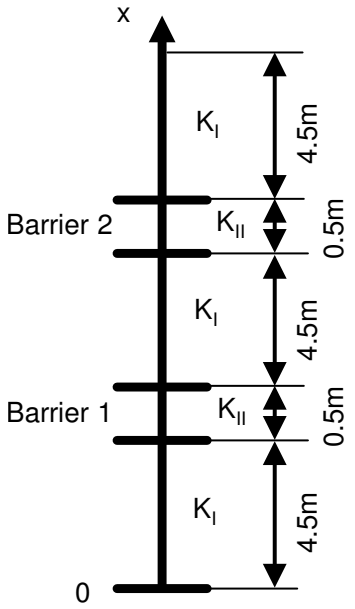

Figure 3.2: 1D geometry

The porosity is defined as 0.25 and the total upwards pore velocity as 0.25 m/day. The pressure and temperature conditions are set to 400 bar and 125 $°C$. All required fluid properties are summarized in Table 3.1 and 3.2.

Table 3.1: Fluid properties at 400 *bar* and 125 °*C*

	Density $[kg/m^3]$	Viscosity $[mPa \cdot s]$
Pure H_2	20	0.010
Pure CO_2	650	0.056
Gas mixture (95%*vol* H_2, 5%*vol* CO_2)	42	0.013
H_2O	1000	0.23

Table 3.2: Two-phase equilibrium composition at 400 *bar* and 125 °*C*

H_2 and H_2O	
Volume fraction of H_2 in liquid phase, c_w^1	0.011
Volume fraction of H_2 in gas phase, c_g^1	0.9978
CO_2 and H_2O	
Volume fraction of CO_2 in liquid phase, c_w^1	0.09
Volume fraction of CO_2 in gas phase, c_g^1	0.977

The density, phase equilibrium and viscosity calculations are done with an EOS software by using the Peng-Robinson equation of state [105] and Lee, Gonzalez and Eakin viscosity correlation [79].

The pore size distribution index for the relative permeability functions λ (cf. section 3.2) is defined as 2 and the residual saturations S_{rg} and S_{rw} are 0.

3.2 Balance equations for compositional two-phase flow

The injection of gas into a water saturated rock requires the modeling of flow for two phases: Gas and water. Each of them consists of n chemical components. The derivation of flow equations is based on the following assumptions which are commonly used in the analytical modeling of multi-phase flow processes in porous media [15, 41, 99]:

- The flow is one-dimensional;
- The phase composition is determined at the local phase equilibrium;
- Capillary pressure and molecular diffusion are neglected;
- The temperature is constant.

Hence, the mass balance can to be written for each component as follows:

$$\phi \frac{\partial \left(\hat{\rho}_g \hat{c}_g^k S + \hat{\rho}_w \hat{c}_w^k (1 - S) \right)}{\partial t} + \frac{\partial \left(\hat{\rho}_g \hat{c}_g^k v_g + \hat{\rho}_w \hat{c}_w^k v_w \right)}{\partial x} = 0, \quad k = 1, 2, ..., n \tag{3.1}$$

where $\hat{\rho}$ is the density in $[kg/m^3]$, $\hat{c}_i^k$ is the mass concentration of component k in phase i, S is the gas saturation, v is the Darcy velocity in $[m/s]$ and n is the number of components. The phases are denoted with g for gas and w for water. The momentum balance is defined by Darcy's law:

$$v_i = -\lambda_i \cdot \left(\frac{\partial P}{\partial x} - \hat{\rho}_i g \right), \quad i = g, w \tag{3.2}$$

where P is the pressure in $[Pa]$, g is the gravity acceleration in $[m/s^2]$ and λ_i is the mobility respectively of gas and water:

$$\lambda_i = \frac{K k_{ri}}{\mu_i}, \quad i = g, w \tag{3.3}$$

where K is the absolute permeability in $[m^2]$, k_r is the relative permeability and μ is the dynamic viscosity in $[Pa \cdot s]$. Two additional assumptions were used:

- The mixing of components in both phases is ideal. This means that the volume of the mixture is equal to the sum of the volumes which would be occupied by the pure components at the same pressure and temperature:

$$\sum_{k=1}^{n} V_i^k = V_i, \quad i = g, w \tag{3.4}$$

  where V is the volume in $[m^3]$.

- The variation in pressure is small, thus, the phase concentrations can be considered as independent of pressure.

From Eq. 3.4 the definition for volume fractions c_i^k can be derived as follows:

$$\frac{V_i^k}{V_i} = \frac{M_i^k/\hat{\rho}^k}{M_i/\hat{\rho}_i} = \frac{\hat{c}_i^k\hat{\rho}_i}{\hat{\rho}^k} = c_i^k, \quad k = 1, 2, ...n, \quad i = g, w \tag{3.5}$$

where M is the mass in $[kg]$ and $\hat{\rho}^k$ is the density of the pure component in $[kg/m^3]$. The sum of volume fractions in each phase is 1:

$$\sum_{k=1}^{n} c_i^k = 1, \quad i = g, w \tag{3.6}$$

Dividing Eq. 3.1 by the densities of pure components (ρ^k) leads to a simplified equation system:

$$\phi\frac{\partial\left(c_g^k S + c_w^k(1-S)\right)}{\partial t} + \frac{\partial\left(c_g^k\hat{f}v + c_w^k(1-\hat{f})v\right)}{\partial x} = 0, \quad k = 1, 2, ..., n \tag{3.7}$$

where v is defined as the total Darcy velocity:

$$v = v_g + v_w \tag{3.8}$$

and $\hat{f}$ is the fractional flow of gas:

$$\hat{f} = \frac{v_g}{v} \tag{3.9}$$

The phase composition is determined by the equilibrium between gas and water by the equality of fugacities:

$$f_g^k(c_g^1, c_g^2, ..., c_g^{n-1}) = f_w^k(c_w^1, c_w^2, ..., c_w^{n-1}) \quad k = 1, 2, ...n \tag{3.10}$$

The relative permeabilities of gas and water are defined by the Brooks-Corey correlation [18].

$$k_{rw}(S_w) = S_{we}^{\frac{2+3\lambda}{\lambda}} \tag{3.11}$$

$$k_{rg}(S_w) = (1 - S_{we})^2(1 - S_{we}^{\frac{2+\lambda}{\lambda}}) \tag{3.12}$$

where S_{we} is the effective water saturation:

$$S_{we} = \frac{S_w - S_{wr}}{1 - S_{wr} - S_{gr}} \tag{3.13}$$

S_{wr} is the residual (or connate) water saturation and S_{gr} is the residual gas saturation.

3.3 Reduction to a canonical model

The canonical form is derived by the following steps:

1. The sum of all equations 3.7 is:

$$\frac{\partial v}{\partial x} = 0 \tag{3.14}$$

2. $\hat{f}$ is transformed in the following way by using Darcy's law (3.2):

$$\begin{aligned} \hat{f} &= \frac{v_g}{v} = \frac{\lambda v_g}{\lambda v} = \frac{\lambda_g v_g + \lambda_w v_g}{\lambda v} = \frac{\lambda_g}{\lambda} + \frac{\lambda_w v_g - \lambda_g v_w}{\lambda v} \\ &= \frac{\lambda_g}{\lambda} - \frac{\lambda_w \lambda_g \left(\frac{\partial P}{\partial x} - \hat{\rho}_g g\right) - \lambda_g \lambda_w \left(\frac{\partial P}{\partial x} - \hat{\rho}_w g\right)}{\lambda v} \\ &= \frac{\lambda_g}{\lambda} - \frac{\lambda_w \lambda_g g(\hat{\rho}_g - \hat{\rho}_w)}{\lambda v} \end{aligned} \tag{3.15}$$

3. The expression for $\hat{f}$ is inserted into Eq. 3.7:

$$\begin{aligned} &\phi \frac{\partial \left(c_g^k S + c_w^k (1 - S)\right)}{\partial t} + u \frac{\partial \left(c_g^k (f - R) + c_w^k (1 - f + R)\right)}{\partial x} = 0, \\ &k = 1, 2, ..., n - 1 \end{aligned} \tag{3.16}$$

where $f = \frac{\lambda_g}{\lambda_g + \lambda_w}$ and $R = \frac{\lambda_w \lambda_g g(\hat{\rho}_g - \hat{\rho}_w)}{\lambda v}$. The number of equations is $n-1$ because one equation was already used for Eq. 3.14.

4. According to Eq. 3.5 the phase densities can be written as:

$$\rho_i = \sum_{j=1}^{n} \hat{\rho}^j c_i^j \tag{3.17}$$

where $\sum_{j=1}^{n}$ is the sum over all components. For the difference in phase densities this results in:

$$\hat{\rho}_w - \hat{\rho}_g = \sum_{j=1}^{n} \hat{\rho}^j (c_w^j - c_g^j) = \sum_{j=1}^{n-1} \hat{\rho}^j (c_w^j - c_g^j) + \hat{\rho}^n (c_w^n - c_g^n) \tag{3.18}$$

According to the sum of volume fractions (Eq. 3.6) the concentration of component n is:

$$c_i^n = 1 - \sum_{j=1}^{n-1} c_i^j \tag{3.19}$$

Inserting this expression into Eq. 3.16 results in:

$$\begin{aligned} &\phi \frac{\partial \left(c_g^k S + c_w^k (1-S) \right)}{\partial t} \\ &+ u \frac{\partial \left(c_g^k f + c_w^k (1-f) + G(c_g^k - c_w^k) \sum_{j=1}^{n-1} (\hat{\rho}^j - \hat{\rho}^n)(c_w^j - c_g^j) \right)}{\partial x} = 0, \\ &k = 1, 2, ..., n-1 \end{aligned} \tag{3.20}$$

The final canonical form is:

$$\frac{\partial C^k}{\partial t} + u \frac{\partial F^k}{\partial x} = 0, \quad k = 1, 2, ..., n-1 \tag{3.21a}$$

where C^k is the total concentration of component k in both phases:

$$C^k = c_g^k S + c_w^k (1-S) \tag{3.21b}$$

and F^k is the generalized fractional flow of component k:

$$F^k = \left(c_w^k (1-f) + c_g^k f \right) + G(c_g^k - c_w^k) \sum_{j=1}^{n-1} (\hat{\rho}^j - \hat{\rho}^n)(c_w^j - c_g^j) \tag{3.21c}$$

where f and G are defined as:

$$f = \frac{\lambda_g}{\lambda_g + \lambda_w} \tag{3.21d}$$

$$G = \frac{g f \lambda_w}{u \phi} \tag{3.21e}$$

u is the total true velocity:

$$u = \frac{v}{\phi} \tag{3.21f}$$

When only one phase is present the generalized fractional flow of component k is equal to C^k. This is shown on the example of an single-phase gas as follows:

$$\begin{aligned} & S = 1 \rightarrow C^k = c_g^k, \lambda_w = 0, \lambda_g = \lambda \\ & \rightarrow f = 1, G = 0 \\ & \rightarrow F^k = c_g^k = C^k \end{aligned} \tag{3.22}$$

For simplicity, it is assumed that the porosity is everywhere the same. The effect of heterogeneity comes only from the permeability which means that only function G is different in a stratified reservoir. In this case the velocity u is everywhere identical. Its value is equal to the injection velocity.

3.4 Initial and boundary conditions

A periodic domain acts as the basis for the model (cf. Fig. 3.2). It is assumed that the reservoir is initially saturated by water. The water can initially contain some concentrations of all components. A pure gas is injected at the bottom of the reservoir. The initial and boundary condition are summarized as:

$$C^k(t = 0, x > 0) = C^{k,0} \tag{3.23a}$$

$$C^k(x = 0) = C^{k,inj} \tag{3.23b}$$

This kind of initial and boundary conditions is equivalent to a Riemann problem [127] where a discontinuity is initially present at the origin.

3.5 Hugoniot conditions, stability conditions and continuity of fractional flow

A classical smooth solution of the non-linear system (Eq. 3.21a to Eq. 3.21f) may not exist. However, as the model describes a physical problem it is obvious that a solution exists. This kind of solution is called weak solution and can be characterized by discontinuities or shocks. The required conditions at a shock are described by Rankine-Hugoniot conditions, which are derived from the mass balance across the shock. For this equation system the Rankine-Hugoniot conditions have the following form for $k = 1, ..., n-1$:

$$\frac{u_s}{u} = \frac{F^{k+} - F^{k-}}{C^{k+} - C^{k-}} \tag{3.24}$$

where u_s is the shock velocity and "+" and "−" denote respectively ahead and behind the shock. However, by using only the Rankine-Hugoniot conditions a multitude of solutions could be constructed which means that the solution is non-unique. To find the physical admissible solution, two additional conditions were applied [15]. The Oleinik entropy condition need to be satisfied for all C^k between C^{k-} and C^{k+}:

$$\frac{uF^k\left(C^k\right) - uF^{k+}}{C^k - C^{k+}} \leq u_s \leq \frac{uF^k\left(C^k\right) - uF^{k-}}{C^k - C^{k-}} \tag{3.25}$$

The Lax entropy condition requires the shock velocity to be between the velocities of the states which are connected to it:

$$u\left.\frac{\partial F^k}{\partial C^k}\right|_+ < u_s < u\left.\frac{\partial F^k}{\partial C^k}\right|_- \tag{3.26}$$

In particular cases, the Lax inequality transforms into an equality:

$$\frac{u_s}{u} = \left.\frac{\partial F^k}{\partial C^k}\right|_+ \quad \text{or} \quad \frac{u_s}{u} = \left.\frac{\partial F^k}{\partial C^k}\right|_- \tag{3.27}$$

Discontinuities at the interface between medium I and medium II are defined by the continuity of fractional flow for each component, which is the

consequence of the mass conservation:

$$F^{k,I-} = F^{k,II+}, \quad \text{or} \quad F^{k,II-} = F^{k,I+} \tag{3.28}$$

All these conditions have a clear graphical interpretation. Based on this a graphical technique was used to select admissible shocks and to construct a continuous path between various admissible segments of the solution (see subsection 3.6.2).

3.6 Two-component flow

In the first part, the number of components is limited to two. In this case the phase equilibrium (Eq. 3.10) depends only on two concentrations (c_g^1 and c_w^1), hence the solution is unique. This means that the phase compositions are constrained by the equilibrium law and do not change when two phases exist. Consequently, the behavior of a two-component system is qualitatively equivalent to an immiscible process when both phases exist at any position at any time. However, the difference comes from the possibility of single-phase states, because then, the phase composition is not constrained by the equilibrium law. E.g. the injection of a gas which is over-saturated by H_2 into water leads to the effect of vaporization of liquid water. Such an effect cannot be represented by an immiscible model.

For the two-components case the canonical model (Eq. 3.21a to Eq. 3.21f) reduces to a unique transport equation.

$$\frac{\partial C^1}{\partial t} + u\frac{\partial F^1}{\partial x} = 0 \tag{3.29a}$$

where:

$$C^1 = c_g^1 S + c_w^1(1-S) \tag{3.29b}$$

$$F^1 = \begin{cases} \left(c_w^1(1-f) + c_g^1 f\right) + G(c_g^1 - c_w^1)^2(\rho^1 - \rho^2) & \text{if } c_w^1 < C^1 \leq c_g^1 \\ C^1 & \text{if } C^1 < c_w^1, \text{or } C^1 > c_g^1 \end{cases} \tag{3.29c}$$

The initial and boundary conditions are:

$$C^1(t=0, x>0) = C^{1,0} \tag{3.29d}$$

$$C^1(x=0) = C^{1,inj} \tag{3.29e}$$

The Rankine-Hugoniot condition at the shock is:

$$\frac{u_s}{u} = \frac{F^{1+} - F^{1-}}{C^{1+} - C^{1-}} \tag{3.29f}$$

The Oleinik entropy condition requires for all C^k between C^{k-} and C^{k+}:

$$\frac{uF^1(C^1) - uF^{1+}}{C^1 - C^{1+}} \leq u_s \leq \frac{uF^1(C^1) - uF^{1-}}{C^1 - C^{1-}} \tag{3.29g}$$

The Lax entropy conditions become:

$$u \left.\frac{\partial F^1}{\partial C^1}\right|_+ < u_s < u \left.\frac{\partial F^1}{\partial C^1}\right|_- \tag{3.29h}$$

$$\frac{u_s}{u} = \left.\frac{\partial F^1}{\partial C^1}\right|_+ \quad \text{or} \quad \frac{u_s}{u} = \left.\frac{\partial F^1}{\partial C^1}\right|_- \tag{3.29i}$$

Discontinuities at the interface between medium I and medium II are defined by the continuity of fractional flow:

$$F^{1,I-} = F^{1,II+}, \quad \text{or} \quad F^{1,II-} = F^{1,I+} \tag{3.29j}$$

3.6.1 Structure of the generalized fractional flow function

The solution of the problem can be derived by using the diagram of F^1 versus C^1. Two diagrams for the systems H_2-H_2O and CO_2-H_2O are shown in Fig. 3.3. According to Eq. 3.29b, F^1 is equal to C^1 in the single-phase zones. Hence, the function is laying on the diagonal within the single-phase zones. If the term G is zero, the function will have the typical monotonic S-shape within the two phase zone. However, term G is non-monotonic. It is zero for low and for high gas saturations and has a bell-shaped curve in between. As the total concentration C^1 is related to the gas saturation by Eq. 3.29b, the function $F^1(C^1)$ becomes also bell-shaped when the influence of G is significant. As the term G is proportional to the permeability K, the maximum of the curve is higher for medium I (reservoir rock) than for medium II (barriers). Additionally, the maximum of the bell-shaped curve is

much higher for the system H_2-H_2O than for the system CO_2-H_2O, because the density difference is much larger in the former case.

3.6.2 Graphical construction of the solution

The solution of the problem (Eq. 3.29a to Eq. 3.29j) consists of different segments:

- *Plateaus* are segments with a constant value of the total concentration C^1.

- *Rarefaction waves* are continuous parts of the solution with having variable total concentration C^1. Their relationships can be obtained by the method of characteristics. Eq. 3.29a can be also written as:

$$\frac{\partial C^1}{\partial t} + uF^{1\prime}\frac{\partial C^1}{\partial x} = 0 \tag{3.30}$$

  where $F^{1\prime} = \frac{\partial F^1}{\partial C^1}$. A characteristic line is defined as the concentration C^1 which is a function of position and time:

$$C^1 = C^1(x(t), t) \tag{3.31}$$

  The time derivative of this function is:

$$\frac{dC^1(x(t),t)}{dt} = \frac{\partial C^1}{\partial t} + \frac{\partial C^1}{\partial x}\frac{dx}{dt} \tag{3.32}$$

  The solution can be obtained by comparing Eq. 3.30 and 3.32:

$$\frac{dC^1(x(t),t)}{dt} = 0 \tag{3.33}$$

  and:

$$\frac{dx}{dt} = uF^{1\prime} \tag{3.34}$$

  This means that a constant concentration C^1 is moving along each characteristic line whereby the velocity is given by $uF^{1\prime}$. Consequently, the position of each concentration at a defined point in time can be

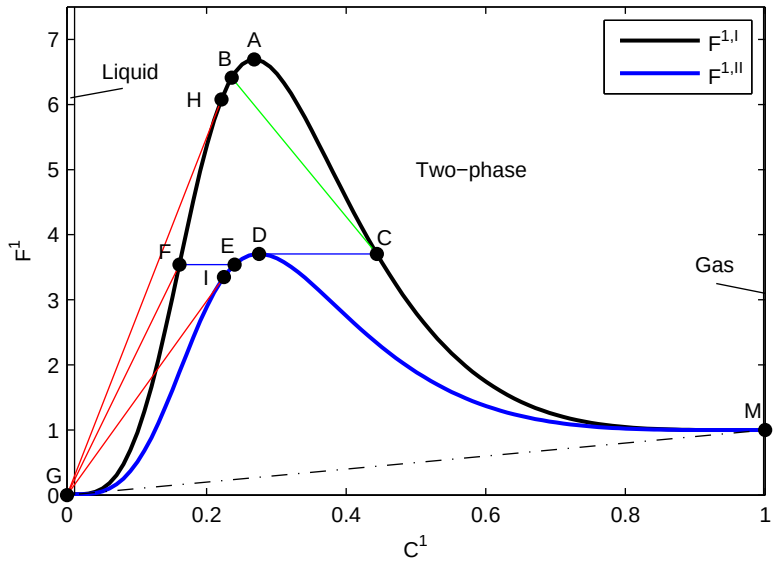

(a) H_2 and H_2O

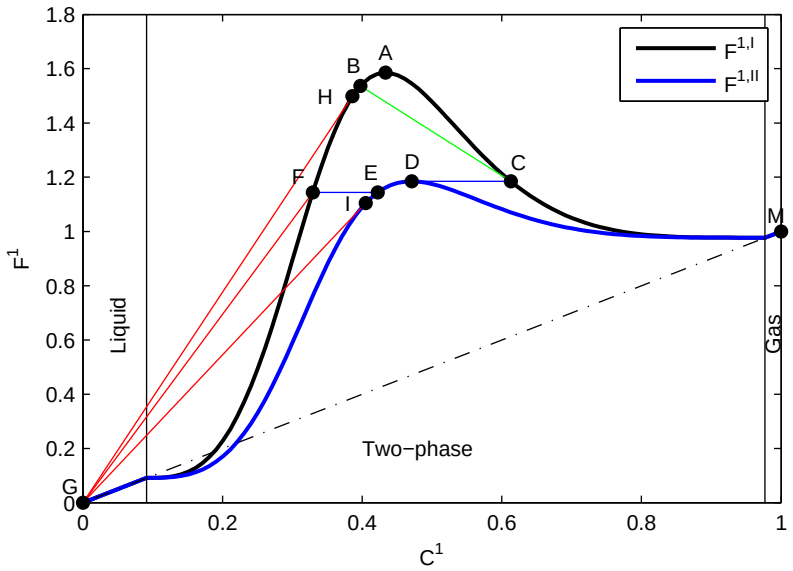

(b) CO_2 and H_2O

Figure 3.3: Diagram of fractional flow F^1 versus total concentration C^1 of the light component and the solution pathway for the two-component mixture of (a) H_2 and H_2O and (b) CO_2 and H_2O; curves I and II correspond to media I and II. Red lines are the upward shocks, green lines are the reverse downward shocks under the barriers, blue lines are the immobile shocks at the contact between two media.

calculated by:

$$x = x^0 + uF^{1\prime}t \tag{3.35}$$

where x^0 is the initial position. Graphically, this means that the velocity of a rarefaction wave is proportional to the tangent of the curve $F^1(C^1)$.

- *Mechanical concentration shocks* are moving discontinuities in the total concentration C^1 whereby the number of phases ahead and behind the shock is identical. Their relations are derived from the Rankine-Hugoniot and entropy conditions and can be constructed in the diagram $F^1(C^1)$. The Rankine-Hugoniot condition (Eq. 3.29f) requires the shock to be a straight line between points "+" and "−" on this function. To fulfill the Oleinik entropy condition (Eq. 3.29g) the straight line must not cross the curve $F^1(C^1)$ between points C^{1+} and C^{1-}. The Lax entropy condition (Eq. 3.29h) requires the tangent of the straight line to be between the tangents of the rarefaction waves just behind and ahead the shock. Related to the Lax equality condition (Eq. 3.29i) the tangent of the shock can be equal to the tangent of the rarefaction wave behind or ahead the shock. The velocity of the shock is proportional to the slope of the straight line in the diagram $F^1(C^1)$.

- *Shocks of phase transition* are moving discontinuities in the total concentration C^1 whereby the number of phases ahead and behind the shock is different. For the two components case their relations are the same as for mechanical concentration shocks.

- *Immobile discontinuities* in the total concentration C^1 are required at the interfaces between media I and media II to fulfill the continuity of fractional flow (Eq. 3.29j). In the diagram $F^1(C^1)$ they are constructed as horizontal straight lines which connect $F^{1,I}$ to $F^{1,II}$.

The solution need to be constructed in the diagram $F^1(C^1)$ as continuous combination of rarefaction waves and straight lines (plateaus, shocks and discontinuities) which represent the solution "pathway". The physical correct and only admissible pathway needs to be found by trial and error. In addition to the requirements for each individual segment, the following rules need to be followed to construct this pathway:

- If a rarefaction wave becomes a non-unique function, it will be replaced by a shock.
- The transport velocity (proportional to the derivative $\frac{\partial F^1}{\partial C^1}$) must not increase along the pathway. The positive direction of the pathway is from the injection point to the initial point.

After solving the problem with respect to the total concentration, the gas saturation S can be calculated by transforming Eq. 3.29b:

$$S = \begin{cases} 0 & \text{if } C^1 \leq c_w^1, \\ \frac{C^1 - c_w^1}{c_g^1 - c_w^1} & \text{if } c_w^1 < C^1 \leq c_g^1 \\ 1 & \text{if } C^1 > c_g^1 \end{cases} \tag{3.36}$$

3.6.3 Solution before reaching the barrier

A pure light component (H_2 or CO_2) is injected which means that the starting point of the pathway is point M. However, the rarefaction MA has a negative derivative which means the corresponding total concentrations would travel downwards, out of the domain which is considered here. Hence, the true starting point is point A which is the maximum of $F^{1,I}$. The solution pathway consists of the rarefaction wave ABH and the shock HG. The segment HG on the curve $F^{1,I}$ would lead to a non-unique solution and is therefore replaced by a shock. Point H is the tangent point of the straight line from point G to the curve $F^{1,I}$. The corresponding behavior of C^1 in the vertical domain is shown in Fig 3.4.

3.6.4 Solution after reaching the barrier

At the point in time when the shock HG reaches the barrier, the concentration at the contact between medium I and medium II is determined by point H. This is similar to the injection of a gas-water mixture at concentration C_H into medium II. However, the fractional flow F^1 at point H is higher than the maximum of curve $F^{1,II}$. Hence, the starting concentration in medium II is the maximal point D. From the continuity of fractional flow (Eq. 3.29j) it follows that the concentration at the contact in medium I has to be placed on the horizontal line passing through point D which is

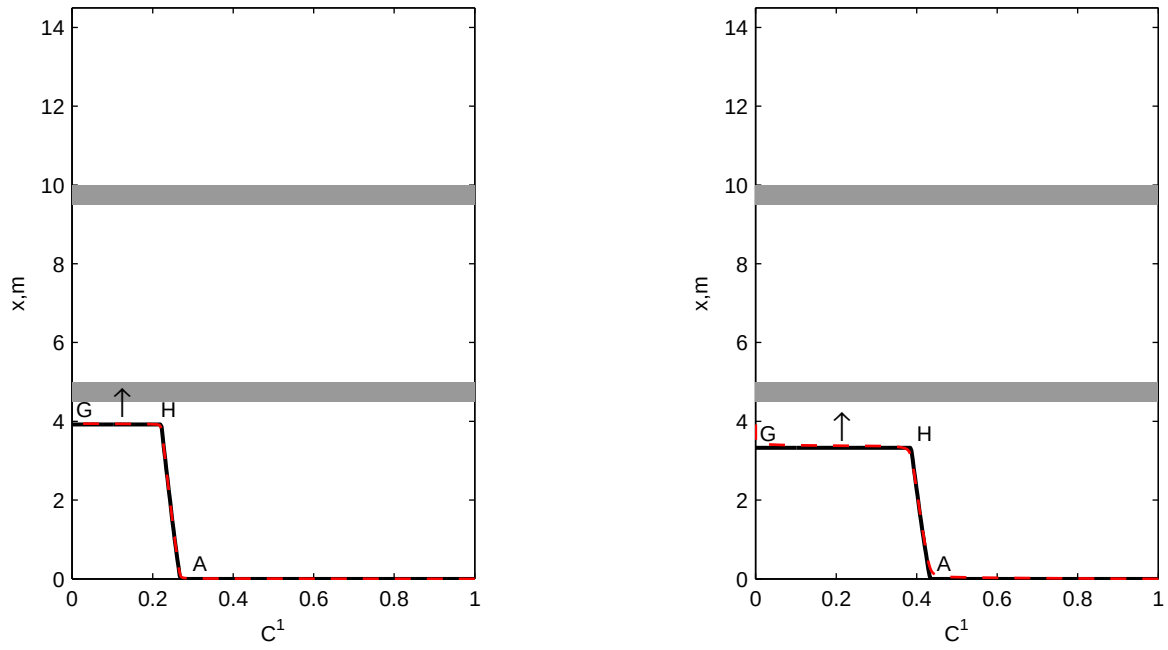

(a) for the system H_2 and H_2O after 0.6 days

(b) for the system CO_2 and H_2O after 3.5 days

Figure 3.4: Propagation of the total concentration C^1 before reaching the first barrier

point C. A new shock occurs between point C and point D. The shock CH has a negative slope which means that it is moving downwards. The concentration behind this shock remains constant and is determined by point C. However, the concentration ahead the shock is increasing on the curve ABH. Consequently, the slope of the shock increases which means that the shock is moving with acceleration. This downwards shock represents the accumulation of gas below the barrier.

Simultaneously, the solution in medium II is the rarefaction wave DEI and shock IG. When this shock has reached the upper limit of the barrier, the solution in medium II reduces to the rarefaction wave DE. Just above the barrier the concentration in medium I corresponds to point F placed on the horizontal line through point E. From point F there is a single possible continuation of the solution pathway which is the shock FG. The complete solution pathway at this point in time consists of the following segments (cf. Fig. 3.3): Rarefaction wave AB, downwards shock BC, discontinuity CD, rarefaction wave DE, discontinuity EF, upwards shock FG. The

corresponding solution in the vertical domain is shown in Fig 3.5.

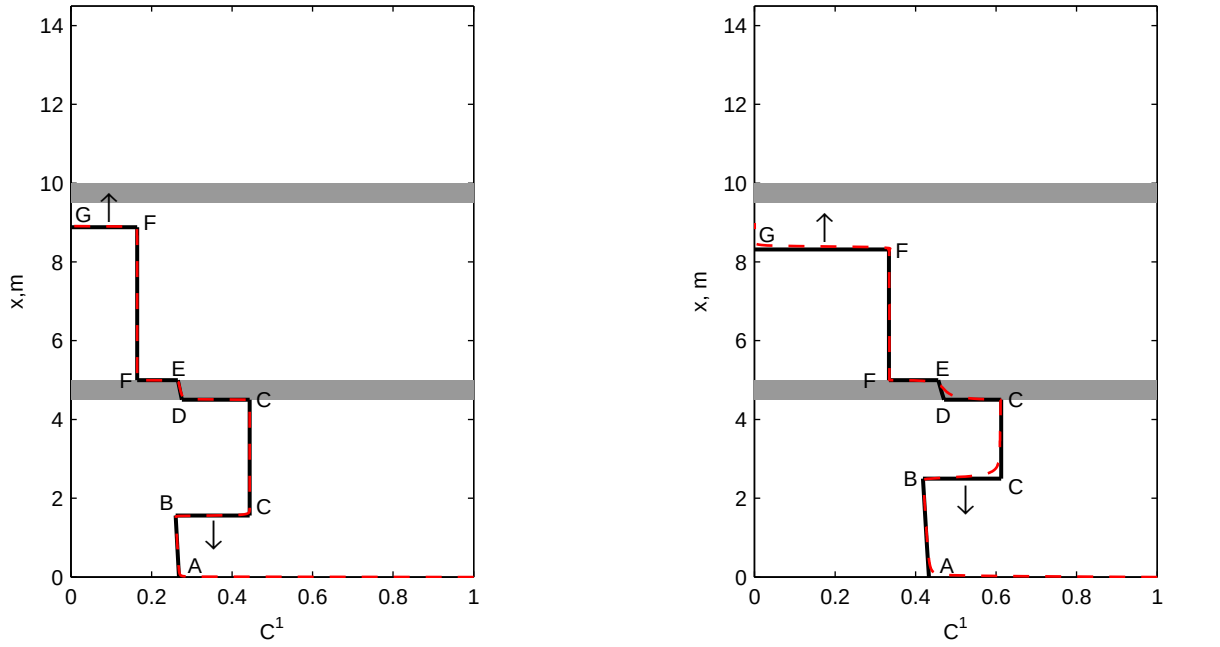

(a) for the system H_2 and H_2O after 1.5 days

(b) for the system CO_2 and H_2O after 9 days

Figure 3.5: Propagation of the total concentration C^1 after passing the first barrier

3.6.5 Characteristic points of the solution

The concentrations at points A, D, G, H, C and I are invariable in time and are determined graphically. A and D are the maximal points of the curves. G is the initial point. C lies on the horizontal line through point D. Points H and I are the tangent points of the straight lines through point G, respectively for $F^{1,I}$ and $F^{1,II}$.

In contrast, points B, E and F are floating and are determined analytically. Point B is located on the rarefaction wave and on the shock BC. Hence, using Eq. 3.35 and Rankine-Hugoniot condition 3.29f, the coordinate of

point B can be determined by:

$$\begin{aligned} x_B &= uF_B^{1,I\prime}t = x_1 + \int_{t_1}^{t} \frac{F_B^{1,I}(t') - F_C^{1,I}}{C_B^1(t') - C_C^1}dt', \\ t_1 &= \frac{x_1 C_H^1}{uF_H^{1,I}} \end{aligned} \tag{3.37}$$

where x_1 is the thickness of the high permeable layer I and t_1 is the arrival time of shock HG at the first barrier. The value C_H^1 is calculated from the Rankine-Hugoniot (Eq. 3.29f) and entropy (Eq. 3.29i) conditions. Inserting the values $C^{1+} = 0$, $F^{1+} = 0$, $C^{1-} = C_H^1$, and $F^{1-} = F^{1,I}\left(C_H^1\right)$ results in:

$$F^{1,I\prime}\left(C_H^1\right) = \frac{F_H^{1,I}}{C_H^1} \tag{3.38}$$

what can be solved for C_H^1. Concentration C_C^1 is obtained by solving the equation for the continuity of fractional flow:

$$F^{1,I}(C_C^1) = F^{1,II}(C_D^1) \tag{3.39}$$

where C_D^1 is the concentration at the maximum of $F^{1,II}$.

The derivative of Eq. 3.37 with respect to t yields to a non-linear differential equation with an initial value:

$$\begin{cases} F^{1,I\prime\prime}\left(C_B^1\right)\dfrac{dC_B^1}{dt}t + F^{1,I\prime}\left(C_B^1\right) = \dfrac{F^{1,I}\left(C_B^1\right) - F_C^{1,I}}{C_B^1 - C_C^1}, \\ C_B^1|_{t=t_1} = C_H^1 \end{cases} \tag{3.40}$$

This initial value problem can be solved numerically with respect to C_B.

The second floating point E is determined by the following implicit expression:

$$x_2 = uF^{1,I\prime}\left(C_E^1\right)(t - t_2), \qquad t_2 = t_1 + \frac{x_2 C_I^1}{uF_I^{1,II}\left(C_I^1\right)} \tag{3.41}$$

where x_2 is the thickness of the barrier (medium II) and t_2 is the time when the shock FG reaches the upper limit of the barrier. The concentration C_F^1

is determined from:

$$F^{1,I}\left(C_F^1\right) = F^{1,II}\left(C_E^1\right) \tag{3.42}$$

It follows that the position of the upward shock FG is obtained by solving the integral equation:

$$x_G = x_1 + x_2 + \int_{t_2}^{t} \frac{F^{1,I}\left(C_F^1(t')\right)}{C_F^1(t')} dt' \tag{3.43}$$

3.6.6 Solution after reaching the second barrier

For identical barriers the downwards shock appears only below the first barrier. However, a second downwards shock appears when the second barrier has a lower permeability than the first one. This means a downwards shock appears below each barrier which has a lower permeability than the previously passed barriers.

In Fig. 3.6 the fractional flow functions are shown for three media: medium I (500 mD), medium II (250 mD), medium III (125 mD).

The concentration in the second barrier (medium III) corresponds to point K which is the maximum of $F^{1,\mathrm{III}}$. According to the continuity of fractional flow (Eq. 3.29j), the concentration at the interface to medium I below the barrier corresponds to point L. Point L is the intersection of a horizontal straight line through point K with $F^{1,\mathrm{I}}$. However, as seen from Fig. 3.5 the upwards shock reaches the second barrier with concentration F. Consequently, the shock FL appears. This shock has a negative slope what means that it is propagating downwards below the second barrier. Within the second barrier the solution is equivalent to the solution within the first barrier. Before the upper limit of the barrier is reached, the solution consists of the rarefaction wave KN and upwards shock NG. After passing the second barrier the concentration at the upper limit of the barrier is determined by point Q which is moving upwards from point N to point K. The concentration at the interface to medium I above the barrier is determined by point P which is the intersection of a horizontal straight line through point Q with $F^{1,\mathrm{I}}$. The solution pathway in medium I above the second barrier continues with shock PG. In Fig. 3.7 the solution is shown in the vertical domain after 3 days.

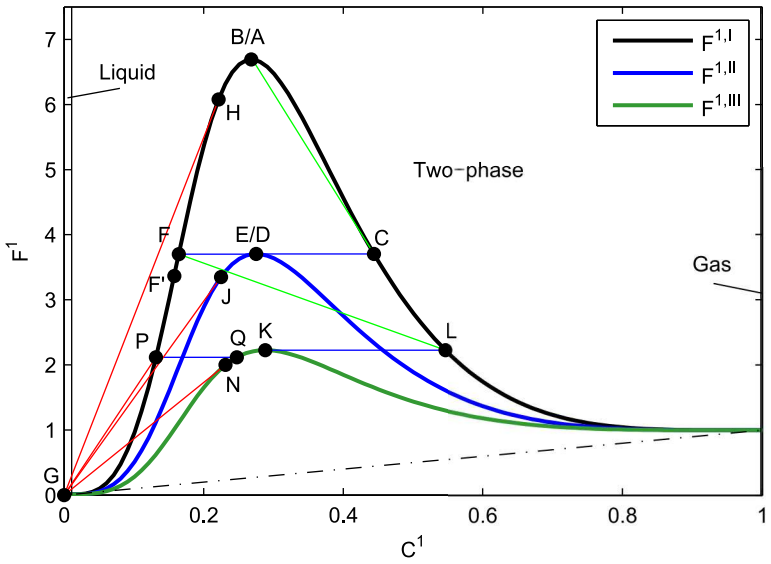

Figure 3.6: Diagram of fractional flow F^1 versus total concentration C^1 for H_2 and H_2O, for highly permeable medium I and two low-permeable barriers II and III: Red lines are the upward shocks, green lines are the reverse downward shocks under the barriers, blue lines are the immobile shocks at the contact between two media.

3.6.7 Gas rising velocity and growth velocity of gas accumulations

As mentioned in the previous sections, the velocities of the upwards and downwards shocks are not constant. This means that the gas rises with a variable velocity and also the gas bubbles below the barriers grow with a variable velocity.

The average growth velocity for the accumulation below the first barrier is determined by the slope of the straight line between HC and AC (cf. Fig 3.6). The average growth velocity of the accumulation below the second barrier is determined by the slope of the straight line between $F'L$ and FL. F' is placed on the horizontal line through J. The corresponding gas saturation can be calculated by Eq. 3.36.

The velocity of gas rising can be also determined from Fig 3.6. Below the first barrier the velocity can be determined from the slope of the tangent line HG. The passage through the barrier corresponds to line JG with a

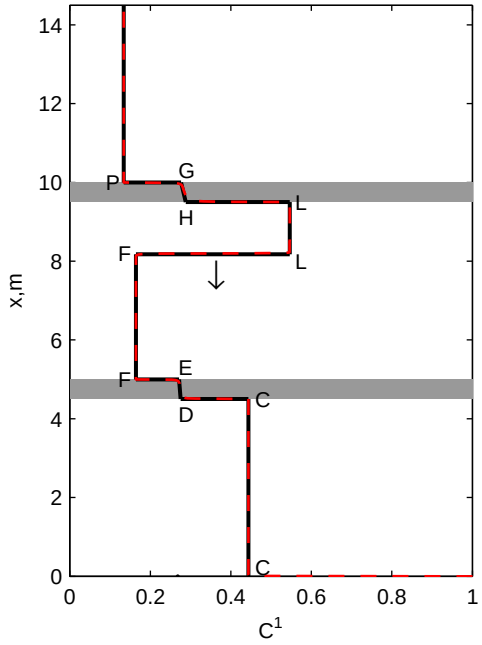

Figure 3.7: Propagation of the total concentration C^1 after passing the second barrier for the system H_2 and H_2O (after 3 days)

much smaller slope and consequently a slower velocity. Between the first and second barrier the gas rises with a velocity which corresponds to the slope of line FG. The velocity is variable because point F is moving upwards. The velocity of passing the second barrier is determined by the slope of line NG. Subsequently, the gas continues to rise in medium I with the velocity which corresponds to the slope of line PG. The gas rising velocity and growth velocity of gas accumulations below the barriers are sketched in Fig. 3.8 and Fig. 3.9. The rates are presented in dimensionless form which means that the velocities are divided by the injection velocity u. It can be seen that the average rate of rising is 20 times the injection velocity and the average rate of gas accumulation growth is 10 times the injection velocity.

3.6.8 Comparison with immiscible two-phase flow

The obtained solutions for two-component mixtures with partial miscibility have been compared to the solution for immiscible flow. The solution for immiscible flow can be found e.g. in Hagemann [51]. Fig. 3.17 shows the gas saturations for H_2 and CO_2 rising in water using the different models. It

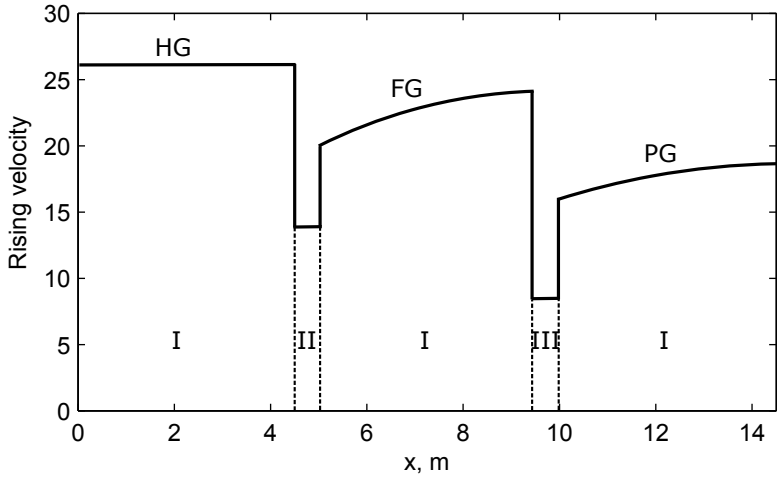

Figure 3.8: Dimensionless rate of hydrogen rising along x

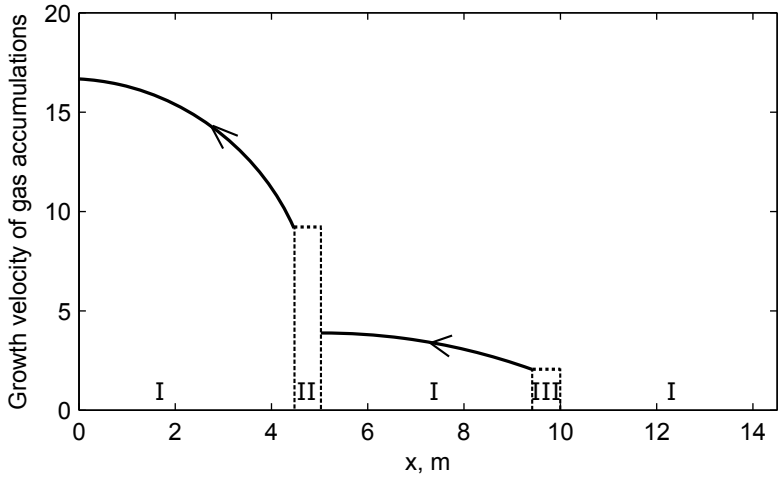

Figure 3.9: Dimensionless growth velocity of the gas accumulation below the barriers

can be seen that the miscibility reduces the velocity of gas rising. For CO_2, which is highly miscible in water, the difference is very significant. For this case the velocity of the upward shock in medium I is 1.28 m/day for the immiscible case and only 0.96 m/day for the miscible case.

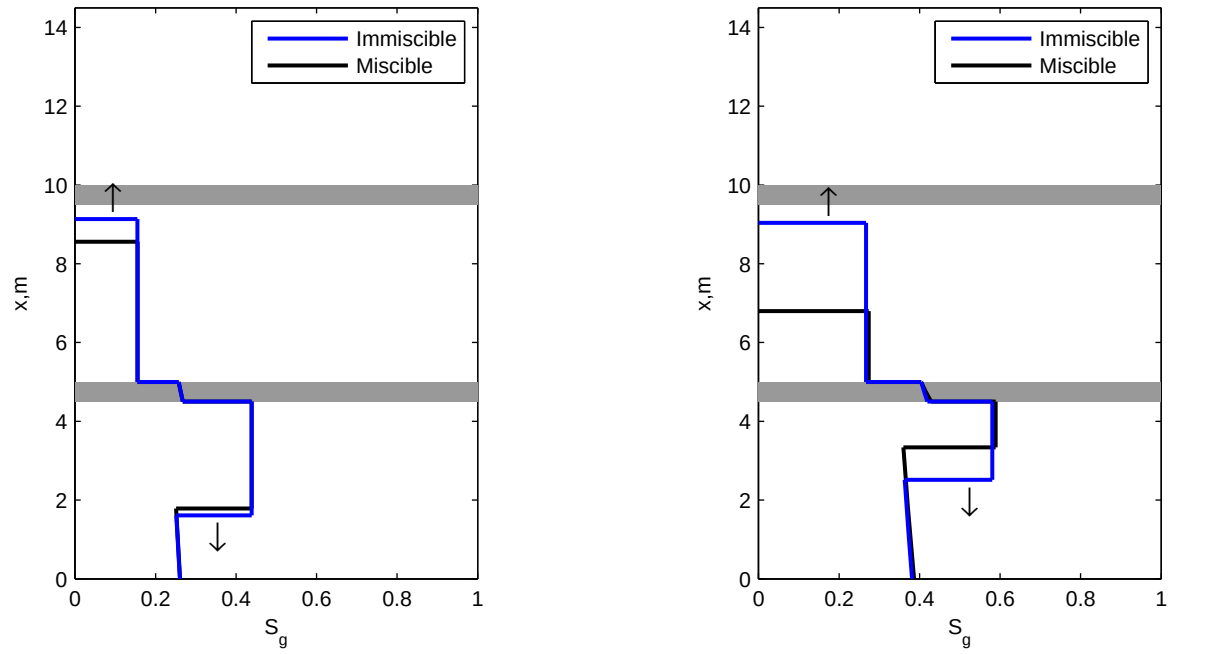

(a) for the system H_2 and water after 1.5 days

(b) for the system CO_2 and water after 7.5 days

Figure 3.10: Comparison of the two-phase miscible flow and immiscible flow

3.7 Three-component flow

The next section considers the mixture of hydrogen and carbon dioxide in water. The system consists of three chemical elements: H_2 (component 1), CO_2 (component 2) and H_2O (component 3).

3.7.1 Thermodynamics of three-component mixtures

The thermodynamics of dissolution for three components in two phases can be represented in a ternary phase diagram which is shown in Fig. 3.11. The diagram was calculated by an EOS software using the Peng-Robinson equation of state [105]. The tie lines and the boundaries of the two-phase region were subsequently simplified as straight lines (cf. Eq. 3.44 and Eq. 3.45). The concentration of H_2O is zero on the diagonal boundary of the triangle and one at the origin. At low H_2O concentration (near to the diagonal boundary) the system is gaseous, while at high water concentrations (near

to the origin) the system is liquid. The remaining area of the diagram corresponds to two-phase states.

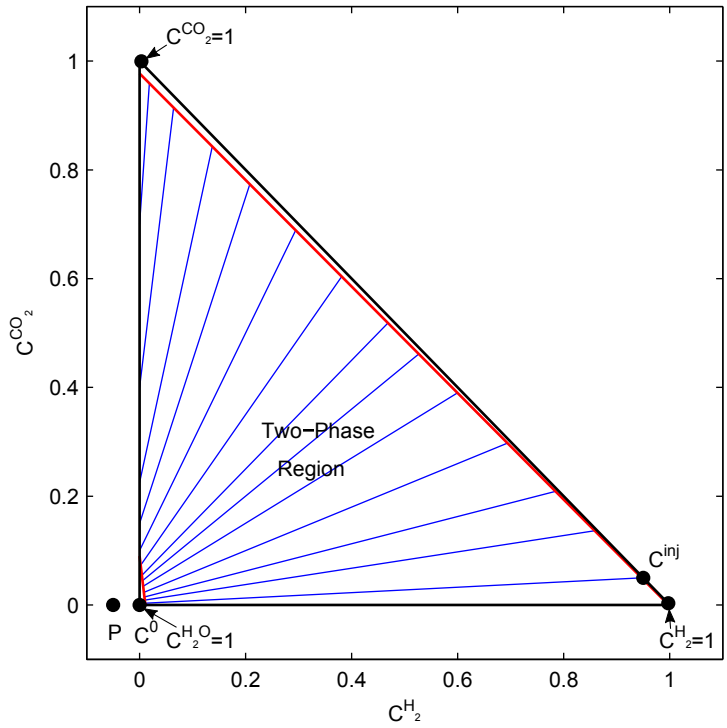

Figure 3.11: Ternary phase diagram for the mixture H_2, CO_2, H_2O at 400 *bar* and 125 $°C$

For a three-component system, the equilibrium between the phases (Eq 3.10) is determined by three equations which have four concentrations: c_g^1, c_g^2, c_w^1, c_w^2. This means that one concentration is free while all others depend on it. The parameter α, which is a combination of phase concentrations, can be introduced to close the system. Parameter α is based on the concept of *tie lines*, which are lines of constant phase composition. They are shown as blue lines in Fig. 3.11. Tie lines are defined to be straight. Hence, it follows from the definition of total concentrations (Eq. 3.21b) that the relationship between C^1 and C^2 is linear:

$$C^2 = \alpha C^1 + \beta, \quad \alpha \equiv \frac{c_g^1 - c_w^1}{c_g^2 - c_w^2}, \quad \beta = c_w^1 - \alpha c_w^2 \tag{3.44}$$

Parameter β depends also on α. It is assumed that $\beta = -\gamma\alpha$ and $\gamma = const$,

which means that all tie lines intersect in one point $(C^1, C^2) = (\gamma, 0)$. Here, γ is assumed to be -0.05. Hence, for a given point on a tie line within the two-phase region, the composition of both phases is determined at the boundary points of the two-phase region on this tie line. For simplicity it is assumed that the two-phase region has straight line boundaries:

$$c_i^2 = m_i\, c_i^1 + b_i, \quad i = g, w \tag{3.45}$$

It follows that the phase composition for three-component flow is variable and additional compositional effects could arise which increase the difference to the immiscible flow.

3.7.2 Canonical model for three-component flow

The canonical model for $k = 1, 2$ becomes:

$$\frac{\partial C^k}{\partial t} + u\frac{\partial F^k}{\partial x} = 0 \tag{3.46a}$$

where:

$$C^k = c_g^k S + c_w^k (1 - S) \tag{3.46b}$$

$$F^k = \begin{cases} \left(c_w^k(1-f) + c_g^k f\right) + G(c_g^k - c_w^k) \sum\limits_{j=1}^{2} \left(\rho^j - \rho^3\right)\left(c_w^j - c_g^j\right) & \text{if two-phase} \\ C^k & \text{if single-phase} \end{cases} \tag{3.46c}$$

The boundary and initial conditions are:

$$\begin{aligned} C^1(t = 0, x > 0) &= C^{1,0} \\ C^2(t = 0, x > 0) &= C^{2,0} \end{aligned} \tag{3.46d}$$

$$\begin{aligned} C^1(x = 0) &= C^{1,inj} \\ C^2(x = 0) &= C^{2,inj} \end{aligned} \tag{3.46e}$$

The fractional flow F^k is a function of the saturation S (or C^k) and α only.

3.7.3 Structure of the solution

The shape of the curves F^k is shown in Fig. 3.12. For the injection of a gas mixture with 95% H_2 and 5% CO_2 the initial and injection concentrations are placed on different tie lines, for the investigated case $\alpha^0 = 0$ and $\alpha^{inj} = 0.05$. Hence, at least two different functions are needed: $F^1(C^1, \alpha^0)$ and $F^1(C^1, \alpha^{inj})$. For the linear dependence between α and β, the behavior of the function $\alpha(x,t)$ is piecewise constant [41]. The function $C^1(x,t)$ can again consist of plateaus, rarefaction waves, shocks and immobile discontinuities. Two types of shocks are admissible: C-shocks, for which only the total concentration C^1 is discontinuous and $C\alpha$-shocks, for which both functions C^1 and α are discontinuous.

For C-shocks, two Rankine-Hugoniot conditions can be reduced to one:

$$\frac{u_s}{u} = \frac{F^{1+} - F^{1-}}{C^{1+} - C^{1-}} \tag{3.47}$$

For $C\alpha$- shocks the total concentration and the tie line change across the shock. The two Rankine-Hugoniot conditions can be presented in the following form:

$$\frac{u_s}{u} = \frac{F^{1+} - F^{1-}}{C^{1+} - C^{1-}}, \quad \frac{u_s}{u} = \frac{F^{1-} + \gamma}{C^{1-} + \gamma} \tag{3.48}$$

Additional conditions are the entropy condition and the continuity of fractional flow at the interface between different media.

The geometrical image of a C-shock, according to these conditions, is a straight line between the points (C^{1-}, F^{1-}) and (C^{1+}, F^{1+}) laying an the same curve (same α). According to the entropy conditions the straight line is tangent to the corresponding curve $F^1(C^1)$.

For a $C\alpha$-shock the image is a straight line which passes through three points (C^{1-}, F^{1-}), (C^{1+}, F^{1+}) and the pole (γ, γ). Points "+" and "−" are placed on two different curves that correspond to two different α. The straight line has to be tangent to one of the curves $F^1(C^1)$.

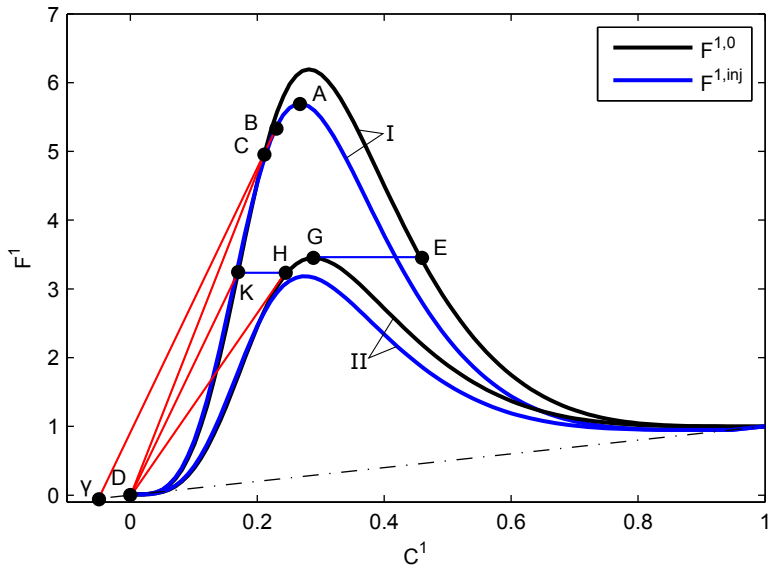

Figure 3.12: Fractional flow of the lightest component, F^1, for α^0 (black curves) and α^{inj} (blues curves) for media I and media II; the straight lines correspond to upward shocks (red), reserve downward shocks (green) and immobile discontinuities (blue)

3.7.4 Solution of the problem before reaching the barrier

For the three-component case the solution is constructed by using the same technique of trial and error but now two diagrams have to be used: The diagram of fractional flow $F^1(C^1)$ and the ternary diagram (Fig. 3.11). In Fig. 3.12 two pairs of functions are shown for α^0 and α^{inj}, each for medium I and for medium II. Hence, the solution has to be constructed by using a total number of four fractional flow curves.

The propagation starts within medium I on the curve which corresponds to α^{inj}. The pathway starts at point A, which is the maximum of $F^1(C^1, \alpha^{\text{inj}})$. The part on this curve between the maximum point A and point $(1, 1)$ is excluded because it leads to a non-physical solution similar to the two-component case. The pathway continues in direction to the initial point $(0, 0)$. It consists of the rarefaction wave ABC which lies on the injection curve (α^{inj}), the $C\alpha$-shock BCP, along which the transition between the injection and initial curve occurs, and C-shock CD corresponding to α^0. The $C\alpha$-shock in medium I is the transition between the injection and initial curve and can be immediately detected by constructing the straight line

PCB which passes through the pole P, crosses two curves for two different values of α and is tangent to one of these curves in point B. The solution for C^1 versus x is shown in Fig. 3.17a.

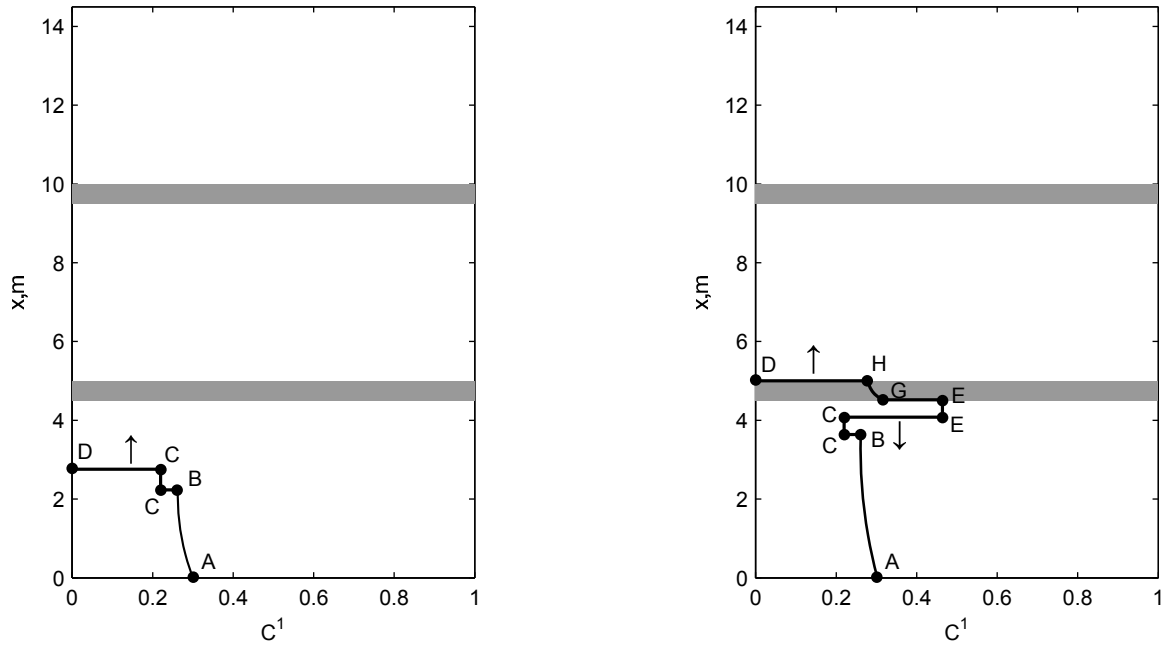

(a) before reaching the barrier

(b) after crossing the barrier

Figure 3.13: Total concentration of the light component (hydrogen)

Behind the second shock BC the system is two-phase whereby the gas has the injected composition and the composition of the non-displaced water is in equilibrium with this gas. Between the two shocks the water has the initial composition. In this case it is pure H_2O and the gas phase consists only of H_2. The upward shock CD is the mechanical front of displacement what means that the phase composition does not change across it.

3.7.5 Moment of reaching the barrier

When the forward shock reaches the barrier (medium II), the gas begins to propagate through medium II. For the C-shock only the total concentration is discontinuous while the parameter α remains continuous (α^0). The pathway jumps to point G which is the maximum of curve $F^1(C^1, \alpha^0)$ that corresponds to medium II. This can be seen in Fig. 3.12. The contact

concentration just below the barrier in medium I corresponds to point E, according to the continuity of fractional flow. This means that the concentration in medium I jumps from C to E, whereby the new shock EC arises. The slope of this shock is negative what means that it propagates downwards. According to Fig. 3.12 the concentrations ahead and behind this shock are constant and correspond to α^0. Hence, the velocity of this shock is also constant.

Within the barrier (medium II) the inlet and outlet phase concentrations correspond to α^0 what means that the solution lies on the upper curve $F^1(C^1)$ in medium II. The pathway continues with the rarefaction wave GH and the C-shock HD propagating upwards. HD is tangent to the upper curve $F^1(C^1)$ in medium II.

When the shock HD reaches the upper limit of the barrier and enters medium I, the concentration ahead jumps, due to the continuity of fractional flow, to point K (cf. Fig. 3.13). The phase concentration remains continuous corresponding to α^0. A single possibility exists to construct a pathway from point K: The straight line KD. The solution above the barrier has the form of a plateau KK and the C-shock KD which corresponds to α^0. As α remains invariable no $C\alpha$-shocks appear within the barrier.

3.7.6 Evolution of the reverse wave under the barrier

Below the barrier two shocks are propagating in opposite directions: The $C\alpha$-shock BC is moving upwards and the EC-shock is moving downwards (cf. Fig. 3.13b). The propagation of the downwards shock becomes very complex after it collides with the shock BC. In Fig. 3.14 the graphical construction is illustrated which shows multiple shocks appearing below the barrier at different moments. After shock EC collides with shock BC the new shock EB is formed (dashed green line). The solution of C^1 versus x at this moment is shown in Fig. 3.15a. However, this shock relates the curve with phase composition α^0 in point E and the curve with phase composition α^{inj} in point B without crossing the pole P. Hence, the shock is unstable and immediately decomposes into two shocks: The C-shock MB' moving down with invariable phase composition and the $C\alpha$-shock EM moving upwards. Point B' is variable and moves along the curve from B towards A. The phase composition below the $C\alpha$-shock EM corresponds to α^{inj} while the

concentration above corresponds to α^0. As the shock EM is not connected to any rarefaction wave it can not be tangent to one of the curves. At large times the shock MB' will reach the bottom of the domain and shock EM will reach the barrier. At this point in time the gas phase below the barrier has the injected composition and the water is in equilibrium with it.

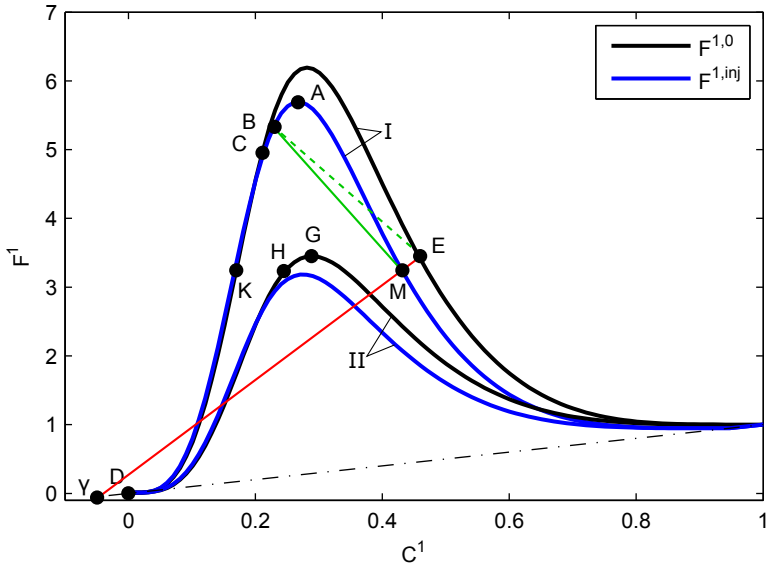

Figure 3.14: Graphical construction of the reverse wave: Decomposition of the unstable shock EB into two shocks EM and MB

3.8 Comparison to two-dimensional problem

The problem was also analyzed in two dimensions by solving it numerically. The model includes three components: H_2, CO_2 and H_2O and it is assumed that H_2O is not present in the gaseous phase.

3.8.1 Formulation of 2D problem

The system of equations (Eq. 3.1) extended by a second dimension becomes:

$$\phi \frac{\partial}{\partial t}\left(\hat{\rho}_g c_g^k S + \hat{\rho}_w c_w^k (1-S)\right) + \nabla \cdot \left(\hat{\rho}_g c_g^k v_g + \hat{\rho}_w c_w^k v_w\right) = 0, \quad k = H_2, CO_2, H_2O \tag{3.49a}$$

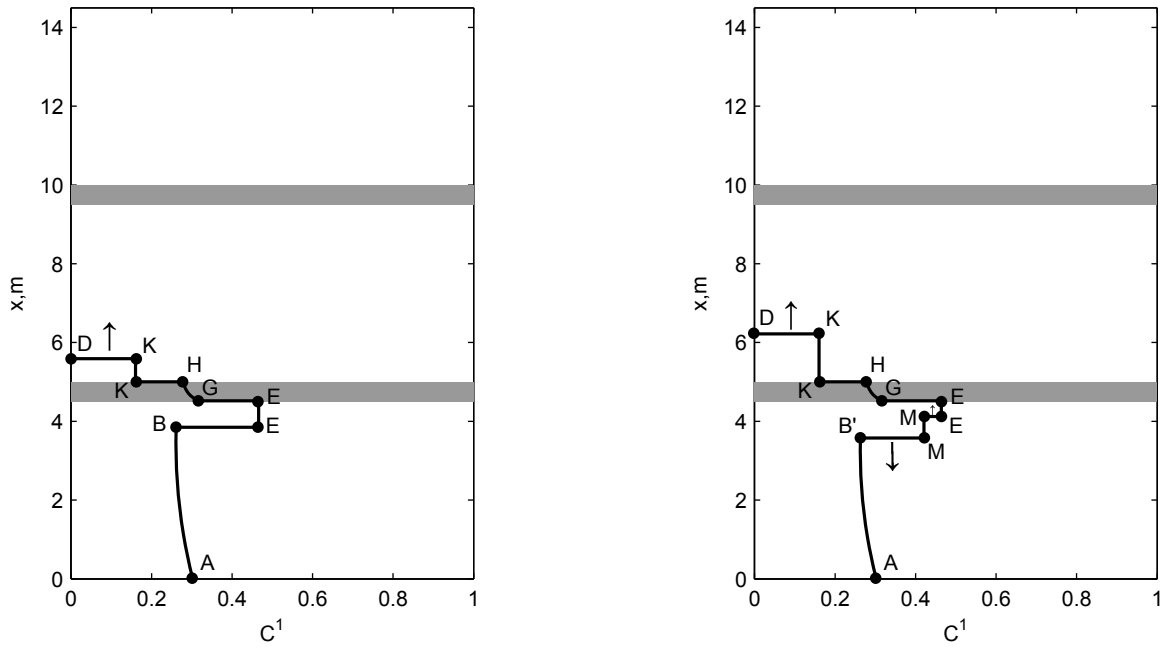

(a) moment of collision **(b)** after collision

Figure 3.15: Evolution of reserve wave for the light component (hydrogen)

$$v_i = -\lambda_i \left(\nabla P - \rho_i g \right), \quad i = g, w \tag{3.49b}$$

where v is Darcy velocity vector and g is the gravity acceleration vector.

The dimensions of the two-dimensional domain are as follows:

- 19.5m in vertical direction
- 100m in horizontal direction
- Dislocated impermeable barriers of 40m width with 10m horizontal spacing and 5m vertical spacing between them.

The initial and boundary conditions are defined to be equivalent to the one-dimensional problem (cf. section 3.8.2)

3.8.2 Numerical implementation

This problem was implemented in the software package COMSOL Multiphysics which uses the finite element method as spatial discretization and

an implicit discretization over time. The equation system 3.49a was rearranged in the following way: The sum of all equations 3.49a and partial differentiation leads to the first equation:

$$\phi(\hat{\rho}_w - \hat{\rho}_g)\frac{\partial S_w}{\partial t} - \nabla \cdot \left(\hat{\rho}_w \frac{K k_{rw}}{\mu_w}(\nabla P - \hat{\rho}_w g) + \hat{\rho}_g \frac{K k_{rg}}{\mu_g}(\nabla P - \hat{\rho}_g g) \right) = 0 \quad (3.50a)$$

The second equation can be derived by inserting the sum of mass fractions ($c_g^{CO_2} = 1 - c_g^{H_2}$) and Henry's law ($c_w^{CO_2} = c_g^{CO_2} H^{CO_2} P$) into equation 3.49a for $k = CO_2$ and differentiate partially:

$$\begin{aligned} &\phi\left(1 - c_g^{H_2}\right)\left(\hat{\rho}_w H^{CO_2} P - \hat{\rho}_g\right)\frac{\partial S_w}{\partial t} - \phi\left(\hat{\rho}_g(1 - S_w) + \hat{\rho}_w H^{CO_2} P S_w\right)\frac{\partial c_g^{H_2}}{\partial t} \\ &+\phi\hat{\rho}_w H^{CO_2} S\left(1 - c_g^{H_2}\right)\frac{\partial P}{\partial t} \\ &-\nabla\left(\left(1 - c_g^{H_2}\right)\frac{K k_{rw}}{\mu_w}(\nabla P - \hat{\rho}_g g) + H^{CO_2} P \frac{K k_{rw}}{\mu_w}(\nabla P - \hat{\rho}_g g)\right) = 0 \end{aligned} \quad (3.50b)$$

The third equation can be derived by inserting Henry's law ($c_w^{H_2} = c_g^{H_2} H^{H_2} P$) into equation 3.49a for $k = H_2$ and again differentiate partially:

$$\begin{aligned} &\phi\left(\hat{\rho}_g(1 - S_w) + \hat{\rho}_w H^{H_2} P S_w\right)\frac{\partial c_g^{H_2}}{\partial t} + \phi c_g^{H_2}\left(\hat{\rho}_w H^{H_2} P - \hat{\rho}_g\right)\frac{\partial S_w}{\partial t} \\ &+\phi\hat{\rho}_w H^{H_2} S c_g^{H_2}\frac{\partial P}{\partial t} - \nabla\left(c_g^{H_2}\frac{K k_{rw}}{\mu_w}(\nabla P - \hat{\rho}_g g) + H^{H_2} P \frac{K k_{rw}}{\mu_w}(\nabla P - \hat{\rho}_g g)\right) = 0 \end{aligned} \quad (3.50c)$$

These equations were entered into the "Coefficient Form PDE Interface" of COMSOL and solved implicitly for P, S_w and $c_g^{H_2}$. The initial and boundary conditions are as follows. The initial pressure follows the hydrostatic gradient:

$$P(t = 0) = \left(4 \cdot 10^7 + 10^4 \cdot (19.5 - x)\right) Pa \quad (3.51)$$

The domain is initially saturated by water and the (non-existing) gas consists of 100% H_2:

$$\begin{aligned} S_w(t = 0) &= 1 \\ c_g^{H_2}(t = 0) &= 1 \\ c_g^{CO_2}(t = 0) &= 0 \end{aligned} \quad (3.52)$$

The upper boundary is defined by Dirichlet conditions:

$$\begin{aligned} P(x = 19.5m) &= 4 \cdot 10^7 Pa \\ S_w(x = 19.5m) &= 1 \\ c_g^{H_2}(x = 19.5m) &= 1 \end{aligned} \tag{3.53}$$

The left and right boundary and all barrier boundaries are defined by Neumann conditions with no flow across:

$$\left.\begin{aligned} -n \cdot (-\hat{\rho}_g \lambda_g (\nabla P - \hat{\rho}_g g) - \rho_w \lambda_w (\nabla P - \hat{\rho}_w g)) &= 0 \\ -n \cdot \left(-\hat{\rho}_g \lambda_g (1 - c_g^{H_2})(\nabla P - \hat{\rho}_g g) - \hat{\rho}_w \lambda_w H^{CO_2} P (1 - c_g^{H_2})(\nabla P - \hat{\rho}_w g)\right) &= 0 \\ -n \cdot \left(-\hat{\rho}_g \lambda_g c_g^{H_2} (\nabla P - \hat{\rho}_g g) - \hat{\rho}_w \lambda_w H^{H_2} P c_g^{H_2} (\nabla P - \hat{\rho}_w g)\right) &= 0 \end{aligned}\right\} \tag{3.54}$$

where n is the normal vector related to the boundaries. The lower boundary is defined with a constant inflow velocity of a gas mixture composed of 95% H_2 and 5% CO_2:

$$\left.\begin{aligned} -n \cdot (-\rho_g \lambda_g (\nabla P - \rho_g g) - \rho_w \lambda_w (\nabla P - \rho_w g)) &= u \\ -n \cdot \left(-\rho_g \lambda_g (1 - c_g^{H_2})(\nabla P - \rho_g g) - \rho_w \lambda_w H^{CO_2} P (1 - c_g^{H_2})(\nabla P - \rho_w g)\right) &= 0.05 \cdot u \\ -n \cdot \left(-\rho_g \lambda_g c_g^{H_2} (\nabla P - \rho_g g) - \rho_w \lambda_w H^{H_2} P c_g^{H_2} (\nabla P - \rho_w g)\right) &= 0.95 \cdot u \end{aligned}\right\} \tag{3.55}$$

The numerical stability was ensured in two ways. An adaptive mesh refinement was used, which is an automatic function of COMSOL Multiphysics. It enables to refine the mesh during processing only where and when it is required, i.e. near high values of saturation and concentration gradients or more explicitly in the vicinity of the shocks. Secondly, small artificial diffusion terms were introduced which regularize the solution around the shocks. The optimal value for the diffusion coefficients obtained by numerical tests is $5 \cdot 10^{-5}$. The validity of the code was verified by solving the one-dimensional problem and comparing it to the analytical solution.

3.8.3 Equivalence between 2D flow around impermeable barriers and 1D flow through low-permeable barriers

Fig. 3.16 shows the total H_2 concentration in the 2D domain after one and after four days. Below each barrier the rising of is stopped until it begins to flow around. A reverse wave below each barrier arises and propagates down. This leads to the formation of gas accumulations similar to the results of the analytical model. The averaged total H_2 concentration over

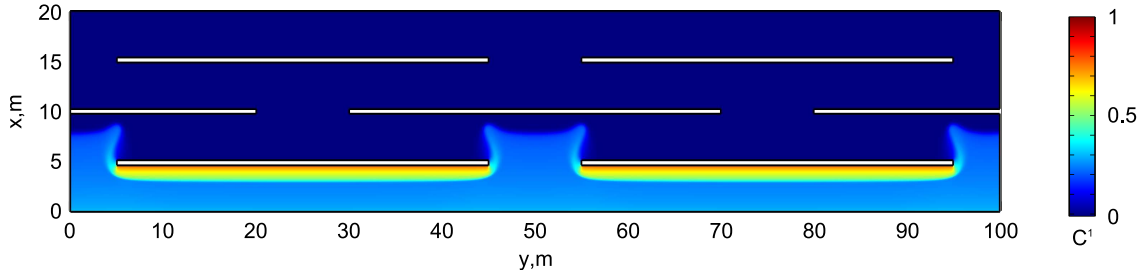

(a) after 1 day

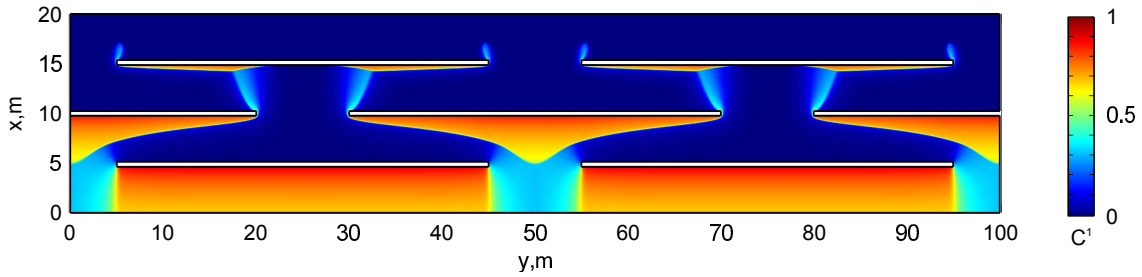

(b) after 4 days

Figure 3.16: H_2 concentration in the 2D domain

the horizontal axis is thereby of interest. In Fig 3.17 this averaged value from the 2D simulation is compared to the analytical solution. It can be observed that the characteristic behavior for the accumulations below the barriers is very similar and also the rising velocity is similar. This means that the characteristic time of flowing around the impermeable barrier in the 2D case is equivalent to the time of flowing through the low-permeable barrier in the 1D case. The permeabilities of the barriers in the analytical solution shown in Fig 3.17 have a ratio of 0.5 and 0.25 compared to the reservoir permeability.

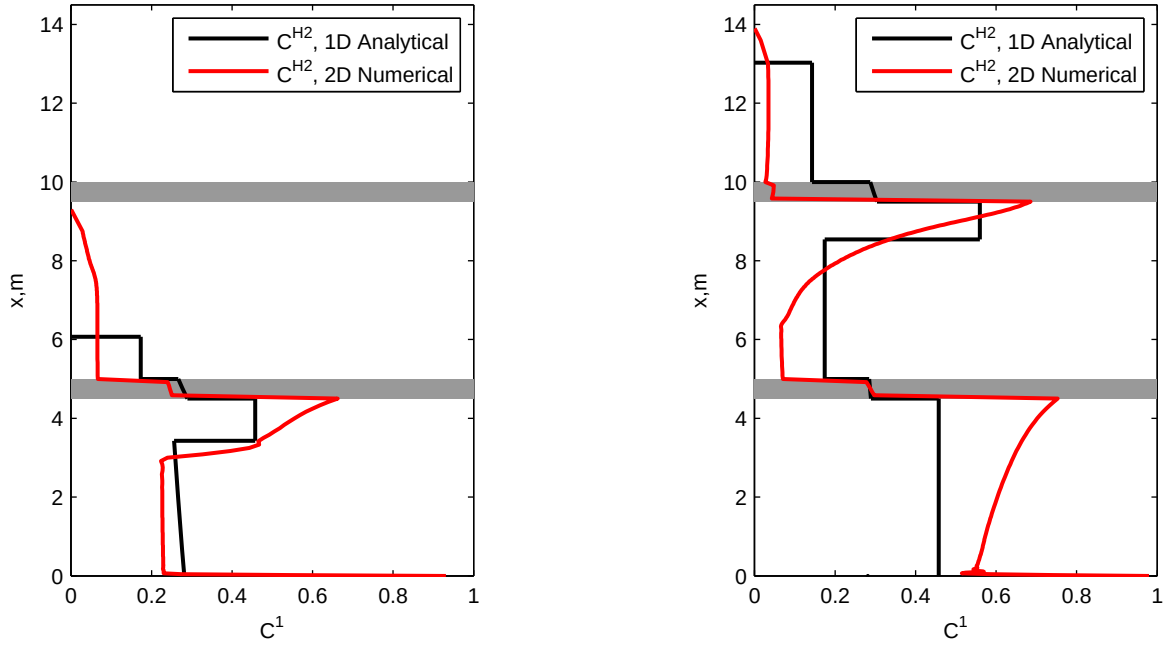

(a) after 1 day **(b)** after 3 days

Figure 3.17: Average total concentration of hydrogen along the vertical axis for the 2D model with impermeable barriers (red curve) and the 1D analytical solution with low permeable barriers (black curve)

3.9 Summary and conclusions

The gas injection at the top of underground reservoirs could lead to gas losses due to uncontrollable spreading of viscous fingers beyond the spill point of the structure. To avoid them the gas could be injected into the bottom of the reservoir whereat the rising would be retarded by horizontal geological barriers. For this concept the analysis of gas rising through water in a stratified reservoir plays a key role. The exact analytical solution of the problem of gas injection for two-component and three-component two-phase systems was derived in this chapter. The model takes into account the dissolution of chemical components in gas and water. The barriers are low-permeable and have different permeabilities. The results of the study allow the following conclusions:

- In the case of two-component mixtures (H_2 and H_2O, or CO_2 and H_2O), the phase composition remains constant. The single qualita-

tive effect which differs this case from the immiscible flow is the phase transition (liquid vaporizing), which occurs when a non-equilibrium gas is injected into water. The elements of the solution are: The upwards shock of water displacement by gas, reverse shocks below each barrier, which are propagating down at high gas saturations and continuous curves (rarefaction waves) within the barriers. The solution behaves qualitatively similar to the case of immiscible flow but the velocity of upwards and downwards shocks are different.

- In the case of three-component flow (H_2, CO_2 and H_2O), the behavior is much more complicated and characterized by a variable phase compositions. This leads to the appearance of a new upward shock (referred to as $C\alpha$-shock). This new shock is caused by the effect of dissolution and corresponds to a sharp variation of the composition of gas and liquid. Behind this shock gas has the injected composition and the composition of liquid corresponds to the equilibrium with this gas. Ahead this shock the liquid has the initial composition while the gas composition corresponds to pure H_2.

- Another phenomenon observed in the three-component case is the collision of the downwards C-shock and the upwards $C\alpha$-shock below the first barrier. The new shock which arises from the collision is unstable and decomposes into two shocks. One of them is a C-shock and moves up while the other one is a $C\alpha$-shock which moves down.

- For a periodic medium where the barriers have the same permeability, a downwards shock or a gas accumulation occurs only below the first barrier. Such shocks appear under each barrier only if the permeability of barriers decreases from the bottom to the top. The growth velocity of gas accumulation under the first barrier is 4 times higher than that under the second barrier (cf. Fig. 3.9).

- Hydrogen rises more than five times faster than CO_2 in periodic domains. H_2 creates more significant gas accumulations under the barriers.

- The two-dimensional model with impermeable barriers also proves the effect of a retarded gas rising due to flowing around the barriers. The wider the barriers, the larger the time of delay.

- It was shown by the comparison to the numerical solution in 2D that a 1D model with low-permeable barriers could replace a 2D model with impermeable barriers. The permeability of low-permeable barriers has to progressively decrease down up according to a specific law.

It can be summarized that both low permeable and impermeable barriers slow down the rising of gas. A layering with increasing heterogeneity towards the reservoir top provides a favorable situation. In any case the barriers need to have a large areal extend which results in a long delayed arrival below the cap rock.

Chapter 4

Mathematical model for bio-reactive two-phase transport

As introduced in the literature review the modeling of UHS includes several physical, chemical and biological processes. In this thesis a model was developed on continuum scale which couples flow and transport to the biochemical processes of multiple microbial species. The reservoir is thereby described as porous medium saturated by up to two phases, gas and/or water. The upscaling from discrete to continuum scale is done by using a representative elementary volume which is the smallest volume for the following average parameters (cf. Fig. 2.2):

- Porosity: Void volume of the porous medium divided by the total volume
- Saturation: Volume of one phase devided by the total void volume
- Concentration (mole fraction): Molar volume of one component in one phase divided by the total molar volume of this phase
- Microbial density: Number of active microbial cells divided by the total volume

The developed mathematical model presented in this chapter was published in the proceedings of the 14th European Conference on the Mathematics of Oil Recovery [54] and in the journal Computational Geosciences [56].

4.1 Physico-chemical processes

The overall conservation of moles for each chemical component is written by using the previously introduced average values on continuum scale. Thereby,

advective and dispersive/diffusive transport is considered [25]:

$$\phi \frac{\partial \left(\rho_g c_g^k S_g + \rho_w c_w^k S_w\right)}{\partial t} + \nabla \cdot \left(\rho_w \; c_w^k v_w + J_w^k + \rho_g c_g^k v_g + J_g^k\right) = q^k \tag{4.1}$$

where ϕ is the porosity, ρ is the molar density in $[mol/m^3]$, c is the mole fraction, S is the saturation, v is the advective flux in $[m/s]$, J is the dispersive/diffusive flux in $[mol/m^2/s]$ and q is the source or sink term. The subscripts g and w denote the gas and water phase respectively and the superscript k refers to the chemical component. Equivalent the conservation of moles can be written for immobile solid components by only considering the rate of reaction:

$$(1-\phi)\frac{\partial(\rho_s c_s^k)}{\partial t} = q^k \tag{4.2}$$

where the subscript s denotes the solid phase.

The volumentric velocity is formulated by Darcy's law:

$$v_i = -\frac{K k_{ri}}{\mu_i}\left(\nabla P_i - \hat{\rho}_i g\right), \quad i = g, w \tag{4.3}$$

where K is the absolute permeability in $[m^2]$, k_r is the relative permeability, μ is the dynamic viscosity in $[Pa \cdot s]$, P is the phase pressure in $[Pa]$, $\hat{\rho}$ is the phase density in $[kg/m^3]$ and g is the gravity acceleration in $[m/s^2]$.

The diffusive/dispersive flux is the sum of molecular diffusion and mechanical dispersion:

$$J_i^k = -\rho_i \left(D_{\text{diff},i}^k + D_{\text{disp},i}^k\right) \nabla c_i^k, \quad i = g, w \tag{4.4}$$

where $D_{\text{diff},i}^k$ is the effective molecular diffusion coefficient of component k in phase i in $[m^2/s]$ and $D_{\text{disp},i}^k$ is the effective mechanical dispersion coefficient of component k in phase i in $[m^2/s]$.

The molecular diffusion in the gas phase is formulated by Stefan-Maxwell equation, which was simplified by Blanc's law [109] while the molecular

diffusion in the water phase is formulated by Fick's law:

$$\begin{aligned} D^k_{\text{diff},g} &= \phi S_g \tau \left(\sum_{j=1\neq i}^{n} \frac{c^j_g}{\tilde{D}^{ij}_{\text{diff},g}} \right)^{-1} \\ D^k_{\text{diff},w} &= \phi S_w \tau \tilde{D}^k_{\text{diff},w} \end{aligned} \tag{4.5}$$

where τ is the tortuosity of the porous medium, $\tilde{D}^{ij}_{\text{diff},g}$ is the binary diffusion coefficient between component i and component j in $[m^2/s]$ and $\tilde{D}^k_{\text{diff},w}$ is the diffusion coefficient of component k in water in $[m^2/s]$.

The mechanical dispersion coeffcient is calculated by accepting its relationship to the Darcy velocity [115]:

$$D^k_{\text{disp},i} = \phi S_i \left(\frac{v_i v_i^T}{\|v_i\|} (a_L - a_T) + \|v_i\| a_T \right) \tag{4.6}$$

where a_L is the longitudinal dispersivity in $[m]$ and a_T is the transverse dispersivity in $[m]$.

The hydraulic properties (capillary pressure and relative permeability) of the porous medium are calculated by using the Brooks-Corey correlation [18]:

$$P_c(S_w) = P_g - P_w = P_e S_{we}^{-\frac{1}{\lambda}} \tag{4.7}$$

$$k_{rw}(S_w) = S_{we}^{\frac{2+3\lambda}{\lambda}} \tag{4.8}$$

$$k_{rg}(S_w) = (1 - S_{we})^2 (1 - S_{we}^{\frac{2+\lambda}{\lambda}}) \tag{4.9}$$

where P_e is the entry capillary pressure in $[Pa]$ and S_{we} is the effective water saturation:

$$S_{we} = \frac{S_w - S_{wr}}{1 - S_{wr} - S_{gr}} \tag{4.10}$$

where S_{wr} is the residual water saturation and S_{gr} is the residual gas saturation.

The mass exchange between the phases is modeled by thermodynamic equilibrium conditions. This assumption is usually used in petroleum reservoir and geochemical simulations because the mass exchange between the phases takes place much faster than the chemical reactions and the flux. However, for bio-chemical reactions the rates could be much faster what implies a limiting factor for this model. The range of validity for such an assumption is discussed in detail in the paper of Golfier et al. [49]. The thermodynamic equilibrium in this model is defined by the equality of fugacities:

$$f_g^k = f_w^k \quad \text{or} \quad c_g^k \varphi_g^k P_g = c_w^k \varphi_w^k P_w \tag{4.11}$$

where f is the fugacity in $[Pa]$ and φ is the fugacity coefficient. The gas phase is treated as ideal gas what means the the fugacity coefficients are equal to 1 whereas in the water phase the fugacity coefficients are calculated by Henry's law. By using an adequate correlation for the Henry constants, this method predicts the thermodynamic equilibrium for a gas-water system with a very low error [109]. The hydrodynamic properties of the phases (density, dynamic viscosity) can be correlated related to pressure, temperature and composition (cf. section 6.1.4).

The system of equations is closed by the sum of saturations and the sum of concentrations:

$$S_g + S_w = 1 \qquad \sum_k c_g^k = 1 \qquad \sum_k c_w^k = 1 \tag{4.12}$$

4.2 Bio-chemical processes

As introduced in chapter 2.2 the behavior of microbial populations in porous media can be complex. The rates of growth and decay can be different dependent on the structure: Biofilm or suspended in water. An exchange between the different structures takes place by attachment and detachment processes and the microorganisms can move due to different biological and hydrodynamic processes.

At continuum scale some simplifications are required for a proper representation. The present model uses an unstructured approach for the microbial populations which means that only one general structure is used for

all present microorganisms. Additionally, the advective and chemotactic transport of microorganisms is neglected. Hence, the microbial population dynamics can be formulated by:

$$\frac{\partial n}{\partial t} = \psi^{\text{growth}}(c^S, c^A) \cdot n - \psi^{\text{decay}} \cdot n + \nabla \cdot (D_m \nabla n) \tag{4.13}$$

where n is the microbial density in $[1/m^3]$, ψ^{growth} is the microbial growth function in $[1/s]$ which is a function of the substrate concentration c_w^S and the electron acceptor concentration c_w^A in the water phase, ψ^{decay} is the decay function in $[1/s]$ and D_m is the microbial diffusion coefficient in $[m^2/s]$. This equation is based on the assumption that the biofilm structure is dominating and the microorganisms are almost immobile. Furthermore, it is assumed that the microbial density has no influence on the hydrodynamic parameters (porosity, absolute and relative permeabilities) of the porous medium. Certainly this assumption has a lack and therefore it is planned to cover these influences in the ongoing research of the HyINTEGER project.

Different models for the growth and decay function are available in the literature which are discussed in section 4.3.

The growth and decay of microorganisms results in bio-chemical reactions what means that substrates are degraded and other substances are produced. As introduced in section 2.2.2 during the metabolism, substrates are used as source of energy and/or source of carbon. Both effects are included in this model. The rate of the bio-chemical reaction for energy uptake is assumed to be proportional to the rate of microbial growth. Based on the assumption that the microorganisms are autotrophic the source of carbon is represented by CO_2. This means that an additional term needs to be introduced for the rate of CO_2 consumption. The other way around CO_2 is produced by microbial decay. Again a proportional relationship is assumed:

$$q^k = \phi \gamma^k \frac{\psi^{\text{growth}}}{Y_e} n, \quad n = 1, ..., n \backslash \{CO_2\} \tag{4.14}$$

$$q^{CO_2} = \phi \left(\gamma^{CO_2} \frac{\psi^{\text{growth}}}{Y_e} + \frac{\psi^{\text{growth}}}{Y_c} - \frac{\psi^{\text{decay}}}{Y_p} \right) n \tag{4.15}$$

where γ is the coefficient which relates the consumption or production of

component k in reaction equations 2.6 to 2.9 to the consumption of H_2. Y are the yield coefficients which relate the rate of energy update (Y_e), the rate of carbon consumption (Y_c) and the rate of carbon production (Y_p) to the rates of microbial growth and decay.

4.3 Review of models for microbial growth and decay

It is important to describe the growth and decay of the microorganisms in an adequate way because this is related to the local rates of the bio-chemical reactions. Analogies can be taken from batch culture experiments, where the microorganisms are exposed to an initially added amount of substrate (cf. section 2.2.3). Monod [87] described the life cycle of a microbial batch culture with up to six phases: (1) the lag, (2) the acceleration, (3) the exponential growth, (4) the deceleration, (5) the stationary and (6) the decay phase. A typical growth function of a batch culture is plotted in Fig. 2.10. It shows the number of microorganisms in a logarithmic scale versus time. However, growth functions can look more simple when one or more of the phases are absent.

Several mathematical models exist in the literature to describe the behavior of the microbial growth function. Classical models consist of a single function which is adjustable by some empirical parameters. More consistent models with the UHS conditions are also taking into account the availability of substrates. Such models are called substrate-limited growth models. Examples are the Monod model, the Moser model and the recent developed model by Panfilov [100]:

- Monod [87]:

$$\psi^{\mathrm{growth}} = \psi^{\mathrm{growth}}_{\mathrm{max}} \left(\frac{c^S}{\alpha + c^S} \right) \tag{4.16}$$

  where $\psi^{\mathrm{growth}}_{\mathrm{max}}$ is the maximum specific growth rate in $[1/s]$, c^S is the concentration of the limiting substrate and α is the half-velocity constant.

- Moser [89]:

$$\psi^{\text{growth}} = \psi^{\text{growth}}_{\text{max}} \left(\frac{(c^S)^\eta}{\alpha + (c^S)^\eta} \right) \tag{4.17}$$

  where η is an additional exponent compared to the Monod model.

- Panfilov [100]:

$$\psi^{\text{growth}} = \frac{1}{t_e} \frac{n}{1 + \frac{n^2}{n^2_{\text{max}}}} \left(\frac{c^S}{\alpha + c^S} \right) \tag{4.18}$$

  where t_e is the characteristic time of eating in [s] and n_{max} is the microbial density of satisfactory in $[1/m^3]$.

The decay rate can also be modeled in different ways. The simplest method is to use a constant decay rate. Further, it is possible to introduce a decay rate which depends linearly on the microbial density:

- Constant decay rate:

$$\psi^{\text{decay}} = b \tag{4.19}$$

- Increasing decay rate:

$$\psi^{\text{decay}} = b \cdot n \tag{4.20}$$

  where b is the decay coefficient.

A batch culture experiment can be simulated by the following pair of ordinary differential equations:

$$\frac{\partial n}{\partial t} = \psi^{\text{growth}} \cdot n - \psi^{\text{decay}} \cdot n \tag{4.21}$$

$$\frac{\partial c^S}{\partial t} = -\frac{\psi^{\text{growth}}}{Y} \cdot n \tag{4.22}$$

In Fig. 4.1 the qualitative behavior of the introduced models is compared.

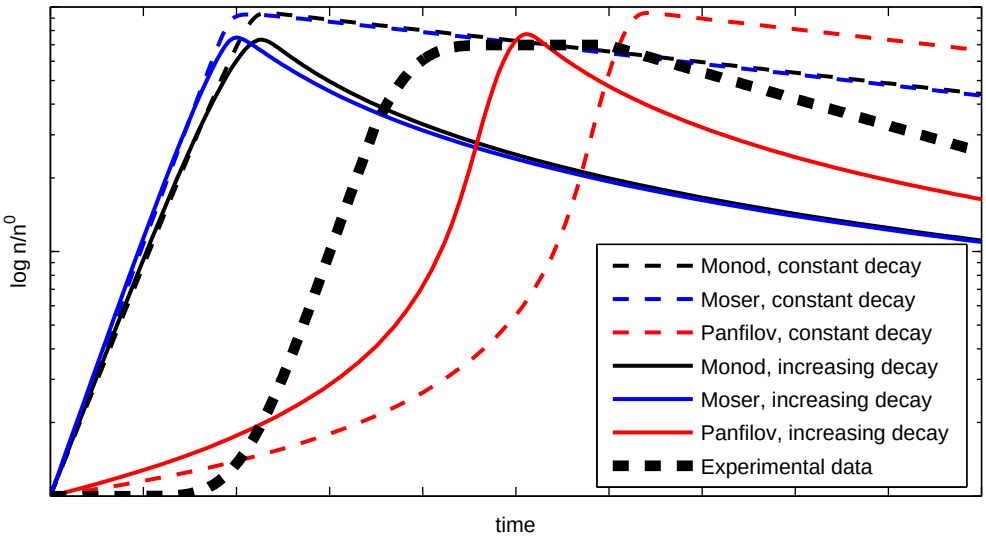

Figure 4.1: Comparison of different models for microbial population dynamics

It should be mentioned that neither of these models is able to predict the lag and stationary phases. For all of them the growth starts immediately and the deceleration phase continues directly in the decay phase. Only the model of Panfilov [100] shows the acceleration phase. The Monod and Moser model start directly with the exponential growth phase. From laboratory experiments it is reported that the lag phase can be in the range of a few minutes up to some hours. In-situ the conditions are different and the lag phase could be longer, up to a few years [84]. Consequently, its consideration could be quite important.

However, these models do not take into account the competitive inhibition which could occur when several microbial species compete for the same substrate. An extended formulation for the competitive inhibition was proposed by Bailey and Ollis [8]. To reduce the complexity this is not considered in the present model.

4.4 Coupling of processes

The coupling of flow, transport, microbial population dynamics and biochemical reactions is required for the formulation of the final model. For

the consideration of four microbial processes, represented by the reaction equations (2.6) to (2.9), the model includes seven mobile and two solid components. The governing system of equations is as follows:

- Microbial population dynamics:

$$\begin{aligned} &\frac{\partial n_m}{\partial t} = \psi_m^{\text{growth}} \cdot n_m - \psi_m^{\text{decay}} \cdot n_m + \nabla \cdot (D_m \nabla n_m), \\ &m = M, A, S, I \end{aligned} \tag{4.23}$$

- Reactive transport for mobile components (except for CO_2):

$$\begin{aligned} &\phi \frac{\partial \left(\rho_g c_g^k S_g + \rho_w c_w^k S_w\right)}{\partial t} \\ &+\nabla \cdot \left(-\rho_g \; c_g^k \frac{K k_{rg}}{\mu_g} \cdot (\nabla P_g - \hat{\rho}_g g) - \rho_w c_w^k \frac{K k_{rw}}{\mu_w} \cdot (\nabla P_w - \hat{\rho}_w g) \right) \\ &+\nabla \cdot \left(-\rho_g \left(D_{\text{diff},g}^k + D_{\text{disp},g}^k \right) \nabla c_g^k - \rho_w \left(D_{\text{diff},w}^k + D_{\text{disp},w}^k \right) \nabla c_w^k \right) \\ &= \phi \sum_m \gamma_m^k \frac{\psi_m^{\text{growth}}}{Y_{m,e}} n_m, \\ &k = H_2, CH_4, H_2O, H_2S, CH_3COOH, SO_4^{2-}, \quad m = M, A, S, I \end{aligned} \tag{4.24}$$

- Reactive transport for CO_2:

$$\begin{aligned} &\phi \frac{\partial \left(\rho_g c_g^k S_g + \rho_w c_w^k S_w\right)}{\partial t} \\ &+\nabla \cdot \left(-\rho_g \; c_g^k \frac{K k_{rg}}{\mu_g} \cdot (\nabla P_g - \hat{\rho}_g g) - \rho_w c_w^k \frac{K k_{rw}}{\mu_w} \cdot (\nabla P_w - \hat{\rho}_w g) \right) \\ &+\nabla \cdot \left(-\rho_g \left(D_{\text{diff},g}^k + D_{\text{disp},g}^k \right) \nabla c_g^k - \rho_w \left(D_{\text{diff},w}^k + D_{\text{disp},w}^k \right) \nabla c_w^k \right) \\ &= \phi \sum_m \left(\gamma_m^{CO_2} \frac{\psi_m^{\text{growth}}}{Y_{m,e}} + \frac{\psi_m^{\text{growth}}}{Y_{m,c}} - \frac{\psi_m^{\text{decay}}}{Y_{m,p}} \right) n_m, \\ &k = CO_2, \quad m = M, A, S, I \end{aligned} \tag{4.25}$$

- Heterogeneous reaction:

$$(1-\phi)\frac{\partial(\rho_s c_s^k)}{\partial t} = \phi\gamma_I^k \frac{\psi_I^{\text{growth}}}{Y_I} n_I, \quad k = Fe_2^{\text{III}}O_3, Fe_3^{\text{II}}O_4 \tag{4.26}$$

where the subscript m relates the four microbial species: (M) Methanogenic archaea, (A) acetogenic archaea, (S) sulfate-reducing bacteria and (I) iron-reducing bacteria, the subscripts s, w, and g denote the solid, water and gas phase and the superscript k relates the nine components of the system: H_2, CO_2, CH_4, H_2O, H_2S, CH_3COOH, SO_4^{2-}, $Fe_2^{\text{III}}O_3$, $Fe_3^{\text{II}}O_4$. The first five can be present in both mobile phases, SO_4^{2-} and CH_3COOH are only present in the water phase and $Fe_2^{\text{III}}O_3$ and $Fe_3^{\text{II}}O_4$ only in the solid phase. The coefficients γ_m^k are relating the consumption or production of component k to the consumption of H_2:

$$\gamma_M = \begin{pmatrix} -1 \\ -\frac{1}{4} \\ \frac{1}{4} \\ \frac{1}{2} \\ 0 \\ 0 \\ 0 \\ 0 \\ 0 \end{pmatrix}, \quad \gamma_A = \begin{pmatrix} -1 \\ -\frac{1}{2} \\ 0 \\ \frac{1}{2} \\ 0 \\ \frac{1}{4} \\ 0 \\ 0 \\ 0 \end{pmatrix}, \quad \gamma_S = \begin{pmatrix} -1 \\ 0 \\ 0 \\ \frac{4}{5} \\ \frac{1}{5} \\ 0 \\ -\frac{1}{5} \\ 0 \\ 0 \end{pmatrix}, \quad \gamma_I = \begin{pmatrix} -1 \\ 0 \\ 0 \\ 1 \\ 0 \\ 0 \\ 0 \\ -3 \\ 2 \end{pmatrix} \tag{4.27}$$

For the microbial growth functions ψ_m^{growth} it is important to consider the availability of the substrate and the corresponding electron acceptor. For this purpose an extension of the Monod model was initially proposed by Megee et al. [86] which is often called "double Monod model". Related to this the microbial growth functions are defined as follows:

- for methanogenic archaea:

$$\psi_M^{\text{growth}} = \psi_{M,\max}^{\text{growth}} \left(\frac{c_w^{H_2}}{\alpha_{M,1} + c_w^{H_2}} \right) \left(\frac{c_w^{CO_2}}{\alpha_{M,2} + c_w^{CO_2}} \right) \tag{4.28}$$

- for acetogenic archaea:

$$\psi_A^{\text{growth}} = \psi_{A,\max}^{\text{growth}} \left(\frac{c_w^{H_2}}{\alpha_{A,1} + c_w^{H_2}} \right) \left(\frac{c_w^{CO_2}}{\alpha_{A,2} + c_w^{CO_2}} \right) \tag{4.29}$$

- for sulfate-reducing bacteria:

$$\psi_S^{\text{growth}} = \psi_{S,\max}^{\text{growth}} \left(\frac{c_w^{H_2}}{\alpha_{S,1} + c_w^{H_2}} \right) \left(\frac{c_w^{SO_4^{2-}}}{\alpha_{S,2} + c_w^{SO_4^{2-}}} \right) \tag{4.30}$$

- for iron-reducing bacteria:

$$\psi_I^{\text{growth}} = \psi_{I,\max}^{\text{growth}} \left(\frac{c_w^{H_2}}{\alpha_{I,1} + c_w^{H_2}} \right) \left(\frac{c_s^{Fe_2^{\text{III}}O_3}}{\alpha_{I,2} + c_s^{Fe_2^{\text{III}}O_3}} \right) \tag{4.31}$$

Each species has its particular empirical parameters which control the rate of growth and consequently the rate of the bio-chemical reaction. An equivalent extension is possible for the other growth models introduced in section 4.3.

4.5 Transformation to dimensionless form

The following dimensionless parameters were introduced to obtain a dimensionless form:

$$\begin{aligned} &\bar{\rho} = \frac{\rho}{\rho^\star}, \quad \bar{\hat{\rho}} = \frac{\hat{\rho}}{\hat{\rho}^\star}, \quad \bar{\mu} = \frac{\mu}{\mu^\star}, \quad \bar{P} = \frac{P}{P^\star}, \quad \bar{D} = \frac{D}{D^\star}, \quad \tau = \frac{t}{t^\star}, \\ &\bar{g} = \frac{g}{g^\star}, \quad \bar{x} = \frac{x}{L}, \quad \bar{n} = \frac{n}{n^\star}, \quad \bar{K} = \frac{K}{K^\star}, \quad \bar{\psi}^{\text{growth}} = t^\star \cdot \psi^{\text{growth}}, \\ &\bar{\psi}^{\text{decay}} = t^\star \cdot \psi^{\text{decay}}, \quad \bar{\hat{q}} = \frac{\hat{q}}{\hat{q}^\star} \end{aligned} \tag{4.32}$$

where the $\star$ denotes the characteristic value of the parameter. The characteristic time was selected as the time of advective flow:

$$t^\star = \frac{L^2 \mu^\star}{K^\star P^\star} \tag{4.33}$$

The resulting dimensionless system of equations is as follows:

- Microbial population dynamics:

$$\begin{aligned}&\frac{\partial \bar{n}_m}{\partial \tau} = \bar{\psi}_m^{\text{growth}} \cdot \bar{n}_m - \bar{\psi}_m^{\text{decay}} \cdot \bar{n}_m + \beta \nabla \cdot (\bar{D}_m \nabla \bar{n}_m),\\ &m = M, A, S, I\end{aligned} \tag{4.34}$$

- Reactive transport for mobile components (except for CO_2):

$$\begin{aligned}&\phi \frac{\partial \left(\bar{\rho}_g c_g^k S_g + \bar{\rho}_w c_w^k S_w\right)}{\partial \tau}\\ &+\nabla \cdot \left(-\bar{\rho}_g \; c_g^k \frac{\bar{K} k_{rg}}{\bar{\mu}_g} \left(\nabla \bar{P}_g - \epsilon \bar{\hat{\rho}}_g \bar{g}\right) - \bar{\rho}_w c_w^k \frac{\bar{K} k_{rw}}{\bar{\mu}_w} \left(\nabla \bar{P}_w - \epsilon \bar{\hat{\rho}}_w \bar{g}\right)\right)\\ &+\beta \nabla \cdot \left(-\bar{\rho}_g \left(\bar{D}_{\text{diff},g}^k + \bar{D}_{\text{disp},g}^k\right) \nabla c_g^k - \bar{\rho}_w \left(\bar{D}_{\text{diff},w}^k + \bar{D}_{\text{disp},w}^k\right) \nabla c_w^k\right)\\ &=\phi \sum_m \delta_{m,e} \gamma_m^k \bar{\psi}_m^{\text{growth}} \bar{n}_m,\\ &k = H_2, CH_4, H_2O, H_2S, CH_3COOH, SO_4^{2-}, \quad m = M, A, S, I\end{aligned} \tag{4.35}$$

- Reactive transport for CO_2:

$$\begin{aligned}&\phi \frac{\partial \left(\bar{\rho}_g c_g^k S_g + \bar{\rho}_w c_w^k S_w\right)}{\partial \tau}\\ &+\nabla \cdot \left(-\bar{\rho}_g \; c_g^k \frac{\bar{K} k_{rg}}{\bar{\mu}_g} \cdot \left(\nabla \bar{P}_g - \epsilon \bar{\hat{\rho}}_g \bar{g}\right) - \bar{\rho}_w c_w^k \frac{\bar{K} k_{rw}}{\bar{\mu}_w} \cdot \left(\nabla \bar{P}_w - \epsilon \bar{\hat{\rho}}_w \bar{g}\right)\right)\\ &+\beta \nabla \cdot \left(-\bar{\rho}_g \left(\bar{D}_{\text{diff},g}^k + \bar{D}_{\text{disp},g}^k\right) \nabla c_g^k - \bar{\rho}_w \left(\bar{D}_{\text{diff},w}^k + \bar{D}_{\text{disp},w}^k\right) \nabla c_w^k\right)\\ &=\phi \sum_m \left(\delta_{m,e} \gamma_m^k \bar{\psi}_m^{\text{growth}} + \delta_{m,c} \bar{\psi}_m^{\text{growth}} - \delta_{m,p} \bar{\psi}_m^{\text{decay}}\right) n_m,\\ &k = CO_2, \quad m = M, A, S, I\end{aligned} \tag{4.36}$$

- Heterogeneous reaction:

$$(1-\phi) \frac{\partial (\bar{\rho}_s c_s^k)}{\partial \tau} = \phi \delta_I \gamma_m^k \bar{\psi}_I^{\text{growth}} \bar{n}_I, \quad k = Fe_2^{\text{III}} O_3, Fe_3^{\text{II}} O_4 \tag{4.37}$$

where β, δ and ϵ are dimensionless coefficients:

$$\begin{aligned} \beta &= \frac{\mu^\star D^\star}{K^\star P^\star}, \quad \delta_{m,e} = \frac{n^\star}{\rho^\star Y_{m,e}}, \quad \delta_{m,c} = \frac{n^\star}{\rho^\star Y_{m,c}}, \\ \delta_{m,p} &= \frac{n^\star}{\rho^\star Y_{m,p}}, \quad \epsilon = \frac{\hat{\rho}^\star g^\star L}{P^\star} \end{aligned} \tag{4.38}$$

β can be also written as:

$$\beta = \frac{t^\star}{t^{\star\star}} \tag{4.39}$$

where $t^{\star\star}$ is the characteristic time of diffusion which is defined as:

$$t^{\star\star} = \frac{L^2}{D^\star} \tag{4.40}$$

This means that β is the ratio of the time of advection to the time of diffusion which is similar to the reciprocal of the Péclet number. The product $\left(\delta_{m,e} \cdot \bar{\psi}_m^{\text{growth}}\right)$ relates the time of advection to the time of the bio-chemical reaction and could be defined as the reciprocal of the Damköhler number. ϵ is the dimensionless gravitational number which is relating the gravitational flow to the advective flow.

4.6 Parameters for microbial population dynamics

The values for the parameters in the microbial population dynamics and bio-reaction terms can be found with some restrictions in the literature. Many publications deal with the investigation of microbial growth by performing batch experiments in the laboratory. The results of these experiments allow to determine the parameters in mathematical expressions for growth, decay and substrate consumption. Most of the publications are related to the Monod model (Eq. 4.16). In Table 4.1 to Table 4.3 the values from the literature are summarized for the different microbial species: Methanogenic archaea, homoacetogenic archaea and sulfate-reducing bacteria. For iron-reducing bacteria no information about the parameter values could be found. The tables provide the values already in the unit for the developed mathematical model (Eq. 4.23 to Eq. 4.26). The conversion of the units was done

in the following way:

- The maximum specific growth rate ($\psi_{\max}^{\text{growth}}$) and the decay coeffcient (b) are usually provided in $[1/day]$ what can be easility converted into $[1/s]$:

$$1\frac{1}{day} = \frac{1}{86400}\frac{1}{s} \tag{4.41}$$

- The half-velocity constants (α) are provided in $[\mu M]$ or $[mM]$. The unit M refers to the molar concentration in $[mol/L]$. The conversion into $[mol/mol]$ requires the molar concentration of water (55.555 mol/L):

$$1\mu M = 1 \cdot 10^{-3} mM = 10^{-6} \cdot \frac{1}{55.555}\frac{mol}{mol} \tag{4.42}$$

- The yield coefficient has the unit $[g/mol(H_2)]$. For the conversion the mass of one microorganism needs to be known. This mass was calculated by assumuning a simplified cell shape which is a cylinder with a diameter and height of 1 μm plus two hemispheres with a diameter of 1 μm. The cell density is assumed to be the water density (1000 kg/m^3). The result is a cell mass of $1.309 \cdot 10^{-15}$ kg.

$$1\frac{g}{mol(H_2)} = \frac{1}{1.309 \cdot 10^{-15}} \cdot 10^{-3}\frac{1}{mol(H_2)} \tag{4.43}$$

Table 4.1: Kinetic parameters for methanogenic archaea

Source	$\psi^{\text{growth}}_{M,\max}$ $[1/s]$	$\alpha_{M,1}$ $[mol/mol]$	$\alpha_{M,2}$ $[mol/mol]$	$Y_{M,e}$ $[1/mol(H_2)]$	b_M $[1/s]$
[40, 39]	$2.488 \cdot 10^{-5}$			$6.875 \cdot 10^{11}$	
[40, 39]	$1.273 \cdot 10^{-5}$			$4.584 \cdot 10^{11}$	
[68]	$8.912 \cdot 10^{-6}$	$3.240 \cdot 10^{-7}$		$2.483 \cdot 10^{11}$	$1.019 \cdot 10^{-6}$
[40, 39]	$1.447 \cdot 10^{-5}$			$8.403 \cdot 10^{11}$	
[112]	$1.433 \cdot 10^{-5}$			$1.222 \cdot 10^{11}$	
[112]	$1.447 \cdot 10^{-5}$	$1.179 \cdot 10^{-7}$			
[112]	$1.528 \cdot 10^{-5}$	$1.170 \cdot 10^{-7}$			
[40, 39]	$1.736 \cdot 10^{-5}$	$1.179 \cdot 10^{-7}$		$3.056 \cdot 10^{11}$	
[40, 39]	$3.009 \cdot 10^{-5}$				
[76]		$1.188 \cdot 10^{-7}$			
[40, 39]	$2.373 \cdot 10^{-5}$			$7.257 \cdot 10^{11}$	
[40, 39]	$1.852 \cdot 10^{-5}$			$1.451 \cdot 10^{12}$	
[40, 39]	$1.794 \cdot 10^{-5}$				
[112]	$1.472 \cdot 10^{-5}$	$1.188 \cdot 10^{-7}$		$1.093 \cdot 10^{13}$	
[38]	$7.523 \cdot 10^{-6}$	$8.999 \cdot 10^{-8}$	$5.400 \cdot 10^{-6}$	$3.820 \cdot 10^{11}$	$6.944 \cdot 10^{-7}$
[119]	$2.546 \cdot 10^{-5}$				
[35]		$8.999 \cdot 10^{-8}$	$4.140 \cdot 10^{-6}$		
[132]	$1.505 \cdot 10^{-6}$	$2.160 \cdot 10^{-11}$	$2.340 \cdot 10^{-8}$	$2.925 \cdot 10^{11}$	
[132]	$1.736 \cdot 10^{-5}$	$9.000 \cdot 10^{-12}$		$7.697 \cdot 10^{10}$	
Mean	$1.643 \cdot 10^{-5}$	$1.094 \cdot 10^{-7}$	$3.188 \cdot 10^{-6}$	$1.376 \cdot 10^{12}$	$8.565 \cdot 10^{-7}$

Additionally, it is important to know the microbial density in subsurface systems for each microbial species. Many values are available in the literature which come from water or rock samples. As the subsurface systems are usually under substrate limited conditions these values can be used as initial values for the simulations. In most publications the cell counts are provided in $[cells/ml]$ or $[cells/g(\text{porous medium})]$. The conversion of the units was done by assuming a porosity of 0.2 or a saturated rock density of 2500 kg/m^3:

$$1\frac{cells}{ml} = 0.2 \cdot 10^6 \frac{1}{m^3} \tag{4.44}$$

$$1\frac{cells}{g(\text{porous medium})} = 1000 \cdot 2500 \frac{1}{m^3} \tag{4.45}$$

Table 4.2: Kinetic parameters for sulfate-reducing bacteria

Source	$\psi_{S,\max}^{\text{growth}}$ $[1/s]$	$\alpha_{S,1}$ $[mol/mol]$	$\alpha_{S,2}$ $[mol/mol]$	$Y_{S,e}$ $[1/mol(H_2)]$	b_S $[1/s]$
[112]	$1.620 \cdot 10^{-5}$	$5.940 \cdot 10^{-8}$			
[112]	$1.852 \cdot 10^{-5}$	$7.559 \cdot 10^{-8}$			
[40, 39]	$1.620 \cdot 10^{-5}$	$5.941 \cdot 10^{-8}$		$1.299 \cdot 10^{12}$	
[112]	$1.389 \cdot 10^{-5}$	$5.400 \cdot 10^{-8}$			
[112]	$1.817 \cdot 10^{-5}$	$7.505 \cdot 10^{-8}$		$5.424 \cdot 10^{11}$	
[112]	$1.352 \cdot 10^{-5}$	$4.356 \cdot 10^{-8}$		$7.563 \cdot 10^{11}$	
[7]	$4.167 \cdot 10^{-5}$				
[76]		$2.340 \cdot 10^{-8}$			
[95]	$6.366 \cdot 10^{-5}$				
[40, 39]	$3.414 \cdot 10^{-5}$			$1.451 \cdot 10^{12}$	
[40, 39]	$3.588 \cdot 10^{-5}$			$1.413 \cdot 10^{12}$	
[40, 39]	$1.157 \cdot 10^{-5}$				
[40, 39]	$1.042 \cdot 10^{-5}$				
[40, 39]	$1.100 \cdot 10^{-5}$				
[40, 39]	$1.620 \cdot 10^{-5}$				
[112]	$1.583 \cdot 10^{-5}$	$5.940 \cdot 10^{-8}$		$4.640 \cdot 10^{13}$	
[85]		$1.800 \cdot 10^{-9}$	$1.800 \cdot 10^{-6}$		
Mean	$2.246 \cdot 10^{-5}$	$5.018 \cdot 10^{-8}$	$1.800 \cdot 10^{-6}$	$8.639 \cdot 10^{12}$	

Table 4.3: Kinetic parameters for homoacetogenic archaea

Source	$\psi_{A,\max}^{\text{growth}}$ $[1/s]$	$\alpha_{A,1}$ $[mol/mol]$	$\alpha_{A,2}$ $[mol/mol]$	$Y_{A,e}$ $[1/mol(H_2)]$	b_A $[1/s]$
[132]	$1.574 \cdot 10^{-6}$	$2.160 \cdot 10^{-6}$	$2.340 \cdot 10^{-9}$	$3.079 \cdot 10^{10}$	$1.157 \cdot 10^{-7}$
[132]	$3.704 \cdot 10^{-6}$	$2.160 \cdot 10^{-6}$	$2.340 \cdot 10^{-9}$	$6.157 \cdot 10^{10}$	$1.157 \cdot 10^{-7}$
[132]	$1.505 \cdot 10^{-6}$	$2.160 \cdot 10^{-6}$	$2.340 \cdot 10^{-9}$	$2.309 \cdot 10^{10}$	$1.157 \cdot 10^{-7}$
[71]	$1.331 \cdot 10^{-5}$				
[75]	$5.972 \cdot 10^{-7}$				
[71]				$4.584 \cdot 10^{11}$	
[63]				$2.101 \cdot 10^{12}$	
[38]	$4.630 \cdot 10^{-6}$	$8.999 \cdot 10^{-8}$	$1.800 \cdot 10^{-6}$	$3.820 \cdot 10^{11}$	$6.944 \cdot 10^{-7}$
Mean	$4.220 \cdot 10^{-6}$	$1.642 \cdot 10^{-6}$	$4.517 \cdot 10^{-7}$	$5.094 \cdot 10^{11}$	$2.604 \cdot 10^{-7}$

4.7 Summary and conclusions

- A mathematical model was developed which describes the hydrodynamic behavior of UHS coupled with bio-chemical reactions and mi-

Table 4.4: Density of methanogenic archaea

Source	Depth $[m]$	n $[1/m^3]$
[65]	330	$5.600 \cdot 10^{13}$
[129]	376	$4.800 \cdot 10^{12}$
[74]	68–446	$3.600 \cdot 10^{9}$
[69]	200–1800	$4.400 \cdot 10^{12}$
[69]	200–1800	$7.800 \cdot 10^{12}$
[69]	200–1800	$1.120 \cdot 10^{13}$
[98]	1264–1742	$2.000 \cdot 10^{8}$
[104]	129–1240	$1.001 \cdot 10^{11}$
[24]	14–182	$1.000 \cdot 10^{13}$
[88]	647	$2.000 \cdot 10^{11}$
Mean		$9.450 \cdot 10^{12}$

Table 4.5: Density of sulfate-reducing bacteria

Source	Depth $[m]$	n $[1/m^3]$
[133]	65–686	$7.400 \cdot 10^{10}$
[104]	129–1240	$1.001 \cdot 10^{11}$
[34]	10–263	$1.001 \cdot 10^{10}$
[24]	14-182	$1.000 \cdot 10^{13}$
[98]	1264–1742	$2.000 \cdot 10^{8}$
[9]	430	$6.000 \cdot 10^{9}$
[57]	683.5–688.5	$9.800 \cdot 10^{7}$
[57]	484–499	$9.800 \cdot 10^{8}$
[57]	438–443	$8.400 \cdot 10^{7}$
[57]	540–545	$1.580 \cdot 10^{9}$
Mean		$1.019 \cdot 10^{12}$

Table 4.6: Density of homoacetogenic archaea

Source	Depth $[m]$	n $[1/m^3]$
[37]	800	$2.000 \cdot 10^{11}$
[133]	900	$2.000 \cdot 10^{10}$
[74]	440	$7.200 \cdot 10^{9}$
[133]	65–686	$7.400 \cdot 10^{10}$
[57]	683.5–688.5	$2.800 \cdot 10^{8}$
[57]	62–66	$1.580 \cdot 10^{8}$
[57]	484–499	$3.400 \cdot 10^{8}$
[57]	438–443	$1.860 \cdot 10^{8}$
[57]	470–475	$2.200 \cdot 10^{7}$
[57]	540–545	$4.600 \cdot 10^{8}$
Mean		$3.026 \cdot 10^{10}$

Table 4.7: Density of iron(III)-reducing bacteria

Source	Depth $[m]$	n $[1/m^3]$
[106]		$4.600 \cdot 10^{8}$
[88]	65–686	$7.400 \cdot 10^{10}$
[133]	900	$2.000 \cdot 10^{10}$
[133]	1350	$2.000 \cdot 10^{9}$
[57]	683.5–688.5	$4.400 \cdot 10^{8}$
[57]	382–387	$2.600 \cdot 10^{6}$
[57]	62–66	$6.600 \cdot 10^{7}$
[57]	484–499	$3.400 \cdot 10^{9}$
[57]	438–443	$9.200 \cdot 10^{7}$
[57]	470–475	$6.600 \cdot 10^{6}$
Mean		$1.005 \cdot 10^{10}$

crobial population dynamics. It considers the metabolism of four hydrogenotrophic microbial species and includes the flow and transport of seven components in two mobile phases and two rock components.

- A comparison of three substrate-limited growth models and two decay models was presented. None of the models shows the lag and stationary phases which have been observed in batch culture experiments.

Only the model of Panfilov shows the acceleration phase.

- A literature search was performed to find parameters for microbial population dynamics and the bio-reaction terms. Parameters are available for all included microbial species except for iron-reducing bacteria. Some parameters are uncertain in a range of up to two or three orders of magnitude.

Chapter 5

Stability of the dynamic system

Dynamic systems which are described by differential equations can have one or more equilibrium points. The equilibrium points, at which the solution of the system remains unchanged in time, can be stable or unstable. For a stable equilibrium point a small perturbation in the solution is driven back to the equilibrium point. In contrast, for an unstable equilibrium point a small perturbation in the solution is driven away and the solution may not converge to the equilibrium point anymore. Additionally, it is possible that oscillations in space or time occur around an equilibrium point in a dynamic system.

Related to the unexpected behavior, which was reported for the town gas storage in an anticline aquifer structure near Lobodice (Czech Republic), the stability of the dynamic system (Eq. 4.34 to Eq. 4.37) is investigated in the present chapter. The injected gas in the Lobodice town gas storage contained 45-50% H_2, 20-25% CH_4, 8-12% CO_2, 7-11% CO, 8-10% N_2. During storage cycles of seven months drastic increases in the CH_4 concentration and decreases in the CO, CO_2 and H_2 concentrations as well as changes in the gas volume were reported [118]. Smigan et al. [118] analyzed the existence of methanogenic microorganisms in the stratal water and an isotopic analysis of the withdrawn gas indicated a different origin for a part of the CH_4 molecules. Consequently, it was concluded that the microbial activity was responsible for the in-situ generation of methane by one or both of the following reactions:

$$CO_2 + 4H_2 \longrightarrow CH_4 + 2H_2O \tag{5.1}$$

$$CO + 3H_2 \longrightarrow CH_4 + H_2O \tag{5.2}$$

Additionally, Buzek et al. [21] reported that the composition of the produced gas varied in time (cf. Fig. 5.1) and also from well to well. Parts of the storage were enriched in the CH_4 concentration while other parts were enriched in the H_2 concentration.

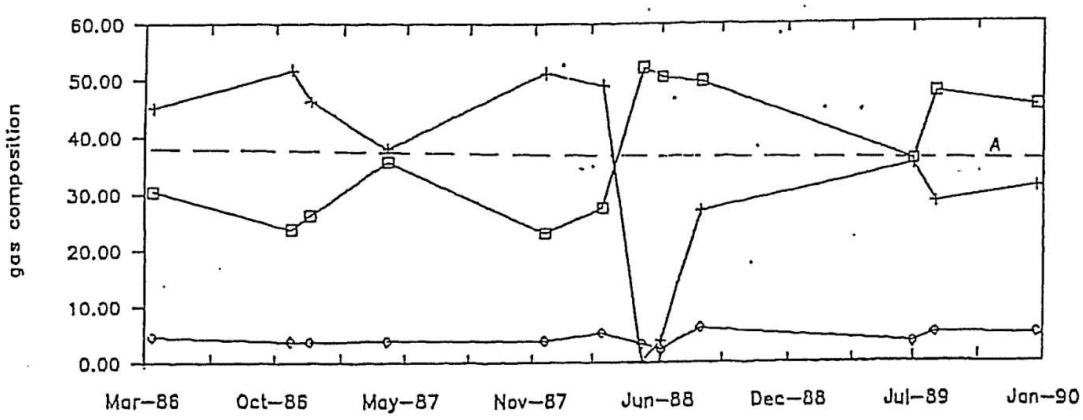

Figure 5.1: Gas composition at well 44 of the Lobodice town gas storage, +: H_2 vol %, □: CH_4 vol %, ◇: CH_4/N_2 ratio [21]

The observations indicate that the underground storage behaved as a bioreactor because both substrates for the bio-chemical reactions were injected. However, the oscillating behavior could not be explained. In this chapter a possible explanation for the variation in the gas composition is derived by the theory of dynamic systems. The results can be important for UHS when a mixture of H_2 and CO_2 is injected.

A shortened version of the present chapter was published in the proceedings of the 15th European Conference on the Mathematics of Oil Recovery [52].

5.1 Reduction to a system of two ordinary differential equations

The following assumptions were applied to perform the stability analysis of the dynamic system:

- Only methanogenesis takes place.

- The rate of growth is proportional to the product of total substrate concentrations and the microbial density. This is a simplified version of the growth model suggested in [100]:

$$\psi^{\text{growth}} = \psi^{\text{growth}}_{\text{max}} C^{CO_2} C^{H_2} n \tag{5.3}$$

- The rate of decay is constant:

$$\psi^{\text{decay}} = \beta \tag{5.4}$$

- The rates of CO_2 consumption and production as source of carbon are neglected.
- Diffusive, dispersive and advective transport is neglected.
- The injection and production of fluids is included in the global balance equations instead of using point or line sources. This assumption can be applied when the number of storage wells is high.

Hence, the model for bio-reactive two-phase transport (Eq. 4.34 to Eq. 4.37) can be reduced to a system of five ordinary differential equations:

$$\frac{dn}{d\tau} = \alpha C^{H_2} C^{CO_2} n^2 - \beta n \tag{5.5}$$

$$\frac{dC^k}{d\tau} = -\delta^k C^{H_2} C^{CO_2} n^2 + q^k, \quad k = H_2, CO_2, CH_4, H_2O \tag{5.6}$$

where $\alpha = \psi^{\text{growth}}_{\text{max}}$, $\delta^k = \psi^{\text{growth}}_{\text{max}} \gamma^k / Y_e$, $C^k = \rho_g c^k_g S_g + \rho_w c^k_w S_w$ and $q = \frac{Q}{\phi}$.

The equation for the microbial population dynamics is independent of the reaction products (CH_4 and H_2O). Therefore, it is sufficient to consider a system of three equations:

$$\frac{dn}{d\tau} = \alpha C^{H_2} C^{CO_2} n^2 - \beta n \tag{5.7}$$

$$\frac{dC^{H_2}}{d\tau} = -\delta^{H_2} C^{H_2} C^{CO_2} n^2 + q^{H_2} \tag{5.8}$$

$$\frac{dC^{CO_2}}{d\tau} = -\delta^{CO_2} C^{H_2} C^{CO_2} n^2 + q^{CO_2} \tag{5.9}$$

For the injection or production rates (q^k) the following considerations are applied:
Underground storages are operated in a cyclic way with alternating periods of injection and production. During injection periods q^k is larger than zero while during production periods q^k is smaller than zero. The composition of the injected gas is known and the injection rate is adjustable. Accordingly, q^k is directly manageable during injection periods. However, during production periods only the total rate $\left(\sum_{k=1}^{4} q^k\right)$ is manageable. The composition and ratio of the produced fluid phases depends on the phase compositions and mobilities in the reservoir. When the time period to be analyzed is much longer than one operation cycle, the mean injection/production rates can be considered:

$$q^k = \frac{1}{t_{\text{cycle}}} \int_0^{t_{\text{cycle}}} q^k(t) dt \tag{5.10}$$

When a mixture of H_2 and CO_2 is injected, it is obvious that less H_2 and CO_2 will be produced during the subsequent production period. The reason is the continuously consumption of these substrates for the metabolism of microorganisms. Therefore, the mean rates q^{H_2} and q^{CO_2} are positive. In contrast, CH_4 and H_2O are not present in the injected gas. Nevertheless, they are present in the produced fluid phases because they are the products of the metabolic process. Consequently, the mean rates q^{CH_4} and $q^{H_2O}$are negative.

Hereafter, the particular case is analyzed where the mean injection and production rates are proportional to the stoichiometry of the bio-chemical reaction:

$$q^{CO_2} = \frac{1}{4} q^{H_2} \left(= -q^{CH_4} = -\frac{1}{2} q^{H_2O} \right) \tag{5.11}$$

It follows from Eq. 5.11:

$$\frac{\delta^{H_2}}{\delta^{CO_2}} = \frac{q^{H_2}}{q^{CO_2}} = \epsilon \tag{5.12}$$

Hence, Eq. 5.8 can be written as:

$$\frac{dC^{H2}}{d\tau} = \epsilon(-\delta^{CO_2} C^{H2} C^{CO2} n^2 + q^{CO2}) \tag{5.13}$$

The time derivative of C^{H_2} is proportional to the time derivative of C^{CO_2}:

$$\frac{dC^{H2}}{d\tau} = \epsilon \left(\frac{dC^{CO2}}{dt} \right) \tag{5.14}$$

Integration on both sides leads to:

$$\begin{aligned} \int \frac{dC^{H2}}{d\tau} d\tau &= \int \epsilon \left(\frac{dC^{CO2}}{d\tau} \right) d\tau \\ \Rightarrow \quad C^{H2} &= \epsilon C^{CO2} + K \end{aligned} \tag{5.15}$$

Eq. 5.15 can be inserted into the system of three equations 5.7 to 5.9 what transforms into the following system of two ordinary differential equations:

$$\frac{dn}{d\tau} = \alpha\epsilon C^2 n^2 + \alpha K C n^2 - \beta n \tag{5.16}$$

$$\frac{dC}{d\tau} = -\delta\epsilon C^2 n^2 - \delta K C n^2 + q \tag{5.17}$$

where $C = C^{CO_2}$, $q = q^{CO_2}$ and $\delta = \delta^{CO_2}$.
K can be determined from the initial values:

$$K = C^{H_2,0} - \epsilon C^{CO_2,0} \tag{5.18}$$

5.2 Linear stability analysis

The stability of the non-linear dynamic system was analyzed by the theory of differential equations [131, 48, 94, 93]. Linear stability analysis is often used in mathematics to analyze the qualitative behavior of dynamic systems. The stability of an ODE system can be assessed by calculating the eigenvalues

of the Jacobian matrix at its equilibrium point (or steady-state). Table 5.1 summarizes the qualitative behavior based on the eigenvalue.

Eigenvalue	Effect on system
Positive real number	Driven away from steady state
Negative real number	Driven back to steady state
Zero	Remains at position to which is was disturbed
Identical to another eigenvalue	Behavior can not be predicted
Complex with positive real number	Oscillates around steady-state value with increasing amplitude
Complex with negative real number	Oscillates around steady-state value with decreasing amplitude
Imaginary	Oscillates around steady-state value with constant amplitude

Table 5.1: Stability of ODE systems [66]

Alternatively, the stability can be assessed by the determinant and trace of the Jacobian matrix (cf. Fig 5.2). The equilibrium point is unstable if the trace is positive and/or the determinant is negative. Otherwise, the equilibrium point is stable.

The system of two ordinary differential equations (Eq. 5.16 and Eq. 5.17) has two equilibrium points. The one in the positive parameter region is of interest:

$$n^\star = \frac{\alpha q}{\beta \delta} \tag{5.19}$$

$$C^\star = \frac{\sqrt{\frac{q\alpha^2 K^2 + 4\beta^2 \epsilon \delta}{q}} - \alpha K}{2\epsilon\alpha} \tag{5.20}$$

The stability can be assessed by linearizing the equation system at the

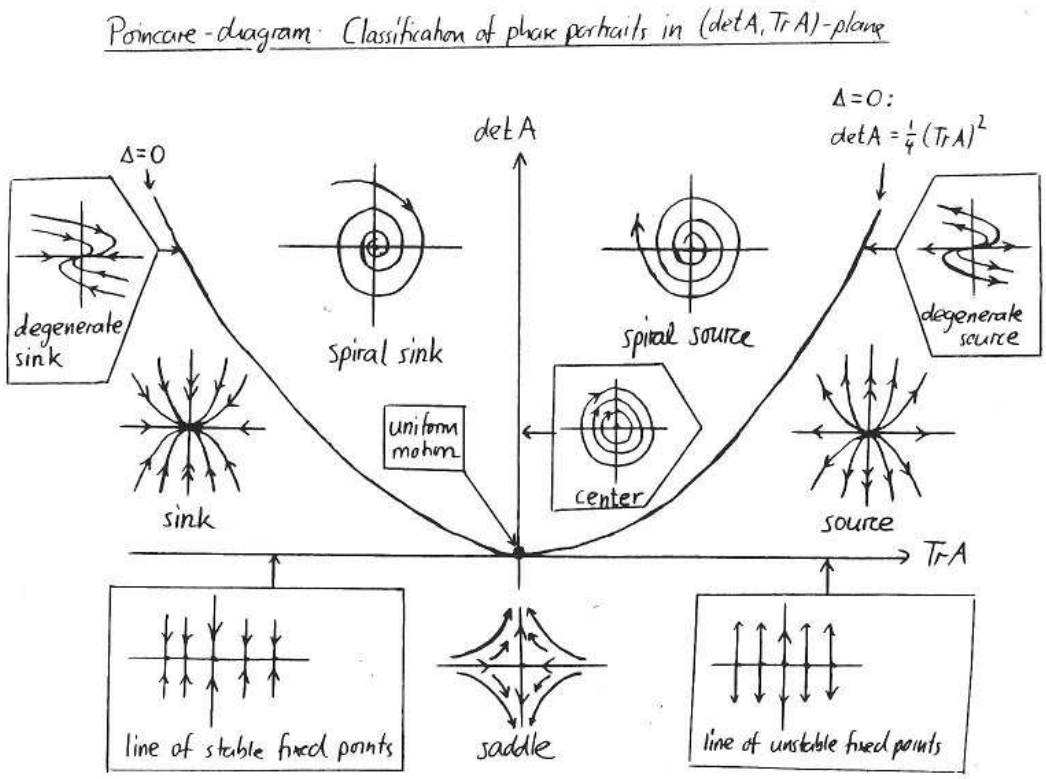

Figure 5.2: Determinant-trace diagram [2]

equilibrium point. The Jacobian matrix at the equilibrium point is:

$$A = \begin{pmatrix} 2\alpha\epsilon C^{\star 2} n^\star + 2\alpha K C^{\star 2} n^\star - \beta & 2\alpha\epsilon C^\star n^{\star 2} + \alpha K n^{\star 2} \\ -2\delta\epsilon C^{\star 2} n^\star - 2\delta K C^{\star 2} n^\star & -2\delta\epsilon C^\star n^{\star 2} - \delta K n^{\star 2} \end{pmatrix} \tag{5.21}$$

The eigenvalues at the steady state are:

$$\lambda_{1/2} = -\frac{P}{2} \pm \sqrt{\left(\frac{P}{2}\right)^2 - Q} \tag{5.22}$$

where

$$P = -2\alpha\epsilon C^{\star 2} n^\star - 2\alpha K C^{\star 2} n^\star + \beta + 2\delta\epsilon C^\star n^{\star 2} + \delta K n^{\star 2} \tag{5.23}$$

$$Q = 2\beta\delta\epsilon C^\star n^{\star 2} + \beta\delta K n^{\star 2} \tag{5.24}$$

Three qualitative different stability behaviors can be obtained what dependents on the values for the input parameters. When the microbial kinetic parameters (α, β and δ) are fixed, it is reasonable to use the rate q as control parameter. In Table 5.2 the different stability behaviors are shown by exemplary phase portraits. The parameter q increases from bottom to top. The critical rates q_{c1} and q_{c2} separate the different behaviors.

Stable focus/node: A stable focus or node (Table 5.2, top) arises when the rate q is sufficiently high, i.e. the eigenvalues must have negative real parts what means that the trace of the Jacobian matrix has to be negative while the corresponding determinant is positive. The required conditions for this behavior are:

$$2\alpha\epsilon C^{\star 2} n^\star + 2\alpha K C^{\star 2} n^\star - \beta - 2\delta\epsilon C^\star n^{\star 2} - \delta K n^{\star 2} < 0 \tag{5.25}$$

$$2\beta\delta\epsilon C^\star n^{\star 2} + \beta\delta K n^{\star 2} > 0 \tag{5.26}$$

Under these conditions a perturbation is always driven back to the equilibrium point (blue point).

Stable limit cycle: The system undergoes a Hopf-bifurcation when the rate is reduced to the critical value q_{c2} [50]. At this point the real parts of both eigenvalues become zero, the focus becomes unstable and a stable limit cycle occurs (Table 5.2, center). The critical rate q_{c2} can be obtained from the following implicit expression:

$$2\alpha\epsilon C^{\star 2} n^\star + 2\alpha K C^{\star 2} n^\star - \beta - 2\delta\epsilon C^\star n^{\star 2} - \delta K n^{\star 2} = 0 \tag{5.27}$$

The further reduction of the rate leads to a growing limit cycle. Under these conditions a perturbation is driven away from the equilibrium point. The solution stabilizes by traveling on an orbit (blue line) around the equilibrium point. The concentration and microbial density are oscillating with constant amplitude.

Unstable focus/node: At a certain rate q_{c1} the limit cycle disappears sharply. Then, the system has a unstable focus or node (Table 5.2, bottom).

stable focus/node for $q = 0.3$:

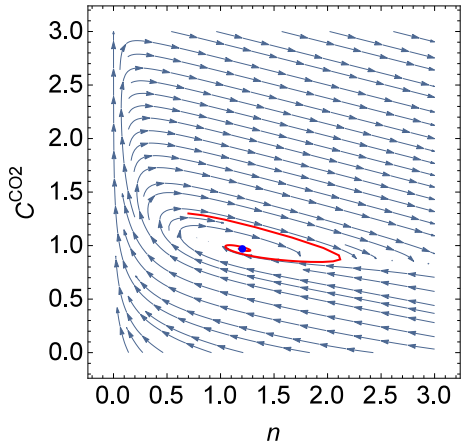

q_{c2}

stable limit cycle for $q = 0.2$:

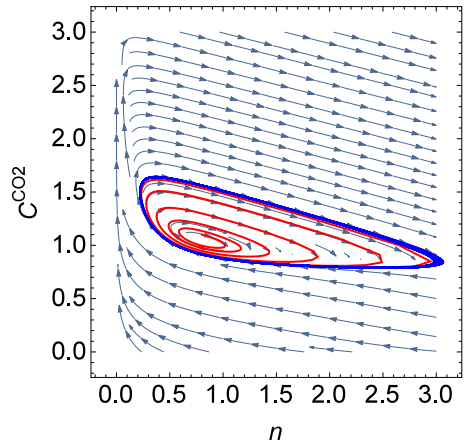

q_{c1}

unstable focus/node for $q = 0.15$:

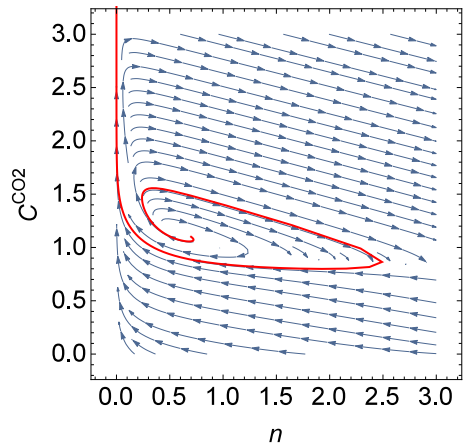

Table 5.2: Stability behaviors for different rates q based on an example parameter set ($\alpha = 1, \beta = 1, \delta^{H_2} = 1, \delta^{CO_2} = 0.25, C^{H_2,0} = 1, C^{CO_2,0} = 1$): The bifurcation occurs at $q_{c2} = 0.219$, the limit cycle disappears when q is reduced below $q_{c1} = 0.195$

The critical rate q_{c1} was determined numerically. Under these conditions a perturbation is again driven away from the equilibrium point but the solution does not stabilize. The microbial density converges to zero while the concentration continues to increase.

Fig. 5.3 and Fig. 5.4 are showing bifurcation diagrams with respect to q for the same example parameter set. The black point represents the bifurcation point (q_{c2} = 0.219). To the left side of this point the system is under limit cycle conditions. The limit cycle disappears sharply at q_{c1} = 0.195. The dotted lines represent the minimum and maximum values of the oscillations within the limit cycle region.

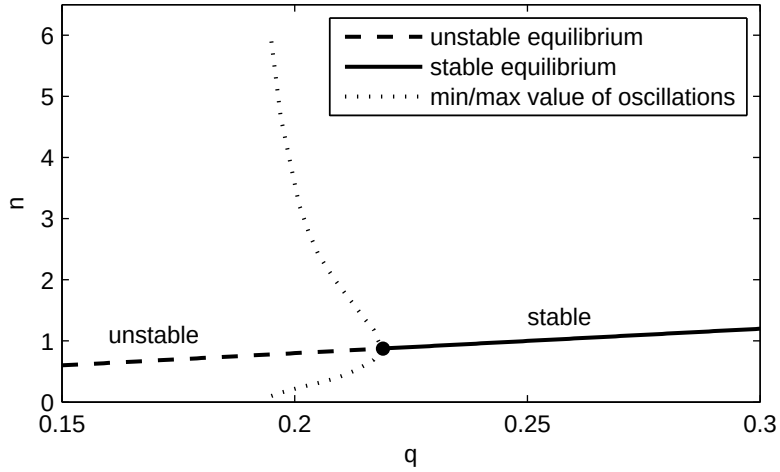

Figure 5.3: Bifurcation diagram for n vs. q based on an example parameter set (α = 1, β = 1, δ^{H_2} = 1, δ^{CO_2} = 0.25 and $C^{H2,0}$ = 1, $C^{CO2,0}$ = 1)

As indicated by Eq. 5.15, C^{H_2} and C^{CO_2} have a proportional relation. The phase portrait under limit cycle conditions in the three-dimensional space (n vs. C^{H_2} vs. C^{CO_2}) is shown in Fig. 5.5. The limit cycle is laying on a plane having an incline in the direction of C^{H_2} vs. C^{CO_2}.

5.3 Turing conditions

Turing instability, also referred to as diffusion-driven instability, is a process of activation, inhibition and diffusion [128]. The mechanism includes two types of agents (e.g. molecules or microorganisms) which interact. The

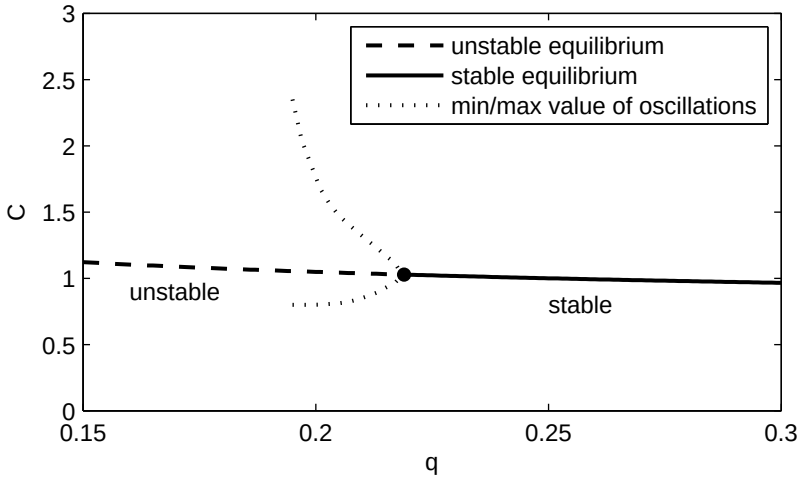

Figure 5.4: Bifurcation diagram for C vs. q based on an example parameter set ($\alpha = 1$, $\beta = 1$, $\delta^{H_2} = 1$, $\delta^{CO_2} = 0.25$ and $C^{H2,0} = 1$, $C^{CO2,0} = 1$)

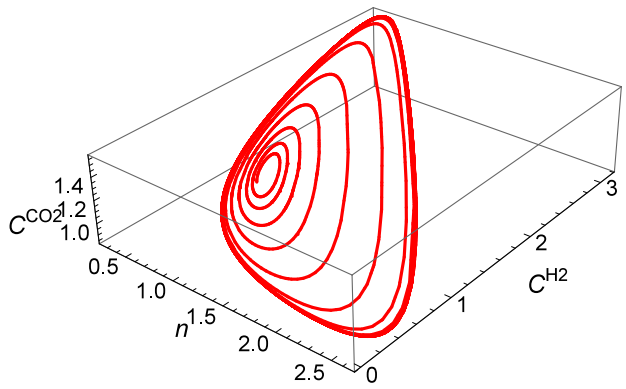

Figure 5.5: Limit cycle in the three-dimensional space according to equation system 5.7 to 5.9 for $\alpha = 1$, $\beta = 1$, $\delta^{H_2} = 1$, $\delta^{CO_2} = 0.25$, $C^{H2,0} = 1$, $C^{CO2,0} = 1$, $q^{H_2} = 0.8$ and $q^{CO_2} = 0.2$

activator produces more of itself and also the inhibitor is produced. Additionally, the presence of the inhibitor reduces the amount of the activator. Both, activator and inhibitor can move by diffusion. Imagine, a small spatially limited concentration of the activator is existing which starts to produce more of itself and diffuses into its vicinity. However, the inhibitor is also present, diffuses faster and stops the spreading of the activator. After this, the activator diffuses beyond the region of high inhibitor concentration and creates a new spot of the activator. This process repeats and a pattern with spatial spots of high activator or high inhibitor concentration arises.

In the case of UHS, the activators are the microorganisms whose rate of growth is catalyzed by itself and the substrates. The inhibition is represented by the decay rate. The inhibitor is then represented by the substrate which is not produced but injected and simultaneously consumed by the microorganisms. The equation system was analyzed for the possibility of this mechanism and conditions were derived for the parameter region which result in a Turing instability.

The Turing mechanism requires a dynamic system which would have a stable equilibrium without diffusion. For equation system 5.16 to 5.17 this was already determined by the following two conditions which are the first two Turing conditions:

$$2\alpha\epsilon C^{\star 2} n^{\star} + 2\alpha K C^{\star 2} n^{\star} - \beta - 2\delta\epsilon C^{\star} n^{\star 2} - \delta K n^{\star 2} < 0 \tag{5.28}$$

$$2\beta\delta\epsilon C^{\star} n^{\star 2} + \beta\delta K n^{\star 2} > 0 \tag{5.29}$$

For the determination of the remaining conditions, diffusive transport has to be included. The diffusion term for CO_2 is simplified by the assumption to depend on the total concentration gradient:

$$\frac{dn}{d\tau} = \alpha\epsilon C^2 n^2 + \alpha K C n^2 - \beta n + \frac{\partial^2}{\partial x^2} n \tag{5.30}$$

$$\frac{dC}{d\tau} = -\delta\epsilon C^2 n^2 - \delta K C n^2 + q + d\frac{\partial^2}{\partial x^2} C \tag{5.31}$$

The stability in the vicinity of the equilibrium point with presence of diffusion can be analyzed by adding a small perturbation to the equilibrium state:

$$n(x,t) = n^{\star} + \zeta n(x,t) \tag{5.32}$$

$$C(x,t) = C^{\star} + \zeta C(x,t) \tag{5.33}$$

The evolution of the perturbed state can be written as:

$$\frac{\partial}{\partial t}U = AU + D\frac{\partial^2}{\partial x^2}U \tag{5.34}$$

where:

$$U = (\zeta n, \zeta C) \tag{5.35}$$

$$A = \begin{pmatrix} 2\alpha\epsilon C^{\star 2}n^{\star} + 2\alpha K C^{\star 2}n^{\star} - \beta & 2\alpha\epsilon C^{\star}n^{\star 2} + \alpha K n^{\star 2} \\ -2\delta\epsilon C^{\star 2}n^{\star} - 2\delta K C^{\star 2}n^{\star} & -2\delta\epsilon C^{\star}n^{\star 2} - \delta K n^{\star 2} \end{pmatrix} \tag{5.36}$$

$$D = \begin{pmatrix} 1 & 0 \\ 0 & d \end{pmatrix} \tag{5.37}$$

The following approach for the solution is assumed:

$$U(x,t) = U_0 e^{\lambda t} cos(kx) \tag{5.38}$$

This equation is a cosine wave whose amplitude is increasing when λ is positive or decreasing when λ is negative. The wave length is $2\pi/k$. The first derivative with respect to time is:

$$\frac{\partial}{\partial t}U(x,t) = \lambda U_0 e^{\lambda t} cos(kx) = \lambda U \tag{5.39}$$

The second derivative with respect to space is:

$$\frac{\partial^2}{\partial x^2}U(x,t) = -k^2 U_0 e^{\lambda t} cos(kx) = -k^2 U \tag{5.40}$$

The outcome is:

$$\lambda U = (A - Dk^2)U \tag{5.41}$$

The stability of the reaction-diffusion equation can be assessed by investi-

gating the eigenvalues of the matrix B:

$$\begin{aligned} B &= A - Dk^2 \\ &= \begin{pmatrix} 2\alpha\epsilon C^{\star 2} n^\star + 2\alpha K C^{\star 2} n^\star - \beta - k^2 & 2\alpha\epsilon C^\star n^{\star 2} + \alpha K n^{\star 2} \\ -2\delta\epsilon C^{\star 2} n^\star - 2\delta K C^{\star 2} n^\star & -2\delta\epsilon C^\star n^{\star 2} - \delta K n^{\star 2} - dk^2 \end{pmatrix} \end{aligned} \tag{5.42}$$

For a Turing instability the same equilibrium point needs to be unstable when diffusion is present. Consequently, either the trace of matrix B has to be positive or its determinant has to be negative:

$$\mathrm{Tr}B > 0 \tag{5.43}$$

or:

$$\det B < 0 \tag{5.44}$$

The trace of matrix B is:

$$\begin{aligned} \mathrm{Tr}B &= 2\alpha\epsilon C^{\star 2} n^\star + 2\alpha K C^{\star 2} n^\star - \beta - 2\delta\epsilon C^\star n^{\star 2} - \delta K n^{\star 2} - (1+d)\, k^2 \\ &= \mathrm{Tr}A - (1+d)\, k^2 \end{aligned} \tag{5.45}$$

Condition 5.28 defines $\mathrm{Tr}A$ to be negative and consequently $\mathrm{Tr}B$ cannot be positive. Therefore, a condition needs to be found which makes the determinant negative:

$$\begin{aligned} 0 >& \det B \\ =& dk^4 - \left(2\delta\epsilon C^\star n^{\star 2} + \delta K n^{\star 2} - d\left(2\alpha\epsilon C^{\star 2} n^\star + 2\alpha K C^{\star 2} n^\star - \beta\right)\right) k^2 \\ &+ 2\beta\delta\epsilon C^\star n^{\star 2} + \beta\delta K n^{\star 2} \end{aligned} \tag{5.46}$$

From condition 5.28 it is known that:

$$2\delta\epsilon C^\star n^{\star 2} + \delta K n^{\star 2} > 2\alpha\epsilon C^{\star 2} n^\star + 2\alpha K C^{\star 2} n^\star - \beta \tag{5.47}$$

Hence, d need to be larger than one which means that the diffusion of CO_2 takes place faster than the diffusion microorganisms. From this it follows the third Turing condition:

$$2\delta\epsilon C^\star n^{\star 2} + \delta K n^{\star 2} - d\left(2\alpha\epsilon C^{\star 2} n^\star + 2\alpha K C^{\star 2} n^\star - \beta\right) > 0 \tag{5.48}$$

Eq. 5.46 can be written as:

$$\det B = dk^4 - pk^2 + q \tag{5.49}$$

The condition 5.44 requires that:

$$dz^2 - pz + q < 0 \tag{5.50}$$

where $z = k^2$. This is true if:

$$\frac{p^2}{4q} > d \tag{5.51}$$

It follows the fourth Turing condition:

$$\begin{aligned}\left(2\delta\epsilon C^\star n^{\star 2} + \delta K n^{\star 2} - d(2\alpha\epsilon C^{\star 2} n^\star + 2\alpha K C^{\star 2} n^\star - \beta)\right)^2 \\ > 4d\left(2\beta\delta\epsilon C^\star n^{\star 2} + \beta\delta K n^{\star 2}\right)\end{aligned} \tag{5.52}$$

Summarized the four conditions are:

$$2\alpha\epsilon C^{\star 2} n^\star + 2\alpha K C^{\star 2} n^\star - \beta - 2\delta\epsilon C^\star n^{\star 2} - \delta K n^{\star 2} < 0 \tag{5.53}$$

$$2\beta\delta\epsilon C^\star n^{\star 2} + \beta\delta K n^{\star 2} > 0 \tag{5.54}$$

$$2\delta\epsilon C^\star n^{\star 2} + \delta K n^{\star 2} - d(2\alpha\epsilon C^{\star 2} n^\star + 2\alpha K C^{\star 2} n^\star - \beta) > 0 \tag{5.55}$$

$$\begin{aligned}\left(2\delta\epsilon C^\star n^{\star 2} + \delta K n^{\star 2} - d(2\alpha\epsilon C^{\star 2} n^\star + 2\alpha K C^{\star 2} n^\star - \beta)\right)^2 \\ > 4d\left(2\beta\delta\epsilon C^\star n^{\star 2} + \beta\delta K n^{\star 2}\right)\end{aligned} \tag{5.56}$$

These conditions allow to find a set of parameters which produces spatial oscillations when the initial conditions have a perturbation. In Fig. 5.6 the Turing parameter space (grey region) for q and d is shown for an exemplary parameter set. The wave length can be calculated from the minimum of the polynomal function:

$$z_{min} = k^2 = \frac{p}{2d} \tag{5.57}$$

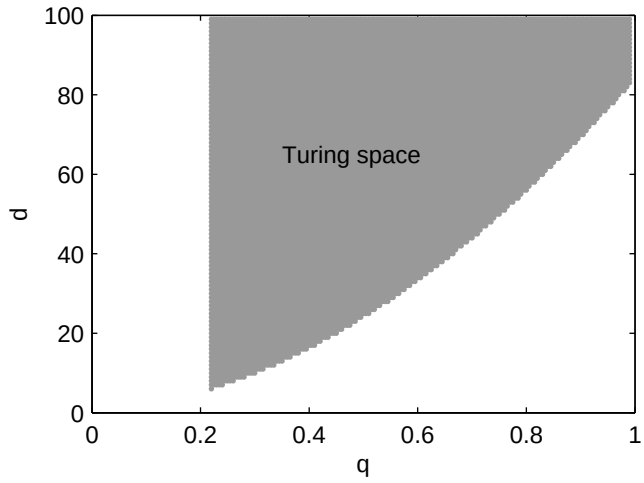

Figure 5.6: Turing space for the rate q versus the ratio of diffusion coefficients d for a fixed set of parameters ($\alpha = 1$, $\beta = 1$, $\delta^{H_2} = 1$, $\delta^{CO_2} = 0.25$, $C^{H2,0} = 1$ and $C^{CO2,0} = 1$)

Then, the wave length λ is:

$$\lambda = \frac{2\pi}{k} \tag{5.58}$$

5.4 Numerical simulations

Different simulation studies were performed under conditions derived from the previous sections. The numerical model is based on DuMu$^{\mathrm{X}}$ as described in chapter 6. The model includes four components (H_2, CO_2, CH_4, H_2O) and one microbial species (methanogenic archaea). A simplified two-dimensional reservoir model was used which represents the top view (cf. section 6.1.5).

Different dynamic behaviors were obtained by varying the injection/production rate, the characteristic parameters and the initial conditions. The most interesting scenarios are presented here.

5.4.1 Limit cycle behavior

The initial conditions for this simulation case are homogeneous: $S_g = 0.5$, $c_g^{H_2} = 0.4$, $c_g^{CO_2} = 0.25$, $c_g^{CH_4} = 0.35$, $n = 2$. The injection/production rates are: $q^{H_2} = 0.8$, $q^{CO_2} = 0.2$, $q^{CH_4} = -0.2$, $q^{H_2O} = -0.4$. Under these conditions the storage undergoes a limit cycle behavior. The microbial density and the gas phase concentrations remain spatially constant but are oscillating in time. In Fig. 5.7 the microbial density and gas phase concentrations are plotted versus time.

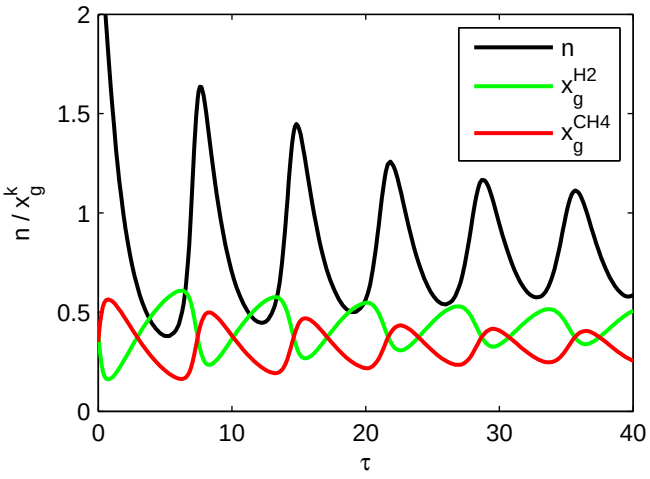

Figure 5.7: Temporal evolution of the microbial density and gas phase concentrations in the reservoir

5.4.2 Turing instability

For the second simulation case the initial conditions are the same as in the previous case except for a small area on the left side of the reservoir. In this spot a perturbation to the initial microbial density is added: $n = 0$ (cf. Fig. 5.8a). The injection/production rates are: $q^{H_2} = 1$, $q^{CO_2} = 0.25$, $q^{CH_4} = -0.25$, $q^{H_2O} = -0.5$. The ratio between the diffusion coefficients d is 10. Under these conditions the reservoir undergoes a Turing instability. Starting from the perturbation on the left side oscillations in the microbial density and the gas phase concentrations are spreading throughout the reservoir. Spatial spots which have a high microbial density and high CH_4

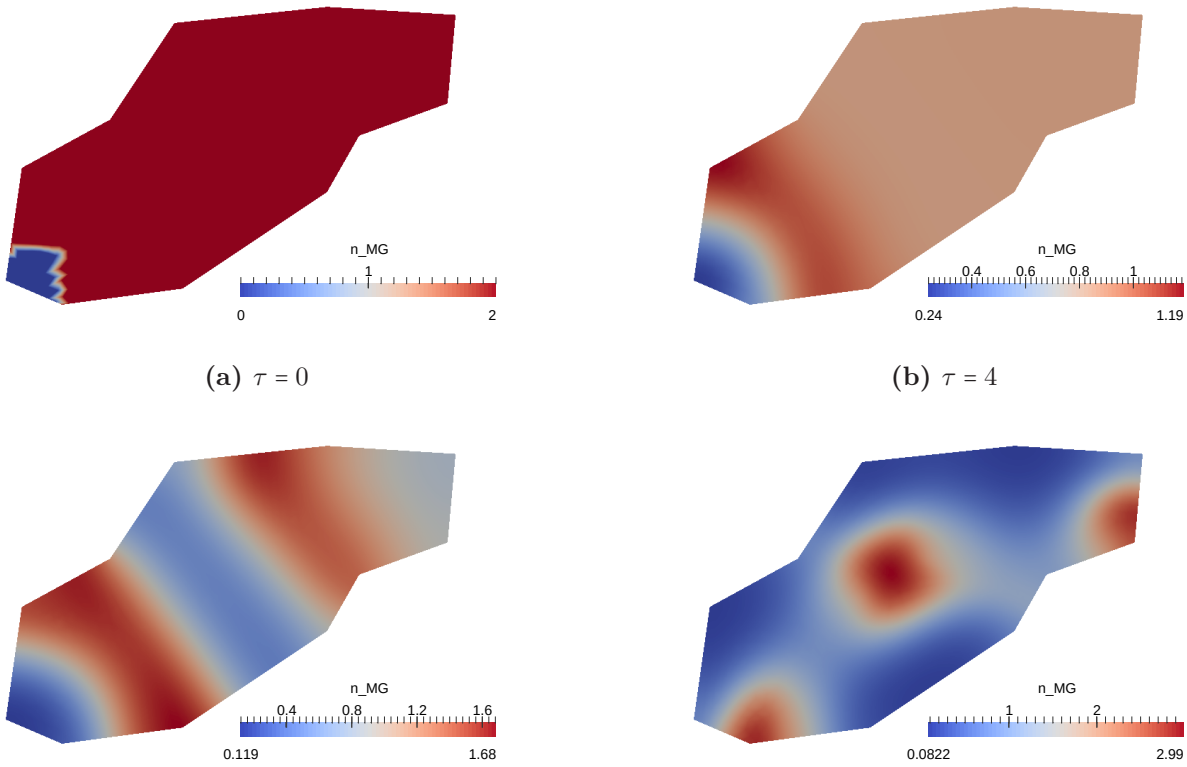

(a) $\tau = 0$ **(b)** $\tau = 4$

(c) $\tau = 10$ **(d)** $\tau = 60$

Figure 5.8: Temporal evolution of number of microorganisms

concentration arise and move through the reservoir. In contrast the H_2 concentration in these spots is low. The behavior of microbial density and gas phase concentrations is shown in Fig. 5.8 to Fig. C.6 for some points in time. Different patterns can be observed at different points in time.

5.5 Summary and conclusions

- Underground hydrogen storages could behave as a bio-reactor similar to the observation in some former town gas storages. When both substrates (H_2 and CO_2) are injected, the methanogenic metabolism leads to a continuous transformation into CH_4 and H_2O.
- When the mean rates of injection and production are equal to the rates of the bio-chemical reaction, the reservoir is in an equilibrium state.

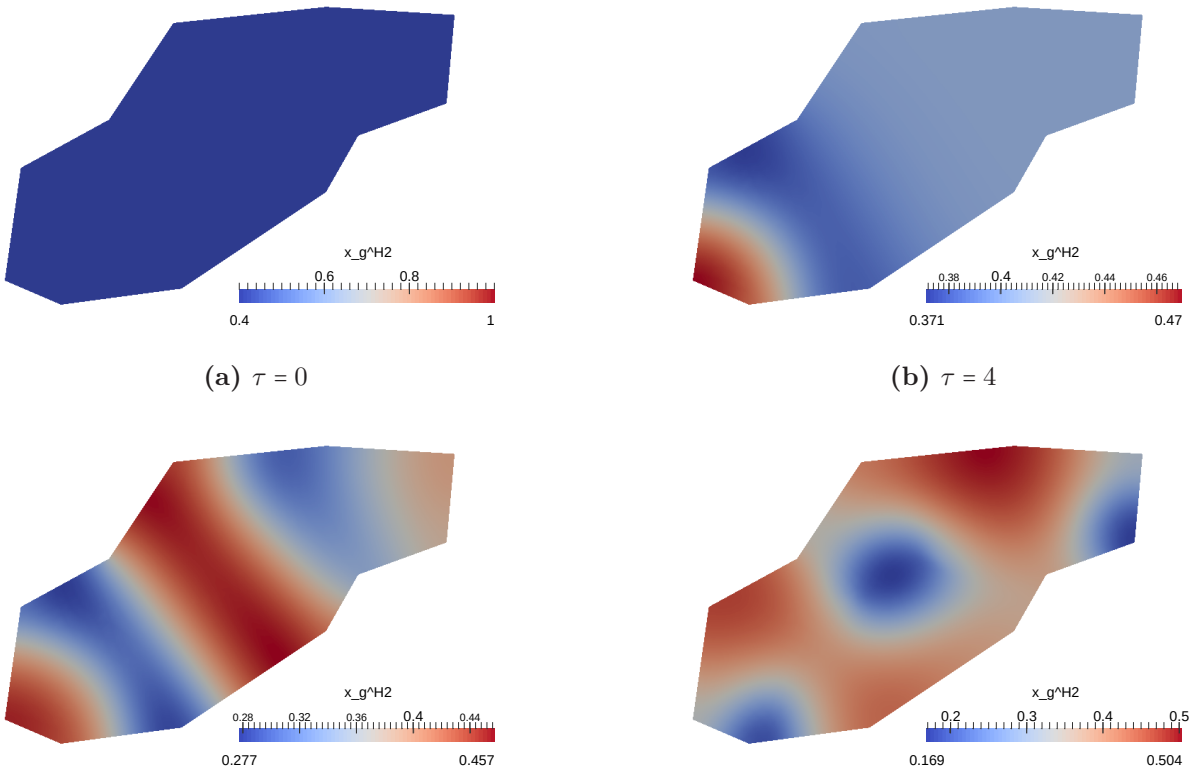

(a) $\tau = 0$ **(b)** $\tau = 4$

(c) $\tau = 10$ **(d)** $\tau = 60$

Figure 5.9: Temporal evolution of H_2 concentration in the gas phase

Dependent on the stability of this equilibrium point the reservoir shows different dynamic behaviors.

- It was shown that the reduced equation system can have an unstable or stable equilibrium point. The rate q can be used as parameter to control this behavior. In a certain range for q a stable limit cycle appears around the equilibrium point. In the literature this behavior is referred to as Hopf-bifurcation.
- The possibility for a Turing instability was derived on the reduced reaction-diffusion model. The presented Turing conditions allow to determine the range for the rate q under which a Turing instability occurs.
- Numerical simulations using the complete model for bio-reactive two-phase transport were performed under the derived conditions. Under limit cycle conditions the simplified reservoir shows oscillations in time

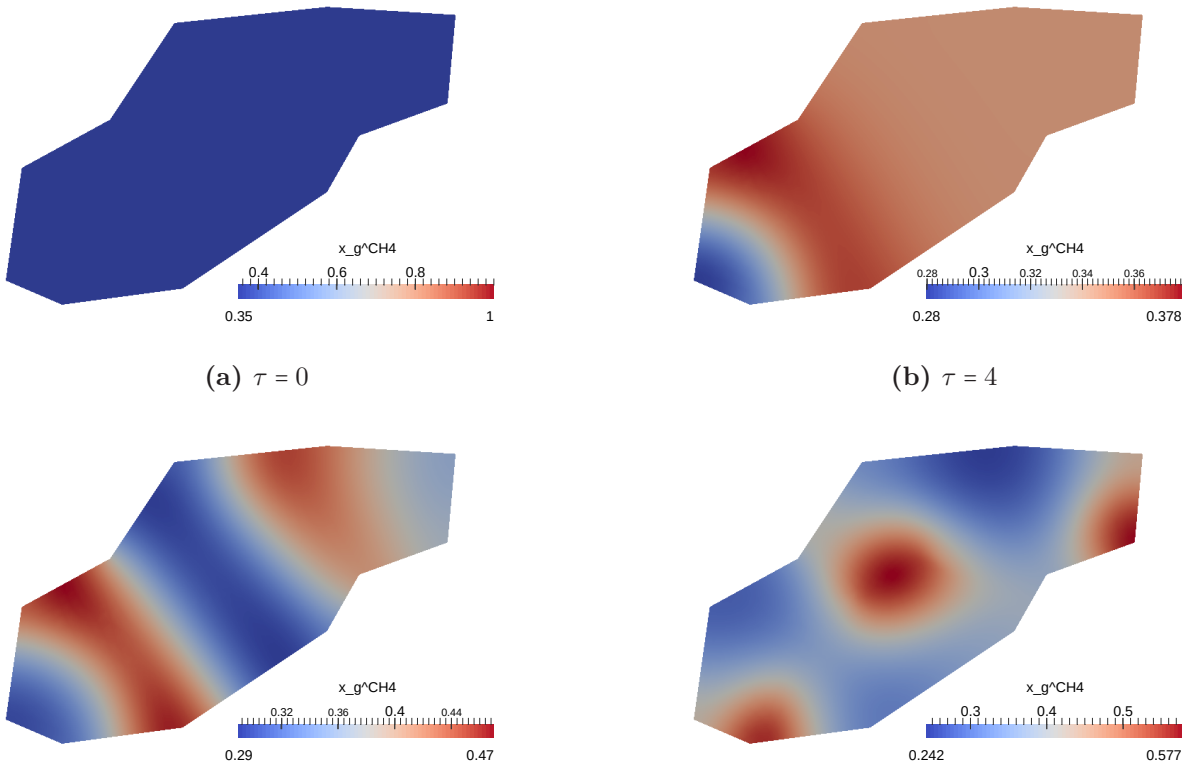

(a) $\tau = 0$ **(b)** $\tau = 4$

(c) $\tau = 10$ **(d)** $\tau = 60$

Figure 5.10: Temporal evolution of CH_4 concentration in the gas phase

for the microbial density and gas phase concentrations. Under Turing conditions the results show spatial oscillations in the microbial density and gas phase concentrations. Different kinds of patterns were observed.

Chapter 6

Numerical modeling of storage cycles

The numerical simulations performed in this thesis were implemented in the open-source software DuMu^{X} [43]. DuMu^{X} was developed by the University of Stuttgart for the simulation of flow and transport processes in porous media. It is based on the "Distributed and Unified Numeric Environment" (DUNE) toolbox which provides an open-source fundament for the solution of partial differential equations using grid based methods [10]. The open-source license allows the user to independently advance the simulator and to implement any kind of changes. This potential was used within this thesis to implement the mathematical model which was developed in chapter 4. The created numerical model was used to simulate different hydrogen storage scenarios.

Parts of this chapter were already published in the journals Environmental Earth Sciences [55, 42] and Computational Geosciences [56] during the work on the thesis.

6.1 Numerical implementation

DuMu^{X} offers several numerical models which differ in their mathematical formulation (e.g. the physical laws, the number of phases or the number of components) or in their numerical implementation (implicitly solved models or decoupled models, e.g. an implicit pressure explicit saturation algorithm). In this section the general algorithmic principles of DuMu^{X} are introduced and subsequently the performed adaptations are explained. The explanations concentrate on the implicit formulation which was used in this thesis.

6.1.1 Spatial and temporal discretization

The mathematical model (Eq. 4.34 to Eq. 4.37) can be considered as a set of conservation laws which apply in the spatial domain and time frame of interest. To solve such a problem mathematically it is required to discretize the model in space and time. DuMu$^{\mathrm{X}}$ offers two different spatial discretization methods: A cell-centered finite volume method and a vertex-centered finite volume (box) method. The discretization in time is done by an implicit (backwards) Euler scheme. On the basis of discretization a non-linear equation system can be derived at each time step. Subsequently, the non-linear equation system can be solved by an iterative method (cf. section 6.1.2). The discretization scheme is shown here on the example of the cell-centered finite volume method combined with an implicit euler method. The mathematical model can be written in the following reduced form which applies on the domain:

$$\frac{\partial}{\partial t} u + \nabla \cdot f(u) = g(u) \tag{6.1}$$

where u is the vector of primary variables, f is the flux function and g is the source function. The domain has to be subdivided into a finite number of non-overlapping control volumes V_i (cf. Fig. 6.1) where i is the index of the control volumes. Subsequently, control volumes for the spatial discretization are also referred to as grid cells. In each of these grid cells the conservation

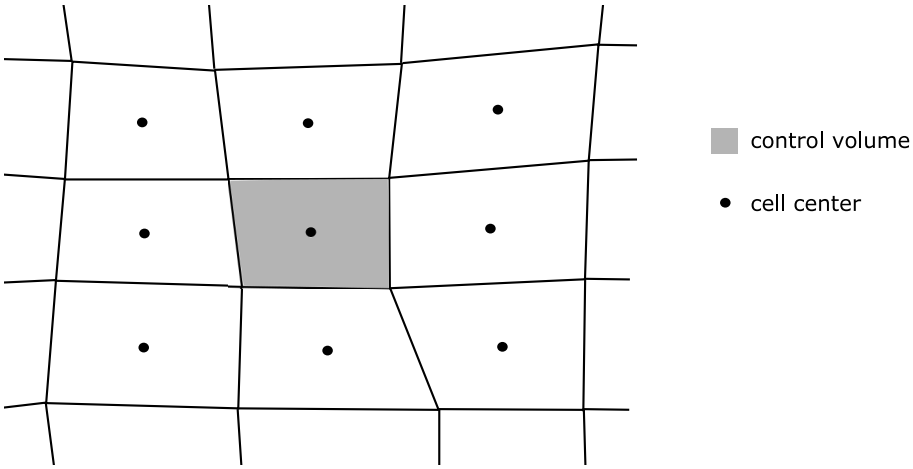

Figure 6.1: Schematic 2D grid for a cell-centered finite volume method

law is valid in its integral form:

$$\frac{\partial}{\partial t}\int_{V_i} u dV_i + \int_{\partial V_i} f(u)\cdot n dA_i = \int_{V_i} g(u) dV_i \tag{6.2}$$

where A is the total surface area of a grid cell and n is the unit normal vector. This means that the quantities u in a grid cell can be only changed by in- or outflow over the boundaries of the grid cell or by creating or vanishing of the quantities within the grid cell. In a cell-centered finite volume method the values for the quantities u are stored at the cell centers which means that it represents an average value over the volume:

$$u_i = \frac{1}{V_i}\int_{V_i} u dV_i \tag{6.3}$$

The same can be applied for the source/sink term:

$$g(u_i) = \frac{1}{V_i}\int_{V_i} g(u) dV_i \tag{6.4}$$

As a consequence, the values of the quantities u are discontinuous at the interfaces between two grid cells. The flux integral has to be approximated by taking into account the values of the quantities u in the individual (i) and the neighboring (j) grid cell:

$$\int_{\partial V_i} f(u)\cdot n dA_i = \sum_{j=1}^{m} k_{ij}(u_i, u_j) \tag{6.5}$$

where m is the number of neighboring grid cells. Function k_{ij} has to take into account the geometrical quantities like distance between the cell centers and area of the interface. Additionally, an averaging of rock and fluid properties like porosity, (relative) permeability, viscosity, density, effective diffusion coefficients has to be included. Dividing Eq. 6.2 by the volume V_i and inserting Eq. 6.3 and Eq. 6.4 results in:

$$\frac{\partial}{\partial t}u_i + \frac{1}{V_i}\sum_{j=1}^{n} k_{ij}(u_i, u_j) = g(u_i) \tag{6.6}$$

Finally, the time derivative can be replaced by using an Euler scheme:

$$\frac{\partial}{\partial t} u_i = \frac{u_i^{t+1} - u_i^t}{\Delta t} \tag{6.7}$$

For an implicit Euler scheme the final equation for each grid cell can be derived as follows:

$$u_i^{t+1} = u_i^t - \frac{\Delta t}{V_i} \sum_{j=1}^{n} k_{ij}(u_i^{t+1}, u_j^{t+1}) = g(u_i^{t+1}) \tag{6.8}$$

6.1.2 Iterative procedure

The discretization in space and time results in a non-linear equation system at each time step. The number of equations is equal to the number of grid cells multiplied by the number of primary variables (degrees of freedom). The algorithmic structure to solve this equation system is shown in Fig. 6.2. After initializing the grid, defining the initial conditions and allocating the

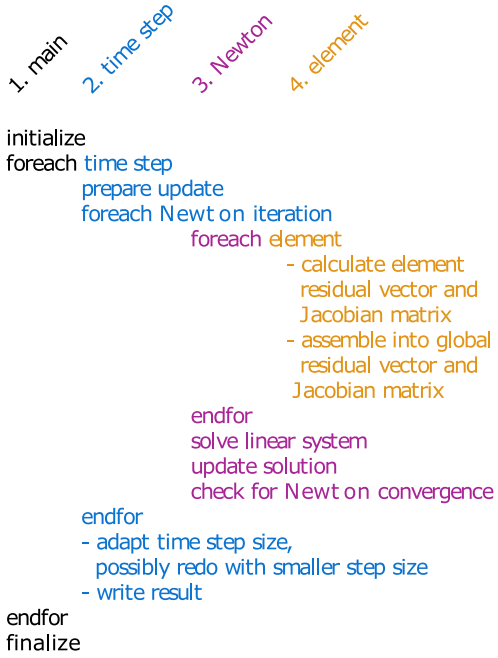

Figure 6.2: Structure of the fully implicit scheme in DuMu$^{\text{X}}$ [43]

memory, three interlaced loops are run through: For each time step, for each newton iteration and for each grid cell. The multidimensional Newton

method is seeking for the zero point of the equation system in the following way:

1. The vector of residuals and the corresponding Jacobian matrix are calculated by running through the loop over each grid cell. The partial differentiation for assembling the Jacobian matrix is done numerically in the following way:
$$\frac{r(x+\epsilon) - r(x-\epsilon)}{2\epsilon} \tag{6.9}$$
where r is the residual of an equation, x is a primary variable and ϵ is a small value.

2. The result is a linear equation system which can be solved for the change in solution (ΔX):
$$J(X_n)\Delta X_n = -R(X_n) \tag{6.10}$$
where J is the Jacobian matrix, ΔX is the change in the solution vector and R is the residual vector. An algebraic multigrid solver, which shows a high efficiency in parallel processing, was used to solve this equation system.

3. The new solution is calculated by:
$$X_{n+1} = X_n + \Delta X_n \tag{6.11}$$

4. The convergence is checked by calculating the maximum relative or absolute error between the new solution vector and the one of the previous iteration.

When the convergence criterion was fulfilled, the solution is written out and a new time step is started. The simulation ends when the final simulation time is reached.

6.1.3 Adaptation of the governing equation system

The molar balance equations (Eq. 4.24 and Eq. 4.25) were implemented by using the already existing model “2p2c”. This model realizes the flow of two fluid phases which consist out of two partially miscible components.

The primary variables in this model are the pressure of one phase and the saturation of the other phase. For the appearance and disappearance of phases additional constraints are implemented which check on the values of saturation and sum of concentrations if a phase is present. When only one phase is present the primary variables are switched. In this case the pressure and the concentration of one component in the existing phase are used as primary variables. The "2p2c" model was extended by the additional components for the implementation of the developed mathematical model. A "2p4c", a "2p6c" and a "2p7c" model were developed during this thesis. The most advanced model with seven components includes H_2, CO_2, CH_4, H_2O, H_2S, N_2 and SO_4^{2-}. The additional primary variables are the concentrations of $n-2$ (in this case 5) components. Additionally, the numerical implementation of the transport equations was extended for effect of mechanical dispersion in both phases. Therefore the longitudinal and transverse dispersivity were introduced as rock parameters and a new method was introduced which calculates the dispersion tensor based on the Darcy velocity.

Additional balance equations were added for the implementation of the microbial population dynamics. Each microbial species appends the model by one primary variable which is the microbial density. Growth and decay of the microorganisms are introduced in the source/sink term of these equations. The movement of microorganisms was added equivalent to the diffusive flux of the components. The terms for the bio-chemical reactions were accordingly added as source/sink terms to the molar balance equations. The most advanced "2p7c2mo" model describes the flow and transport of seven components in two phases coupled to the metabolic processes of two microbial species: Methanogens and sulfate-reducers. The model has 9 primary variables: One pressure, one saturation, five concentrations and two microbial densities. The C++ code which evaluates the source/sink terms for microbial growth and decay and the bio-chemical reactions in each (sub) control volume in listed in appendix A.1.

6.1.4 Phase equilibrium and hydrodynamic parameters

The phase composition and hydrodynamic parameters of the phases are updated during each Newton iteration. DuMu$^{\text{X}}$ provides a large library of

calculation methods for the phase properties. These methods were adapted and extended for the consideration of the additionally introduced chemical components. The following laws and correlations were used in the numerical models for four, six and seven components:

- For the determination of the phase composition it is assumed that the phases are in thermodynamic equilibrium. This means that the fugacities for each component are equal in both phases:

$$f_g^k = f_w^k \quad \text{or} \quad c_g^k \varphi_g^k P_g = c_w^k \varphi_w^k P_w \tag{6.12}$$

  where f is the fugacity in $[Pa]$ and φ is the fugacity coefficient. The gas phase is treated as an ideal gas mixture and consequently the fugacity coefficients are set to 1. In the water phase the coefficients of the gaseous components are calculated by using Henry's law:

$$\varphi_w^k = \frac{H^k}{P_w} \tag{6.13}$$

  where H is the Henry's law constant in $[Pa]$. The fugacity coefficient of H_2O is calculated by using the vapor pressure:

$$\varphi_w^{H_2O} = \frac{P_v^{H_2O}}{P_w} \tag{6.14}$$

  where $P_v^{H_2O}$ is the vapor pressure of pure water in $[Pa]$. Additionally, the sum of concentrations in each phase is needed:

$$\sum_k c_g^k = 1 \qquad \sum_k c_w^k = 1 \tag{6.15}$$

  Eq. 6.12 to Eq. 6.15 are used to assemble a linear equation system of $2 \cdot n$ equations. $n-2$ concentrations are known because they are the primary variables. The linear equation system can be solved to get the remaining $n+2$ concentrations.

- The gas phase density is calculated by using the ideal gas law:

$$\hat{\rho}_g = \frac{P_g \sum_{k=1}^{4} c_g^k M^k}{RT} \tag{6.16}$$

where M is the molar mass in $[kg/mol]$, R is the gas constant in $[J/mol/K]$ and T is the temperature in $[K]$. The water phase density is calculated dependent on the composition by [26]:

$$\hat{\rho}_w = \sum_{k=1}^{4} c_w^k \hat{\rho}^{H_2O} \frac{M^k}{M^{H_2O}} \tag{6.17}$$

where the density of pure H_2O is constant.

- The gas phase viscosity is calculated by the Wilke method which correlates the viscosity dependent on composition and temperature [109]:

$$\mu_g = \sum_{i=1}^{4} \frac{c_g^i \mu_g^i}{\sum_{j=1}^{4} c_g^i \omega^{ij}} \tag{6.18}$$

$$\omega^{ij} = \frac{\left(1 + \sqrt{\frac{\mu_g^i}{\mu_g^j}} \left(\frac{M^i}{M^j}\right)^{\frac{1}{4}}\right)^2}{\sqrt{8\left(1 + \frac{M^i}{M^j}\right)}} \tag{6.19}$$

where μ_g^i is the viscosity of the pure gases which is correlated by using the method of Chung et al. dependent on temperature [109]. The water phase viscosity is constant.

6.1.5 Grid generation and rock parameters

Two different conceptional grid models were created. The first grid model shown in Fig. 6.3 represents a vertical slice through a simplified anticline structure. This grid model was used for simulations in dimensionless form. The horizontal dimension is 1 and the storage formation has a thickness of approximately 0.12. The grid has $137 \times 14 = 1918$ tetragonal cells which have a average size of $7.3 \cdot 10^{-3} \times 8.6 \cdot 10^{-3}$. The second grid model which is shown in Fig. 6.4 represents the top view of a storage reservoir. The unstructured grid has 1466 quadrangular cells.

Both grid models have been created by using the grid generator of COMSOL Multiphysics. A Matlab script was used to transform the grid data into a

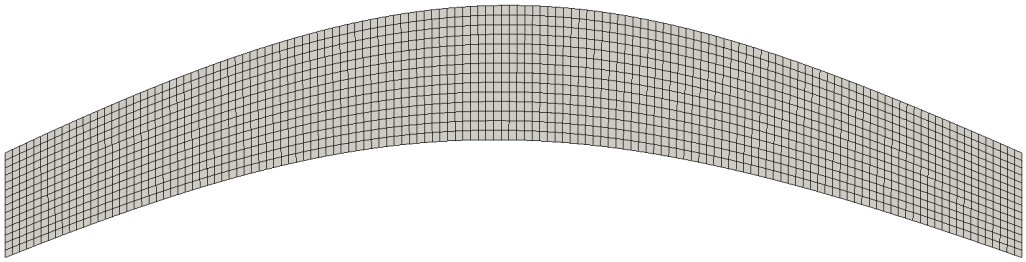

Figure 6.3: 2D grid model representing a vertical slice through an anticline structure

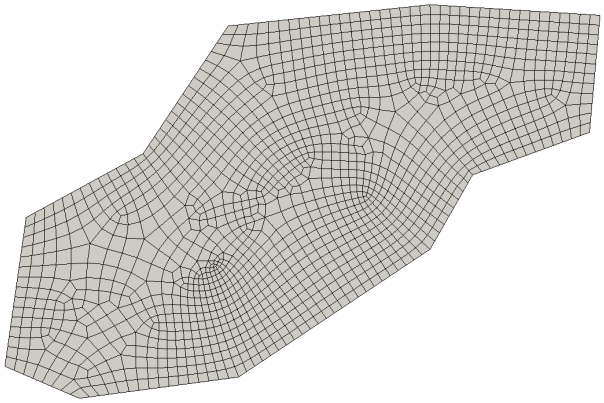

Figure 6.4: 2D grid model representing the top view of an storage reservoir

readable format for DUNE. The grid manager "dune-alugrid" [32] was used to read them into the simulator.

The hydraulic parameters of the storage rock are homogeneous and isotropic ($K_x = K_y$). The relative permeability and the capillary pressure are correlated by using the Brooks-Corey correlation [18]. The rock parameters are summarized in Table 6.1.

A three-dimensional grid model was created from the geological model of a real gas reservoir. The used geological model is a part of one of the largest gas fields in Europe. However, the enormous extensions of the reservoir would require a very large amount of hydrogen to fill the reservoir and provide a sufficient storage deliverability. Therefore, a much smaller prismatic fragment was cut out of the geological model by using Schlumberger Petrel [5]. The created grid model shown in Fig. 6.5 represents a typical anticline structure with the dimensions 1200 m × 800 m × 50 m. The grid has 26 × 37 × 13 = 12506 cells. The cells which represent the sandstone

Table 6.1: List of rock parameters (2D models)

Parameter	Symbol	Value
Porosity	ϕ	0.2
Dimensionless permeability	$\bar{K}$	1
Dimensionless entry capillary pressure	$\bar{P}_e$	$1 \cdot 10^5 / P^\star$
Pore size distribution index	λ	2
Residual gas saturation	S_{gr}	0.2
Residual water saturation	S_{wr}	0.2
Longitudinal dispersivity	a_L	$10/L^\star$
Transverse dispersivity	a_T	$0.05/L^\star$

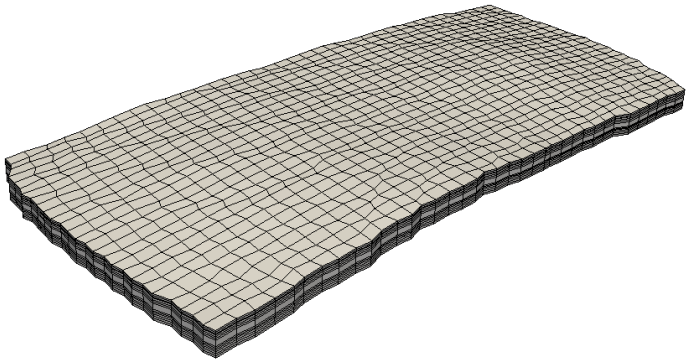

Figure 6.5: 3D grid model

storage formation have a average size of 32 m × 31 m × 3 m. The model has four independent highly porous and highly permeable sandstone layers which are separated by impermeable clay layers. The sandstone layers are defined with the original porosity and permeability values which are shown in Fig. 6.6 and Fig 6.7.

The average porosity is 13.08 % and the average permeability is 22.40 mD. The additional rock parameters are summarized in Table 6.2. The grid which was generated by Petrel [5] in a "corner-point" format was imported for the usage with DuMu$^{\mathrm{X}}$ by using the modules "opm-parser" [4] and "dune-cornerpoint" [3].

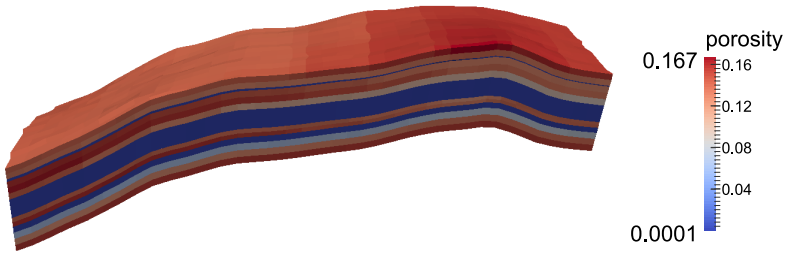

Figure 6.6: Porosity shown on a slice through the 3D grid model (vertically stretched by a factor of 5)

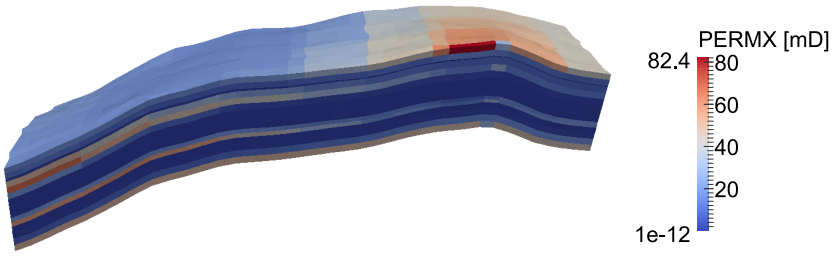

Figure 6.7: Horizontal permeability shown on a slice through the 3D grid model (vertically strechted by a factor of 5)

Table 6.2: List of rock parameters (3D model)

Parameter	Symbol	Value	Unit
Entry capillary pressure	P_e	$1 \cdot 10^5$	Pa
Pore size distribution index	λ	2	
Residual gas saturation	S_{gr}	0.1	
Residual water saturation	S_{wr}	0.1	
Longitudinal dispersivity	a_L	10	m
Transverse dispersivity	a_T	0.05	m

6.1.6 Adjustments for heterogeneous corner-point grids

As already mentioned DuMu$^{\text{X}}$ offers two different spatial discretization schemes. The box-method was used for the 2D models which is appropriate for conforming grids. For the processing of geological more complex reservoir structures in the corner-point format, the more conventional cell-centered finite volume method was used.

Some further numerical challenges occurred during the handling of unstructured three-dimensional grids with strongly heterogeneous rock parameters. Comprehensive geological reservoir models which are created in Petrel [5], typically consist out of very irregular grid geometries and structures. Individual cells can for example deviate from the cuboid cell shape by instead having a rectangular prismatic shape which are also known as "degenerate cells". These cells especially occur in those regions, where grid horizons are merging into each other. At geological faults, where an offset between the layers exits, it is additionally possible that the grid model becomes non-conforming. To meet the complexity of these irregular grid structures, some fundamental computation settings were modified. The flux between two neighboring cells depends on the difference in pressure potential and the transmissibility between the cells. The standard method in DuMu$^{\mathrm{X}}$ for calculating the transmissbility is accomplished by taking the face area, the harmonic mean of the two cell permeabilities and the distance between the cell centers. However, the deviating sizes and shapes of neighboring cells lead to a certain inaccuracy which is resulting in numerical instability. A better solution includes the initial calculation of the two transmissibilities from each cell center to their common face center, referred to as "half-block transmissibility". Subsequently, the total transmissibility between the cells is calculated by taking half of the harmonic mean of these half-block transmissibilities. This option was implemented by the DuMu$^{\mathrm{X}}$ developers and is available since the DuMu$^{\mathrm{X}}$ release 2.8. The importance for this change can be demonstrated on the following example:

- The half-block transmissibility T in one of the six possible directions is defined as following [28, 58]:

$$T = \frac{K \cdot A}{L} \tag{6.20}$$

  where K is the permeability of the grid cell in $[m^2]$, A is the area of the face in $[m^2]$, L is the distance between the cell center and the face center in $[m]$. The total transmissibility T_{12} between two cells is then calculated by taking half of the harmonic mean (a full contact between the cells is assumed) [28, 58]:

$$T_{12} = \frac{1}{2}\frac{2}{\frac{1}{T_1} + \frac{1}{T_2}} = \frac{T_1 T_2}{T_1 + T_2} \tag{6.21}$$

The difference between the ”half-block transmissibility” and the standard ”permeability averaging” method becomes distinct, whenever unstructured grid structures with heterogeneous rock properties are processed (Fig. 6.8). In this case, the two half-block transmissibilities

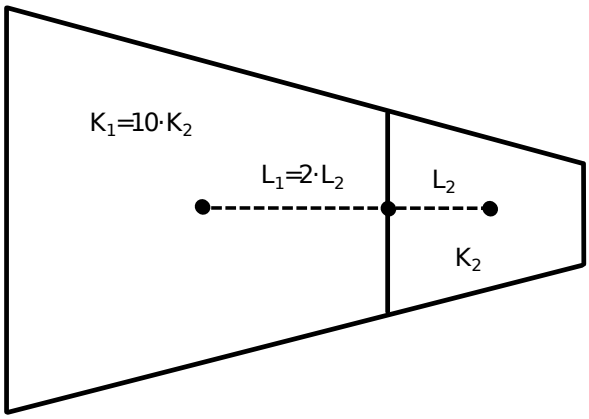

Figure 6.8: Sketch of two cells in an unstructured grid with heterogeneous permeability

result in:

$$T_1 = \frac{K_1 \cdot A}{L_1}, \quad T_2 = \frac{1}{5}\frac{K_1 \cdot A}{L_1} \tag{6.22}$$

Consequently, the total transmissibility yields in:

$$T_{12} = \frac{T_1 T_1}{T_1 + T_2} = \frac{1}{6}\frac{K_1 \cdot A}{L_1} \approx 0.17\frac{K_1 \cdot A}{L_1} \tag{6.23}$$

While the ”half-block transmissibilty” method averages the permeability and the distances between face and cell centers, the other method averages only the permeability:

$$K_{12} = \frac{2}{\frac{1}{K_1} + \frac{10}{K_1}} = \frac{2}{11}K_1 \tag{6.24}$$

The total transmissibility then amounts:

$$T_{12} = \frac{\frac{2}{11}K_1 A}{\frac{3}{2}L_1} = \frac{4}{33}\frac{K_1 \cdot A}{L_1} \approx 0.12\frac{K_1 \cdot A}{L_1} \tag{6.25}$$

Additionally, an adjustment for the cell and face center determination within the "dune-cornerpoint" methods was required. While Petrel [5] exports the grid geometry by specifying the eight corner-point coordinates of each cell, simulation programs initially determine the grid cell and face center points to ensure the mass/mole balance calculation between neighboring cells. The standard setting to determine the cell and face centers is the calculation of its centroids. In contrast, tests in DuMu$^{\mathrm{X}}$ have indicated, that the numerical accuracy and stability can be improved by determining the face center coordinates as the arithmetic mean of its four corner points:

$$x_{fc} = \frac{1}{4}\sum_{i=1}^{4} x_i, \quad y_{fc} = \frac{1}{4}\sum_{i=1}^{4} y_i, \quad z_{fc} = \frac{1}{4}\sum_{i=1}^{4} z_i \tag{6.26}$$

The cell centers are subsequently calculated by taking the arithmetic mean of the center points of the upper and lower faces:

$$x_{cc} = \frac{1}{2}\sum_{i=1}^{2} x_{fci}, \quad y_{cc} = \frac{1}{2}\sum_{i=1}^{2} y_{fci}, \quad z_{cc} = \frac{1}{2}\sum_{i=1}^{2} z_{fci} \tag{6.27}$$

This method is also suggested in Nilsen et al. [96] and is believed to be common in commercial reservoir simulators. Depending on the shape of the grid cell, the above introduced face and cell center determination methods result into considerable deviating results. This adjustment especially helped to improve the mass transfer between degenerate cells and its neighboring cells what can also be demonstrated on an example:

- In Fig. 6.9, a simplified grid with a "degenerate cell" in the center is shown. The length L is significantly longer when the centroid method is used. This results in a drastic underestimation of the transmissibility (cf. Eq. 6.20) in direction to grid cell 2 and 7 while the transmissibility in direction to grid cell 5 is overestimated. Due to the frequent occurrences of degenerate cells inside the processed grid, the arithmetic mean method (Eq. 6.26 and Eq. 6.27) for the face and cell center coordinate determination was used.

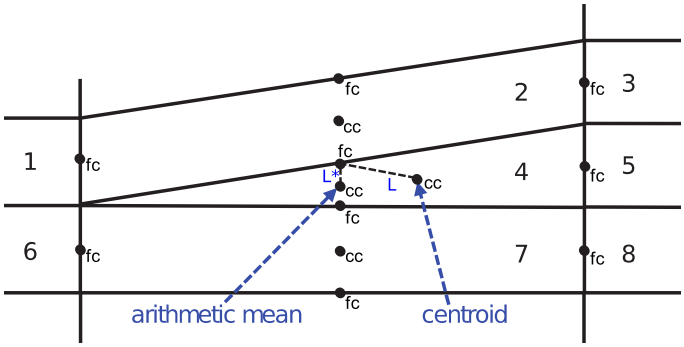

Figure 6.9: Sketch of a "degenerate cell": It can be seen that L and $L^\star$ significantly deviate for the different cell centers

6.1.7 Storage initialization

For the initialization of storage simulations a hydrostatic equilibrium is assumed. A reference pressure at the gas-water contact (GWC) and the depth of the GWC are defined. The phase pressures and saturations were calculated based on the pressure gradients and capillary pressure to saturation relation. The reservoir is separated into three zones as follows:

- In the *water zone*, which is below the GWC, the reservoir is saturated by 100% water. Hence, only water is mobile. The pressure gradient is related to the water pressure gradient:

$$P_w(z) = p_w^{\mathrm{GWC}} - \rho_w g(z^{\mathrm{GWC}} - z) \tag{6.28}$$

  The gas phase pressure within the water zone is the water pressure plus the entry capillary pressure:

$$P_g(z) = P_w(z) + P_c(1 - S_{gr}) \tag{6.29}$$

- In the *transition zone*, which is directly above the GWC, water is risen due to the capillary forces. Hence, both phases are mobile. The water phase pressure is again calculated by the water pressure gradient (Eq. 6.28) and the gas phase pressure is calculated by using the gas pressure gradient:

$$P_g(z) = p_w^{\mathrm{GWC}} + P_c(1 - S_{gr}) - \rho_g g(z^{\mathrm{GWC}} - z) \tag{6.30}$$

The saturation is calculated based on the capillary pressure, which is the difference between the gas and water pressure:

$$S_w(z) = S_w(P_g(z) - P_w(z)) \tag{6.31}$$

The inverse function of the Brooks-Corey correlation has been used to do so (cf. Eq. 4.7).

- In the *gas zone*, which is above the transition zone, the water saturation is equal to the irreducible water saturation. Hence, only the gas phase is mobile and the pressure gradient is related to the gas pressure gradient (Eq 6.32). The water pressure is the gas pressure minus the capillary pressure at this saturation:

$$P_w(z) = P_g(z) - P_c(S_{wr}) \tag{6.32}$$

The initial pressure and saturation distribution is schematically plotted in Fig. 6.10 and Fig. 6.11 where z is the vertical distance from the bottom of the reservoir. The method which is used to set the initial values of all

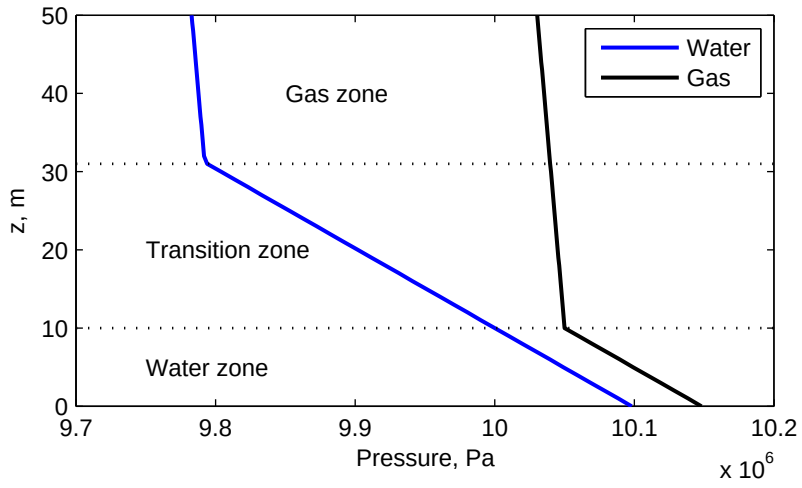

Figure 6.10: Initial pressure on the vertical axis

primary variables is listed in appendix A.2.

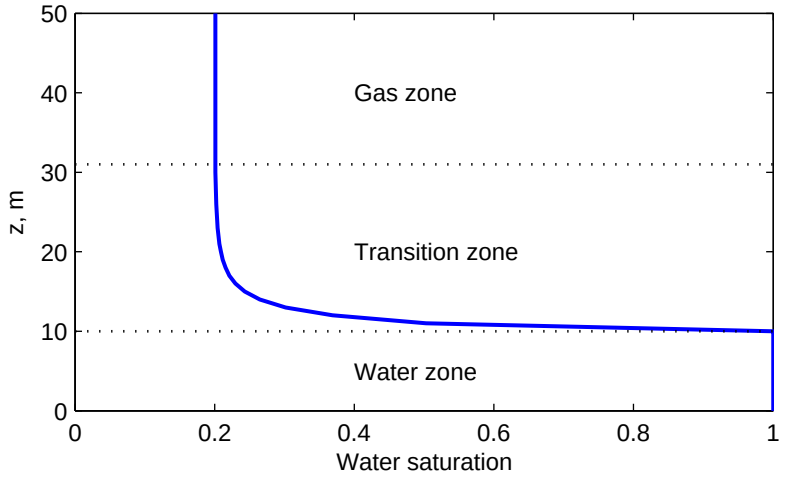

Figure 6.11: Initial water saturation on the vertical axis

6.1.8 Modeling of storage wells

The injection and production of fluids through storage wells is implemented as source/sink term. Two different types of well control mechanisms were implemented. For both it has to be differentiated between injector and producer.

6.1.8.1 Rate-controlled storage wells

For rate-controlled wells the (constant) rate is known. In the case of gas injection also the composition of the injected gas is known. Hence, a constant rate gas injection well can be modeled as:

$$\hat{Q}^k = c_g^{k,\mathrm{inj}} \hat{Q} \tag{6.33}$$

where $\hat{Q}$ is rate in $[mol/s]$, $c_g^{k,\mathrm{inj}}$ is the mole fraction of component k in the injected gas. A scaling is required to transform the point or line source to a volume source, where V_{gc} is the volume of the grid cell which contains the well:

$$q^k = \frac{\hat{Q}^k}{V_{gc}} \tag{6.34}$$

The internal method which is used to evaluate the source/sink terms for a (sub) control volume when H_2 is injected at a constant rate is listed in appendix A.3.

In the case of production the phase mobilities and concentrations of the components in the grid cell which contains the well have to be considered:

$$\hat{Q}^k = \hat{Q} \frac{\left(\lambda_g c_g^k + \lambda_w c_w^k\right)}{\sum_{i=1}^{n} \left(\lambda_g c_g^i + \lambda_w c_w^i\right)} \tag{6.35}$$

where the mobilities λ and the concentrations c are the current values in the grid cell. Again a scaling is required to transform the point or line source to a volume source.

An internal method is used again to evaluate the source/sink term for a (sub) control volume when mass is withdrawn at a constant rate (cf. appendix A.4).

6.1.8.2 Pressure-controlled storage wells

Pressure-controlled wells are realized by implementing Peaceman's approach [103]. In contrast of using a constant injection or production rate, Peaceman's well model automatically adjusts the amount of injected or extracted mass to the reservoir response. This can for example avoid an unrealistic high pressure in the near wellbore area by taking into account the mobilities of the fluids [25]. Peaceman was able to find a connection between the occurring grid cell pressure and the bottom-hole flowing pressure by introducing an equivalent radius. The quantity of the equivalent radius amounts to approximately one fifth of the average grid cell length. The simplest expression of Peaceman's well model is shown below and is valid for a homogeneous reservoirs and single-phase flow:

$$Q = \frac{2\pi\rho K_{xy} h_z}{\mu \left(\ln\left(\frac{r_e}{r_w}\right) + s\right)} \cdot \left(P_{\text{wf}} - P\right) \tag{6.36}$$

where Q is the injection or production rate in $[kg/s]$, ρ is the fluid density in $[kg/m^3]$, K_{xy} is the horizontal permeability of the grid cell containing the well in $[m^2]$, h_z is the grid cell height in $[m]$, μ is the fluid viscosity in

$[Pa \cdot s]$, r_e is the equivalent radius in $[m]$, r_w is the geometrical well radius in $[m]$ and s is the wellbore skin factor. Besides the physical behavior of the fluid density and viscosity, the difference of a defined bottom-hole flowing pressure P_{wf} and the actual reservoir pressure P in the well grid cell adjusts the amount of injected or extracted mass to the arising reservoir response. The multi-compositional two-phase flow formulation of the model for UHS requires the additional consideration of phase mobilities and concentrations of the components. Since the model is based on the balance of moles, a modification of the units is necessary. For injection, it is sufficient to consider the gas phase:

$$\hat{Q}^k = \frac{c_g^{k,\text{inj}} \rho_g k_{rg}}{\mu_g} \cdot \frac{2\pi K_{xy} h_z}{\ln\left(\frac{r_e}{r_w}\right) + s} \cdot (P_{\text{wf}} - P_g) \tag{6.37}$$

where $\hat{Q}$ is the injection or production rate in $[mol/s]$ and $c_g^{k,\text{inj}}$ is the composition of the injected gas. Molar density, dynamic viscosity and relative permeability are the actual values in the well grid cell. A scaling is again required to transform the point or line source to a volume source (cf. Eq. 6.34).

The C++ implementation is listed in appendix A.5:

For production both phases need to be considered:

$$\hat{Q}^k = \frac{2\pi K_{xy} h_z}{\ln\left(\frac{r_e}{r_w}\right) + s} \cdot \left(\frac{c_g^k \rho_g k_{rg}}{\mu_g} (P_{\text{wf}} - P_g) + \frac{c_w^k \rho_w k_{rw}}{\mu_w} (P_{\text{wf}} - P_w) \right) \tag{6.38}$$

where c_g^k and c_w^k in this case are also the actual values in the grid cell containing the well.

The internal method for pressure-controlled wells is listed in appendix A.6:

6.1.9 Operation schedule and time stepping

For the implementation of the cyclic operation of underground storages with alternating periods of injection, production and idle, it has to be switched between the different algorithms for injection and production wells or no well implementation. This can be done by splitting the simulation time

into episodes. The episodes are numbered consecutively by an index and the length of each episode can be individually defined. Based on the index of the current episode it can be distinguished between the different well algorithms.

DuMu$^{\mathrm{X}}$ has an adaptive selection of the time step length by defining only the initial time step. The selection of the time step length is based on a target number of newton iterations. If the number of iterations was more than the target number, the next time step will be shorter. If the number of iterations was less than the target number, the next time step will be longer. However, tests have shown that some restrictions have to be made. At first, a maximum time step length has to be set. Dependent on the model and the used parameters a value around two days has proved to be suitable. Additionally, a reduction of the time step length was implemented after each change in the storage operation. A reduction to one-tenth of the maximum time step length was experienced to be a good choice.

6.1.10 Material balance error

The numerical simulations performed in this thesis intend to predict gas and consequently energy losses due to the bio-chemical reactions which are in the single digit percentage range. Consequently, the errors in the simulations which are unavoidable in numerical approximations need to be sufficiently small. The used numerical formulation is generally mass (or mole) conservative, however, small material balance errors might still occur. The fluid state which includes the phase equilibrium and phase densities is updated in each Newton iteration. After that, the new values for the primary variables are obtained by solving the linear equation system. Hence, the saturations and concentrations do not necessarily sum up exactly to one and an error in the material balance might occur. The magnitude of this error can be controlled by the convergence criterion which was selected as the maximum relative error with a value smaller than 10^{-10}. A larger value for the convergence criterion would potentially result in a larger material balance error.

A calculation of the material balance error was implemented to verify that the predicted gas losses are reliable. To do so this error (also referred to as

residual) for H_2 was calculated after each time step in the following way:

$$\text{MBE}^{H_2} = \sum_i R^{H_2} = \sum_i \phi C^{H_2,t} V - \sum_i \phi C^{H_2,t+1} V - \sum_i q^{H_2,t+1} V \Delta t \quad (6.39)$$

where $C^{H_2} = \rho_g c_g^{H_2} S_g + \rho_w c_w^{H_2} S_w$, $\sum_i$ is the sum over all grid cells, V is the volume of the grid cell and q is the source/sink term which includes injection/production and the bio-chemical consumption. In addition, the cumulative material balance error was calculated as:

$$\begin{aligned} \text{cumulative MBE}^{H_2} = & \sum_i \phi C^{H_2,t_{\text{final}}} V - \sum_i \phi C^{H_2,t_0} V \\ & - \sum_t \sum_i q^{H_2,t+1} V \Delta t \end{aligned} \quad (6.40)$$

where $\sum_t$ is the sum over all time steps.

In Fig. 6.12 the material balance error is shown for the 3D simulation study in section 6.2.3 (with 100 *mol*% H_2 injection and methanogenesis). It can be

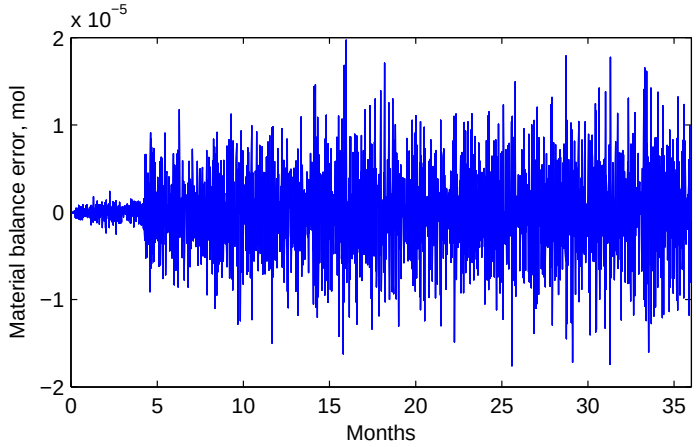

Figure 6.12: Material balance error versus time (3D study with 100 *mol*% H_2 injection and methanogenesis)

seen that the error oscillates randomly around zero. The maximum absolute error during one time step with a value around $2 \cdot 10^{-5}$ *mol* is quite low. The cumulative material balance error with a value of $5.7 \cdot 10^{-6}$ *mol* is even lower because the positive and negative errors balance each other. As the gas inventory in this simulation study is in the order of 10^9 *mol* the material balance error is much less than acceptable.

6.1.11 Post-processing and visualization

After each time step or at selected points in time, DuMu^{X} writes the grid information combined with the values of the primary variables and other selected secondary variables into a output file using the VTK format [117]. ParaView [60] was used to visualize the results and to generate spatial plots of the variables.

In addition to that, an algorithm was developed which evaluates general information after each time step. Values as e.g. the injection/production rate, the average gas phase pressure, the produced hydrogen concentration and the total reaction rate are determined and written into separate output files. A Matlab script was used to read these files and to generate different time dependent plots.

6.2 Case studies

Based on the numerical model different simulation studies are performed in the following sections. The simulation study in section 6.2.1 investigates the process of gas-water displacement during the development process of an UHS in an aquifer or in a depleted gas reservoir which had a strong water influx. The second study in section 6.2.2 investigates the influence of mechanical dispersion and the coupled bio-reactive effects when methanogenic archaea and sulfate-reducing bacteria are present. Finally, in section 6.2.3 a storage scenario is simulated in a realistic three-dimensional reservoir which considers the coupled hydrodynamic and bio-reactive effects of methanogenic archaea.

6.2.1 Gas-water displacement in a 2D synthetic reservoir

The simulation in this section aims to investigate the lateral spreading of hydrogen compared to methane. The simulation study was performed in dimensionless form. The used characteristic parameters are summarized in Table 6.3. The parameters result in a characteristic time of:

Table 6.3: List of characteristic parameters

Characteristic parameter	Symbol	Value	Unit
Pressure	$P^\star$	$6 \cdot 10^6$	Pa
Density	$\bar{\rho}^\star$	10	kg/m^3
Viscosity	$\mu^\star$	$1 \cdot 10^{-5}$	$Pa \cdot s$
Diffusion coefficient	$D^\star$	$1 \cdot 10^{-6}$	m^2/s
Length	L	500	m
Permeability	$K^\star$	100	mD
Molar density	$\rho^\star$	5000	mol/m^3
Gravity acceleration	$g^\star$	9.81	m/s^2

$$t^\star = \frac{L^2 \mu^\star}{K^\star P^\star} \approx 48.2 days \tag{6.41}$$

The geometry is two dimensional and represents a vertical slice through an anticline structure (cf. section 6.1.5). The initialization was done in hydrostatic equilibrium by defining the gas-water contact at a certain depth with a dimensionless pressure of 1 (cf. section 6.1.7). The initial gas saturation is shown in Fig. 6.13a. The upper and lower boundaries of the reservoir were set by Neumann conditions with no flow across. The left and right boundaries were defined by Dirichlet conditions using the initial values.

Two different simulation cases were set up. In the first case hydrogen was injected into a reservoir containing an initial amount of hydrogen while in the second case methane was injected into a reservoir containing an initial amount of methane. The injection of pure H_2 or pure CH_4 takes place at the top center of the reservoir at a constant rate. Each case was simulated at 10 different injection rates, ranging from very low to very high.

The interpretation of the simulation results lead to the division into three different displacement regimes which are caused by either the domination of gravitational forces or the domination of viscous forces or their combined action. For low injection rates the behavior is controlled by gravitational forces. In this case the gas-water contact lowers evenly and remains horizontal. In Fig. 6.13b the gas saturation is shown for the hydrogen case with a dimensionless rate of $\hat{\bar{Q}} = 1 \cdot 10^{-5}$ after a dimensionless time of $\tau = 108$. No differences were detected for the injection of methane at the same rate.

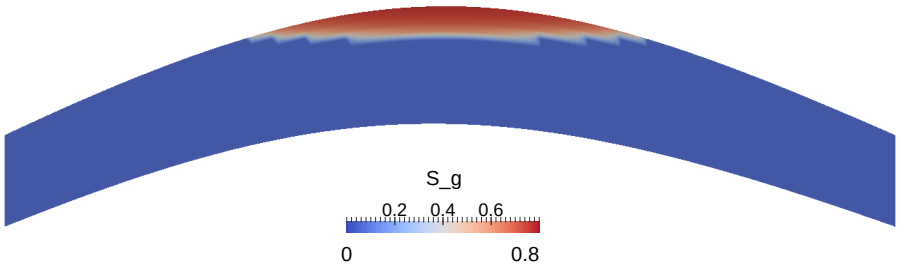

(a) Initial gas saturation

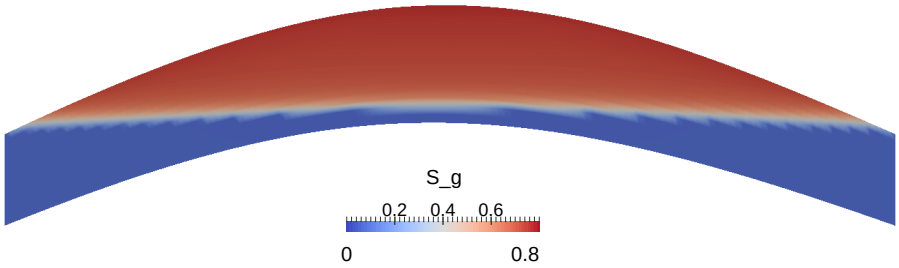

(b) Gas saturation after injecting pure H_2 with a low dimensionless rate ($\bar{\hat{Q}} = 1 \cdot 10^{-5}$) at a dimensionless time of $\tau = 108$

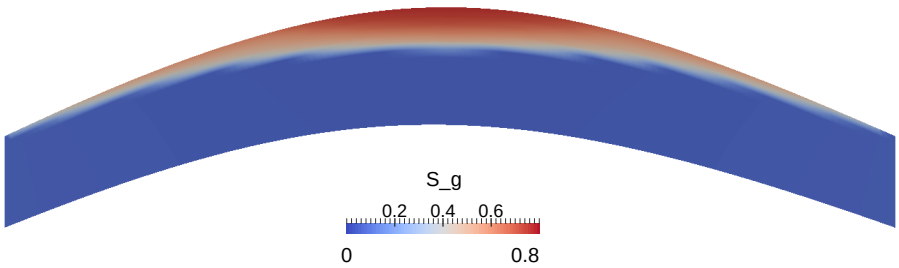

(c) Gas saturation after injecting pure H_2 with a medium dimensionless rate ($\bar{\hat{Q}} = 2 \cdot 10^{-4}$) at a dimensionless time of $\tau = 1.04$

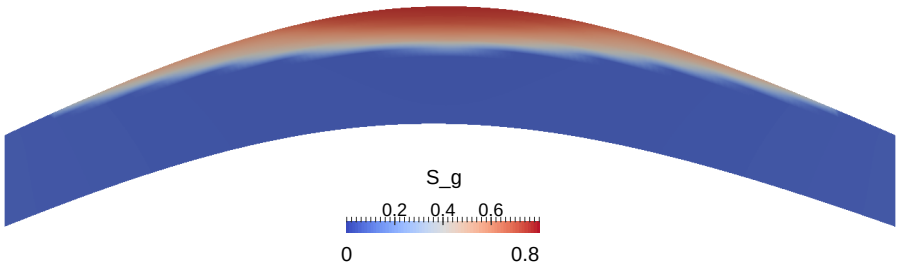

(d) Gas saturation after injecting pure CH_4 with a medium dimensionless rate ($\bar{\hat{Q}} = 2 \cdot 10^{-4}$) at a dimensionless time of $\tau = 1.04$

Figure 6.13: Gas injection into the top center of a synthetic two-dimensional anticline structure

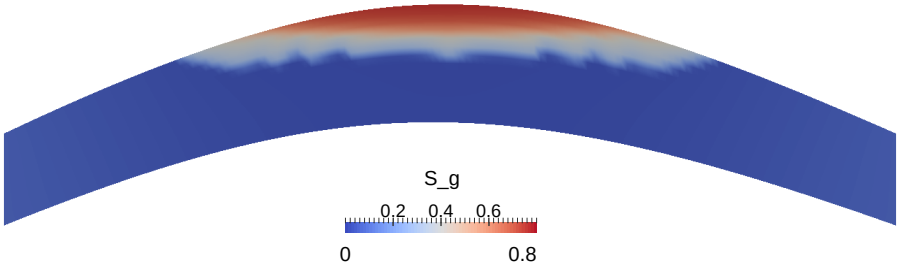

(e) Gas saturation after injecting pure H_2 with a high dimensionless rate ($\bar{\hat{Q}} = 1 \cdot 10^{-2}$) at a dimensionless time of $\tau = 0.05$

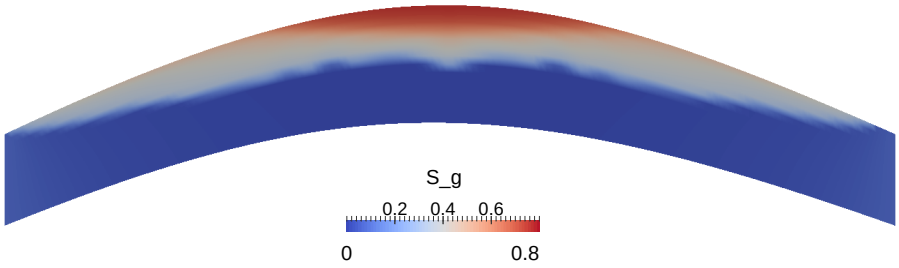

(f) Gas saturation after injecting pure H_2 with a high dimensionless rate ($\bar{\hat{Q}} = 1 \cdot 10^{-2}$) at a dimensionless time of $\tau = 0.128$

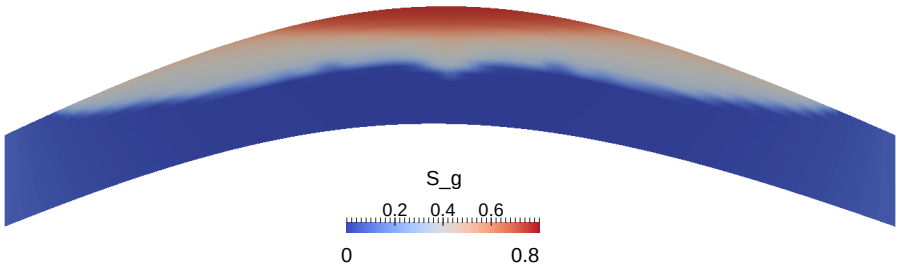

(g) Gas saturation after injecting pure CH_4 with a high dimensionless rate of ($\bar{\hat{Q}} = 1 \cdot 10^{-2}$) at a dimensionless time of $\tau = 0.128$

Figure 6.12: Gas injection into the top center of a synthetic two-dimensional anticline structure (continued)

A different regime was observed for medium injection rates (cf. Fig. 6.13c and Fig. 6.13d). In this case gravitational and viscous forces were influencing the behavior of the gas. The gas-water contact lowered only slightly in the middle part while the gas spreads laterally below the cap rock. The comparison of Fig. 6.13c and Fig. 6.13d indicates that the lateral spreading of hydrogen is faster than that of methane.

For high injection rates, the viscous forces were dominant. Initially the

gas-water contact lowered more or less evenly (cf. Fig. 6.13e). However, the displacement took place at relatively low gas saturation (grey region). Subsequently, the vertical displacement almost stopped and lateral fingering started to propagate towards the left and right boundaries. Again it could be observed that the lateral spreading of hydrogen was faster than that of methane (cf. Fig. 6.13f and Fig. 6.13g).

6.2.2 Storage scenario in a 2D synthetic reservoir

A storage scenario was simulated in the same two-dimensional grid model. The used numerical model, which is again formulated dimensionless, includes six components (H_2, CO_2, CH_4, H_2O, H_2S, and SO_4^{2-}) and two microbial species (methanogenic archaea and sulfate-reducing bacteria). The reservoir is initialized in a hydrostatic equilibrium (cf. section 6.1.7), however, the initial GWC is defined in a greater depth than before. The initial gas saturation is shown in Fig. 6.13. The initial gas is composed of 80

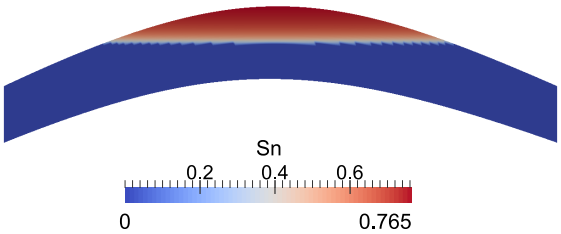

Figure 6.13: Initial gas saturation (2D study)

mol% CH_4 and 20 *mol*% CO_2. Some SO_4^{2-} is dissolved in the initial water (0.18 *mol*%). The boundary conditions and the characteristic parameters are equivalent to the previous case study. The microbial growth functions used in this study are the double Monod model (cf. Eq. 4.28 and Eq. 4.30). For the decay an increasing rate is used (cf. Eg. 4.20). CO_2 consumption and production as a source of carbon was neglected. The used dimensionless microbial kinetic parameters for methanogenic archaea and sulfate-reducing bacteria are within the range of the values from the literature search in section 4.6. For the dimensionless formulation the maximum specific growth rates and the decay coefficients are divided by the characteristic time. A summary of the parameters is listed in Table 6.4.

Table 6.4: List of dimensionless microbial kinetic parameters

Parameter	Symbol	Value
Methanogenic archaea		
Maximum specific growth rate	$\psi_{M,\max}^{\text{growth}}$	$3.6 \cdot 10^{-12}$
H_2 half-velocity constant	$\alpha_{M,1}$	$1.1 \cdot 10^{-7}$
CO_2 half-velocity constant	$\alpha_{M,2}$	$3.2 \cdot 10^{-6}$
Dimensionless coefficient	$\delta_{M,e}$	$1.1 \cdot 10^{-3}$
Decay coefficient	b_M	$5.5 \cdot 10^{-13}$
Sulfate-reducing bacteria		
Maximum specific growth rate	$\psi_{S,\max}^{\text{growth}}$	$4.8 \cdot 10^{-12}$
H_2 half-velocity constant	$\alpha_{S,1}$	$5.0 \cdot 10^{-8}$
SO_4^{2-} half-velocity constant	$\alpha_{S,2}$	$1.8 \cdot 10^{-6}$
Dimensionless coefficient	$\delta_{S,e}$	$1.7 \cdot 10^{-5}$
Decay coefficient	b_S	$5.5 \cdot 10^{-13}$

The total dimensionless simulation time is 22, during which three operation cycles are carried out. The alternating periods of injection and production are interrupted by idle periods. Each of these periods lasts for a dimensionless time of 2. The storage is operated by one well which is located at the top center of the anticline structure. The injected gas is composed of 100 $mol\%$ H_2. The injection and production rates are constant and have a dimensionless value of $2.8 \cdot 10^{-4}$, respectively.

Three different cases were simulated and compared. The base case was simulated without mechanical dispersion and bio-reactive influences. The second case was simulated with mechanical dispersion and in the third case the bio-reactive effects of methanogenic archaea and sulfate-reducing bacteria were included.

In Fig. 6.14 the H_2 concentration in the gas phase is shown for the base case after the first injection and the first idle period. It can be seen that a region with a high H_2 concentration was created around the storage well. The injected H_2 tends to override the initial gas and predominately spreads below the cap rock. Also during the idle period the H_2 "bubble" further rises and spreads below the cap rock. This behavior, which was already

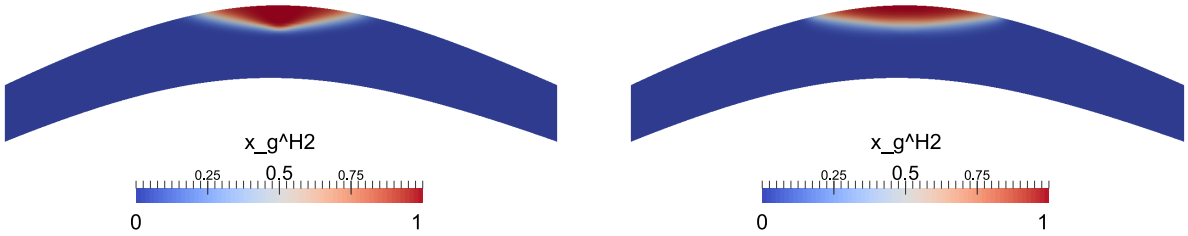

(a) H_2 mole fraction after $\tau = 2$ **(b)** H_2 mole fraction after $\tau = 4$

Figure 6.14: H_2 mole fraction for the base case after the first injection and the first idle period

discussed in the literature review, originated from the lower density and viscosity of H_2 compared to the initial gas in this study. In Fig. 6.15 the same plots are shown for the simulation with mechanical dispersion. A clear

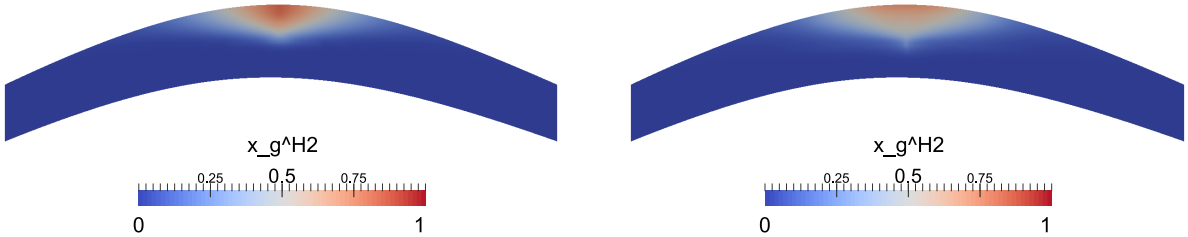

(a) H_2 mole fraction after $\tau = 2$ **(b)** H_2 mole fraction after $\tau = 4$

Figure 6.15: H_2 mole fraction for the case with mechanical dispersion after the first injection and the first idle period

difference can be seen. In the simulation with mechanical dispersion the region around the well has a lower H_2 concentration while the zone, where the injected H_2 is mixed with the initial gas, is larger. It can be concluded that the mixing by mechanical dispersion has a strong influence at the occurring flow velocities in this study. As a consequence, the subsequently produced gas has a much lower H_2 concentration than in the simulation without mechanical dispersion (cf. Fig. 6.21). In Fig. 6.16 the H_2 concentrations for the simulation with included bio-reactive effects are shown after the first injection and the first idle period. Again a clear difference can be observed compared to the base case. With included bio-reactive effects the region which is highly concentrated by H_2 is smaller and additionally the diffusive H_2 front is much more sharp. The behavior can be explained by observing the microbial density. In Fig. 6.17 the microbial densities of methanogenic

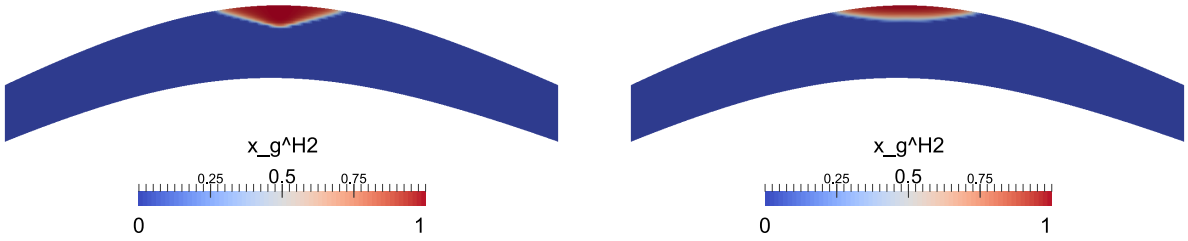

(a) H_2 mole fraction after $\tau = 2$ **(b)** H_2 mole fraction after $\tau = 4$

Figure 6.16: H_2 mole fraction for the case with bio-reactive effects after the first injection and the first idle period

archaea and sulfate-reducing bacteria are shown after a dimensionless time of 0.3. Both species started to grow and have created a spot with high

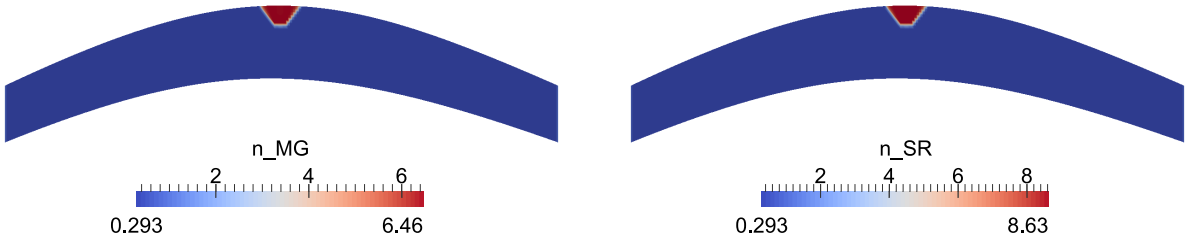

(a) Dimensionless density of methanogenic archaea **(b)** Dimensionless density of sulfate-reducing bacteria

Figure 6.17: Microbial densities after $\tau = 0.3$

microbial densities around the storage well. Fig. 6.18 shows the microbial densities after the first injection period whereat the region with high microbial densities has traveled like a wave away from the storage well. The

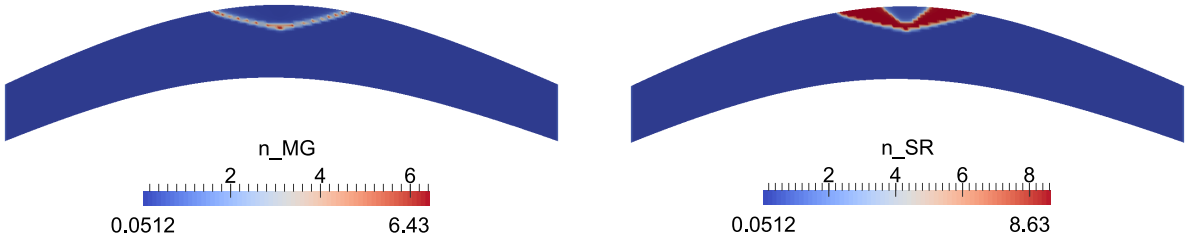

(a) Dimensionless density of methanogenic archaea after $\tau = 2$ **(b)** Dimensionless density of sulfate-reducing bacteria after $\tau = 2$

Figure 6.18: Microbial densities after the first injection period

position of these waves with high microbial densities is exactly the position

of the H_2 concentration front. At this diffusive front the microorganisms have access to both substrates: The injected H_2 and the initially present CO_2 or SO_4^{2-}. Behind the front the electron acceptor (CO_2 or SO_4^{2-}) is quickly consumed and the microorganisms become inactive. The concentration of the products from the bio-reactions (CH_4 and H_2S) are plotted in Fig. 6.19 after the first injection period. The methanogenesis results in a

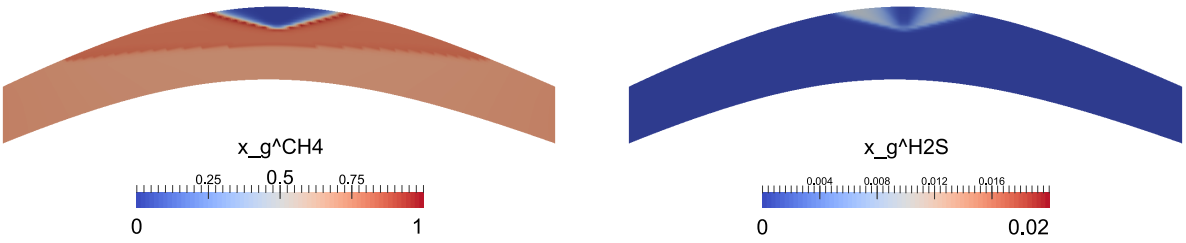

(a) CH_4 mole fraction after $\tau = 2$ **(b)** H_2S mole fraction after $\tau = 2$

Figure 6.19: Mole fraction of the reaction products after the first injection period

line with a high CH_4 concentration ($> 95\ mol\%$) ahead the H_2 front. The sulfate-reducing bacteria create a larger region with a small H_2S concentration. Also the produced gas stream contains up to 0.6 $mol\%$ H_2S (cf. Fig. 6.20). The H_2 losses, which occur due to the bio-chemical reactions,

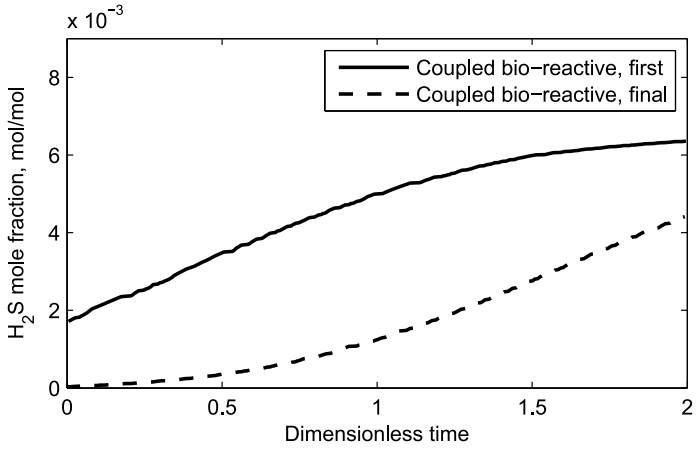

Figure 6.20: H_2S concentration in the produced gas stream (2D study)

can be also recognized by plotting the H_2 concentration in the produced gas stream shown in Fig. 6.21 and the hysteresis shown in Fig. 6.22. In the coupled bio-reactive simulation the produced H_2 concentration is up to 30 percentage points less than in the base case. Especially a faster decrease in

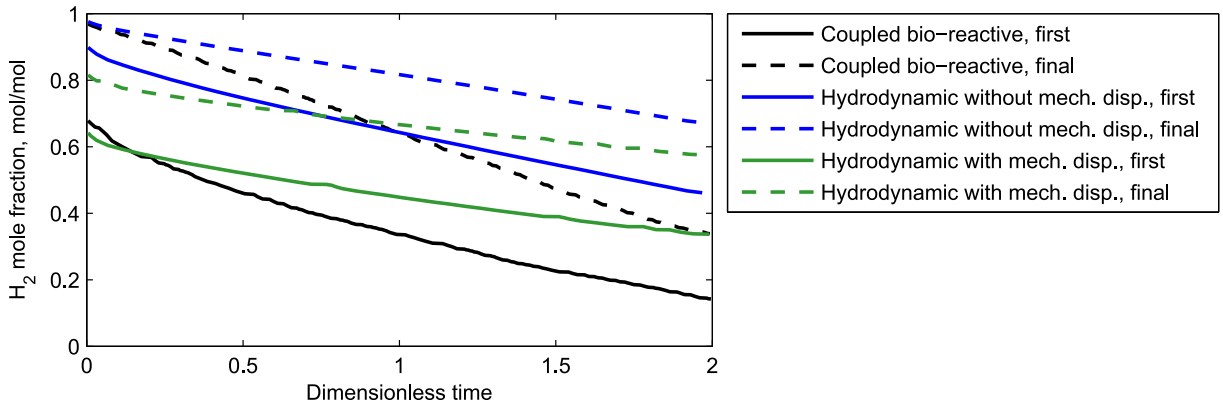

Figure 6.21: H_2 concentration in the produced gas stream (2D study)

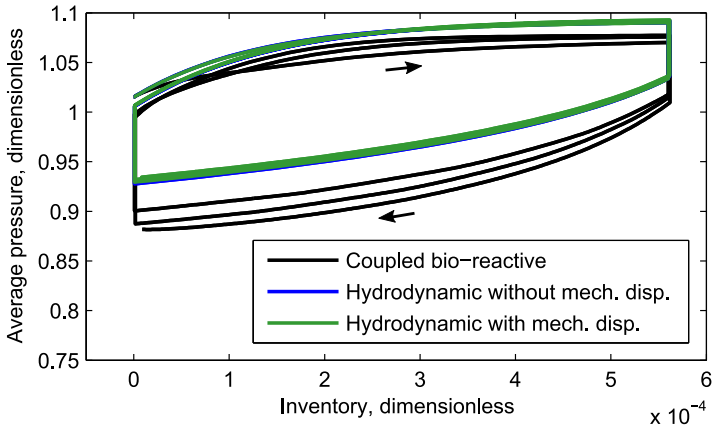

Figure 6.22: Hysteresis plot: Gas inventory versus average gas phase pressure (2D study)

the H_2 concentration can be observed when bio-reactions are included. The hysteresis plot, which shows the development of gas inventory versus the average reservoir pressure, is in practice used to identify gas losses. For the two purely hydrodynamic simulations the value of inventory versus pressure travels during the three storage cycles on the same circular path around (in Fig. 6.22 the blue line is almost hidden behind the green line). Hence, it can be identified that no gas was lost. However, for the coupled bio-reactive simulation the value of inventory versus average pressure is always below and additionally decreases from cycle to cycle. Hence, recognizable gas losses can be identified. In appendix B additional spatial plots of the gas saturations, gas component concentrations and microbial densities are shown after the first injection, the first idle and the first production period.

6.2.3 Storage scenario in a 3D realistic reservoir

Another case study was performed in the three-dimensional grid model which represents a fragment of a real gas reservoir (cf. section 6.1.5). This study was simulated with dimensions. The storage scenario was initialized in hydrostatic equilibrium as explained in section 6.1.7. The GWC was defined in a depth of 3452.3 m with a reference pressure of 170 bar. The temperature is set to 125 $°C$. The initial gas phase pressure and the initial gas saturation are shown in Fig. 6.23 and Fig. 6.24. The initial gas is

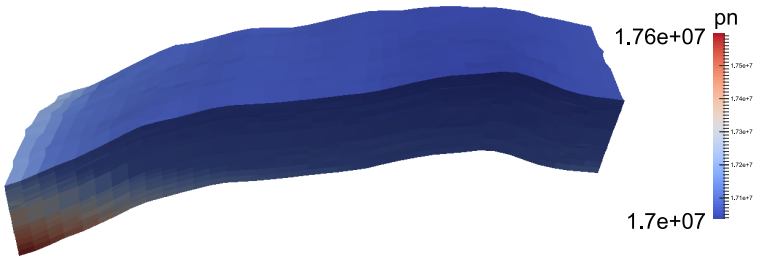

Figure 6.23: Initial gas phase pressure in $[Pa]$ (3D study)

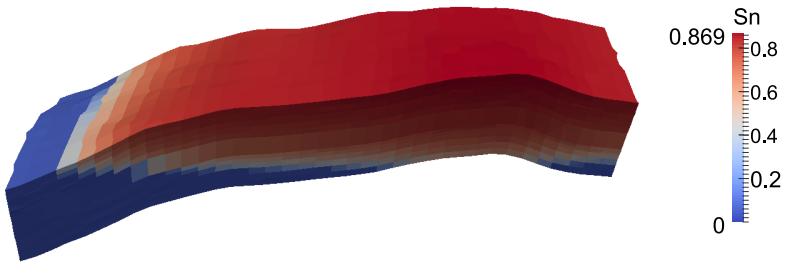

Figure 6.24: Initial gas saturation (3D study)

composed of 79 mol% N_2, 20 mol% CH_4 and 1 mol% CO_2. All boundaries are defined with no flow across by using Neumann conditions.

The storage is operated by one storage well which is bottom-hole pressure-controlled using Peaceman's well model as described in section 6.1.8.2. The well model is included in 10 grid cells which are marked in Fig. C.1a by the black bars. The scenario was simulated for a total time of three years. The first year is the storage development during which the storage is filled with hydrogen or a H_2/CO_2 mixture. The step-wise fill-up by three injection

periods of two months was interrupted by idle periods of two months. The bottom-hole flowing pressure of the injection well is thereby increased in the following way: First injection period with 200 *bar*, second injection period with 230 *bar*, third injection period with 260 *bar*. Subsequently, two years of cyclic operation were simulated. The injection periods have again a duration of two months which are controlled by a bottom-hole flowing pressure of 290 *bar*. The production periods have a duration of one month and are controlled by a bottom-hole flowing pressure of 240 *bar*. Between the changes from injection to production and vise versa idle periods of half a month are included. Hence, a total number of six storage cycles was simulated.

A total number of four simulations were run with different settings for the injected gas composition and the initial number of microorganisms. The injected gas consists two times out of 100 $mol\%$ H_2 and two times out of a mixture with 95 $mol\%$ H_2 and 5 $mol\%$ CO_2. Each of these scenarios was run one time with no microorganisms and one time with a value of $9 \cdot 10^{12}$ $1/m^3$ for the initial microbial density of methanogens. Hence, a comparison between the purely hydrodynamic and the coupled bio-reactive behavior was performed for two different injected gas compositions.

The growth function which was used for these simulations is the double Monod model (cf. Eq. 4.28). For the decay an increasing rate is used (cf. Eg. 4.20). The used microbial kinetic parameters, which are again within the range of the values from the literature search in section 4.6, are summarized in Table 6.5. The CO_2 consumption as a source of carbon and the related CO_2 production during decay is again neglected. In Fig. 6.25 to Fig. 6.28

Table 6.5: List of microbial kinetic parameters

Parameter	Symbol	Value	Unit
Maximum specific growth rate	$\psi_{M,\max}^{\text{growth}}$	$1.5 \cdot 10^{-5}$	$1/s$
H_2 half-velocity constant	$\alpha_{M,1}$	$1.1 \cdot 10^{-7}$	mol/mol
CO_2 half-velocity constant	$\alpha_{M,2}$	$3.2 \cdot 10^{-6}$	mol/mol
Yield coefficient	$Y_{M,e}$	$1.7 \cdot 10^{12}$	$1/mol$
Decay coefficient	b_M	$2.3 \cdot 10^{-6}$	$1/s$

observation plots are shown to evaluate and compare the two simulations

with 100 $mol\%$ H_2 injection. In Fig. 6.25 the injection and production rates are shown versus time. A positive value means injection while a negative

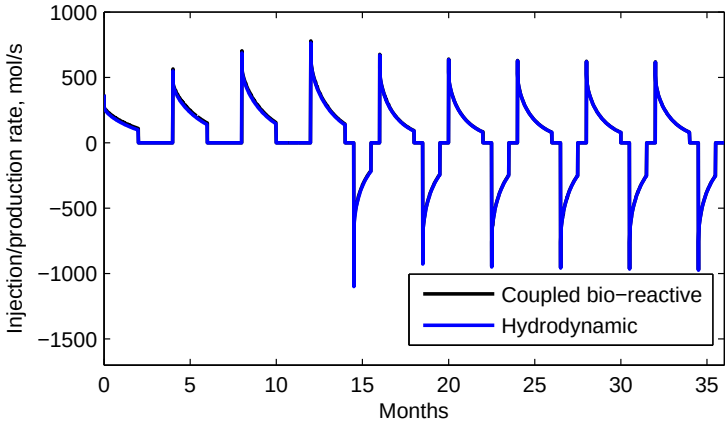

Figure 6.25: Rate versus time: A positive rate refers to injection and a negative rate refers to withdrawal (3D study with 100 mol% H_2 injection)

value means production. The average injection rate is around 225 mol/s and the average production rate around 400 mol/s. Fig. 6.26 shows the average reservoir pressure versus time. A stepwise increase of the pressure up to ap-

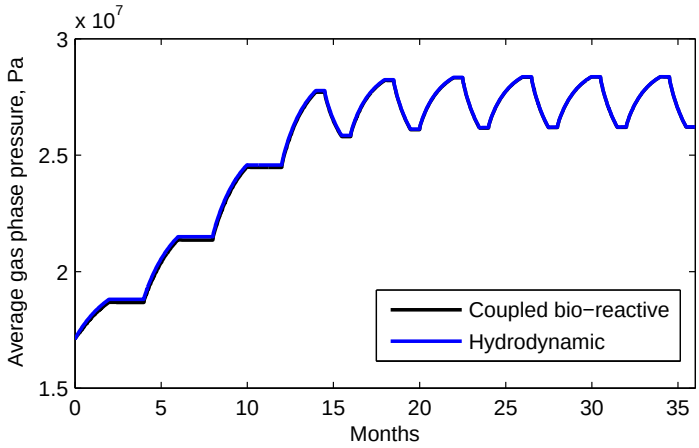

Figure 6.26: Average gas phase pressure versus time (3D study with 100 $mol\%$ H_2 injection)

proximately 280 bar can be observed during the first four injection periods. Subsequently during the cyclic operation, the pressure varies between 260 and 280 bar. For both plots no clear deviation between the purely hydrodynamic and the coupled bio-reactive simulation can be observed. However, a clear difference can be observed in the hysteresis plot (Fig. 6.27) and the

hydrogen concentration in the produced gas stream (Fig. 6.28). In the

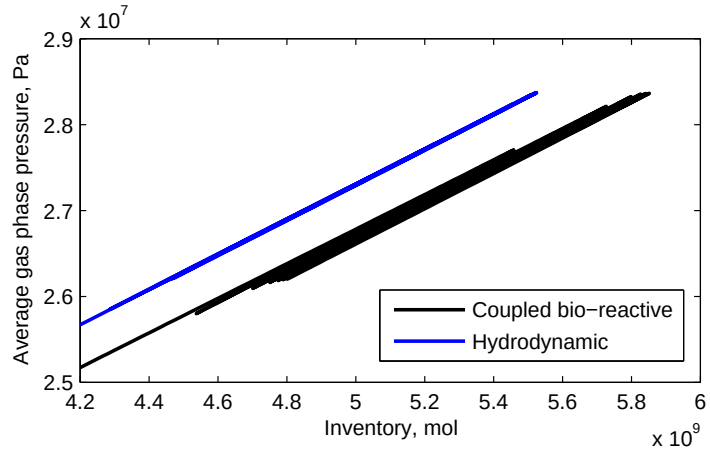

Figure 6.27: Hysteresis plot: Gas inventory in $[mol]$ versus average gas phase pressure (3D study)

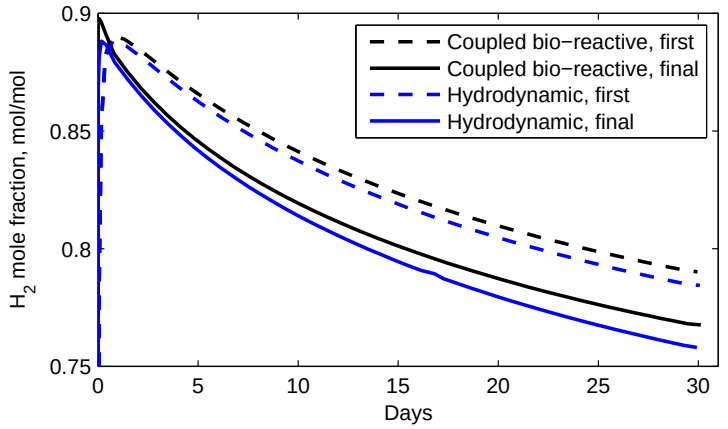

Figure 6.28: H_2 concentration in the withdrawn gas stream (3D study with 100 $mol\%$ H_2 injection)

hysteresis plot it can be seen that for the purely hydrodynamic simulation the value moves up and down on the same line what means that no gas was lost. This is obvious because all boundaries are closed and no reactions occur. In contrast, for the coupled bio-reactive simulation the value moves slightly to the right during each operation cycle what means that gas losses occured. Additionally, it can be observed that the inventory, when the cyclic operation starts, is not the same for both simulations. This is due to the gas losses which occur in the coupled bio-reactive simulation already during the development period. Fig. 6.28 shows the hydrogen concentration in the

produced gas stream for the first and the final production period. During each production period the produced H_2 concentration decreases with time. The average is around 80 – 85 $mol\%$. For the coupled bio-reactive simulation the produced H_2 concentration is always a bit higher. In contrast, in the previous two-dimensional study the produced H_2 concentration was lower in the bio-reactive simulation. However, here the initial CO_2 concentration is much lower so that the overall influence of the bio-chemical reactions is much less. Still the mixing between the different gas components is reduced by the microbial activity at the diffusive front what results in an increased H_2 concentration in the produced gas. Fig. 6.29 shows the total reaction rate in terms of $mol(H_2)/s$ versus time. Two effects can be recognized from

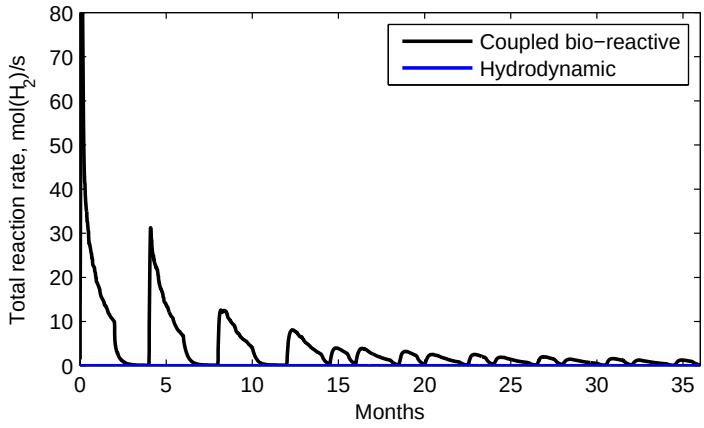

Figure 6.29: Total bio-chemical reaction rate versus time (3D study with 100 $mol\%$ H_2 injection)

this plot. At first the rate is high at the beginning but decreases with time. Secondly, the reaction rate is only high in periods of injection or production. During idle periods almost no hydrogen is consumed. The total amount of hydrogen which is consumed by the microorganisms during three years is $3.7 \cdot 10^8$ mol (or 8.3 million Sm^3). This is an already recognizable amount because it is around 13.4 % of the working gas volume (when 50 % of the inventory at 280 bar is considered as working gas). However, in terms of energy the losses are less because the consumption of hydrogen leads to a production of methane in the ratio $4:1$. The molar energy density of H_2 compared to CH_4 is around $1:3$ and consequently only one sixth of the energy gets lost by this bio-chemical reaction. The summed up energy losses are 4.1 GWh what is 2.2 % of the working gas energy content (when the working gas consists out of 100 $mol\%$ H_2). A positive effect is the increas-

ing energy density of the storage by this reaction which results is a larger storage capacity.

Spatial plots for the gas component concentrations and the microbial density of methanogenic archaea are shown after 2, 14 and 36 months in appendix C.1. For the purely hydrodynamic simulation it can be observed that H_2 displaces the initial gas and a circular region with a high H_2 concentration arises around the storage well. The size of this region varies in the different storage layers what can be explained by the different conductivities. The zone where the injected H_2 mixes with the initial gas enlarges during time and finally involves some hundred meters around the storage well. The difference to the coupled bio-reactive study is not very pronounced in the spatial plots. However, it can be observed that a ring-shaped region with a high microbial density arises around the storage well. The reason for this behavior is the regional exposure of the microorganisms to both substrates (H_2 and CO_2) and consequently the start of growth. This region of high microbial activity travels with the diffusive H_2 front. In the CH_4 concentration plots a slight increase of the concentration can be observed at the current position of high microbial activity. The maximum CH_4 concentration with 21.5 $mol\%$ is slightly higher than the initial one.

In the second comparison, where a mixture of H_2 and CO_2 is injected, the influence of the bio-chemical reactions is much more pronounced. In Fig. 6.30 it can be seen that the injection rate in the coupled bio-chemical simulation is always a bit higher than in the purely hydrodynamic simulation. In contrast, the production rate is always a bit lower in the coupled bio-chemical simulation. This effect, which originates from the large gas losses, can be also recognized in Fig. 6.31 where the average gas phase pressure of the coupled bio-chemical simulation is always a bit less. A very strong difference can be seen in the hysteresis plot (Fig. 6.32). The difference in the inventory, when the first storage cycle starts, is already more than $1 \cdot 10^9$ mol. Further losses around $2 \cdot 10^8$ mol can be recognized during each storage cycle. Also the differences in the produced H_2 concentration shown in Fig. 6.33 are stronger. At the beginning of both shown production periods the H_2 concentration is around 5 percentage points less than in the coupled bio-reactive simulation. In Fig. 6.34 it can be seen that the total bio-chemical reaction rate is very high during each injection period. Only a small decrease in the total reaction rate can be observed from one injection period to the next. The total amount of hydrogen which is consumed by

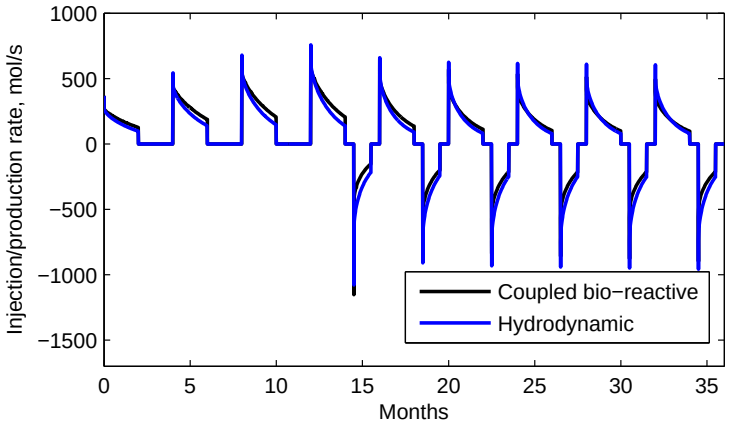

Figure 6.30: Rate versus time: A positive rate refers to injection and a negative rate refers to withdrawal (3D study with 95 $mol\%$ H_2 and 5 $mol\%$ CO_2 injection)

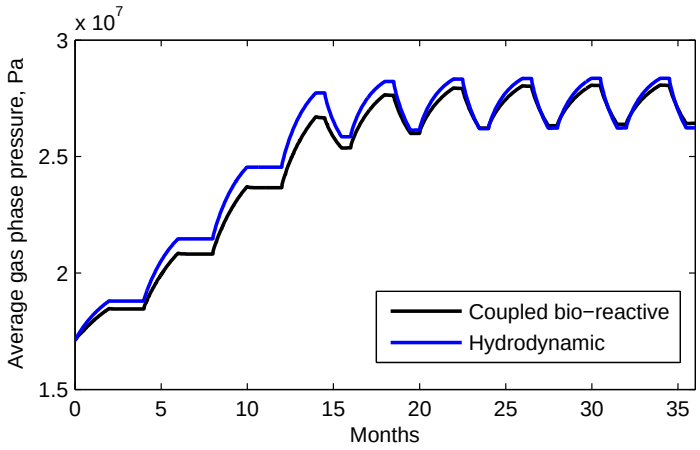

Figure 6.31: Average gas phase pressure versus time (3D study with 95 $mol\%$ H_2 and 5 $mol\%$ CO_2 injection)

the microorganisms is $3.1 \cdot 10^9$ mol (or 69 million Sm^3) what is 112.7 % of the working gas. In terms of energy losses this is around 34.7 GWh (18.8 % of the storage capacity).

The spatial plots for the gas component concentrations and the density of methanogenic archaea are shown after 2, 14 and 36 months in appendix C.1. The difference compared to the study with 100 $mol\%$ H_2 injection is an additional small spot with a high microbial density which arises in the vicinity of the injection well. The injected CO_2 is quickly almost totally consumed and the consequent methane production leads to recognizable higher methane

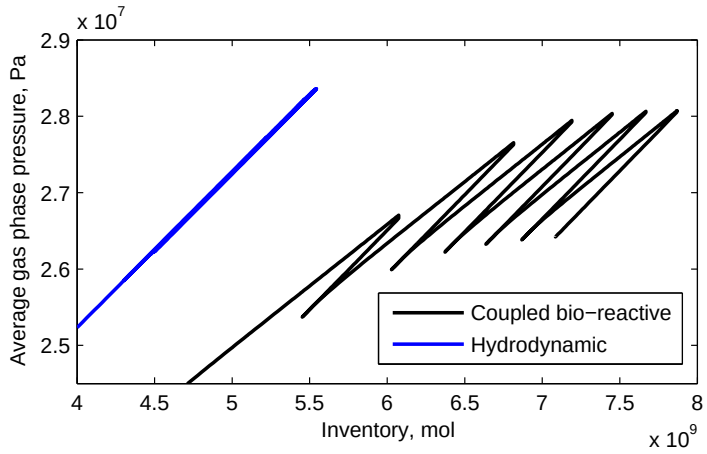

Figure 6.32: Hysteresis plot: Gas inventory in $[mol]$ versus average gas phase pressure (3D study with 95 $mol\%$ H_2 and 5 $mol\%$ CO_2 injection)

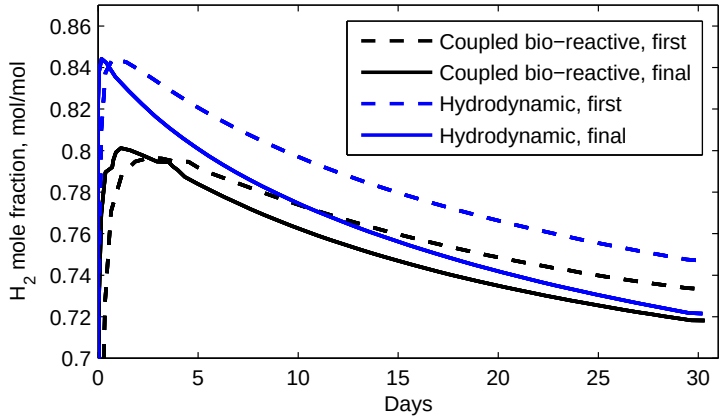

Figure 6.33: H_2 concentration in the withdrawn gas stream (3D study with 95 $mol\%$ H_2 and 5 $mol\%$ CO_2 injection)

concentrations in the reservoir.

6.3 Summary and conclusions

- The mathematical model from chapter 4 was numerically implemented on the basis of DuMu$^{\text{X}}$. The governing equations in DuMu$^{\text{X}}$ were adapted and adjustments were conducted concerning the additional components and the grid. Several new algorithms were implemented

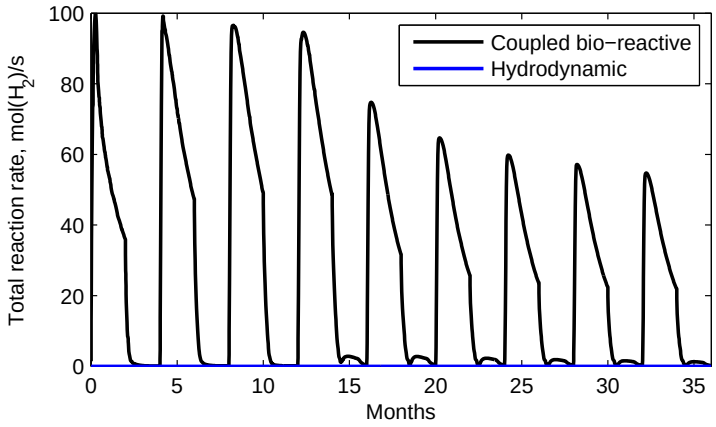

Figure 6.34: Total bio-chemical reaction rate versus time (3D study with 95 $mol\%$ H_2 and 5 $mol\%$ CO_2 injection)

for the storage initialization, fluid injection and production, post-processing and so on.

- The simulation study of gas injection into a 2D synthetic reservoir shows some significant differences depending on the injection rate. For low injection rates, gravitational forces are dominant and the displacement of water is uniform. However, for higher injection rates, the viscous forces become dominant and the displacement becomes unstable. Lateral gas fingers start to propagate below the cap rock toward the left and right boundaries of the reservoir. It has been shown that hydrogen spreads laterally faster than methane.

- The simulated storage scenario in the 2D synthetic reservoir identifies the importance of mechanical dispersion and the bio-chemical reactions in such predictive simulation studies. The mixing zone between the initial gas and the injected gas becomes much larger when mechanical dispersion is included. As a consequence, the predicted hydrogen concentration in the produced gas stream is around 15 percentage points less than in the simulation without mechanical dispersion. In the coupled bio-reactive simulation, microorganisms start to grow quickly when hydrogen is injected into the reservoir. The initially occurring spot with a high microbial density around the injection point spreads out into the reservoir like a wave. The highest microbial activity is always at the H_2 concentration front where the microorganisms have access to both substrates. The bio-chemical reactions lead to con-

siderable productions of CH_4 and H_2S in the reservoir. Consequently, the H_2 concentration in the produced gas stream is much lower than in the simulation without bio-chemical effects. Also a considerable amount of H_2S will be produced.

- A realistic storage scenario was simulated in the 3D grid model. The simulations indicate that the behavior can be characteristically different dependent on the injected gas composition. When pure H_2 is injected, only at the beginning bio-chemical reactions have a strong influence. The electron acceptor (in this case CO_2) is depleted very soon and the reaction rates become very low. The resulting summed up energy losses during three years simulation are around 2.2 % of the storage capacity. However, when a gas mixture out of H_2 and CO_2 is injected the bio-chemical reaction rates remain high because the reservoir is recharged with both substrates during each injection period. In this case the summed up energy losses during three years of simulation are around 18.8 % of the storage capacity.

Chapter 7

Conclusions

The work in this thesis was structured in four parts: The analytical modeling of gravity-driven displacement, the development of the mathematical model for bio-reactive two-phase transport, the analysis of the stability of the dynamic system and the numerical modeling of storage cycles. Each of these chapters has its individual detailed conclusions in sections 3.9, 4.7, 5.5 and 6.3. Summarized the following conclusions can be drawn:

- Compared to the underground storage of natural gas, which is established since many years, UHS shows some significant differences. Hydrogen has a very low density and viscosity which involves a high tendency for an instable displacement including gravity overriding and viscous fingering when water is displaced. When a residual gas is displaced, a strong mixing by molecular diffusion and especially by mechanical mixing occurs between the gases with different compositions. In addition to the hydrodynamic effects, hydrogen is a universal electron donor for the metabolism of different microbial species which are present in subsurface structures. Hence, the injection of hydrogen stimulates their activity and problems could arise. Four different hydrogenotrophic species could be important for UHS: Methanogenic archaea, acetogenic archaea, sulfate-reducing bacteria, and iron-reducing bacteria. All these processes have to be considered for the numerical modeling of UHS operations. None of the existing simulation tools for flow and transport processes in underground reservoirs or porous media is able to reflect all these effects in its original version.

- An alternative storage operation method, which avoids the lateral spreading of hydrogen, was introduced. The so called ”selective technology” implies the hydrogen injection at the bottom of a subsurface structure with low-permeable or impermeable horizontal barriers. The

hydrogen gas is produced back when it reaches the cap rock. The delay in the gas rising plays a key role in this method. Analytical and numerical investigations demonstrated the possibility of this operation method. It was shown that gas accumulations arise below the barriers resulting in a significant reduction of rising velocity. The exact rising velocity can be obtained from the analytical solution. The one-dimensional analytical solution was confirmed by a comparison to the two-dimensional numerical solution.

- A mathematical model for the bio-reactive two-phase flow in UHS was developed on continuum scale. The model couples the hydrodynamic processes (advection, molecular diffusion and mechanical dispersion) with the microbial population dynamics and bio-chemical reactions. Four metabolic processes are included: Methanogenesis, sulfate-reduction, homoacetogenesis and iron-reduction. Parameters for the microbiological effects were provided from a literature search.

- Related to the observations from a former town gas storage, the stability of the coupled mathematical model was investigated. The analytical analysis indicates the possibility for temporal and spatial oscillations in the gas component concentrations and microbial density when a mixture of H_2 and CO_2 is injected. Numerical simulations under particular derived conditions have demonstrated this behavior. In such a way the underground storage behaves as a bio-reactor.

- The mathematical model for bio-reactive two-phase transport in UHS was numerically implemented on the basis of the numerical simulator DuMu$^{\mathrm{X}}$. Several simulation studies were performed in synthetic two-dimensional and in realistic three-dimensional geological models. It was shown that the low density and viscosity of hydrogen make the displacement of water more instable than in the case of methane injection. The simulation of different storage scenarios has proven that mechanical dispersion and bio-chemical reactions have an important influence in predictive studies. Significant energy losses could occur due to bio-chemical reactions. Especially, the energy losses are very high when a gas mixture of H_2 and CO_2 is injected. Also it was demonstrated in one of the storage scenarios that H_2S is produced by sulfate-reducing bacteria and the produced gas gets acidic.

- It was shown that the developed numerical tool can be used for predictive studies of the coupled hydrodynamic and bio-reactive behavior of UHS. Such studies would be required by gas storage companies for the planning and operation of underground hydrogen storages. However, a history match should be performed to validate the model before it is used for reliable predictive studies. In this way the uncertain parameters, as e.g. the microbial kinetic parameters and the dispersivities, can be determined by comparing the simulation results to the observed data from the field. A validation of the model could not be performed within this thesis, because field data are not available to date.

Bibliography

[1] COMSOL Multiphysics. https://www.comsol.de/. Accessed: 2016-12-14.

[2] Differential Equations Math 244, Fall 2012. http://people.whitman.edu/~hundledr/courses/M244F12/M244.html. Accessed: 2016-08-17.

[3] Distributed and Unified Numerics Environment. http://dune-project.org/. Accessed: 2016-02-19.

[4] Open Porous Media. http://opm-project.org/. Accessed: 2016-02-19.

[5] Schlumberger. https://www.software.slb.com/products/petrel. Accessed: 2016-06-22.

[6] T. Ahmed et al. *Reservoir engineering handbook*. Gulf Professional Publishing, 2006.

[7] W. Badziong and R.K. Thauer. Growth yields and growth rates of desulfovibrio vulgaris (marburg) growing on hydrogen plus sulfate and hydrogen plus thiosulfate as the sole energy sources. *Archives of Microbiology*, 117(2):209–214, 1978.

[8] J.E. Bailey and D.F. Ollis. Biochemical engineering fundamentals. *Chemical Engineering Education*, 1976.

[9] O. Basso, P. Caumette, and M. Magot. Desulfovibrio putealis sp. nov., a novel sulfate-reducing bacterium isolated from a deep subsurface aquifer. *International journal of systematic and evolutionary microbiology*, 55(1):101–104, 2005.

[10] P. Bastian, M. Blatt, A. Dedner, C. Engwer, R. Klöfkorn, M. Ohlberger, and O. Sander. A generic grid interface for parallel and adaptive scientific computing. Part I: Abstract framework. *Computing*, 82(2–3):103–119, 2008.

[11] S. Bauer and A. Dahmke. *Unterirdische geologische Energiespeicher und Raumplanung des Untergrunds, das Projekt ANGUS+.* Project launch invitation, 2013.

[12] S. Bauer, A. Gubik, M. Pichler, A.P. Loibner, K. Scherr, J. Schritter, G. Mori, K. Vidic, and R. Tichler. Underground Sun Storage: Erneuerbare Energie untertage speichern. *energie wasser-praxis*, (9):50–54, 2014.

[13] L.K. Baumgartner, R.P. Reid, C. Dupraz, A.W. Decho, D.H. Buckley, J.R. Spear, K.M. Przekop, and P.T. Visscher. Sulfate reducing bacteria in microbial mats: Changing paradigms, new discoveries. *Sedimentary Geology*, 185(3):131–145, 2006.

[14] S. Becker and A. Kuznetsov. *Heat Transfer and Fluid Flow in Biological Processes.* Academic Press, 2014.

[15] P. Bedrikovetsky. *Mathematical theory of oil and gas recovery: with applications to ex-USSR oil and gas fields*, volume 4. Springer Science & Business Media, 1993.

[16] F.C. Boait, N.J. White, M.J. Bickle, R.A. Chadwick, J.A. Neufeld, and H.E. Huppert. Spatial and temporal evolution of injected CO2 at the Sleipner Field, North Sea. *Journal of Geophysical Research: Solid Earth (1978–2012)*, 117(B3), 2012.

[17] J.O. Bockris. A hydrogen economy. *Science (New York, NY)*, 176(4041):1323, 1972.

[18] R.H. Brooks and A.T. Corey. Hydraulic properties of porous media and their relation to drainage design. *Transactions of the ASAE*, 7(1):26–0028, 1964.

[19] S.E. Buckley and M.C. Leverett. Mechanism of fluid displacement in sands. *Transactions of the AIME*, 146(01):107–116, 1942.

[20] U. Bünger and O. Kruck. Overview and public launch of the HyUnder project. HyUnder Project Launch Conference, 2012.

[21] F. Buzek, V. Onderka, P. Vančura, and I. Wolf. Carbon isotope study of methane production in a town gas storage reservoir. *Fuel*, 73(5):747–752, 1994.

[22] P.O. Carden and L. Paterson. Physical, chemical and energy aspects of underground hydrogen storage. *International Journal of Hydrogen Energy*, 4(6):559–569, 1979.

[23] J.F. Carriere, G. Fasanino, M.R. Tek, et al. Mixing in underground storage reservoirs. In *SPE Annual Technical Conference and Exhibition*. Society of Petroleum Engineers, 1985.

[24] F.H. Chapelle, J.L. Zelibor, D.J. Grimes, and L.L. Knobel. Bacteria in deep coastal plain sediments of Maryland: a possible source of CO2 to groundwater. *Water Resources Research*, 23(8):1625–1632, 1987.

[25] Z. Chen. *Reservoir Simulation: Mathematical Techniques in Oil Recovery*, volume 77. SIAM, 2007.

[26] H. Class, R. Helmig, and P. Bastian. Numerical simulation of nonisothermal multiphase multicomponent processes in porous media.: 1. An efficient solution technique. *Advances in Water Resources*, 25(5):533–550, 2002.

[27] R. Cord-Ruwisch, H.-J. Seitz, and R. Conrad. The capacity of hydrogenotrophic anaerobic bacteria to compete for traces of hydrogen depends on the redox potential of the terminal electron acceptor. *Archives of Microbiology*, 149(4):350–357, 1988.

[28] J. Cordazzo, C.R. Maliska, and A.F.C. Silva. Interblock transmissibility calculation analysis for petroleum reservoir simulation. In *2nd Meeting on Reservoir Simulation, Universidad Argentina de la Empresa, Buenos Aires, Argentina, November*, pages 5–6, 2002.

[29] F. Crotogino, S. Donadei, U. Bünger, and H. Landinger. Large-scale hydrogen underground storage for securing future energy supplies. In *18th World hydrogen energy conference*, pages 16–21, 2010.

[30] H. Cypionka. *Grundlagen der Mikrobiologie*. Springer-Verlag, 2010.

[31] L.P. Dake. *Fundamentals of reservoir engineering*, volume 8. Elsevier, 1983.

[32] A. Dedner, R. Klöfkorn, and M. Nolte. The DUNE-ALUGrid module. *arXiv preprint arXiv:1407.6954*, 2014.

[33] D.N. Dietz. A theoretical approach to the problem of encroaching and by-passing edge water. In *Proc*, pages 83–92, 1953.

[34] W.S. Dockins, G.J. Olson, G.A. McFeters, and S.C. Turbak. Dissimilatory bacterial sulfate reduction in montana groundwaters. *Geomicrobiology Journal*, 2(1):83–98, 1980.

[35] P. Dornseiffer, B. Meyer, and E. Heinzle. Modeling of anaerobic formate kinetics in mixed biofilm culture using dynamic membrane mass spectrometric measurement. *Biotechnology and Bioengineering*, 45(3):219–228, 1995.

[36] DVGW. *Arbeitsblatt G262: Nutzung von Gasen aus regenerativen Quellen in der öffentlichen Gasversorgung*, 2011.

[37] M. Dworkin, S. Falkow, E. Rosenberg, K.-H. Schleifer, and E. Stackebrandt. *The Prokaryotes Third Edition - A handbook on the biology of bacteria: Ecophysiology and Biochemistry*. Springer, 2006.

[38] A. Ebigbo, F. Golfier, and M. Quintard. A coupled, pore-scale model for methanogenic microbial activity in underground hydrogen storage. *Advances in Water Resources*, 61:74–85, 2013.

[39] S.O. Elferink, R.N. Maas, H. Harmsen, and A.J. Stams. Desulforhabdus amnigenus gen. nov. sp. nov., a sulfate reducer isolated from anaerobic granular sludge. *Archives of microbiology*, 164(2):119–124, 1995.

[40] S.O. Elferink, A. Visser, L.W.H. Pol, and A.J. Stams. Sulfate reduction in methanogenic bioreactors. *FEMS Microbiology Reviews*, 15(2-3):119–136, 1994.

[41] V.M. Entov and A. Zazovsky. Nonlinear waves in physicochemical hydrodynamics of enhanced oil recovery. Multicomponent flows. In *International Conference on Porous Media: Physics, Models, Simulation, Moscow*. World Scientific, 1997.

[42] F. Feldmann, B. Hagemann, L. Ganzer, and M. Panfilov. Numerical simulation of hydrodynamic and gas mixing processes in underground hydrogen storages. *Environmental Earth Sciences*, 75(16):1165, 2016.

[43] B. Flemisch, M. Darcis, K. Erbertseder, B. Faigle, A. Lauser, K. Mosthaf, S. Müthing, P. Nuske, A. Tatomir, M. Wolff, et al. DuMu^x: DUNE for multi-{phase, component, scale, physics,...} flow and transport in porous media. *Advances in Water Resources*, 34(9):1102–1112, 2011.

[44] Federal Minitry for Education and Research. Förderinitiative Energiespeicher. http://www.bmbf.de/foerderungen/16431.php, 2011. Accessed: 2013-06-15.

[45] C. Ganser and B. Eng. New energy storage concept for renewable energies in the form of potential energy storage. *Techniken zur Energiewende*, page 70, 2013.

[46] L. Ganzer, V. Reitenbach, D. Pudlo, M. Panfilov, D. Albrecht, R. Gaupp, et al. The H2STORE project-experimental and numerical simulation approach to investigate processes in underground hydrogen reservoir storage. In *EAGE Annual Conference & Exhibition incorporating SPE Europec*. Society of Petroleum Engineers, 2013.

[47] T.R. Ginn, B.D. Wood, K.E. Nelson, T.D. Scheibe, E.M. Murphy, and T.P. Clement. Processes in microbial transport in the natural subsurface. *Advances in Water Resources*, 25(8):1017–1042, 2002.

[48] P. Glendinning. *Stability, instability and chaos: An introduction to the theory of nonlinear differential equations*, volume 11. Cambridge university press, 1994.

[49] F. Golfier, B.D. Wood, L. Orgogozo, M. Quintard, and M. Buès. Biofilms in porous media: development of macroscopic transport equations via volume averaging with closure for local mass equilibrium conditions. *Advances in Water Resources*, 32(3):463–485, 2009.

[50] J. Guckenheimer and P. Holmes. *Nonlinear oscillations, dynamical systems, and bifurcations of vector fields*, volume 42. Springer Science & Business Media, 2013.

[51] B. Hagemann. Hydrodynamics of Hydrogen in Underground Storages. Master thesis, Clausthal University of Technology, 2013.

[52] B. Hagemann, M. Panfilov, and L. Ganzer. Modelling bio-reactive transport in underground hydrogen storages - Spatial separation of gaseous components. In *ECMOR XV-15th European Conference on the Mathematics of Oil Recovery*, 2016.

[53] B. Hagemann, M. Panfilov, and L. Ganzer. Multicomponent gas rising through water with dissolution in stratified porous reservoirs - Application to underground storage of H2 and CO2. *Journal of Natural Gas Science and Engineering*, 31:198 – 213, 2016.

[54] B. Hagemann, M. Rasoulzadeh, M. Panfilov, L. Ganzer, and V. Reitenbach. Hydrogenization of underground storage of natural gas-impact of hydrogen on bio-chemical transformations of stored gas. In *ECMOR XIV-14th European Conference on the Mathematics of Oil Recovery*, 2014.

[55] B. Hagemann, M. Rasoulzadeh, M. Panfilov, L. Ganzer, and V. Reitenbach. Mathematical modeling of unstable transport in underground hydrogen storage. *Environmental Earth Sciences*, 73(11):6891–6898, 2015.

[56] B. Hagemann, M. Rasoulzadeh, M. Panfilov, L. Ganzer, and V. Reitenbach. Hydrogenization of underground storage of natural gas. *Computational Geosciences*, 20(3):595–606, 2016.

[57] S.A. Haveman, E.L. Nilsson, and K. Pedersen. Regional distribution of microbes in groundwater from hastholmen, kivetty, olkiluoto and romuvaara, finland. *Helsinki, Finland: Posiva Oy, Report POSIVA*, 6:35, 2000.

[58] Z.E. Heinemann. *Introduction to Reservoir Simulation.* Montanunivertät Leoben, 2005.

[59] R. Helmig. *Multiphase flow and transport processes in the subsurface: A contribution to the modeling of hydrosystems.* Springer-Verlag, 1997.

[60] A. Henderson, J. Ahrens, C. Law, et al. *The ParaView Guide.* Kitware Clifton Park, NY, 2004.

[61] Jeremy Norman's HistoryofInformation.com. An early vision of transhumanism, and the first proposal of a hydrogen-based renewable

energy economy. http://www.historyofinformation.com/expanded.php?id=4107, 2013. Accessed: 2013-06-15.

[62] C.K. Ho and S.W. Webb. *Gas transport in porous media*, volume 20. Springer, 2006.

[63] A. Husain. Mathematical model of the kinetics of anaerobic digestio - a selected review. *Biomass Bioenergy*, 14(5-6):561–571, 1998.

[64] HyUnder. Assessment of the potential, the actors and relevant business cases for large scale and long term storage of renewable electricity by hydrogen underground storage in europe. Executive Summary HyUnder, 2012.

[65] E.J. Jones, M.A. Voytek, M.D. Corum, and W.H. Orem. Stimulation of methane generation from nonproductive coal by addition of nutrients or a microbial consortium. *Applied and Environmental Microbiology*, pages 7013–7022, 2010.

[66] I. Kalfas. Dynamics of cortical networks segregated into layers and columns. 2015.

[67] A. Kantzas, J. Bryan, and S. Taheri. *FUNDAMENTALS OF FLUID FLOW IN POROUS MEDIA*. PERM Inc., 2016.

[68] F. Karadagli and B.E. Rittmann. Kinetic characterization of methanobacterium bryantii moh. *Environmental science & technology*, 39(13):4900–4905, 2005.

[69] T. Katayama, H. Yoshioka, Y. Muramoto, J. Usami, K. Fujiwara, S. Yoshida, Y. Kamagata, and S. Sakata. Physicochemical impacts associated with natural gas development on methanogenesis in deep sand aquifers. *The ISME journal*, 9(2):436–446, 2015.

[70] J. Kepplinger, F. Crotogino, S. Donai, and M. Wohlers. Present trends in compressed air energy and hydrogen storage in germany. In *Solution Mining Research Institute Fall Technical Conference*, 2011.

[71] S.K. Khanal. Anaerobic biotechnology for bioenergy production. *Iowa: Wiley-Blackwell. p*, 179, 2008.

[72] W. Kleinitz and E. Boehling. Underground gas storage in porous media–operating experience with bacteria on gas quality (SPE94248). In *67th EAGE Conference & Exhibition*, 2005.

[73] O. Kolditz, S. Bauer, L. Bilke, N. Böttcher, J.-O Delfs, T. Fischer, U.J. Görke, T. Kalbacher, G. Kosakowski, C.I. McDermott, et al. Opengeosys: An open-source initiative for numerical simulation of thermo-hydro-mechanical/chemical (THM/C) processes in porous media. *Environmental Earth Sciences*, 67(2):589–599, 2012.

[74] S. Kotelnikova and K. Pedersen. Evidence for methanogenic archaea and homoacetogenic bacteria in deep granitic rock aquifers. *FEMS Microbiology Reviews*, 20(3-4):339–349, 1997.

[75] O.R. Kotsyurbenko, M.V. Glagolev, A.N. Nozhevnikova, and R. Conrad. Competition between homoacetogenic bacteria and methanogenic archaea for hydrogen at low temperature. *FEMS Microbiology Ecology*, 38(2-3):153–159, 2001.

[76] J.K. Kristjansson, P. Schönheit, and R.K. Thauer. Different ks values for hydrogen of methanogenic bacteria and sulfate reducing bacteria: an explanation for the apparent inhibition of methanogenesis by sulfate. *Archives of Microbiology*, 131(3):278–282, 1982.

[77] B.H. Kueper and E.O. Frind. An overview of immiscible fingering in porous media. *Journal of Contaminant Hydrology*, 2(2):95–110, 1988.

[78] J.P. Laille, C. Coulomb, M.R. Tek, et al. Underground storage in Cerville-Velaine, France: A case history in conversion and inert gas injection as cushion substitute. In *SPE Annual Technical Conference and Exhibition*. Society of Petroleum Engineers, 1986.

[79] A.L. Lee, M.H. Gonzalez, and B.E. Eakin. The viscosity of natural gases. *Journal of Petroleum Technology*, 18(08):997–1, 1966.

[80] W. Leonhard. *Energiespeicher in Stromversorgungssystemen mit hohem Anteil erneuerbarer Energieträger: Bedeutung, Stand der Technik, Handlungsbedarf*. VDE, ETG Task Force Energiespeicher, 2008.

[81] D.R. Lovley and E.J.P. Phillips. Competitive mechanisms for inhibition of sulfate reduction and methane production in the zone of ferric

iron reduction in sediments. *Applied and Environmental Microbiology*, 53(11):2636–2641, 1987.

[82] Computer Modeling Group Ltd. CMG user's guide. 2012.

[83] X. Luo, J. Wang, M. Dooner, and J. Clarke. Overview of current development in electrical energy storage technologies and the application potential in power system operation. *Applied Energy*, 137:511 – 536, 2015.

[84] R.M. Maier, I.L. Pepper, and C.P. Gerba. *Environmental microbiology*, volume 397. Academic press, 2009.

[85] K.U. Mayer, D.W. Blowes, and E.O. Frind. Reactive transport modeling of an in situ reactive barrier for the treatment of hexavalent chromium and trichloroethylene in groundwater. *Water Resources Research*, 37(12):3091–3103, 2001.

[86] R.D. Megee III, J.F. Drake, A.G. Fredrickson, and H.M. Tsuchiya. Studies in intermicrobial symbiosis. saccharomyces cerevisiae and lactobacillus casei. *Canadian journal of microbiology*, 18(11):1733–1742, 1972.

[87] J. Monod. The growth of bacterial cultures. *Annual Reviews in Microbiology*, 3(1):371–394, 1949.

[88] D. Morozova, M. Zettlitzer, D. Let, H. Würdemann, et al. Monitoring of the microbial community composition in deep subsurface saline aquifers during CO2 storage in Ketzin, Germany. *Energy Procedia*, 4:4362–4370, 2011.

[89] A. Moser. *Bioprocess Technology: Kinetics and Reactors*. Springer, 1988.

[90] G. Müller-Syring, M. Henel, W. Köppel, H. Mlaker, M. Sterner, and T. Höcher. Entwicklung von modularen Konzepten zur Erzeugung, Speicherung und Einspeisung von Wasserstoff und Methan ins Erdgasnetz. *DVGW Deutscher Verein des Gas-und Wasserfaches e.V., Bonn*, 2013.

[91] G. Müller-Syring, M. Henel, H. Krause, H. Rasmusson, H. Mlaker, W. Köppel, T. Höcher, M. Sterner, and T. Trost. Power-to-gas: Entwicklung von Anlagenkonzepten im Rahmen der DVGW-Innovationsoffensive. *Artikel aus gwf-Gas/Erdgas November*, pages 770–777, 2011.

[92] E.M. Murphy and T.R. Ginn. Modeling microbial processes in porous media. *Hydrogeology Journal*, 8(1):142–158, 2000.

[93] J.D. Murray. *Mathematical Biology II: Spatial Models and Biomedical Applications, vol. 18 of Interdisciplinary Applied Mathematics*. Springer-Verlag New York Incorporated, 2001.

[94] J.D. Murray. *Mathematical Biology I: An Introduction, vol. 17 of Interdisciplinary Applied Mathematics*. Springer-Verlag New York Incorporated, 2002.

[95] R. Nethe-Jaenchen and R.K. Thauer. Growth yields and saturation constant of desulfovibrio vulgaris in chemostat culture. *Archives of microbiology*, 137(3):236–240, 1984.

[96] H.M. Nilsen, J.R. Natvig, K.-A. Lie, et al. Accurate modeling of faults by multipoint, mimetic, and mixed methods. *SPE Journal*, 17(02):568–579, 2012.

[97] C.M. Oldenburg. Carbon dioxide as cushion gas for natural gas storage. *Energy & Fuels*, 17(1):240–246, 2003.

[98] G.J. Olson, W.S. Dockins, G.A. McFeters, and W. Iverson. Sulfate-reducing and methanogenic bacteria from deep aquifers in Montana. *Geomicrobiology Journal*, 2(4):327–340, 1981.

[99] F.M. Orr. *Theory of gas injection processes*. Tie-Line Publications Copenhagen, 2007.

[100] M. Panfilov. Underground storage of hydrogen: In situ self-organisation and methane generation. *Transport in porous media*, 85(3):841–865, 2010.

[101] L. Paterson. Radial fingering in a hele shaw cell. *Journal of Fluid Mechanics*, 113(1):513–529, 1981.

[102] L. Paterson. The implications of fingering in underground hydrogen storage. *International journal of hydrogen energy*, 8(1):53–59, 1983.

[103] D.W. Peaceman et al. Interpretation of well-block pressures in numerical reservoir simulation (includes associated paper 6988). *Society of Petroleum Engineers Journal*, 18(03):183–194, 1978.

[104] K. Pedersen. Preliminary investigations of deep ground water microbiology in swedish granitic rock. *SKB Tech. Rep.*, 88(1):22, 1987.

[105] D.-Y. Peng and D.B. Robinson. A new two-constant equation of state. *Industrial & Engineering Chemistry Fundamentals*, 15(1):59–64, 1976.

[106] L. Petrie, N.N. North, S.L. Dollhopf, D.L. Balkwill, and J.E. Kostka. Enumeration and characterization of iron (iii)-reducing microbial communities from acidic subsurface sediments contaminated with uranium (vi). *Applied and environmental microbiology*, 69(12):7467–7479, 2003.

[107] W.T. Pfeiffer and S. Bauer. Subsurface porous media hydrogen storage–scenario development and simulation. *Energy Procedia*, 76:565–572, 2015.

[108] T.R.R. Pintelon, C. Picioreanu, M. van Loosdrecht, and M.L. Johns. The effect of biofilm permeability on bio-clogging of porous media. *Biotechnology and bioengineering*, 109(4):1031–1042, 2012.

[109] B.E. Poling, J.M. Prausnitz, O'C. John Paul, and R.C. Reid. *The properties of gases and liquids*, volume 5. McGraw-Hill New York, 2001.

[110] K. Porsch, J. Meier, S. Kleinsteuber, and K. Wendt-Potthoff. Importance of different physiological groups of iron reducing microorganisms in an acidic mining lake remediation experiment. *Microbial Ecology*, 57(4):701–717, 2009.

[111] Roads2HyCom. Large hydrogen underground storage. 2008. Accessed: 2013-06-15.

[112] J.A. Robinson and J.M. Tiedje. Competition between sulfate-reducing and methanogenic bacteria for H2 under resting and growing conditions. *Archives of microbiology*, 137(1):26–32, 1984.

[113] P. Ryan and E. Colleran. The role of homoacetogenic bacteria in anaerobic digester sludges. In *National Symposium of The Irish Research Council for Science, Engineering and Technology*, page 318. Citeseer, 2005.

[114] Hychico S.A. *Didema Wind Power Hydrogen Production Plant*. Hychico Brochure, 2013.

[115] A.E. Scheidegger. The physics of flow through porous media. *Soil Science*, 86(6):355, 1958.

[116] Schlumberger. ECLIPSE Reservoir Simulator. *Technical description*, 2009.

[117] W.J. Schroeder, B. Lorensen, and K. Martin. *The visualization toolkit*. Kitware, 2004.

[118] P. Smigáň, M. Greksak, J. Kozankova, F. Buzek, V. Onderka, and I. Wolf. Methanogenic bacteria as a key factor involved in changes of town gas stored in an underground reservoir. *FEMS Microbiology Ecology*, 6(3):221–224, 1990.

[119] A.J.M. Stams, S.O. Elferink, and P. Westermann. Metabolic interactions between methanogenic consortia and anaerobic respiring bacteria. In *Biomethanation I*, pages 31–56. Springer, 2003.

[120] C. I. Steefel, C. A. J. Appelo, B. Arora, D. Jacques, T. Kalbacher, O. Kolditz, V. Lagneau, P. C. Lichtner, K. U. Mayer, J. C. L. Meeussen, S. Molins, D. Moulton, H. Shao, J. Šimůnek, N. Spycher, S. B. Yabusaki, and G. T. Yeh. Reactive transport codes for subsurface environmental simulation. *Computational Geosciences*, 19(3):445–478, 2015.

[121] H.B.J. Stone, R.N. Richardson, and I. Veldhuis. An investigation into large-scale hydrogen energy storage in the UK. 2005.

[122] T. Straube and C. Müller. How to do a proper cell culture quick check.

[123] M.R. Tek. *Underground storage of natural gas: Theory and practice*, volume 171. Springer Science & Business Media, 1989.

[124] R.E. Terry. Enhanced oil recovery. *Encyclopedia of physical science and technology*, 18:503–518, 2001.

[125] R.K. Thauer and G. Fuchs. Methanogene Bakterien. *Naturwissenschaften*, 66(2):89–94, 1979.

[126] A. Toleukhanov, M. Panfilov, I. Panfilova, and A. Kaltayev. Bioreactive two-phase transport and population dynamics in underground storage of hydrogen: Natural self-organisation. In *ECMOR XIII-13th European Conference on the Mathematics of Oil Recovery*, 2012.

[127] E.F. Toro. *Riemann solvers and numerical methods for fluid dynamics: A practical introduction*. Springer Science & Business Media, 2013.

[128] A.M. Turing. The chemical basis of morphogenesis. *Philosophical Transactions of the Royal Society of London B: Biological Sciences*, 237(641):37–72, 1952.

[129] B. Ünal, V.R. Perry, M. Sheth, V. Gomez-Alvarez, K.-J. Chin, and K. Nüsslein. Trace elements affect methanogenic activity and diversity in enrichments from subsurface coal bed produced water. *Deep Subsurface Microbiology*, page 262, 2015.

[130] K. Vafai. *Porous media: Applications in biological systems and biotechnology*. CRC Press, 2010.

[131] G.A.K. van Voorn. Phd mini course: Introduction to bifurcation analysis. 2006.

[132] V.A. Vavilin, L.Y. Lokshina, S.V. Rytov, O.R. Kotsyurbenko, and A.N. Nozhevnikova. Description of two-step kinetics in methane formation during psychrophilic H2/CO2 and mesophilic glucose conversions. *Bioresource technology*, 71(3):195–209, 2000.

[133] R. Wilms, H. Sass, B. Köpke, H. Cypionka, and B. Engelen. Methane and sulfate profiles within the subsurface of a tidal flat are reflected by the distribution of sulfate-reducing bacteria and methanogenic archaea. *FEMS microbiology ecology*, 59(3):611–621, 2007.

[134] T. Xu, N. Spycher, E. Sonnenthal, G. Zhang, L. Zheng, and K. Pruess. TOUGHREACT Version 2.0: A simulator for subsurface reactive transport under non-isothermal multiphase flow conditions. *Computers & Geosciences*, 37(6):763–774, 2011.

Appendices

Appendix A

Excerpts from the source code

A.1 Evaluation of source/sink terms

The following C++ code shows how the source/sink terms for microbial growth and decay and the bio-chemical reactions are evaluated in each (sub) control volume. It is here shown on the example of methanogenesis:

```
void computeSource(PrimaryVariables& source, const int scvIdx)
{
    this->problem_().solDependentSource(source,
        this->element_(),
        this->fvGeometry_(),
        scvIdx,
        this->curVolVars_());

    const ElementVolumeVariables &elemVolVars =  this->curVolVars_();

    Scalar C_H2;
    Scalar C_CO2;
    Scalar decay;

    //To replace the discontinuity in the growth function for negative H2
        concentrations (improves the numerical stability)
    if (elemVolVars[scvIdx].moleFraction(wPhaseIdx,H2Idx)<0) {
        C_H2 = (1/alphaH2_)*elemVolVars[scvIdx].moleFraction(wPhaseIdx,H2Idx)
            ;
    } else {
        C_H2 = (elemVolVars[scvIdx].moleFraction(wPhaseIdx,H2Idx)/(
            elemVolVars[scvIdx].moleFraction(wPhaseIdx,H2Idx)+alphaH2_));
    }

    //To replace the discontinuity in the growth function for negative CO2
        concentrations (improves the numerical stability)
    if (elemVolVars[scvIdx].moleFraction(wPhaseIdx,CO2Idx)<0) {
        C_CO2 = (1/alphaCO2_)*elemVolVars[scvIdx].moleFraction(wPhaseIdx,
            CO2Idx);
    } else {
        C_CO2 = (elemVolVars[scvIdx].moleFraction(wPhaseIdx,CO2Idx)/(
            elemVolVars[scvIdx].moleFraction(wPhaseIdx,CO2Idx)+alphaCO2_));
```

```
27      }
28
29      for (int compIdx = 0; compIdx < numTotalComponents; ++compIdx) {
30
31          //Defines gamma for each component
32          switch (compIdx) {
33              case H2OIdx : { gammaK=2; break; }
34              case H2Idx : { gammaK=-4; break; }
35              case CO2Idx : { gammaK=-1; break; }
36              case CH4Idx : { gammaK=1; break; }
37              case H2SIdx : { gammaK=0; break; }
38              case SO4Idx : { gammaK=0; break; }
39              case N2Idx : { gammaK=0; break; }
40          }
41
42          //Calculates the source/sink due to the bio-chemical reaction for
                each component
43          source[conti0EqIdx + compIdx] += growthRateMax_*delta_*gammaK_/yield_
                *C_H2*C_CO2*elemVolVars[scvIdx].microbes(MGIdx)*elemVolVars[
                scvIdx].porosity();
44      }
45
46      //To make the decay function negative for negative numbers of
            microorganisms (improves the numerical stability)
47      if (elemVolVars[scvIdx].microbes(MGIdx)<0) {
48          decay = -elemVolVars[scvIdx].microbes(MGIdx)*elemVolVars[scvIdx].
                microbes(MGIdx)*decayRate_;
49      } else {
50          decay = elemVolVars[scvIdx].microbes(MGIdx)*elemVolVars[scvIdx].
                microbes(MGIdx)*decayRate_;
51      }
52
53      //Calculation of the growth and decay in the balance equation of
            methanogens
54      source[contiMGEqIdx] += growthRateMax_*C_H2*C_CO2*elemVolVars[scvIdx].
            microbes(MGIdx)-decay;
55  }
```

A.2 Reservoir initialization

The method which is used to set the initial values of all primary variables is listed as follows:

```
1   void initial_(PrimaryVariables &values,
2       const GlobalPosition &globalPos) const
3       {
4       const MaterialLawParams &matParams = this->spatialParams().
            materialLawParamsAtPos(globalPos);
5
```

```
6     //Declaration of locally used variables and objects
7     FluidState fs;
8     Scalar pC;
9     Scalar Sw;
10    Scalar thresholdPressure;
11    Scalar xgH2O;
12    Scalar pw;
13    Scalar pn;
14
15    fs.setTemperature(temperature_);
16
17    //Calculation of threshold pressure by using the material law (Brooks-
          Corey)
18    thresholdPressure = MaterialLaw::pc(matParams,1-matParams.snr());
19
20    //Below the gas-water contact
21    if (onWaterZone_(globalPos))
22    {
23        //Calculation of the water and gas phase pressure. The water pressure
              is calculated by the hydrostatic gradient of water. The gas
              pressure is the water pressure plus threshold pressure.
24        pw = pressureGasWaterContact_- (waterDensity_*gravity_[dim-1]*(
              gasWaterContact_-globalPos[dim-1]));
25        pn = pw+thresholdPressure;
26
27        //Defines the values to the fluid state
28        fs.setPressure(wPhaseIdx,pw);
29        fs.setPressure(nPhaseIdx,pn);
30
31        //sets the initial values for pressure and saturation
32        values[pressureIdx] = pw;
33        values[switchIdx]   = 0.0;
34
35    //Above the gas water contact
36    } else {
37        // The water pressure is calculated by the hydrostatic gradient of
              water. This is only true in the transition zone, otherwise it
              will be overwritten. The gas pressure is calculated by the
              hydrostatic gradient of gas. This is true in the transition zone
              and the gas zone
38        pw = pressureGasWaterContact_-(waterDensity_*gravity_[dim-1]*(
              gasWaterContact_-globalPos[dim-1]));
39        pn = pressureGasWaterContact_+thresholdPressure-(gasDensity_*gravity_
              [dim-1]*(gasWaterContact_-globalPos[dim-1]));
40
41        //Defines the values to the fluid state
42        fs.setPressure(wPhaseIdx,pw);
43        fs.setPressure(nPhaseIdx,pn);
44
45        //Calculation of the water saturation dependent on the capillary
              pressure by using the material law (Brooks-Corey)
46        Sw = MaterialLaw::sw(matParams, pn-pw);
47
```

```
48          //In the gas zone
49          //For Corey-Brooks the if statement would never become true,
                therefore 0.01 is added which means that the saturation is very
                close to the residual water saturation
50          if (Sw <= matParams.swr()+0.01) {
51
52               Sw = matParams.swr()+0.01;
53
54               //Defines the initial value for the saturation
55               values[switchIdx] = 1-Sw;
56
57               //Calculating the water pressure by the gas pressure minus
                     capillary pressure
58               pC = MaterialLaw::pc(matParams, Sw);
59               pw = pn - pC;
60               fs.setPressure(wPhaseIdx,pw);
61
62               //Defines the initial value for the pressure
63               values[pressureIdx] = pw;
64
65          //In the transition zone
66          } else {
67              //Defines the initial value for pressure and saturation
68              values[pressureIdx] = pw;
69              values[switchIdx] = 1-Sw;
70          }
71      }
72
73      //Defines the additional primary variables: Concentration of the gaseous
            components in the water phase and the initial number of
            microorganisms
74      xgH2O = (FluidSystem::fugacityCoefficient(fs,wPhaseIdx,H2OIdx)* pw) / pn;
75      values[contiCO2EqIdx]  = 0.0108*(1-xgH2O) * pn / (FluidSystem::
            fugacityCoefficient(fs,wPhaseIdx,CO2Idx) * pw);
76      values[contiH2EqIdx]  =  0;
77      values[contiH2SEqIdx]  =  0;
78      values[contiCH4EqIdx]  =  0.199*(1-xgH2O) * pn / (FluidSystem::
            fugacityCoefficient(fs,wPhaseIdx,CH4Idx) * pw);
79      values[contiSO4EqIdx]  =  0.0018;
80      values[contiMGEqIdx]  = 1;
81      values[contiSREqIdx]  = 1;
82
83  }
```

A.3 Rate-controlled injection well

The following internal method is used to evaluate the source/sink term for a (sub) control volume when H_2 is injected at a constant rate. The 'values'

parameter stores the mole generation/extraction rate in $[mol/m^3/s]$ for each conservation equation.

```
void injection_(PrimaryVariables &values,
    const FVElementGeometry &fvGeometry,
    const int scvIdx) const
    {
        //divide the H2 injection rate by the volume of the (sub) control volume
        values[contiH2EqIdx] = H2InjectionRate_/fvGeometry.subContVol[scvIdx].volume;
    }
```

A.4 Rate-controlled production well

The follwoing internal method is used to evaluate the source/sink term for a (sub) control volume when mass is withdrawn at a constant rate.

```
void production_(PrimaryVariables &values,
    const FVElementGeometry &fvGeometry,
    const ElementVolumeVariables &elemVolVars,
    const int scvIdx) const
    {
        const FluidState &fs = elemVolVars[scvIdx].fluidState();

        //Calculation of the water phase mobility
        Scalar mobilityWater = elemVolVars[scvIdx].relativePermeability(wPhaseIdx)/fs.viscosity(wPhaseIdx)*fs.molarDensity(wPhaseIdx);

        //Calculation of the gas phase mobility
        Scalar mobilityGas = elemVolVars[scvIdx].relativePermeability(nPhaseIdx)/fs.viscosity(nPhaseIdx)*fs.molarDensity(nPhaseIdx);

        //Calculation of the mobility for each component
        Scalar H2OMobility = mobilityWater*fs.moleFraction(wPhaseIdx,H2OIdx)+mobilityGas*fs.moleFraction(nPhaseIdx,H2OIdx);
        Scalar H2Mobility = mobilityWater*fs.moleFraction(wPhaseIdx,H2Idx)+mobilityGas*fs.moleFraction(nPhaseIdx,H2Idx);
        Scalar CO2Mobility = mobilityWater*fs.moleFraction(wPhaseIdx,CO2Idx)+mobilityGas*fs.moleFraction(nPhaseIdx,CO2Idx);
        Scalar CH4Mobility = mobilityWater*fs.moleFraction(wPhaseIdx,CH4Idx)+mobilityGas*fs.moleFraction(nPhaseIdx,CH4Idx);
        Scalar H2SMobility = mobilityWater*fs.moleFraction(wPhaseIdx,H2SIdx)+mobilityGas*fs.moleFraction(nPhaseIdx,H2SIdx);

        //Calculation of the source/sink term for each conservation equation
        Scalar mobilitySum = H2OMobility_+H2Mobility_+CO2Mobility+CH4Mobility_+H2SMobility_;
```

```
23          values[conti0EqIdx+H2OIdx] = -productionRate_*H2OMobility/(
                mobilitySum*fvGeometry.subContVol[scvIdx].volume);
24          values[conti0EqIdx+H2Idx] = -productionRate_*H2Mobility/(mobilitySum*
                fvGeometry.subContVol[scvIdx].volume);
25          values[conti0EqIdx+CO2Idx] = -productionRate_*CO2Mobility/(
                mobilitySum*fvGeometry.subContVol[scvIdx].volume);
26          values[conti0EqIdx+CH4Idx] = -productionRate_*CH4Mobility/(
                mobilitySum*fvGeometry.subContVol[scvIdx].volume);
27          values[conti0EqIdx+H2SIdx] = -productionRate_*H2SMobility/(
                mobilitySum*fvGeometry.subContVol[scvIdx].volume);
28       }
```

A.5 Pressure-controlled injection well

The C++ implementation for a pressure controlled injection well is listed as follows:

```
1  void injection_(PrimaryVariables &values,
2      const ElementVolumeVariables &elemVolVars,
3      const int scvIdx,
4      const FVElementGeometry &fvGeometry,
5      Scalar InjectionPressure) const
6      {
7          const FluidState &fs = elemVolVars[scvIdx].fluidState();
8
9          //Calculation of the equivalent radius
10         Scalar equivalentRadius = 0.14*sqrt(deltaX_*deltaX_+deltaY_*deltaY_);
11
12         //Calculation of the gas phase mobility
13         Scalar mobilityGas = elemVolVars[scvIdx].relativePermeability(
               nPhaseIdx)/fs.viscosity(nPhaseIdx)*fs.molarDensity(nPhaseIdx);
14
15         //Calculation of the well index
16         Scalar WellIndex = ((2*M_PI*elemVolVars[scvIdx].permX()*(fvGeometry.
               subContVol[scvIdx].volume/(deltaX_*deltaY_)))/(log(
               equivalentRadius/(WellRadius_))));
17
18        //Calculation of the mole generation rate in mol/m^3/s
19        values[contiH2EqIdx] = mobilityGas*WellIndex*(InjectionPressure-fs.
              pressure(nPhaseIdx))*(1/fvGeometry.subContVol[scvIdx].volume);
20     }
```

A.6 Pressure-controlled production well

The internal method for a pressure-controlled well is listed as follows:

```
void production_(PrimaryVariables &values,
    const ElementVolumeVariables &elemVolVars,
    const int scvIdx,
    const FVElementGeometry &fvGeometry,
    Scalar ProductionPressure) const
    {
        const FluidState &fs = elemVolVars[scvIdx].fluidState();

        Scalar equivalentRadius = 0.14*sqrt(deltaX_*deltaX_+deltaY_*deltaY_);

        //Calculation of the water phase mobility
        Scalar mobilityWater = elemVolVars[scvIdx].relativePermeability(
            wPhaseIdx)/fs.viscosity(wPhaseIdx)*fs.molarDensity(wPhaseIdx);

        //Calculation of the gas phase mobility
        Scalar mobilityGas = elemVolVars[scvIdx].relativePermeability(
            nPhaseIdx)/fs.viscosity(nPhaseIdx)*fs.molarDensity(nPhaseIdx);

        //Calculation of the well index
        Scalar WellIndex = ((2*M_PI*elemVolVars[scvIdx].permX()*(fvGeometry.
            subContVol[scvIdx].volume/(deltaX_*deltaY_)))/(log(
            equivalentRadius/(WellRadius_))));

        //Calculation of molar H2O extraction rate
        values[conti0EqIdx+H2OIdx] = (mobilityWater*fs.moleFraction(wPhaseIdx
            ,H2OIdx)*WellIndex*(ProductionPressure-fs.pressure(wPhaseIdx)))
            +(mobilityGas*fs.moleFraction(nPhaseIdx,H2OIdx)*WellIndex*(
            ProductionPressure-fs.pressure(nPhaseIdx)))*(1/fvGeometry.
            subContVol[scvIdx].volume);

        //it has to be checked if the water phase will be produced
        if (ProductionPressure < fs.pressure(wPhaseIdx))
        {
            //Calculation of molar H2 extraction rate
            values[conti0EqIdx+H2Idx] = (mobilityGas*fs.moleFraction(
                nPhaseIdx,H2Idx)*WellIndex*(ProductionPressure-fs.pressure(
                nPhaseIdx)))*(1/fvGeometry.subContVol[scvIdx].volume);

            //Calculation of molar CO2 extraction rate
            values[conti0EqIdx+CO2Idx] = (mobilityGas*fs.moleFraction(
                nPhaseIdx,CO2Idx)*WellIndex*(ProductionPressure_-fs.pressure
                (nPhaseIdx)))*(1/fvGeometry.subContVol[scvIdx].volume);

            //Calculation of molar CH4 extraction rate
            values[conti0EqIdx+CH4Idx] = (mobilityGas*fs.moleFraction(
                nPhaseIdx,CH4Idx)*WellIndex*(ProductionPressure-fs.pressure(
                nPhaseIdx)))*(1/fvGeometry.subContVol[scvIdx].volume);

            //Calculation of molar H2S extraction rate
            values[conti0EqIdx+H2SIdx] = (mobilityGas*fs.moleFraction(
                nPhaseIdx,H2SIdx)*WellIndex*(ProductionPressure-fs.pressure(
                nPhaseIdx)))*(1/fvGeometry.subContVol[scvIdx].volume);

```

```
38              //Calculation of molar N2 extraction rate
39              values[conti0EqIdx+N2Idx] = (mobilityGas*fs.moleFraction(
                    nPhaseIdx,N2Idx)*WellIndex*(ProductionPressure-fs.pressure(
                    nPhaseIdx)))*(1/fvGeometry.subContVol[scvIdx].volume);
40          }
41          else
42          {
43              //Calculation of molar H2 extraction rate
44              values[conti0EqIdx+H2Idx] = (mobilityWater*fs.moleFraction(
                    wPhaseIdx,H2Idx)*WellIndex*(ProductionPressure-fs.pressure(
                    wPhaseIdx))+mobilityGas*fs.moleFraction(nPhaseIdx,H2Idx)*
                    WellIndex*(ProductionPressure-fs.pressure(nPhaseIdx)))*(1/
                    fvGeometry.subContVol[scvIdx].volume);
45
46              //Calculation of molar CO2 extraction rate
47              values[conti0EqIdx+CO2Idx] = (mobilityWater*fs.moleFraction(
                    wPhaseIdx,CO2Idx)*WellIndex*(ProductionPressure_-fs.pressure
                    (wPhaseIdx))+mobilityGas*fs.moleFraction(nPhaseIdx,CO2Idx)*
                    WellIndex*(ProductionPressure_-fs.pressure(nPhaseIdx)))*(1/
                    fvGeometry.subContVol[scvIdx].volume);
48
49              //Calculation of molar CH4 extraction rate
50              values[conti0EqIdx+CH4Idx] = (mobilityWater*fs.moleFraction(
                    wPhaseIdx,CH4Idx)*WellIndex*(ProductionPressure-fs.pressure(
                    wPhaseIdx))+mobilityGas*fs.moleFraction(nPhaseIdx,CH4Idx)*
                    WellIndex*(ProductionPressure-fs.pressure(nPhaseIdx)))*(1/
                    fvGeometry.subContVol[scvIdx].volume);
51
52              //Calculation of molar H2S extraction rate
53              values[conti0EqIdx+H2SIdx] = (mobilityWater*fs.moleFraction(
                    wPhaseIdx,H2SIdx)*WellIndex*(ProductionPressure-fs.pressure(
                    wPhaseIdx))+mobilityGas*fs.moleFraction(nPhaseIdx,H2SIdx)*
                    WellIndex*(ProductionPressure-fs.pressure(nPhaseIdx)))*(1/
                    fvGeometry.subContVol[scvIdx].volume);
54
55              //Calculation of molar N2 extraction rate
56              values[conti0EqIdx+N2Idx] = (mobilityWater*fs.moleFraction(
                    wPhaseIdx,N2Idx)*WellIndex*(ProductionPressure-fs.pressure(
                    wPhaseIdx))+mobilityGas*fs.moleFraction(nPhaseIdx,N2Idx)*
                    WellIndex*(ProductionPressure-fs.pressure(nPhaseIdx)))*(1/
                    fvGeometry.subContVol[scvIdx].volume);
57          }
58      }
```

Appendix B

Spatial plots from the 2D storage scenario

On the following pages spatial plots are shown from the 2D storage scenario in section 6.2.2. The plots of gas component concentrations, microbial densities and gas saturation were generated after the first injection period ($\tau = 2$), after the first idle period ($\tau = 4$) and after the first production period ($\tau = 6$).

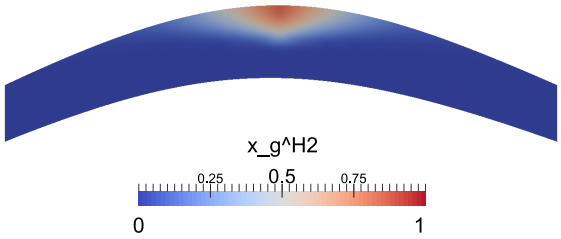

(a) H_2 mole fraction (with mechanical dispersion)

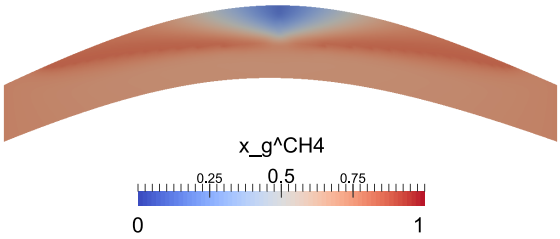

(b) CH_4 mole fraction (with mechanical dispersion)

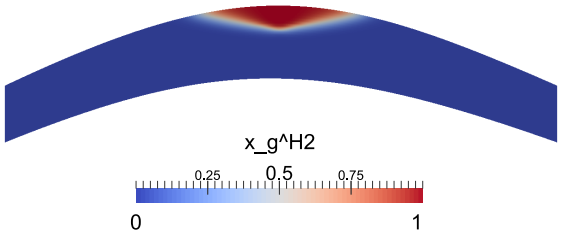

(c) H_2 mole fraction (base case)

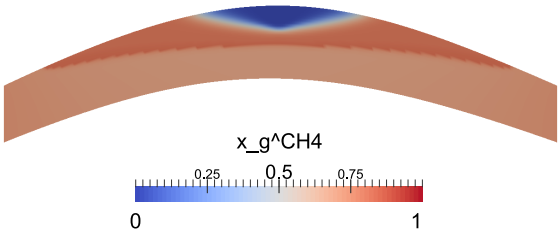

(d) CH_4 mole fraction (base case)

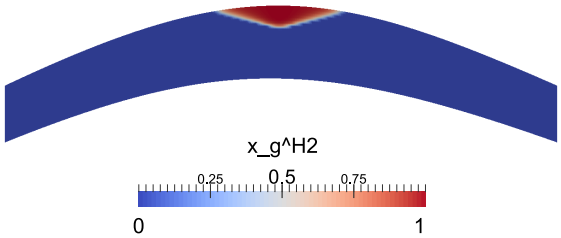

(e) H_2 mole fraction (with bio-chemical reactions)

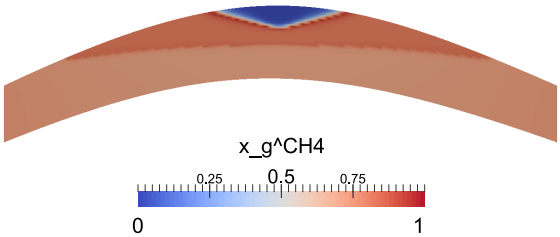

(f) CH_4 mole fraction (with bio-chemical reactions)

Figure B.1: Spatial plots for the 2D case study after at dimensionless time of 2 (after the first injection period)

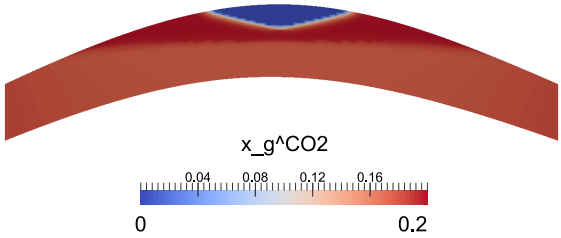

(a) CO_2 mole fraction (with bio-chemical reactions)

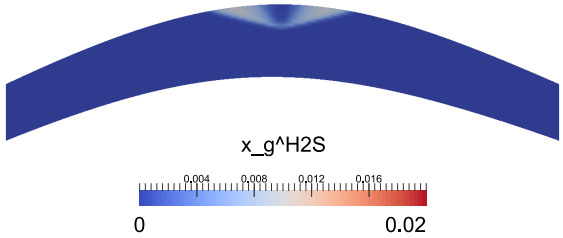

(b) H_2S mole fraction (with bio-chemical reactions)

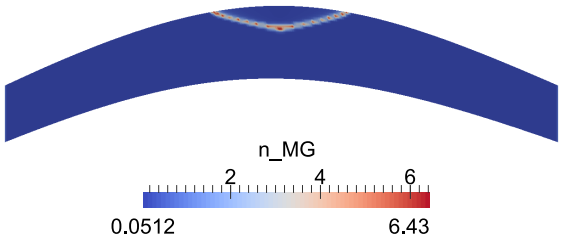

(c) Dimensionless density of methanogenic archaea

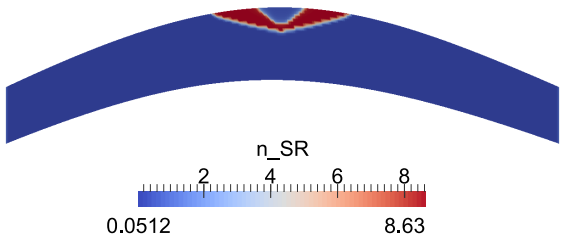

(d) Dimensionless density of sulfate-reducing bacteria

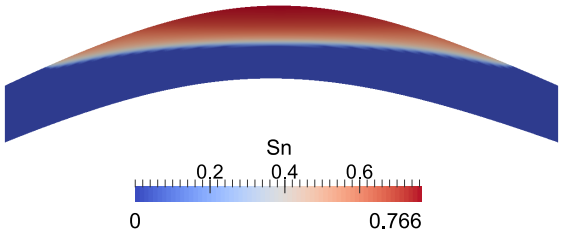

(e) Gas saturation (with mechanical dispersion)

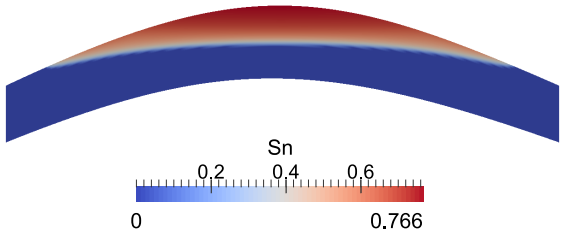

(f) Gas saturation (base case)

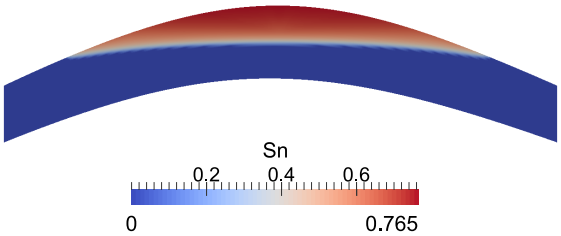

(g) Gas saturation (with bio-chemical reactions)

Figure B.2: Spatial plots for the 2D case study after at dimensionless time of 2 (after the first injection period)

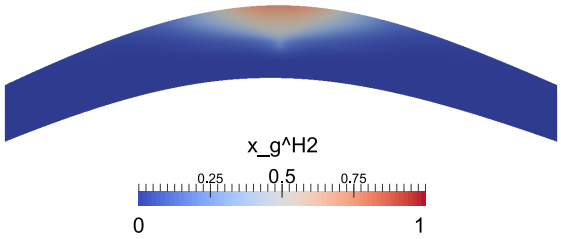

(a) H_2 mole fraction (with mechanical dispersion)

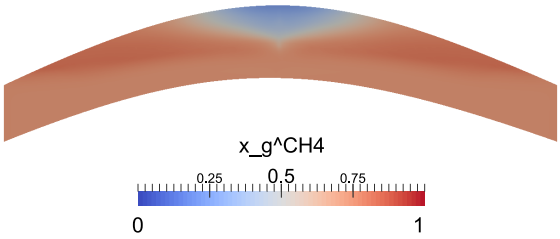

(b) CH_4 mole fraction (with mechanical dispersion)

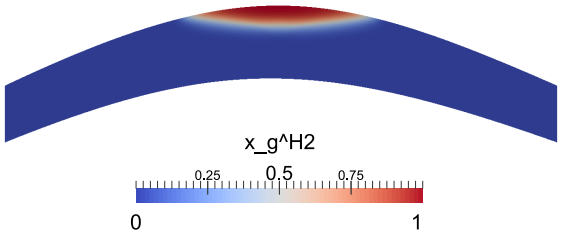

(c) H_2 mole fraction (base case)

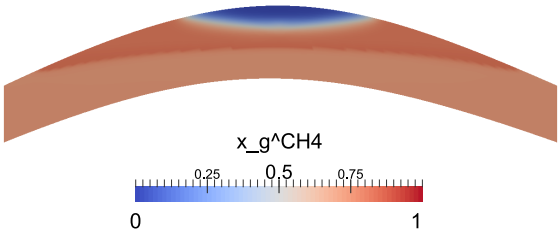

(d) CH_4 mole fraction (base case)

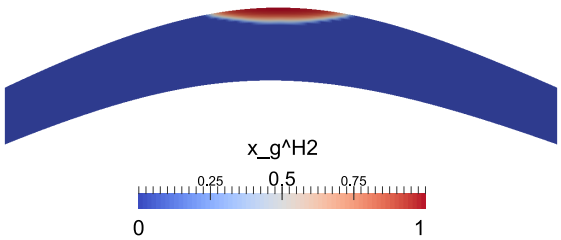

(e) H_2 mole fraction (with bio-chemical reactions)

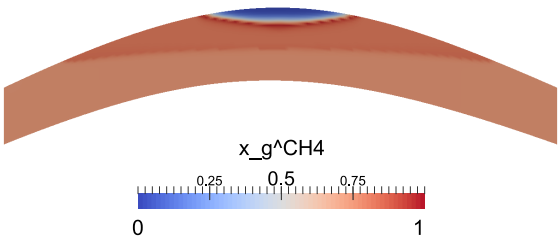

(f) CH_4 mole fraction (with bio-chemical reactions)

Figure B.3: Spatial plots for the 2D case study after at dimensionless time of 4 (after the first idle period)

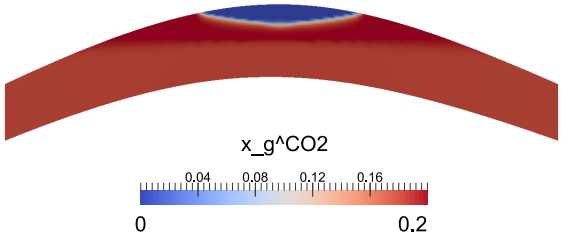

(a) CO_2 mole fraction (with bio-chemical reactions)

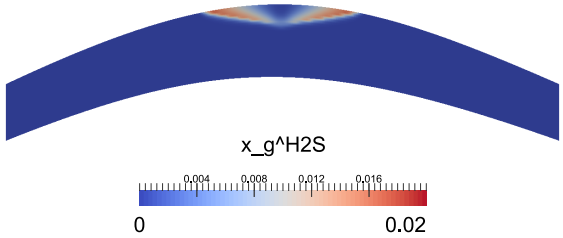

(b) H_2S mole fraction (with bio-chemical reactions)

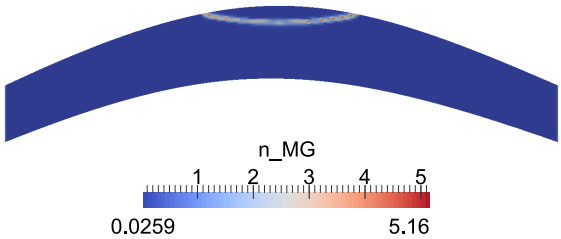

(c) Dimensionless density of methanogenic archaea

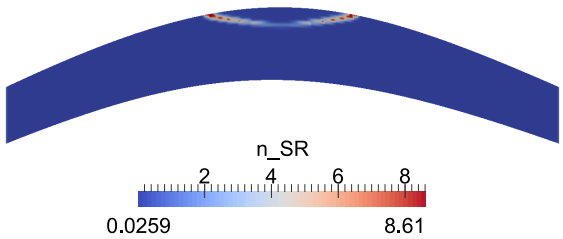

(d) Dimensionless density of sulfate-reducing bacteria

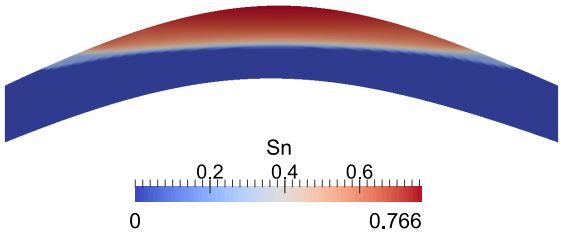

(e) Gas saturation (with mechanical dispersion)

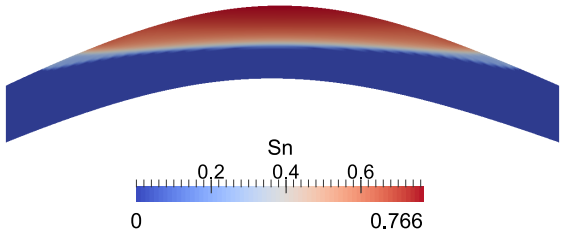

(f) Gas saturation (base case)

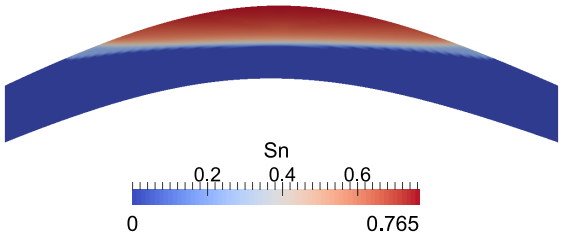

(g) Gas saturation (with bio-chemical reactions)

Figure B.4: Spatial plots for the 2D case study after at dimensionless time of 4 (after the first idle period)

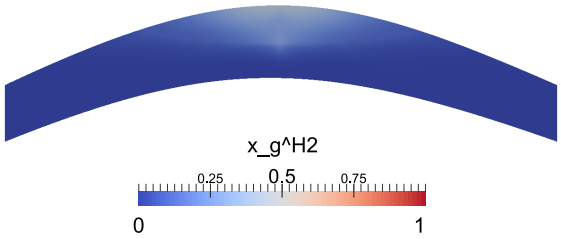

(a) H_2 mole fraction (with mechanical dispersion)

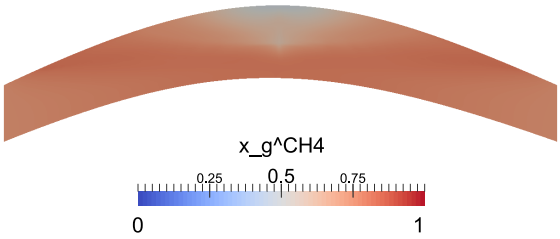

(b) CH_4 mole fraction (with mechanical dispersion)

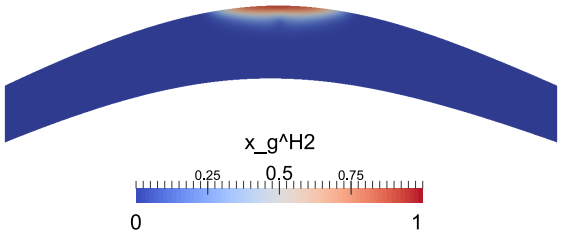

(c) H_2 mole fraction (base case)

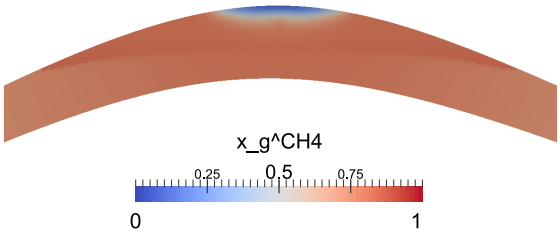

(d) CH_4 mole fraction (base case)

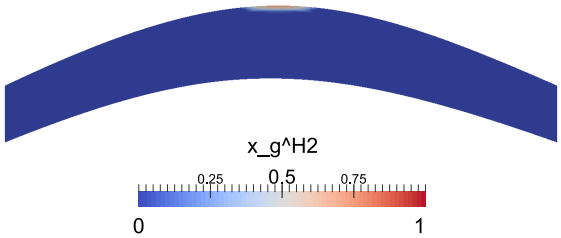

(e) H_2 mole fraction (with bio-chemical reactions)

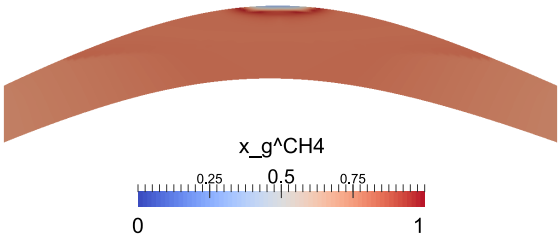

(f) CH_4 mole fraction (with bio-chemical reactions)

Figure B.5: Spatial plots for the 2D case study after at dimensionless time of 6 (after the first production period)

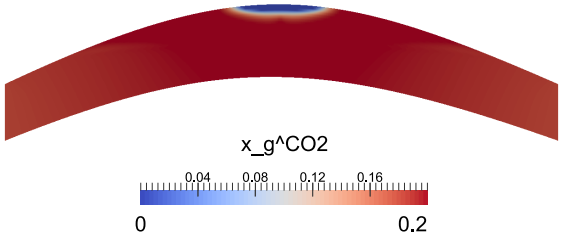

(a) CO_2 mole fraction (with bio-chemical reactions)

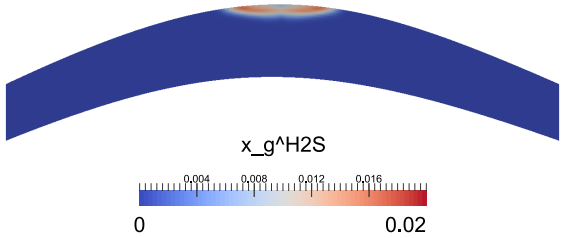

(b) H_2S mole fraction (with bio-chemical reactions)

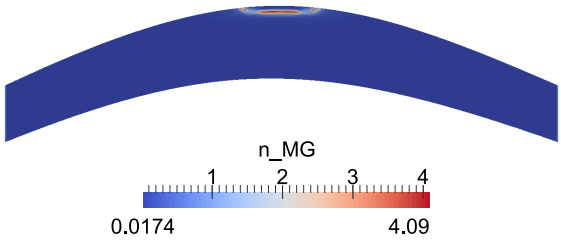

(c) Dimensionless density of methanogenic archaea

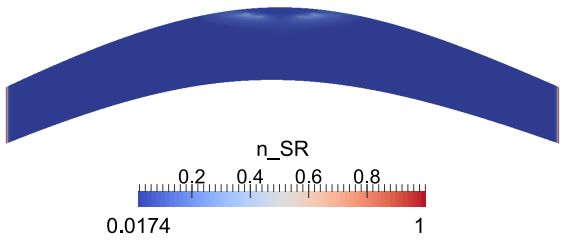

(d) Dimensionless density of sulfate-reducing bacteria

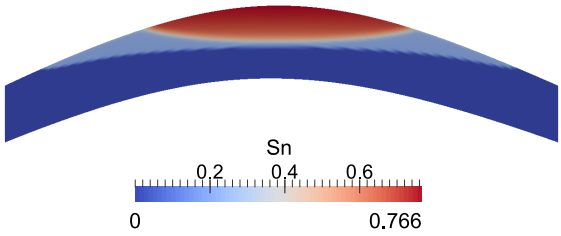

(e) Gas saturation (with mechanical dispersion)

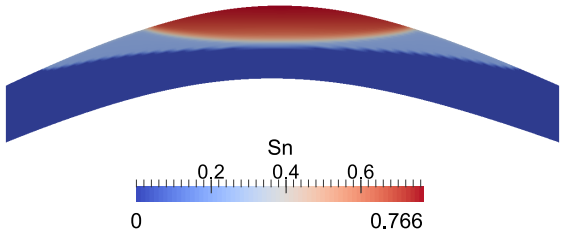

(f) Gas saturation (base case)

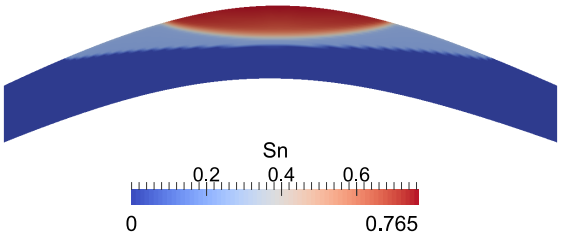

(g) Gas saturation (with bio-chemical reactions)

Figure B.6: Spatial plots for the 2D case study after at dimensionless time of 6 (after the first production period)

Appendix C

Spatial plots from the 3D storage scenario

On the following pages spatial plots are shown from the 3D storage scenario in section 6.2.3. In section C.1 the figures were generated for case with 100 mol% H_2 injection and in section C.1 for the case with a gas mixture injection (95 $mol\%$ H_2 and 5 $mol\%$ CO_2). All figures are shown at different points in time: After 2 months, after 14 months and after 36 months. Each of them compares the H_2 and CO_2 mole fractions for the case with and without methanogenesis. For the case with methanogenesis the CO_2 mole fraction and the dimensionless microbial density are shown additionally.

C.1 100 $mol\%$ H_2 injection

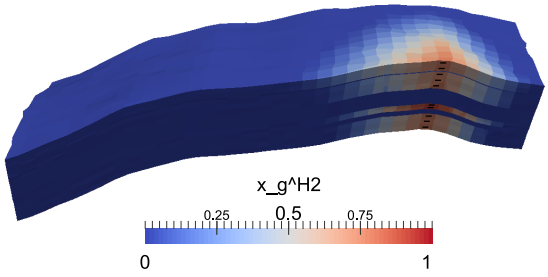

(a) H_2 mole fraction with methanogenesis

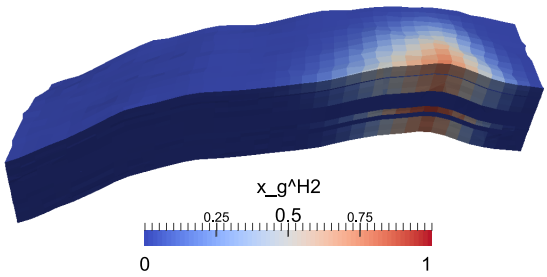

(b) H_2 mole fraction without methanogenesis

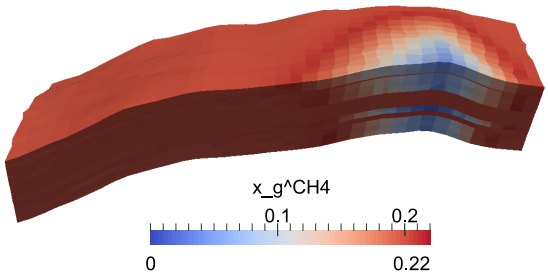

(c) CH_4 mole fraction with methanogenesis

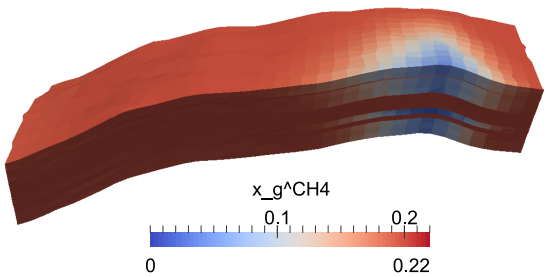

(d) CH_2 mole fraction without methanogenesis

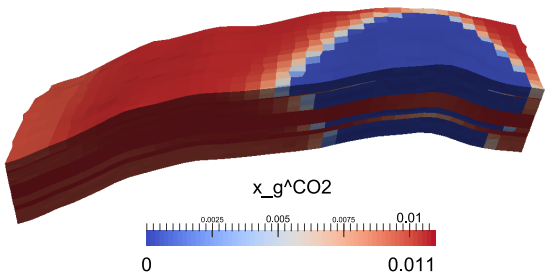

(e) CO_2 mole fraction with methanogenesis

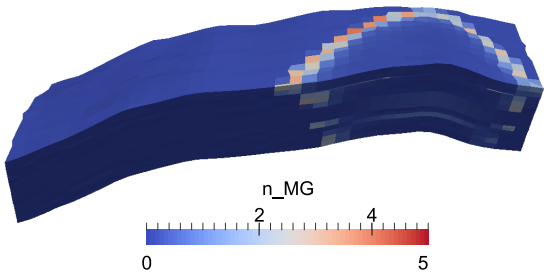

(f) Dimensionless density of methanogenic archaea

Figure C.1: Spatial plots for the case study with 100 $mol\%$ H_2 injection after two months

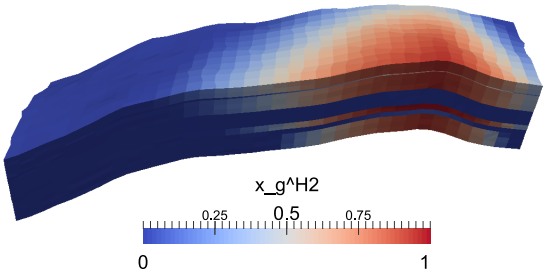

(a) H_2 mole fraction with methanogenesis

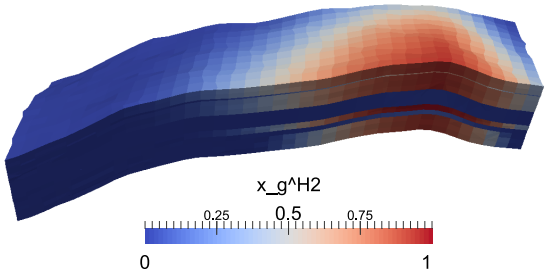

(b) H_2 mole fraction without methanogenesis

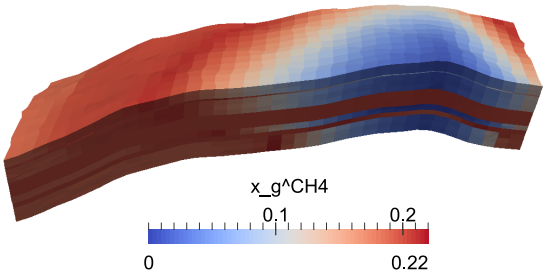

(c) CH_4 mole fraction with methanogenesis

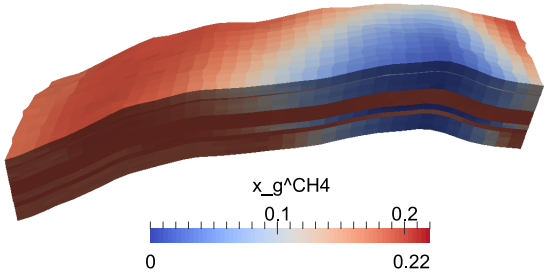

(d) CH_4 mole fraction without methanogenesis

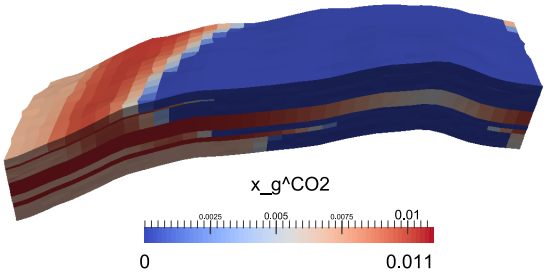

(e) CO_2 mole fraction with methanogenesis

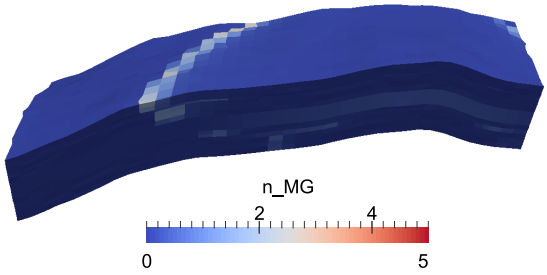

(f) Dimensionless density of methanogenic archaea

Figure C.2: Spatial plots for the case study with 100 $mol\%$ H_2 injection after 14 months

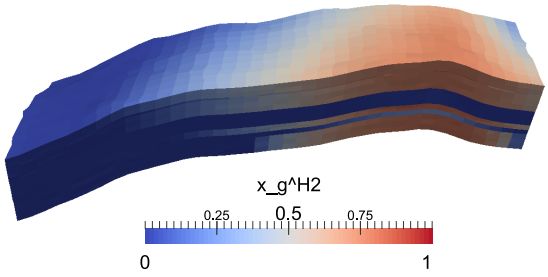

(a) H_2 mole fraction with methanogenesis

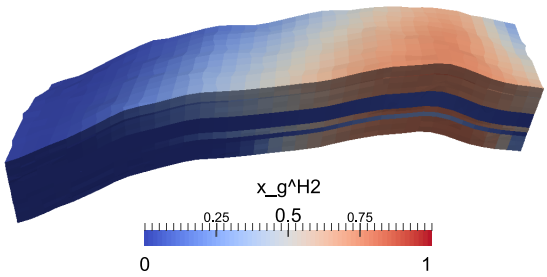

(b) H_2 mole fraction without methanogenesis

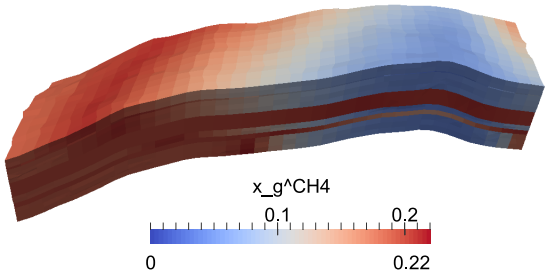

(c) CH_4 mole fraction with methanogenesis

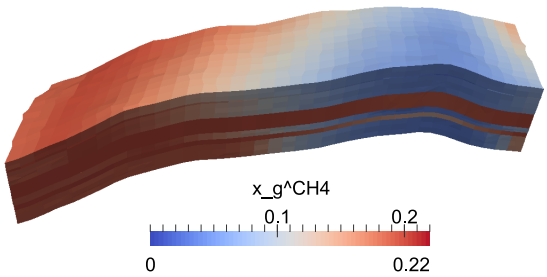

(d) CH_4 mole fraction without methanogenesis

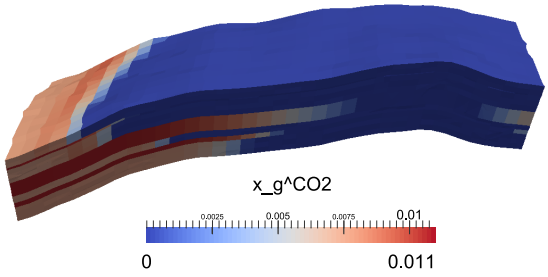

(e) CO_2 mole fraction with methanogenesis

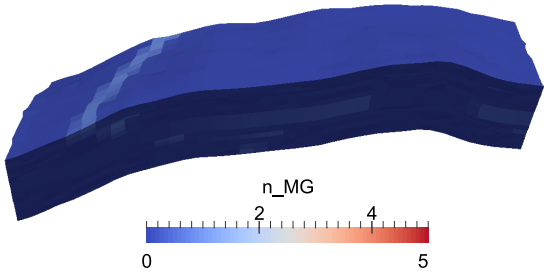

(f) Dimensionless density of methanogenic archaea

Figure C.3: Spatial plots for the case study with 100 $mol\%$ H_2 injection after 36 months

C.2 95 $mol\%$ H_2 and 5 $mol\%$ CO_2 injection

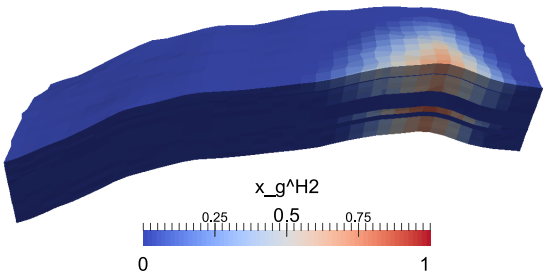

(a) H_2 mole fraction with methanogenesis

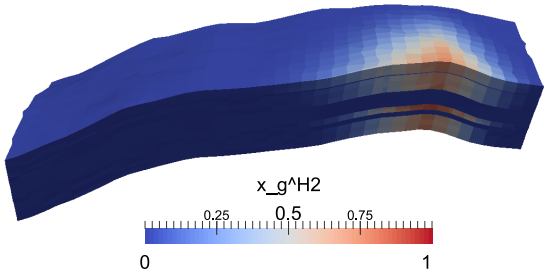

(b) H_2 mole fraction without methanogenesis

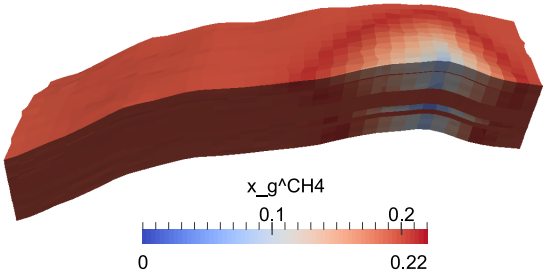

(c) CH_4 mole fraction with methanogenesis

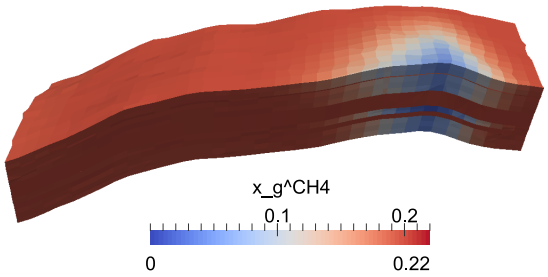

(d) CH_4 mole fraction without methanogenesis

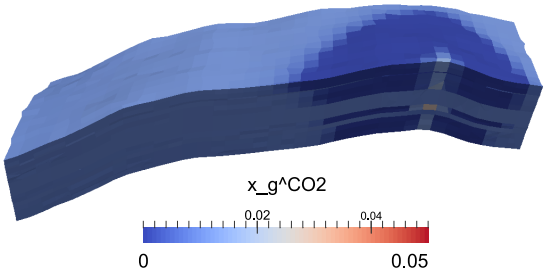

(e) CO_2 mole fraction with methanogenesis

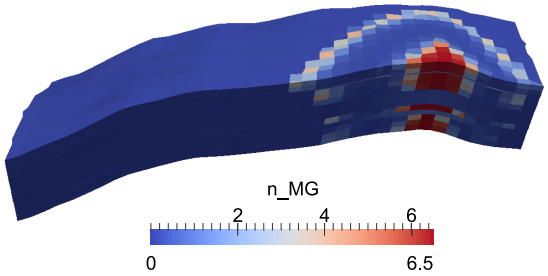

(f) Dimensionless density of methanogenic archaea

Figure C.4: Spatial plots for the case study with 95 $mol\%$ H_2 and 5 $mol\%$ CO_2 injection after two months

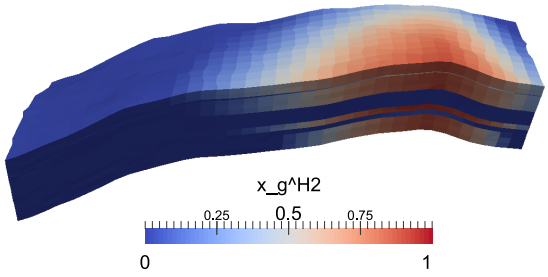

(a) H_2 mole fraction with methanogenesis

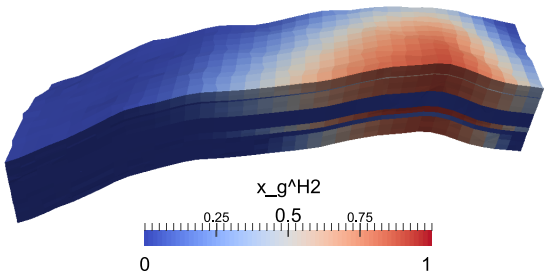

(b) H_2 mole fraction without methanogenesis

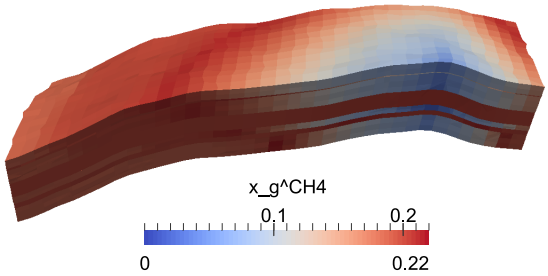

(c) CH_4 mole fraction with methanogenesis

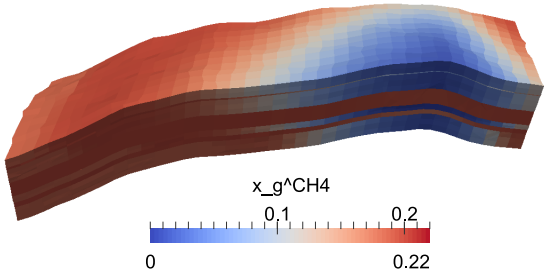

(d) CH_4 mol fraction without methanogenesis

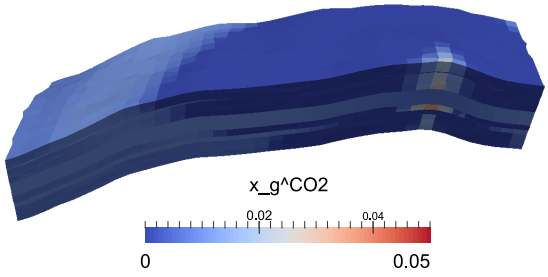

(e) CO_2 mole fraction with methanogenesis

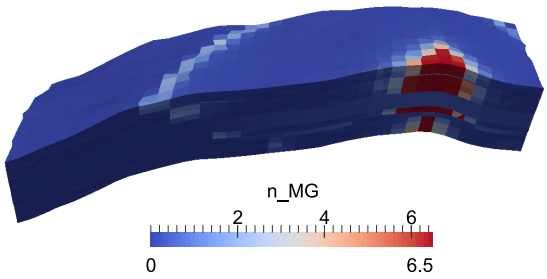

(f) Dimensionless density of methanogenic archaea

Figure C.5: Spatial plots for the case study with 95 $mol\%$ H_2 and 5 $mol\%$ CO_2 injection after 14 months

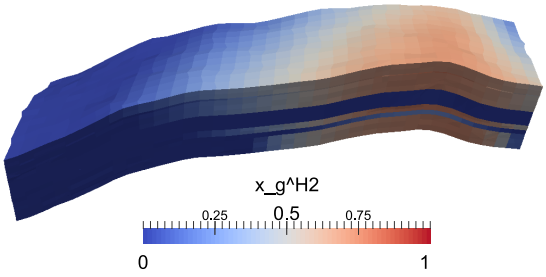

(a) H_2 mole fraction with methanogenesis

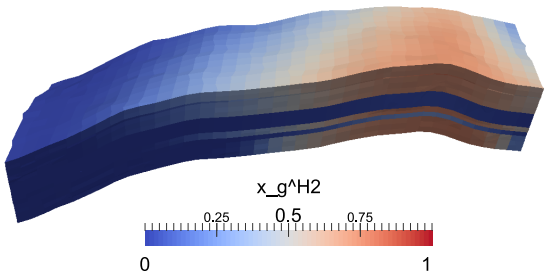

(b) H_2 mole fraction without methanogenesis

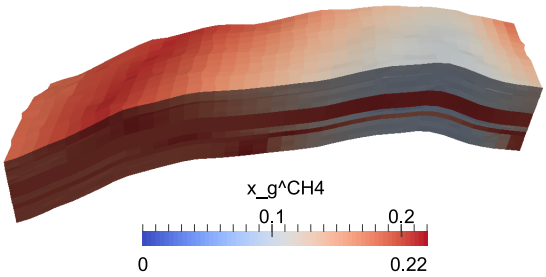

(c) CH_4 mole fraction with methanogenesis

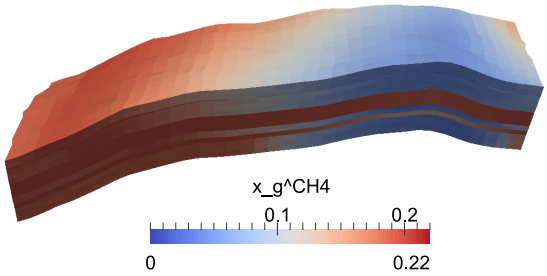

(d) CH_4 mole fraction without methanogenesis

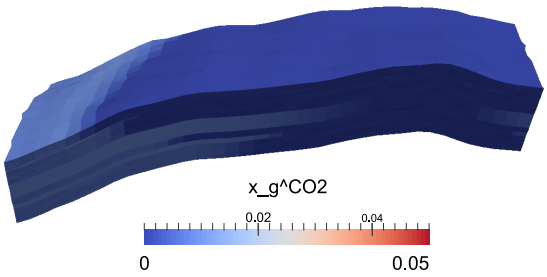

(e) CO_2 mole fraction with methanogenesis

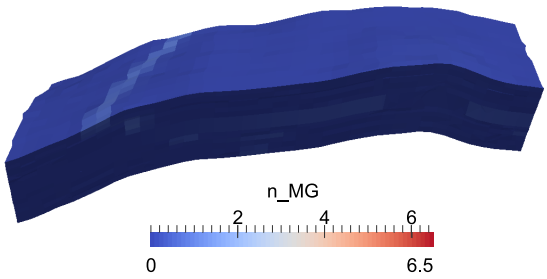

(f) Dimensionless density of methanogenic archaea

Figure C.6: Spatial plots for the case study with 95 $mol\%$ H_2 and 5 $mol\%$ CO_2 injection after 36 months

Appendix D

Ausführliche Zusammenfassung

Einleitung

Die Untergrundwasserstoffspeicherung ist ein vielversprechender Lösungsvorschlag für den Ausgleich der elektrischen Energieversorgung, welcher aufgrund der fluktuierenden Produktion aus erneuerbaren Energiequellen nötig ist. Erneuerbare Energie, die primär durch Wind- und Solarkraftwerke erzeugt wird, ist stark witterungsabhängig. Zusätzlich variiert die Nachfrage nach Strom auf einer täglichen und saisonalen Zeitskala. Daher ist für den Ausgleich dieser Schwankungen eine temporäre Speicherung der Energie notwendig, wofür derzeit mehrere Optionen diskutiert werden [70]. Untergrundwasserstoffspeicher, in denen die Energie als chemische Energie gespeichert wird, weisen eine hohe Energiedichte auf und bieten somit die Möglichkeit, elektrische Energie langfristig oder sogar saisonal zu speichern [29]. Diese Technologie umfasst Elektrolyseanlagen, die übermäßig produzierte elektrische Energie verwenden, um Wasser in Sauerstoff und Wasserstoff zu spalten [70]. Für die anschließende Speicherung und Nutzung von Wasserstoff stehen verschiedene Konzepte zur Verfügung [91, 45, 29]:

- „POWER-to-GAS“: Der erzeugte Wasserstoff wird in das bestehende Erdgasnetz eingespeist. Untersuchungen haben gezeigt, dass Konzentrationen im einstelligen Prozentbereich annehmbar sind [90]. Das bedeutet, dass auch die bestehenden unterirdischen Erdgasspeicher mit einer niedrigen Wasserstoffkonzentration betrieben werden.
- „POWER-to-GAS-to-POWER“: Der Wasserstoff wird unvermischt in Untergrundformationen, z.B. ausgeförderten Erdgas- oder Erdöllagerstätten, Aquiferen oder Salzkavernen, gespeichert [111]. In Zeiten eines hohen Energiebedarfs wird der Wasserstoff wieder entnommen und

kann als Brennstoff für stationäre Brennstoffzellen oder Motorgeneratoren, die an das Stromnetz angeschlossen sind sowie für Brennstoffzellenfahrzeuge genutzt werden.

Das Konzept der Speicherung von Gasen im Untergrund ist seit fast 100 Jahren etabliert. Die Speicherung von Wasserstoff in Salzkavernen wird als problemlos angesehen [80]. Solche Speicher gibt es derzeit in Teesside, Großbritannien und Texas, USA. In Porenspeichern wurden bisher nur Erfahrungen mit Erdgas und Gasgemischen, z.B. Stadtgas, gesammelt. In Stadtgasspeichern, bei denen das gespeicherte Gas eine Wasserstoffkonzentration von bis zu 50 % hat, sind teilweise Ungewöhnlichkeiten aufgetreten. Reduktionen des Gasvolumens und Schwankungen in der Gaszusammensetzung wurden bei mehreren dieser Speicher festgestellt. Es wird vermutet, dass biochemische Reaktionen für diese Effekte verantwortlich waren, da ein Anstieg in der Anzahl der mikrobiellen Zellen im Lagerstättenwasser gemessen wurde [118, 21].

Um die Nutzung von Porenspeichern auf die Wasserstoffverträglichkeit zu testen begann die argentinische Firma Hychico S.A. im Jahr 2013 einen Pilotversuch [114]. Sie fügten Wasserstoff als Tracer dem Erdgasstrom zu und speicherten das Gasgemisch in einem ausgeförderten Gas- und Ölfeld. Die Ergebnisse dieses Tests sind bisher unveröffentlicht. Außerdem startete die RAG (Rohöl-Aufsuchungs Aktiengesellschaft) in Österreich im Jahr 2015 ebenfalls einen Pilotversuch [12]. Sie injizierten ein Gasgemisch aus Erdgas mit 10% Wasserstoff in eine kleine ausgeförderte Erdgaslagerstätte. Die Wiederentnahme begann im Sommer 2016. Ergebnisse des Feldversuchs werden 2017 erwartet.

Auch in Deutschland wurden durch den Start der „Förderinitiative Energiespeicher“ seit 2011 einige Forschungsprojekte gestartet, die sich mit dem Thema Wasserstoff als Energieträger beschäftigen. Diese Projekte befassen sich mit den verschiedenen Bereichen in der Kette von Wasserstoffproduktion über Speicherung und Transport bis hin zur Nutzung von Wasserstoff.

Literaturrecherche

Als besonders geeignete Porenspeicher zeigen sich ausgeförderte Erdgaslagerstätten und Aquifere. Für Aquifere, die zu Beginn nur mit Wasser bzw.

Sole gesättigt sind und ausgeförderte Erdgaslagerstätten, die eine Restgassättigung aufweisen, sind die maßgebenden Prozesse während der Entwicklungsphase jedoch unterschiedlich.

In den Aquiferen wird während der Entwicklungsphase eine Gasblase gebildet, wofür das Aquiferwasser verdrängt werden muss. Die Effizienz der Verdrängung zwischen den zwei nahezu unmischbaren Fluiden hängt von mehreren Faktoren ab. Zum einen können durch eine instabile Verdrängungsfront bei einem ungünstigen Verhältnis der Mobilitäten fiskose Finger entstehen. Für das System Wasserstoff-Wasser ergab eine Schätzung ein Mobilitätsverhältnis zwischen 2 und 5, womit eine instabile Verdrängung und die Bildung von viskosen Fingern zu erwarten ist. Außerdem besteht durch die sehr geringe Dichte von Wasserstoff die Tendenz zu einer schwerkraftgetriebenen Segregation. Bei diesem Effekt wird die Verdrängungfront ebenfalls instabil. Wenn bei der Injektion eine kritische Strömungsgeschwindigkeit überschritten wird, überströmt der Wasserstoff das Wasser und breitet sich hauptsächlich im oberen Bereich der Lagerstätte aus. Dadurch können Gasverluste über den tiefsten Punkt der Struktur hinaus entstehen.

Ausgeförderte Erdgaslagerstätten haben häufig eine hohe Restgassättigung. Die Verdrängung des mit Wasserstoff vollständig mischbaren Restgases verursacht eine Vermischung an der Verdrängungsfront. Diese Vermischung wird durch Heterogenitäten und Anisotropien des porösen Mediums und Mobilitätsverhältnisse, Dichteunterschiede, molekulare Diffusion und mechanische Dispersion zwischen den verschiedenen Gasen beeinflusst [123]. Bei den zu erwartenden Strömungsgeschwindigkeiten in Gasspeichern ist die Berücksichtigung der mechanischen Dispersion wichtig, da diese einen deutlich größeren Einfluss haben kann als die strömungsunabhängige molekulare Diffusion.

Der Betrieb von Untergrundwasserstoffspeichern erfolgt zyklisch mit abwechselnden Phasen von Injektion, Entnahme und Leerlauf. Die treibende Kraft während des Betriebs ist die Kompression und Expansion der Gasblase. Eine bestimmte Menge des Gases bleibt dabei immer in der Lagerstätte als sogenanntes Kissengas. Während des Betriebs können Mischprozesse zwischen verschiedenen Gasen weiterhin von Bedeutung sein, z.B. wenn das Restgas nicht vollständig verdrängt wurde oder wenn ein alternatives Gas als Kissengas verwendet wird (z.B. N_2 oder CO_2 [123, 107, 97]).

Mikroorganismen sind in den meisten Untergrundstrukturen bis in eine Teufe von über 1000 m vorhanden. Die Injektion von Wasserstoff könnte den Stoffwechsel vorhandener mikrobieller Spezies stimulieren. Mikrobielle Spezies, die Wasserstoff als Substrat verwenden können, werden als hydrogenotroph bezeichnet. Die damit verbundene Zellteilung führt zu einem Wachstum der mikrobiellen Populationen, die im porösen Gestein als Biofilm, verbunden mit einer Oberfläche oder frei schwimmend in der Wasserphase leben. Ein Beweis für dieses Verhalten ist z.B. die Aktivität methanogener Archaeen, welche in einigen der ehemaligen Stadtgasspeicher beobachtet wurde. Ebenfalls wurde die Aktivität von sulfatreduzierenden Bakterien in Stadtgas- und Erdgasspeichern beobachtet. Indikationen sind häufig die Produktion von H_2S und die daraus resultierenden Korrosionsprobleme [72]. Andere Quellen geben Hinweise, dass auch homoacetogene Archaeen und eisenreduzierende Bakterien stimuliert werden und Wasserstoff für ihren Stoffwechsel nutzen können [27, 81].

Die Verknüpfung zwischen Transport von Mikroorganismen, Wachstum, Substratverfügbarkeit und biologischer Umsetzung der Substrate resultiert in ein stark gekoppeltes dynamisches System [92]. Beteiligte physikochemische Prozesse sind Advektion, Diffusion, Dispersion, Größenausschluss, Siebung und Filtration. Die biologischen Prozesse sind Wachstum, Zerfall, Stoffwechsel, Chemotaxis, physiologische Anpassung, Anhaftung und Ablösung [92]. Verschiedene mathematische Modelle, die das gekoppelte Verhalten wiederspiegeln, sind für Grundwasser- und Gasspeicheranwendungen entwickelt worden. Die Modelle sind jedoch sehr unterschiedlich was die berücksichtigten Prozesse, die Längenskala und die Zeitskala betrifft.

Für die Modellierung von Transportprozessen in Untergrundwasserstoffspeichern steht eine große Auswahl an numerischen Werkzeugen zur Verfügung. Die Auswahl reicht von kommerziellen Softwarepaketen aus der Erdölindustrie über kombinierte kommerzielle und wissenschaftliche Softwarepakete bis hin zu Open-Source-Codes, die in der Regel nur für wissenschaftliche Anwendungen angewandt werden. Jedoch ist keines dieser Tools in seiner ursprünglichen Version in der Lage, alle relevanten Prozesse zu modellieren. Folglich ist es sinnvoll, ein Werkzeug zu verwenden, für das der Quellcode verfügbar ist und Anpassungen im mathematischen Modell möglich sind. Die Auswahl für diese Doktorarbeit war DuMu$^{\mathrm{X}}$ [43], das für die Implementierung eines bioreaktiven Transportmodells für Untergrundwasserstoffspeicher am geeignetsten erschien.

Analytische Modellierung des schwerkraftgetriebenen Zweiphasenflusses

Die herkömmliche Gasinjektion in den oberen Bereich der Lagerstätte könnte, aufgrund einer instabilen Verdrängung und somit einer unkontrollierten Ausbreitung der Gasblase über die tiefste Stelle der Struktur („spill point“) hinaus, zu Gasverlusten führen. Um dies zu vermeiden, kann das Gas in den unteren Bereich einer Lagerstätte mit horizontalen Barrieren injiziert werden. Bei dieser sogenannten „Selektiven Technologie“ spielt der durch die Barrieren verzögerte Aufstieg des Gases in einer wassergesättigten Lagerstätte eine entscheidende Rolle. Die exakte analytische Lösung des Problems der Gasinjektion für Zwei- und Dreikomponenten-Zweiphasensysteme wurde hergeleitet. Das Modell berücksichtigt die Lösung chemischer Komponenten in der Gas- und Wasserphase. Die Barrieren sind niedrig permeabel und haben unterschiedliche Permeabilitäten.

Im Fall von Zweikomponentengemischen (H_2 und H_2O oder CO_2 und H_2O) bleibt die Phasenzusammensetzung konstant. Der einzige qualitative Effekt, der diesen Fall von der nicht mischbaren Strömung unterscheidet, ist der Phasenübergang (Verdampfung), der auftritt, wenn ein im Ungleichgewicht stehendes Gas in eine wassergesättigte Lagerstätte injiziert wird. Die Elemente der Lösung sind: der Aufwärtsschock der Wasserverdrängung durch die Gasphase, Abwärtschocks unter jeder Barriere, die sich mit einer hohen Gassättigung ausbreiten und kontinuierliche Kurven (”rarefaction waves”) innerhalb der Barrieren. Die Lösung verhält sich qualitativ ähnlich wie bei der nicht mischbaren Strömung. Jedoch ist die Geschwindigkeit von Aufwärts- und Abwärtsschocks abweichend.

Im Fall der Dreikomponentenströmung (H_2, CO_2 und H_2O) ist das Verhalten komplizierter und durch eine variable Phasenzusammensetzung gekennzeichnet. Dies führt zum Auftreten eines neuen Aufwärtsschocks (bezeichnet als $C\alpha$-Schock). Dieser neue Schock wird durch den Effekt der Lösung verursacht und entspricht einer starken Veränderung der Zusammensetzung von Gas und Flüssigkeit. Hinter diesem Schock hat das Gas die injizierte Zusammensetzung und die Zusammensetzung der Flüssigkeit entspricht dem Gleichgewicht mit diesem Gas. Vor diesem Schock hat die Flüssigkeit jedoch die anfängliche Zusammensetzung, während die Gaszusammensetzung reinem H_2 entspricht.

Ein weiteres Phänomen, das im Fall mit drei Komponenten beobachtet wurde, ist die Kollision des abwärts gerichteten C-Schocks und des aufwärts gerichteten $C\alpha$-Schocks unterhalb der ersten Barriere. Der neue Schock, der durch die Kollision entsteht, ist instabil und zerfällt in zwei Schocks. Einer von ihnen ist ein C-Schock und bewegt sich nach oben, während der andere ein $C\alpha$-Schock ist, der sich nach unten bewegt.

Für ein periodisches Medium, bei dem die Barrieren die gleiche Permeabilität aufweisen, tritt ein Abwärtsschock bzw. eine Gasansammlung nur unterhalb der ersten Barriere auf. Zusätzliche Abwärtsschocks unter den darüberliegenden Barrieren erscheinen nur dann, wenn die Permeabilität der Barrieren von unten nach oben abnimmt. Die Wachstumsgeschwindigkeit der Gasansammlung unter der ersten Barriere ist viermal höher als die unter der zweiten Barriere (siehe Abb. 3.9).

Wasserstoff steigt in periodischen Domänen mehr als fünfmal schneller nach oben als CO_2. Dabei erzeugt H_2 signifikantere Gasansammlungen unter den Barrieren.

Das zweidimensionale numerische Modell mit undurchlässigen Barrieren zeigt ebenfalls den Effekt eines verzögerten Gasaufstiegs, wobei die Barrieren umströmt werden müssen. Je größer die areale Ausdehnung der Barrieren, desto größer ist die zeitliche Verzögerung des Gasaufstiegs.

Durch einen Vergleich mit der numerischen Lösung in 2D wurde gezeigt, dass ein 1D-Modell mit niedrig permeablen Barrieren ein 2D-Modell mit undurchlässigen Barrieren ersetzen kann. Die Permeabilität der niedrig permeablen Barrieren muss nach einem bestimmten Gesetz nach oben hin abnehmen.

Es kann zusammengefasst werden, dass sowohl niedrig permeable als auch undurchlässige Barrieren den Aufstieg des Gases verlangsamen. Eine Schichtung mit zunehmender Heterogenität nach oben bietet eine günstige Situation. In jedem Fall müssen die Barrieren eine große areale Ausdehnung haben, was zu einer stark verzögerten Ankunft des Gases unterhalb des Deckgesteins führt.

Mathematisches Modell für den bioreaktiven Zweiphasenfluss

Es wurde ein mathematisches Modell entwickelt, welches das hydrodynamische Verhalten von Untergrundwasserstoffspeichern gekoppelt mit biochemischen Reaktionen und mikrobieller Populationsdynamik beschreibt. Es berücksichtigt den Stoffwechsel von vier hydrogenotrophen mikrobiellen Spezies und umfasst den Fluss und Transport von sieben Komponenten in zwei mobilen Phasen und zwei Gesteinskomponenten. Das mathematische Modell besteht aus zwei Gruppen von Bilanzgleichungen. Die erste Gleichungsgruppe ist die Populationsdynamik für alle beteiligten mikrobiellen Spezies:

$$\frac{\partial n_m}{\partial t} = \underbrace{\psi_m^{\text{growth}} \cdot n_m}_{\text{Wachstum}} - \underbrace{\psi_m^{\text{decay}} \cdot n_m}_{\text{Zerfall}} + \underbrace{\nabla \cdot (D_m \nabla n_m)}_{\text{Transport/Diffusion}} \tag{D.1}$$

Die zweite Gruppe ist die molare Bilanz für alle beteiligten chemischen Komponenten:

$$\begin{aligned}
&\phi \frac{\partial \left(\rho_g c_g^k S_g + \rho_w c_w^k S_w\right)}{\partial t} \\
&+ \underbrace{\nabla \cdot \left(-\rho_g \; c_g^k \frac{K k_{rg}}{\mu_g} \cdot (\nabla P_g - \hat{\rho}_g g) - \rho_w c_w^k \frac{K k_{rw}}{\mu_w} \cdot (\nabla P_w - \hat{\rho}_w g) \right)}_{\text{Advektiver Transport}} \\
&+ \underbrace{\nabla \cdot \left(-\rho_g \left(D_{\text{diff},g}^k + D_{\text{disp},g}^k \right) \nabla c_g^k - \rho_w \left(D_{\text{diff},w}^k + D_{\text{disp},w}^k \right) \nabla c_w^k \right)}_{\text{Diffusiver/dispersiver Transport}} \\
&= \underbrace{\phi \sum_m \gamma_m^k \frac{\psi_m^{\text{growth}}}{Y_{m,e}} n_m}_{\text{Biochemische Reaktionen}}
\end{aligned} \tag{D.2}$$

Für CO_2 als Kohlenstoffquelle und die Gesteinskomponenten wurde die Bilanzgleichung leicht abweichend formuliert. Die Kopplung beider Gleichungsgruppen entsteht durch den Term der biochemischen Reaktionen, wel-

cher einen proportionalen Zusammenhang mit dem mikrobiellen Wachstum und der Populationsgröße hat.

Für die Formulierung der Populationsdynamik wurden drei substratlimitierte Wachstumsmodelle und zwei Zerfallsmodelle verglichen. Keines der Modelle zeigt die anfängliche Verzögerung und die stationäre Phase, welche häufig in Batchkulturversuchen im Labor beobachtet wird. Nur das Modell von Panfilov [100] zeigt die Beschleunigungsphase.

Parameter für die mikrobielle Populationsdynamik und die biochemischen Reaktionen wurden in der Literatur gesucht und zusammengefasst. Die Parameter sind für alle enthaltenen mikrobiellen Spezies außer für eisenreduzierende Bakterien verfügbar. Einige der Parameter sind in einem Bereich über bis zu zwei oder drei Größenordnungen unsicher.

Stabilität des dynamischen Systems

In Bezug auf das unerwartete Verhalten, das für den Stadtgasspeicher in einer antiklinalen Aquiferstruktur in der Nähe von Lobodice (Tschechische Republik) berichtet wurde, ist die Stabilität des dynamischen Systems untersucht worden. Dafür wurde das mathematische Modell auf ein System von zwei gewöhnlichen Differentialgleichungen reduziert und anhand der Theorie für Differentialgleichungen analysiert.

Wenn zwei Substrate (H_2 und CO_2) injiziert werden, führt der methanogene Metabolismus zu einer kontinuierlichen Umsetzung in CH_4 und H_2O. Wenn die mittleren Injektions- und Produktionsraten identisch mit den Raten der biochemischen Reaktion sind, befindet sich die Lagerstätte in einem Gleichgewichtszustand. Abhängig von der Stabilität des Gleichgewichtspunktes zeigt die Lagerstätte unterschiedliche dynamische Verhaltensweisen.

Es wurde gezeigt, dass das reduzierte Gleichungssystem einen instabilen oder stabilen Gleichgewichtspunkt haben kann. Die Rate q kann als Parameter verwendet werden, um dieses Verhalten zu kontrollieren. In einem gewissen Bereich für q erscheint ein stabiler Grenzzyklus, der den Gleichgewichtspunkt umläuft. In der Literatur wird dieses Verhalten als Hopf-Bifurkation bezeichnet.

Die Möglichkeit einer Turinginstabilität wurde aus einem reduzierten Reaktions-Diffusions-Modell mit zwei Gleichungen abgeleitet. Anhand der hergeleiteten Turingbedingungen kann der Wertebereich für q bestimmt werden, der zu einer Turinginstabilität führt.

Numerische Simulationen des vollständigen Modells für den bioreaktiven Zweiphasentransport wurden unter den hergeleiteten Bedingungen durchgeführt. Unter Grenzzyklusbedingungen zeigt die vereinfachte Lagerstätte zeitliche Oszillationen in der mikrobiellen Dichte und den Gasphasenkonzentrationen. Unter Turingbedingungen zeigen die Ergebnisse räumliche Oszillationen. Dabei wurden verschiedene räumliche Muster mit abwechselnden Bereichen hoher mikrobieller Dichte oder hoher Wasserstoffkonzentration beobachtet.

Numerische Modellierung von Speicherzyklen

Das mathematische Modell ist numerisch auf der Grundlage von DuMu$^{\mathrm{X}}$ implementiert worden. Die zugrundeliegenden Gleichungen in DuMu$^{\mathrm{X}}$ wurden adaptiert und Anpassungen hinsichtlich der zusätzlichen Komponenten und des Gitters wurden durchgeführt. Zusätzlich sind mehrere neue Algorithmen, z.B. für die Speicherinitialisierung, die Fluidinjektion/-produktion und die Nachverarbeitung, implementiert worden.

Eine Simulationsstudie der Gasinjektion in eine zweidimensionale synthetische Lagerstätte zeigte einige signifikante Unterschiede in Abhängigkeit von der Injektionsrate. Bei niedriger Injektionrate sind die Gravitationskräfte dominant und die Verdrängung des Wassers ist gleichmäßig. Bei höherer Injektionsrate werden jedoch die viskosen Kräfte dominant und die Verdrängung des Wassers wird instabil. Laterale Gasfinger beginnen sich unterhalb des Deckgesteins in Richtung des linken und rechten Rands der Lagerstätte auszubreiten. Es wurde gezeigt, dass sich Wasserstoff lateral schneller ausbreitet als Methan.

Ein simuliertes Speicherszenario in einer zweidimensionalen synthetischen Lagerstätte zeigte, dass in vorhersagenden Simulationsstudien die mechanische Dispersion und biochemischen Reaktionen bedeutend sein können. Die Mischzone zwischen dem initialen und dem injizierten Gas ist viel größer,

wenn die mechanische Dispersion in der Simulation berücksichtigt wird. Infolgedessen ist die vorhergesagte Wasserstoffkonzentration im produzieren Gas um 15 Prozentpunkte geringer als in der Simulation ohne mechanische Dispersion. In einer gekoppelten bioreaktiven Simulation beginnen mikrobielle Populationen zu wachsen, wenn Wasserstoff in die Lagerstätte injiziert wird. Der anfänglich auftretende Bereich mit einer hohen mikrobiellen Dichte um den Injektionspunkt breitet sich ähnlich einer Welle in der Lagerstätte aus. Die höchste mikrobielle Aktivität befindet sich immer an der H_2-Konzentrationsfront, an welcher die Mikroorganismen Zugang zu beiden Substraten haben. Die biochemischen Reaktionen führen zu beträchtlichen Produktionen von CH_4 und H_2S in der Lagerstätte. Folglich ist die H_2-Konzentration im produzierten Gas viel geringer als in der Simulation ohne biochemische Effekte. Eine geringe Menge an H_2S wird ebenfalls mitproduziert.

Ein realistisches Speicherszenario wurde in einem dreidimensionalen Gittermodell simuliert. Die Simulationen zeigten, dass das Verhalten in Abhängigkeit von der injizierten Gaszusammensetzung charakteristisch unterschiedlich sein kann. Wenn reiner Wasserstoff injiziert wird, haben nur zu Beginn biochemische Reaktionen einen starken Einfluss. Der Elektronenakzeptor (in diesem Fall CO_2) ist sehr schnell verbraucht und die Reaktionsgeschwindigkeiten werden sehr niedrig. Die resultierenden kumulativen Energieverluste während der dreijährigen Simulation sind ungefähr $2,2$ % der Speicherkapazität. Wenn jedoch ein Gasgemisch aus H_2 und CO_2 injiziert wird, bleiben die biochemischen Reaktionsraten hoch, da die Lagerstätte während jeder Injektionsphase mit beiden Substraten aufgefüllt wird. In diesem Fall beläuft sich der kumulative Energieverlust über drei Jahre auf etwa $18,8$ % der Speicherkapazität.

Schlussfolgerungen

- Im Vergleich zu der Untergrundspeicherung von Erdgas, welche seit vielen Jahren etabliert ist, zeigt die Untergrundwasserstoffspeicherung einige signifikante Unterschiede. Wasserstoff hat eine sehr geringe Dichte und Viskosität, wodurch der Verdrängungsprozess von Wasser instabil sein kann und Effekte wie z.B. „viscous fingering“ und „gravity overriding“ auftreten. Wenn hingegen ein Restgas verdrängt wird,

findet eine starke Vermischung der Gase mit verschiedenen Zusammensetzungen statt. Zusätzlich zu den hydrodynamischen Effekten ist Wasserstoff ein geeigneter Elektronendonator für den Stoffwechsel verschiedener mikrobieller Spezies, welche sich häufig in Untergrundstrukturen befinden. Folglich stimuliert die Injektion von Wasserstoff die Aktivität der Mikroorganismen und Probleme können entstehen. Vier verschiedene hydrogenotrophe Spezies können für Wasserstoffspeicher von Bedeutung sein: methanogene Archaeen, homoacetogene Archaeen, sulfatreduzierende Bakterien und eisenreduzierende Bakterien. All diese Prozesse müssen bei der numerischen Modellierung von Wasserstoffspeicheroperationen berücksichtigt werden. In der originalen Version ist jedoch keines der existierenden Modellierungswerkzeuge für Fluss- und Transportprozesse in Untergrundstrukturen in der Lage alle Prozesse wiederzuspiegeln.

- Eine alternative Operationsmethode für Gasspeicher, welche die laterale Ausbreitung des Wasserstoffs verhindert, wurde vorgestellt. Bei der sogenannten „Selektiven Technologie“ wird der Wasserstoff unten in eine Speicherstruktur mit niedrig permeablen oder impermeablen horizontalen Barrieren injiziert. Das Wasserstoffgas wird zurückproduziert sobald es das Deckgestein erreicht hat. Die Verzögerung durch den Aufstieg des Gases spielt eine zentrale Rolle bei dieser Methode. Analytische und numerische Untersuchungen haben die Machbarkeit dieser Methode demonstriert. Es wurde gezeigt, dass Gasansammlungen unter den Barrieren entstehen, welche die Aufstiegsgeschwindigkeit des Gases stark reduzieren. Die exakte Aufstieggeschwindigkeit ist anhand der analytischen Lösung bestimmt worden. Die eindimensionale analytische Lösung bestätigte sich durch einen Vergleich mit der zweidimensionalen numerischen Lösung.

- Ein mathematisches Modell für die bioreaktive Zweiphasenströmung in Untergrundwasserstoffspeichern wurde im Kontinuumsmaßstab entwickelt. Das Modell koppelt die hydrodynamischen Prozesse (Advektion, molekulare Diffusion und mechanische Dispersion) mit der mikrobiellen Populationsdynamik und biochemischen Reaktionen. Vier metabolische Prozesse sind enthalten: Methanogenese, Sulfatreduktion, Homoacetogenese und Eisenreduktion. Parameter für die mikrobiologischen Effekte wurden aus einer Literaturrecherche bereitgestellt.

- In Bezug auf die Beobachtungen bei einem ehemaligen Stadtgasspeicher ist die Stabilität des gekoppelten mathematischen Modells untersucht worden. Die analytische Analyse zeigt die Möglichkeit zeitlicher und räumlicher Schwankungen in den Gaskomponentenkonzentrationen und der mikrobiellen Dichte, wenn eine Mischung aus H_2 und CO_2 injiziert wird. Numerische Simulationen unter bestimmten abgeleiteten Bedingungen haben dieses Verhalten demonstriert. Auf diese Weise verhält sich der Untergrundspeicher wie ein Bioreaktor.
- Das mathematische Modell für den bioreaktiven Zweiphasentransport in Untergrundwasserstoffspeichern wurde numerisch auf der Grundlage von DuMu$^{\mathrm{X}}$ implementiert. Mehrere Simulationsstudien sind in synthetischen zweidimensionalen und in realistischen dreidimensionalen geologischen Modellen durchgeführt worden. Es zeigte sich, dass die geringe Dichte und Viskosität von Wasserstoff eine instabilere Verdrängung verursacht als bei der Methaninjektion. Die Simulation verschiedener Speicherszenarien hat zusätzlich bewiesen, dass mechanische Dispersion und biochemische Reaktionen einen wichtigen Einfluss in Vorhersagestudien haben. Signifikante Energieverluste können durch biochemische Reaktionen auftreten. Insbesondere sind die Energieverluste sehr hoch, wenn ein Gasgemisch aus H_2 und CO_2 injiziert wird. Ebenfalls wurde in einer der Speicherszenarien gezeigt, dass H_2S durch sulfatreduzierende Bakterien produziert wird und das entnommene Gas sauer ist.
- Es ist gezeigt worden, dass das entwickelte numerische Werkzeug für Vorhersagestudien des gekoppelten hydrodynamischen und bioreaktiven Verhaltens in Untergrundwasserstoffspeichern verwendet werden kann. Es ist ratsam, dass solche Studien von Gasspeicherbetreibern für die Planung und den Betrieb durchgeführt werden. Jedoch sollte zuerst ein Abgleich mit gemessenen Daten durchgeführt werden, um das Modell zu validieren, bevor es für zuverlässige Vorhersagestudien verwendet wird. Auf diese Weise können die unsicheren Parameter, wie z.B. die kinetischen Parameter der Mirkoorganismen und die Dispersivität, durch einen Vergleich der Simulationsergebnisse mit den beobachteten Daten aus dem Feld bestimmt werden. Eine Validierung des Modells konnte in dieser Arbeit nicht durchgeführt werden, da Felddaten bisher nicht verfügbar sind.

Appendix E

Résumé détaillé

Introduction

Le stockage de l'hydrogène souterrain est une proposition de solution prometteuse pour la compensation de l'approvisionnement en énergie électrique, qui est indispensable en raison de la variation de la production des sources d'énergie renouvelable. L'énergie renouvelable, qui est primairement produit au travers des centrales éoliennes et solaires est très dépendant des conditions météorologiques. En plus, la demande en courant varie à une échelle de temps journalière et saisonnière. Un stockage temporaire de l'énergie pour compenser cette variation apparait donc nécessaire ; pour cela plusieurs options sont actuellement en discussion [70]. Les stockages souterrains de l'hydroène, dans lesquels l'énergie est stockée sous forme d'énergie chimique indiquent une haute densité énergétique et offrent ainsi la possibilité de stocker l'énergie électrique à long terme ou de façon saisonnière [29]. Cette technologie englobe des installations d'électrolyses, qui utilisent excessivement l'énergie électrique produit, pour décomposer l'eau en oxygène et en hydrogène [70]. Pour le stockage et l'utilisation ultérieure de l'hydrogène, divers concepts sont disponibles [91, 45, 29] :

- « POWER-to-GAS » : l'hydrogène produit sera intégré dans les réseaux de gaz naturel existant. Les recherches ont montrées, que les concentrations dans une plage de pourcentage à un chiffre sont acceptables [90]. Ceci signifie, que même les stockages souterrains de gaz naturel seront exploités avec de faibles concentrations en hydrogène.
- « POWER-to-GAS-to-POWER » : l'hydrogène sera stocké pur dans les formations souterraines à l'instar des gisements de gaz naturel ou pétrolifère exploités, des aquifères ou des cavités salines [111]. Dans les périodes de hauts besoins en énergie, l'hydrogène sera extrait et

pourra être utilisé comme combustible pour des piles combustibles stationnaires ou des générateurs à moteur, qui sont reliés aux réseaux électriques de même qu'il pourra étre utilisé pour les les véhicules à piles combustibles.

Le concept de stockage des gaz souterrains est établi depuis près de 100 ans. Le stockage de l'hydrogène dans les cavités de sel est considéré comme facile [80]. Ce type de stockage existe actuellement en Teesside, en Grande Bretagne et au Texas aux Etats Unis. Jusqu'ici, l'expérience a été faite dans les réservoirs poreux uniquement avec le gaz naturel et les mélanges gazeux à l'instar des gaz de ville. Dans les réservoirs de gaz de ville, pour lesquels le gaz stocké a une concentration en hydrogène de 50 %, des anomalies se sont partiellement prouduites. Les réductions de volumes de gaz et les variations dans la composition du gaz ont été observées dans plusieurs de ces stockages. Il est supposé, que les réactions biochimiques sont responsables de cet effet, car une augmentation du nombre de cellules microbiennes dans l'eau de gisement a été mesurée [118, 21].

Pour tester l'utilisation des réservoirs poreux à la sensibilité à l'hydrogène, l'entreprise Hychico S.A. d'Argentine a débuté en 2013 une expérience préliminaire [114]. Ils ajoutèrent l'hydrogène comme traceur en écoulements de gaz et stockèrent le mélange gazeux dans un gisement de gaz et de pétrole épuisé. Les résultats de cette expérience sont jusqu'ici inédits. En outre, le RAG (Rohöl-Aufsuchungs Aktiengesellschaft) en Autriche commença également en 2015 un test préliminaire [12]. Ils injectèrent un mélange gazeux obtenu de gaz naturel à 10 % d'hydrogène dans un petit gisement de gaz naturel épuisé. Le prélèvement commença en été 2016. Les résultats de cet essai in situ sont attendus en 2017.

En Allemagne également, quelques projets de recherche ont été lancés depuis 2011 au travers du lancement du « initiative de stockage énergétique ». Ces projets traitent du thème hydrogène en tant que source d'énergie, et portent sur différents domaines de la chaîne de production de l'hydrogène, de son stockage et son transport jusqu'à son utilisation.

Revue de la littérature

Les gisements de gaz naturel épuisés et les aquifères se révèlent être des stockages poreux appropriés. Cependant, les processus déterminants pendant la phase de développement sont différents pour les aquifères, qui sont au début saturès en eau ou en saumure, et pour les gisements de gaz naturel épuisés, qui présentent une saturation en gaz résiduel.

Dans les aquifères pendant la phase de développement, une bulle de gaz, pour laquelle l'eau de l'aquifère doit être déplacée, est formée. L'efficacité du déplacement entre deux fluides immiscibles dépend de plusieurs facteurs. D'une part, les doigts visqueux peuvent créer au travers d'un front instable de déplacement par un relation défavorable des mobilités. Pour le système hydrogène-eau, il apparaît une estimation d'une relation des mobilités entre 2 et 5, pour laquelle un déplacement instable et la formation des doigts visqueux est à attendre. En outre, il existe, en raison de la faible densité de l'hydrogène, une tendance à une ségrégation par gravité. Par cet effet, le front de déplacement sera également instable. Si une vitesse de déplacement critique sera dépassée lors de l'injection, l'hydrogène inonde l'eau et se répand principalement sur la partie supérieure du gisement. De ce fait, les pertes de gaz peuvent se créer au-delà du point le plus bas de la structure.

Les gisements de gaz naturel épuisés ont très souvent une haute saturation en gaz résiduel. Le déplacement des gaz résiduels complètement miscible avec l'hydrogène, cause un mélange au niveau du front de déplacement. Ce mélange est influencé au travers de l'hétérogénéité et de l'anisotropie du milieu poreux, du relation des mobilités, de la différence des densités, de la diffusion moléculaire et de la dispersion mécanique entre différents gaz. Compte tenu des vitesses d'écoulement prévu dans les stockages de gaz, la prise en considération de dispersion mécanique est importante, car elle peut avoir une nette importante influence que la diffusion moléculaire, qui est indénpendant de la vitesse d'écoulement.

Les opérations des stockages souterrains de l'hydrogène se font de façon cyclique avec des phases alternées d'injection, d'extraction et de point mort. La force motrice durant ces opérations est la compression et l'expansion de la bulle de gaz. Une quantité déterminée de gaz demeure toujours dans le stockage en tant que gaz coussin. Durant l'opération, les processus de

mélange entre différents gaz peuvent également être importants ; tel est par exemple le cas lorsque le gaz résiduel n'a pas été complètement déplacé ou lorsqu'un gaz alternatif est utilisé comme gaz coussin (par ex. N_2 ou CO_2 [123, 107, 97]).

Les microorganismes sont présents dans la plupart des structures souterraines jusqu'à une profondeur de 1000 m. L'injection de l'hydrogène peut stimuler le métabolisme des espèces microbiennes existantes. Les espèces microbiennes capable d'utiliser l'hydrogène comme substrat, peuvent être qualifiés d'hydrogènotrophes ; la division cellulaire associée conduit à une croissance des populations microbiennes qui vivent dans les roches poreuses comme biofilm relié à une surface ou flottant librement dans la phase aqueuse. Une preuve de ce comportement est par exemple l'activité des archéens méthanogènes, qui ont été observés dans quelques anciens stockages de gaz de ville. L'activité des bactéries sulfato-réductrices a également été observée dans les stockages du gaz de ville et du gaz naturel. Les indications sont fréquemment, la production de H_2S et le problème de corrosion qui en résulte [72]. D'autres sources indiquent, que les archéens homoacétogènes et les bactéries ferro-réductrices sont stimulés et peuvent utiliser l'hydrogène pour leur métabolisme [27, 81].

La combinaison entre transport des microorganismes, disponibilité de substrat, croissance et transformation biologique de substrat aboutit à un fort système dynamique couplé [92]. Les processus physicochimiques participants sont l'advection, la diffusion, la dispersion, l'exclusion de taille, le tamisage et la filtration. Les processus biologiques sont la croissance, la désagrégation, le métabolisme, la chimiotaxie, l'ajustement physiologique, l'adhésion et le détachement. Différents modèles mathématiques, qui reflètent ce comportement couplé, ont été développés pour des applications en eau souterraine et en stockage du gaz. Les modèles sont cependant très différents, en ce qui concerne les processus considérés, l'échelle de longueur et de temps.

Pour la modélisation des processus de transport dans les stockages de l'hydrogène souterrains, un large éventail d'outils numériques est disponible au choix. Le choix s'étend des prologiciels commerciaux de l'industrie pétrolière en passant par les prologiciels commerciaux et académiques, jusqu'aux codes open sources, qui en règle générale ne sont utilisés que pour des applications académiques. Cependant, aucun de ces outils n'est capable, dans sa version originelle, de modéliser tous les processus pertinents. Par conséquent, il est

judicieux d'utiliser un outil, pour lequel le code source est disponible et les ajustements aux modèles mathématiques sont possibles ; l'outil choisi dans ce travail de doctorat est DuMu^{X} [43]. Ce dernier est apparu le plus approprié pour l'implémentation d'un modèle de transport bioréactif pour les stockages souterrains de l'hydrogène.

Modélisation analytique de flux à deux phases par gravité

La traditionnelle injection de gaz dans la région supérieure du gisement pourrait conduire à des pertes de gaz, en raison d'un déplacement instable et par conséquent, d'une propagation incontrôlée de la bulle de gaz au-delà des lieux les plus bas de la structure (« spill point »). Pour éviter celà, le gaz peut être injecté dans les régions inférieures du gisement avec des barrières horizontales. Par cette « technologie sélective », le ralentissement de la montée de gaz (dû aux barrières) dans un gisement saturé en eau a un rôle décisif. L'exacte solution analytique du problème de l'injection de gaz pour des systèmes à deux phases et à deux ou trois composants a été déduite. Le modèle considère la solution des composants chimiques dans la phase gazeuse et aqueuse. Les barrières sont faiblement perméables et ont des perméabilités différentes.

Dans le cas du mélange à deux composants (H_2 et H_2O ou CO_2 et H_2O), la composition des phases reste constante. L'unique effet qualitatif, qui distingue ce cas de l'écoulement immiscible est le changement de phase (évaporation) qui se produit, lorsqu'un gaz en état de déséquilibre est injecté dans un gisement saturé en eau. Les éléments de cette solution sont : le choc vers le haut du déplacement de l'eau au travers de la phase gazeuse, le choc vers le bas sous chaque barrières, qui se propagent avec une haute saturation en gaz et les coudes continuellement (« rarefaction waves ») à l'intérieure des barrières. Qualitativement, la solution se comporte similairement à un écoulement immiscible. Cependant, les vitesses des chocs vers le haut et vers le bas sont divergentes.

Dans le cas d'un écoulement à trois composants (H_2, CO_2 et H_2O), le comportement est compliqué et est marqué par une composition variable des phases. Ceci conduit à l'apparition d'un nouveau choc vers le haut (connu

sous le nom de Cα-choc). Ce nouveau choc est causé par l'effet de la solution, et correspond à un fort changement de la composition du gaz et du fluide. Derrière ce choc, le gaz a la composition injectée et la composition du fluide correspond à l'équilibre avec ce gaz. À l'avant de ce choc, le fluide a cependant la composition initiale, alors que la composition du gaz correspond à l'hydrogène pur.

Un autre phénomène, qui est observé dans le cas de trois composants, est la collision du C-choc orienté vers le bas et du Cα-choc orienté vers le haut sous la première barrière. Le nouveau choc, qui se crée lors de la collision est instable et se décompose en deux chocs ; l'un de ces derniers est un C-choc et se déplace vers le haut, tandis que l'autre, un Cα-choc, se déplace vers le bas.

Pour un milieu périodique, pour lequel les barrières présentes la même perméabilité, un choc vers le bas ou alors une accumulation du gaz se produit uniquement sous la première barrière. Des chocs supplémentaires sous les barrières se situant au-dessus apparaissent uniquement lorsque la perméabilité des barrières décroît du bas vers le haut. La vitesse de croissance d'accumulation des gaz sous la première barrière est quatre fois plus élevée que celle sous la deuxième barrière (voir Fig. 3.9).

L'hydrogène monte dans des domaines périodiques cinq fois plus rapidement vers le haut que le CO_2. En même temps, le H_2 produit une plus signifiante accumulation de gaz sous les barrières.

Le modèle numérique à deux dimensions et à barrières imperméable montre également l'effet d'un retard dans la montée du gaz, alors que les barrières doivent être entourées. Plus l'extension de la zone des barrières est grande, plus le retard temporel de la montée du gaz est grand.

Il a été montré, au travers d'une comparaison avec la solution numérique à deux dimensions, qu'un modèle unidimensionnel (1D) et à barrière à faible perméabilité peut remplacer un modèle bidimensionnel (2D) à barrière imperméable. La perméabilité des barrières faiblement perméable doit décroitre vers le haut selon une certaine loi.

Il peut être résumé, que la montée du gaz est ralenti aussi bien pour les barrières à faible perméabilité que pour les barrières imperméable. Une stratification à hétérogénéité croissante vers le haut offre une situation favorable.

Dans tous les cas, les barrières ont une grande zone d'extension, ce qui conduit à un fort retard dans l'arrivée des gaz sous la roche couverture.

Modèle mathématique pour le transport bioréactif à deux phases

Un modèle mathématique, qui décrit le comportement hydrodynamique des stockages de l'hydrogène souterrains couplé aux réactions biochimiques et à la dynamique des populations microbiennes, a été développé. Il considère le métabolisme de quatre espèces microbiennes hydrogènotrophes, et englobe l'écoulement et le transport de sept constituants dans deux phases mobiles et deux composantes rocheuses. Le modèle mathématique se compose de deux groupes d'équations bilans. La première équation bilan est la dynamique de la population pour toutes les espèces microbiennes participantes :

$$\frac{\partial n_m}{\partial t} = \underbrace{\psi_m^{\text{growth}} \cdot n_m}_{\text{Croissance}} - \underbrace{\psi_m^{\text{decay}} \cdot n_m}_{\text{Désagrégation}} + \underbrace{\nabla \cdot \left(D_m \nabla n_m\right)}_{\text{Transport/Diffusion}} \tag{E.1}$$

Le deuxième groupe est le bilan molaire pour tous les constituants chimiques participants :

$$\begin{aligned}
&\phi \frac{\partial \left(\rho_g c_g^k S_g + \rho_w c_w^k S_w\right)}{\partial t} \\
&+ \underbrace{\nabla \cdot \left(-\rho_g \; c_g^k \frac{K k_{rg}}{\mu_g} \cdot \left(\nabla P_g - \hat{\rho}_g g\right) - \rho_w c_w^k \frac{K k_{rw}}{\mu_w} \cdot \left(\nabla P_w - \hat{\rho}_w g\right) \right)}_{\text{Transport advectif}} \\
&+ \underbrace{\nabla \cdot \left(-\rho_g \left(D_{\text{diff},g}^k + D_{\text{disp},g}^k\right) \nabla c_g^k - \rho_w \left(D_{\text{diff},w}^k + D_{\text{disp},w}^k\right) \nabla c_w^k \right)}_{\text{Transport diffusif/dispersif}} \\
&= \underbrace{\phi \sum_m \gamma_m^k \frac{\psi_m^{\text{growth}}}{Y_{m,e}} n_m}_{\text{Réactions biochimiques}}
\end{aligned} \tag{E.2}$$

Pour le CO_2 (en tant que source de carbone) et les constituants rocheux, l'équation bilan a été juste formulée un peu différemment. Le couplage des deux groupes d'équations se fait au travers du terme des réactions biochimiques, qui ont un rapport de proportionnalité avec la croissance microbienne et la taille de la population.

Pour la formulation de la dynamique de population, trois modèles de croissance à substrat limité et deux modèles de désagrégation ont été comparés. Aucun de ces modèles n'a montré la phase du latence et la phase stationnaire, qui est fréquemment observé en laboratoire dans les essais de culture par lot. Le modèle de Panfilov [100] est le seul à avoir présenté une phase d'accélération.

Les paramètres pour la dynamique de population microbienne et les réactions biochimiques ont été cherchés et résumés de la littérature. Les paramètres sont disponibles pour toutes les espèces microbiennes contenues, sauf pour les bactéries ferro-réductrices. Certains paramètres sont incertains dans un domaine au dessus de deux ou de trois ordres de grandeur.

Stabilité du système dynamique

Par rapport au comportement inattendu, qui a été rapporté dans le cas d'un stockage du gaz de ville dans une structure d'aquifère anticlinale à proximité de Lobodice (République Tchèque), la stabilité du système dynamique a été analysée. Pour ce faire, le modèle mathématique a été réduit à un système à deux équations différentielles ordinaires, et analysé à l'aide de la théorie des équations différentielles.

Lorsque deux substrats (H_2 und CO_2) sont injectés, le métabolisme du méthanogène conduit à une transformation continuelle en CH_4 et H_2O. Lorsque les débits moyens d'injection et de production sont identiques aux vitesses des réactions biochimiques, le gisement se trouve dans un état d'équilibre. Dépendamment de la stabilité du point d'équilibre, le gisement présente différents comportements dynamiques.

Il a été montré que, le système d'équation réduit peut avoir un point d'équilibre stable ou instable. Le débit q peut être utilisé comme paramètre pour contrôler ce comportement. Dans un certain domaine pour q, il apparaît un

cycle limite stable qui tourne autour du point d'équilibre. Dans la littérature, ce comportement est désigné par « Hopf-Bifurcation ».

La possibilité d'une instabilité de Turing a été dérivée d'un modèle réaction-diffusion réduit à deux équations. À l'aide des conditions de Turing dérivées, le domaine des valeurs de q, qui conduit à une instabilité de Turing, peut être déterminé.

Les simulations numériques du modèle complet des transports bioréactifs à deux phases ont été effectuées sous les conditions dérivées. Sous des conditions cycliques limites, le gisement simplifié montre une oscillation temporelle dans la densité microbienne et les concentrations dans la phase gazeus. Sous les conditions de Turing, les résultats présentent des oscillations spatiales. Ce faisant, diverses maquettes spatiales à domaines alternés, à haute densité microbienne ou à haute concentration en hydrogène ont été observés.

Modélisation numérique des cycles de stockage

Le modèle mathématique a été numériquement implémenté sur la base de DuMu$^{\mathrm{X}}$. Les équations sous-jacentes dans DuMu$^{\mathrm{X}}$ ont été adaptées et ajustments au vue des constituants additionnels et la grille ont été introduits. En plus, plusieurs nouveaux algorithmes, à l'instar des algorithmes pour l'initialisation du stockage, l'injection/production du fluide et le traitement ultérieure, ont été implémentés. Une étude de simulation de l'injection de gaz dans un gisement synthétique à deux dimensions, montre quelques différences significatives dépendantes du débit d'injection. Pour un faible débit d'injection, les forces de gravité sont dominantes et le déplacement de l'eau est régulier. Pour un haut débit d'injection, les forces de viscosité sont dominantes et le déplacement de l'eau devient instable. Les doigts de gaz latéraux commencent à se répandre sous la roche couverture vers le bord gauche et droite du gisement. Il a été montré, que l'hydrogène se répand latéralement plus rapidement que le méthane.

Un scénario de stockage simulé dans un gisement synthétique à deux dimensions montre, que dans les études de simulations prédictives, le mécanisme de dispersion mécanique et les réactions biochimiques peuvent être significatifs. La zone de mélange entre le gaz initiale et le gaz injecté est plus

grande, lorsque le mécanisme de dispersion est considéré dans la simulation. Par conséquent, la concentration d'hydrogène prédite dans la production du gaz est de 15 points de pourcentage plus faible que dans la simulation sans mécanisme de dispersion. Dans une simulation bioréactif couplée, la population microbienne commence à croître, lorsque l'hydrogène est injecté dans le gisement. La région initiale se produisant avec une haute densité microbienne autour du point d'injection se répand comme une vague dans le gisement. La plus haute activité microbienne se trouve toujours au front de concentration de H_2, auquel les microorganismes ont un accès aux deux substrats. Les réactions biochimiques conduisent à une production considérable de CH_4 et H_2S dans le gisement. Par conséquent, la concentration de H_2 du gaz produit est très faible comparée à la simulation sans effet biochimique. Une faible quantité en H_2S est également extraire.

Un scénario de stockage réaliste a été simulé dans un grille à trois dimensions. Les simulations montrent, que le comportement dépendant de la composition du gaz injecté peut être caractéristiquement différent. Lorsque l'hydrogène pur est injecté, c'est uniquement au début que les réactions biochimiques ont une forte influence. L'accepteur d'électron (dans ce cas CO_2) est très vite consommé et les vitesses de réaction deviennent très basses. Les pertes d'énergie cumulatives résultantes des trois années de simulations, représentent environ 2,2 % de la capacité de stockage. Cependant, lorsque le mélange gazeux à partir de H_2 et CO_2 est injecté, les vitesses de réactions biochimiques restent hauts, puisque le gisement est rempli avec les deux substrats au cours de chaque phase d'injection. Dans ce cas, la perte d'énergie cumulative sur trois ans s'élève à environ 18,8 % de la capacité de stockage.

Conclusions

- En comparaison avec le stockage souterrain du gaz naturel qui est établi depuis plusieurs années, le stockage souterrain de l'hydrogène montre des différences significatives. L'hydrogène a une très faible densité et une faible viscosité, à cause desquelles le processus de déplacement de l'eau peut être instable et des effets tels que « viscous fingering » et « gravity overriding » se produisent. Si par contre, un gaz résiduel est déplacé, un fort mélange de gaz de compositions différentes

s'observe. En plus des effets hydrodynamiques, l'hydrogène est un donneur d'électron approprié pour le métabolisme d'espèces microbiennes différentes, qui se trouvent fréquemment dans les structures souterraines. Par conséquent, l'injection de l'hydrogène simule l'activité des microorganismes et des problèmes peuvent apparaitre. Quatre espèces hydrogènotrophes différentes peuvent être importantes pour le stockage de l'hydrogène : les archéens méthanogènes, les archéens homoacetogènes, les bactéries sulfato-réductrices et les bactéries ferro-réductrices. Tous ces processus doivent être considérés par la modélisation numérique des opérations de stockage de l'hydrogène. Dan leurs versions originales, aucun des outils de modélisation existants (pour les processus d'écoulement et de transport dans les structures souterraines) n'est à même de refléter tous les processus.

- Une méthode alternative pour le stockage du gaz, qui empêche l'extension latérale de l'hydrogène a été présentée. Par la méthode dite « technologie sélective », l'hydrogène est injecté en bas d'une structure de stockage avec des barrières horizontales faible perméabilité ou imperméables. L'hydrogène gazeux est reproduit dès qu'il atteint la roche couverture. Le retard à la montée de gaz joue un rôle central dans cette méthode. Les analyses analytiques et numériques ont démontrées la faisabilité de cette méthode. Il a été montré, que les accumulations de gaz sous les barrières, qui réduisent fortement la vitesse de montée de gaz, apparaissent. L'exacte vitesse de montée de gaz a été déterminée sous la base de la solution analytique. La solution analytique unidimensionnelle se confirme au travers d'une comparaison avec la solution numérique bidimensionnelle.

- Un modèle mathématique pour le transport bioréactif à deux phases dans les stockages souterrains de l'hydrogène a été développé dans une échelle de continuum. Le modèle couple les processus hydrodynamiques (advection, diffusion moléculaire et dispersion mécanique) avec la dynamique de population microbienne et les réactions biochimiques. Quatre processus métabolitiques sont inclus : méthanogenèse, réduction du sulfate, homoacétogenèse et réduction du fer. Les paramètres pour les effets microbiologiques ont été proviennent de la revue de la littérature.

- En rapport aux observations dans des anciens stockages du gaz de

ville, la stabilité du modèle mathématique couplé a été étudiée. L'analyse analytique montre la possibilité d'une oscillation temporelle et spatiale dans la concentration des constituants des gaz et la densité microbienne, lorsqu'un mélange de H_2 et de CO_2 est injecté. Les simulations numériques sous des conditions dérivées ont démontrées ce comportement. De cette manière, le stockage souterrain se comporte comme un bioréacteur.

- Le modèle mathématique pour le transport bioréactif à deux phases dans les stockages de l'hydrogène souterrains a été numériquement implémenté sur la base de DuMu$^{\mathrm{X}}$. Plusieurs études de simulation ont été conduites dans des modèles synthétiques bidimensionnelles et dans un modèle géologique réaliste à trois dimensions. Il en ressort, que la faible densité et la faible viscosité de l'hydrogène cause un déplacement plus instable, comparé à l'injection du méthane. La simulation de divers scénarios de stockage indique de plus, que le mécanisme de dispersion mécanique et des réactions biochimiques ont une influence importante dans les études prédictives. Les pertes significatives d'énergie sont très hautes, lorsque le mélange gazeux de H_2 et de CO_2 est injecté. En outre, il a été montré dans l'un des scénarios de stockage, que H_2S est produit par des bactéries sulfato-réductrices et que le gaz extrait est acide.

- L'outil numérique développé peut être utilisé pour les études de prédiction du comportement couplé hydrodynamique et bioréactif dans les stockages souterrains de l'hydrogène. Il est opportun, que de telles études doivent être menées par des opérateurs de stockage de gaz pour la planification et l'opération. Cependant, une comparaison avec les données mesurées doit tout d'abord être réalisée pour valider le modèle, avant qu'il ne soit utilisé pour des études fiables de prédiction. De cette manière les paramètres incertains (comme par exemple les paramètres cinétiques des microorganismes et la dispersion mécanique) peuvent être déterminés au travers d'une comparaison des résultats de simulation avec les données observés sur le terrain. Une validation du modèle n'a pas pu être réalisée dans ce travail, car les données de terrain sont jusqu'ici indisponibles.